DYNAMIQUE DU RIFTING CONTINENTAL DE 30 Ma A L'ACTUEL DANS LA PARTIE SUD EST DU TRIANGLE AFAR. TECTONIQUE ET MAGMATISME DU RIFT DE TADJOURA ET DES DOMAINES DANAKIL ET D'ALI SABIEH, REPUBLIQUE DE DJIBOUTI.

Mohamed Ahmed Daoud

THESE

Présentée pour l'obtention du diplôme de

DOCTORAT de l'Université de Bretagne Occidentale
Spécialité : GEOSCIENCES MARINES

Par

Mohamed AHMED DAOUD

Dynamique du rifting continental de 30 Ma à l'Actuel dans la partie Sud Est du Triangle Afar. Tectonique et magmatisme du rift de Tadjoura et des domaines Danakil et d'Ali Sabieh, République de Djibouti.

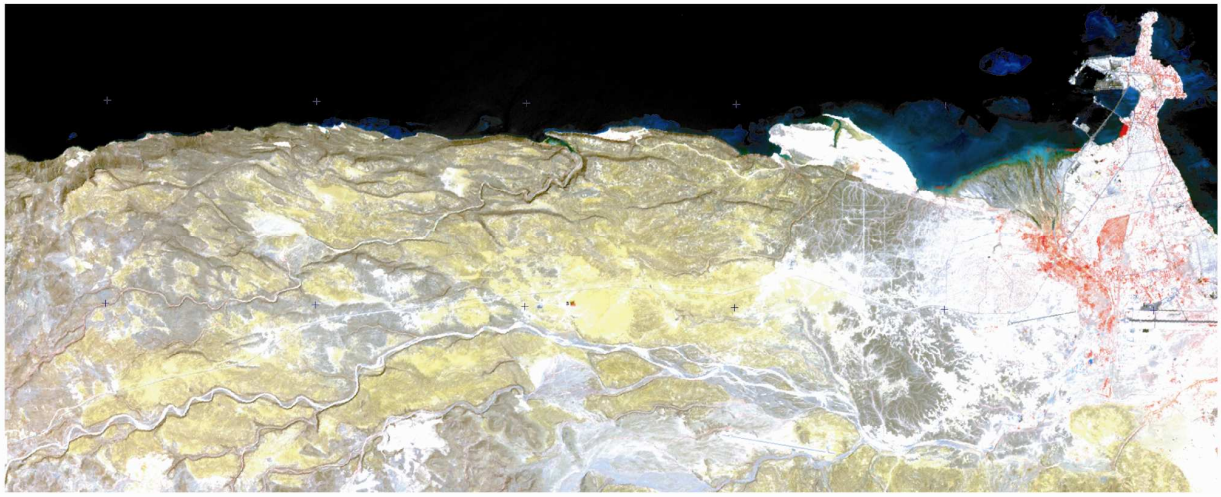

Soutenue le 19 juin 2008 devant le jury composé de :

M. Gilles Chazot	Professeur, IUEM, Brest	Examinateur
M. Bernard Colletta	Ingénieur, IFP	Examinateur
M. Jean Yves Cottin	Professeur, Univ. St Etienne	Rapporteur
M. Philippe Huchon	Professeur, Univ. Paris VI	Rapporteur
M. Mohamed Jalludin	Directeur Général, CERD Djibouti	Examinateur
M. Bernard Le Gall	CR/CNRS, IUEM, Brest	Directeur de thèse
M. René Maury	Professeur, IUEM, Brest	Co-encadrant
M. Joel Rolet	MC, IUEM, Brest	Co-encadrant

Brest, 2008

THESE

Présentée pour l'obtention du diplôme de

DOCTORAT de l'Université de Bretagne Occidentale
Spécialité : GEOSCIENCES MARINES

Par

Mohamed AHMED DAOUD

Dynamique du rifting continental de 30 Ma à l'Actuel dans la partie Sud Est du Triangle Afar. Tectonique et magmatisme du rift de Tadjoura et des domaines Danakil et d'Ali Sabieh, République de Djibouti.

Soutenue le 19 juin 2008 devant le jury composé de :

M. Gilles Chazot	Professeur, IUEM, Brest	Examinateur
M. Bernard Colletta	Ingénieur, IFP	Examinateur
M. Jean Yves Cottin	Professeur, Univ. St Etienne	Rapporteur
M. Philippe Huchon	Professeur, Univ. Paris VI	Rapporteur
M. Mohamed Jalludin	Directeur Général, CERD Djibouti	Examinateur
M. Bernard Le Gall	CR/CNRS, IUEM, Brest	Directeur de thèse
M. René Maury	Professeur, IUEM, Brest	Co-encadrant
M. Joel Rolet	MC, IUEM, Brest	Co-encadrant

Brest, 2008

REMERCIEMENTS

Je tiens à exprimer mes remerciements les plus sincères à toutes les personnes qui m'ont aidé et soutenu à réaliser ce travail.

Je tiens à remercier en tout premier lieu Bernard Le Gall qui a dirigé cette thèse dans la continuité de mon stage de DEA. Tout au long de ces années, il a su orienter mes recherches en me faisant découvrir la géologie structurale aussi bien sur le terrain que dans le laboratoire. Toujours disponible, il a su répondre à mes interrogations et mes besoins (scientifiques et autres) et s'est beaucoup investi dans la réalisation de ce travail avec passion et beaucoup d'amitiés. 'Kaxxa gadda gey' pour ton soutien !!

J'adresse mes remerciements aux membres de jury qui ont bien voulu accepter de juger ce travail.

Les résultats présentés ici sont le fruit d'un travail d'équipe. Mes plus vifs remerciements à René Maury, Joël Rolet et Jean-Alix Barrat pour leur participation et contribution dans leurs domaines respectifs.

Je tiens à exprimer toute ma gratitude à Jalludin Mohamed, Directeur du CERD, pour la confiance qu'il m'a accordé en m'acceptant dans son équipe scientifique du CERD et pour tout le soutien qu'il m'a apporté.

Je remercie également l'équipe et collègues du CERD qui ont participé et facilité les missions de terrain effectuées à Djibouti dans le cadre de ce travail. Plus particulièrement, un grand merci à Ali Abdillahi, agent comptable du CERD qui a toujours veillé à ce que les missions se déroulent dans les meilleurs conditions.

J'ai eu également un grand plaisir d'effectuer les missions de terrain à Djibouti avec Antoine Caminitti alias Tony. Toujours de bonne humeur et fin connaisseur de la géologie djiboutienne. Merci Tony pour tes conseils et ta participation fructueuse.

Ce travail a bénéficié du financement du projet Mawari géré par le CIFEG avec à la direction François Pinard et Sylvie Orlyk qui ont toujours répondu rapidement à mes sollicitations (administratives et financières). Merci beaucoup pour votre professionnalisme et efficacité sans égales.

Le travail scientifique initié dans le cadre de ma thèse, a aboutit à la signature d'une convention entre l'UBO et le CERD et tous mes remerciements s'adressent à Anne-Marie Galliou-Scanvion responsable au bureau des Relations Internationales de l'UBO pour avoir facilité cette démarche.

L'IUEM est un cadre privilégié pour effectuer une thèse. Merci à tous ceux qui m'ont aidé et conseillé durant mes travaux au sein de l'IUEM . Je remercie tout spécialement Dominique Gac pour son aide indispensable dans ma recherche bibliographique et pour sa disponibilité chaque fois que j'ai eu besoin d'elle.

Merci aussi à tous mes collègues thésards et amis de longue date du bureau et du laboratoire qui se reconnaitront ici.

Un grand merci à tonton Houmed Daoud et à sa chère épouse Amina Kamilo pour votre soutien et encouragement au quotidien.

Plus proche de moi, malgré la distance (c'est loin Brest !), je te remercie Rahma, pour ton soutien, ta patience et pour l'encouragement au quotidien que tu m'as témoigné.

SOMMAIRE

Résumé

Les résultats acquis au cours de ce travail à propos (i) des basaltes récents du Golfe de Tadjoura et (ii) les séries synrift initiales des domaines Ali Sabieh et Danakil apportent de nouvelles contraintes sur, respectivement, la cinématique récente du Rift Tadjoura et celle, plus ancienne, des zones marginales de la dépression Afar. Mais, ils apportent aussi des éléments permettant de discuter, à une échelle plus vaste, certains aspects de la dynamique du rift Afar, *sensu lato*.

- L'étude structurale des basaltes récents (2.8-1.1 Ma) des marges du Golfe de Tadjoura nous conduit à interpréter la structure générale du rift Tadjoura en termes d'hémi-graben, à vergence sud, développé au-dessus de traps antérieurs, et accommodant une extension estimée à 25-30%. L'âge décroissant des structures vers la partie axiale, immergée, du dispositif reflète la concentration progressive des déformations au cours du temps. L'analyse géométrique et statistique des populations de failles exposées le long des deux flancs de l'hémi-graben met en évidence, au niveau du système extensif méridional, un gradient croissant de déformation vers l'W, en direction de la zone transverse d'Arta. Ce dispositif est attribué au blocage frontal de la propagation des structures axiales du Golfe contre une discontinuité mécanique pré-existante. Dans le modèle cinématique proposé, le transfert de l'extension depuis le rift Tadjoura vers la zone du Ghoubbet s'effectue, non pas par l'intermédiaire de structures en échelon, mais par un saut de rift (en sénestre) de part et d'autre de cette discontinuité sub-méridienne à polarité 'Mer Rouge'.
- L'étude structurale et géochimique/géochronologique des séries volcaniques d'Ali Sabieh et de leur substratum mésozoïque démontre les faits suivants :

. Les ensembles volcaniques initiaux se mettent en place entre 26-19 Ma (complexe intrusif-effusif d'Ali Sabieh), cad. environ 6 Ma après les traps éthiopiens et yemenites qui n'ont donc pas d'équivalents dans ce secteur intermédiaire.

. La partie intrusive du complexe magmatique est interprétée en termes de laccolithe dont la mise en place provoque la structuration antiformale de la couverture mésozoïque, puis son démantelement partiel, sous forme d'enclaves, lors d'un processus de 'block stoping'.

. L'antiforme d'Ali Sabieh implique jusqu'aux séries acides Mablas (15-11 Ma) et il est scéllé, sur ses flancs, par les basaltes Somali (7.2-3.0 Ma) et du Dalha (8.6-3.8 Ma).

- Un tout autre mécanisme est proposé pour l'édification des reliefs Danakil qui résultent de mouvements verticaux beaucoup plus jeunes, postérieurs (ou synchrones) des Basaltes Stratoïdes, et d'origine probablement tectonique, en liaison avec le rifting Tadjoura et/ou Asal.
- Ces résultats ont aussi des implications sur la dynamique de l'ensemble du dispositif Afar, et de nouvelles hypothèses sont proposées au sujet (i) du sens de propagation des axes de rift récents-actifs recoupant la dépression Afar et de leur appartenance aux systèmes Golfe d'Aden ou Mer Rouge, (ii) de la distribution spatiale du magmatisme initial (à 30 Ma), de type trap, au niveau de deux sous-provinces, séparées par un domaine amagmatique, et (iii) de l'évolution du domaine Danakil et de la nature de sa limite orientale avec la Mer Rouge, considérée comme une discontinuité héritée de premier ordre, de part et d'autre de laquelle les mécanismes de l'extension sont dominés par des processus, soit magmatiques (W), soit tectoniques (E).

Abstract

The results of our study about (i) the recent basaltic series in the Tadjoura Gulf and (ii) the oldest rift series in the Ali Sabieh and Danakil area supply new constraints about the recent-active kinematical history of the Tadjoura rift, and those previously recorded by the marginal zones of the Afar depression. Hypotheses are also attempted at a wider scale about the kinematic development of he Afar extensional system over the past 30 Ma.

- The structural analysis of the recent basaltic series in the TG allows us to regard the overall structure of the Tadjoura rift as a typical half-graben facing to the S, developed over older trap complexes, and accommodating a bulk extension of about 25-30%. The progressive younging of faulting towards the inner trough of the half-graben is the expression of focussing of strain with time along the axial part of the rift. From the geometrical and statistical analyses of onshore fault networks, a marked westerly increase of strain is documented along the southern fault belt, and is mechanically assigned to the frontal locking of axial fault tip propagation against the Arta submeridian fault zone. According to our alternative kinematic model, transfer of extension from the Tadjoura rift into the Ghoubbet-Asal trough operated via a rift jump on both sides of the Arta discontinuity (hard linkage), unstead of being accommodated by newly-formed en echelon fault structures (soft linkage).
- The structural and geochemical-radiometrical studies of older synrift volcanics and their Mesozoic substratum in the Ali Sabieh range shows the flowing facts as :

. Initial volcanics of the Ali Sabieh mafic complex were emplaced in the time range 26-19 Ma, i .e. 6 Ma later than the Ethiopian and Yemen trap series which are thus totally missing in the Ali Sabieh intermediate region.

. The intrusive part of the magmatic complex is interpreted as a mafic laccolith causing the antiformal structure of the Mesozoic cover during its uprise through shallow crustal level. Over the rising antiform, the arched Jurassico-Cretaceous sedimentary cover underwent fragmentation into detached xenoliths which later collapsed into the magma, as roof pendants typical of a block-stoping process.

. The ali Sabieh antiform involved up to the 15-11 Ma Mablas acidic series, whereas it is sealed by the trap basalts of the (7.2-3.0 Ma) Somali and (8.6-3.8 Ma) Dalha series.

- The causative mechanisms responsible for the edification of the Danakil range to the N are much younger, since they partly involved the Stratoid Basalts, and they are likely related to Tadjoura and/or Asal rift tectonics.
- Our results have some implications on the dynamical history of the Afar extensional system, as a whole, and new hypotheses are tentatively proposed to a number of key-issues dealing with : (i) the sens of propagation of the active rift axes extending throughout the Afar depression, as well as their belonging to either the Gulf of Aden or Red Sea spreading systems, (ii) the spatial distribution of the initial trap volcanism emplaced at 30 Ma over two disconnected magmatic sub-provinces, separated by a submeridian amagmatic crustal domain involving the Danakil and Ali Sabieh domains, and (iii) the evolution of the Danakil domain, as well as the nature of its eastern margin which is regarded as one of the fundamental discontinuity of the entire Afar framework, on either sides of which mechanisms of crustal extension vary dramatically, as being exclusively accommodated by either magmatic accretion to the W (Afar), or by tectonic faulting and associated basin development to the E (Red Sea).

Chapitre 1. Introduction. Problématiques.

Le dispositif extensif regroupant les fossés de Mer Rouge (MR) et du Golfe d'Aden (GA) est l'une des structures de référence de propagateurs océaniques évoluant latéralement en rifts intra-continentaux. La propagation de ces deux axes d'accrétion, initiée vers 10 Ma (GA) et 6 Ma (MR) (Cande and Kent, 1992, 1995), s'effectue selon deux axes quasi orthogonaux, en limites de trois plaques lithosphériques (Arabia, Nubia et Somalia, Figure 1A) (Tazieff et al., 1969 ; Barbéri et al., 1970 ; Stieljes, 1973). Ces deux axes convergent et interfèrent depuis 3 Ma au niveau du Triangle ou dépression Afar où ils se connectent vers le SO, au segment éthiopien du Rift Est Africain pour former une sorte de jonction triple (Figure 1A) (McKenzie, 1970). Les processus d'accrétion s'expriment à travers cette jonction triple par la mise en place, dans l'intervalle 1-3 Ma, d'un complexe de traps basaltiques d'origine fissurale - les Basaltes Stratoïdes (Lahitte et al., 2003) - ultérieurement recoupés par un système relativement complexe d'axes tectono-magmatiques, assimilés aux proto-limites de plaques (Tapponnier et al. 1990; Manighetti, 1993 ; Manighetti et al., 1998). Les Basaltes Stratoïdes recouvrent la presque totalité de la dépression Afar (Barbéri et Varet, 1977), masquant ainsi partiellement les témoins des stades précoces du rifting dont les principales manifestations sont actuellement exposées au niveau des traps basaltiques des plateaux éthiopiens (~30Ma, Hoffman et al., 1997) et yéménites (31-26 Ma, Baker et al., 1996) (Figure 1A), associés à la remontée du panache Afar. Sur la base de reconstitutions paléomagnétiques, la structuration du Triangle Afar est attribuée à la rotation anti-horaire (~23°) du bloc Danakil depuis l'Oligocène (Figure 1A) (Sichler, 1980 ; Courtillot, 1984). Toutefois, les modalités exactes des processus de rifting demeurent très mal contraintes, interprétées par les auteurs en termes de déformation diffuse (Barbéri and Varet, 1977), ou de micro-blocs sans déformation interne (Acton et al., 1991).

L'unique moyen de contraindre avec le maximum de fiabilité la dynamique du rifting Afar pendant les 30 derniers Ma consiste à combiner, d'une part, les modèles cinématiques existants, et d'autre part, l'histoire géologique enregistrée par les terrains synrift anciens (>3 Ma), localement exposés à la périphérie de la dépression actuelle. Il s'agit (1) des complexes volcaniques, jalonnant vers l'W le pied de l'escarpement éthiopien, et mis en place entre 29 et 7 Ma en relation avec la formation de la marge W Afar (Wolfenden et al., 2005), et (2) de

séries magmatiques et de leur substratum anté-rift formant vers l'E, les deux reliefs linéamentaires de Danakil et d'Ali Sabieh qui séparent la dépression Afar des domaines GA-MR en voie d'océanisation (Figure 1A)**.** Le présent travail concerne ces deux derniers domaines, et plus particulièrement celui d'Ali Sabieh, qui montrent à l'affleurement (1) le substratum anté-rift, composé d'un socle protérozoïque (Danakil) et de sa couverture sédimentaire méso-cénozoïque (Ali Sabieh), ainsi que (2) les séries magmatiques synrift initiales dont les plus anciennes sont datées à 26.7 Ma (Fm. d'Ali Sabieh) pour la zone d'Ali Sabieh (Chessex et al., 1975; Barberi et al., 1975), et à ~ 18 Ma (Fm. Mablas) au niveau de la zone Danakil (in Gasse et al., 1985). Contrairement au dispositif récent-actif de l'Afar qui a fait l'objet de très nombreuses études au cours des deux dernières décennies, les domaines Danakil et Ali Sabieh ont été largement délaissés, et l'on doit constater de plus que, malgré les travaux de cartographie systématique entrepris à partir des années 80 sur l'ensemble de la République de Djibouti (Gasse et al., 1985 ; 1986, Vellutini et al., 1995), leur signification géodynamique demeure encore énigmatique comme en témoigne leurs diverses interprétations en termes (1) de micro-plaques (Sichler, 1980 ; Manighetti et al., 1998 ; Collet et al., 2000), (2) de blocs (Barbéri and Varet, 1977 ; Hofsetter and Beyth, 2003), (3) de horsts (Sichler, 1980 ; Clin, 1991 ; Eagle et al., 2002), (4) d'anticlinaux (Clin and Pouchan, 1970), ou enfin (5) de dômes (Dreyfuss, 1932).

L'objectif principal de ce travail de thèse consiste à apporter des informations sur l'évolution précoce, à la fois tectonique et magmatique, de ces deux secteurs particuliers du rift Afar, en nous focalisant plus particulièrement sur celle du domaine d'Ali Sabieh. Etant donné la période de temps considérée (~30 Ma), ainsi que le caractère polystructuré de la zone de rift étudiée, il en résulte un dispositif tectonique et magmatique relativement complexe dont l'interprétation structurale nécessite de répondre à un certain nombre d'interrogations énumérées ci-dessous.

(1) Quelle est l'origine des reliefs bordiers Danakil et Ali Sabieh et de leurs structures dont le caractère non cylindrique (Ali Sabieh) contraste avec la régularité du réseau, plus classique, en horst-grabens, de la dépression Afar?

(2) En d'autres termes, quelle est la part respective des processus magmatiques et tectoniques dans l'inversion positive des structures?

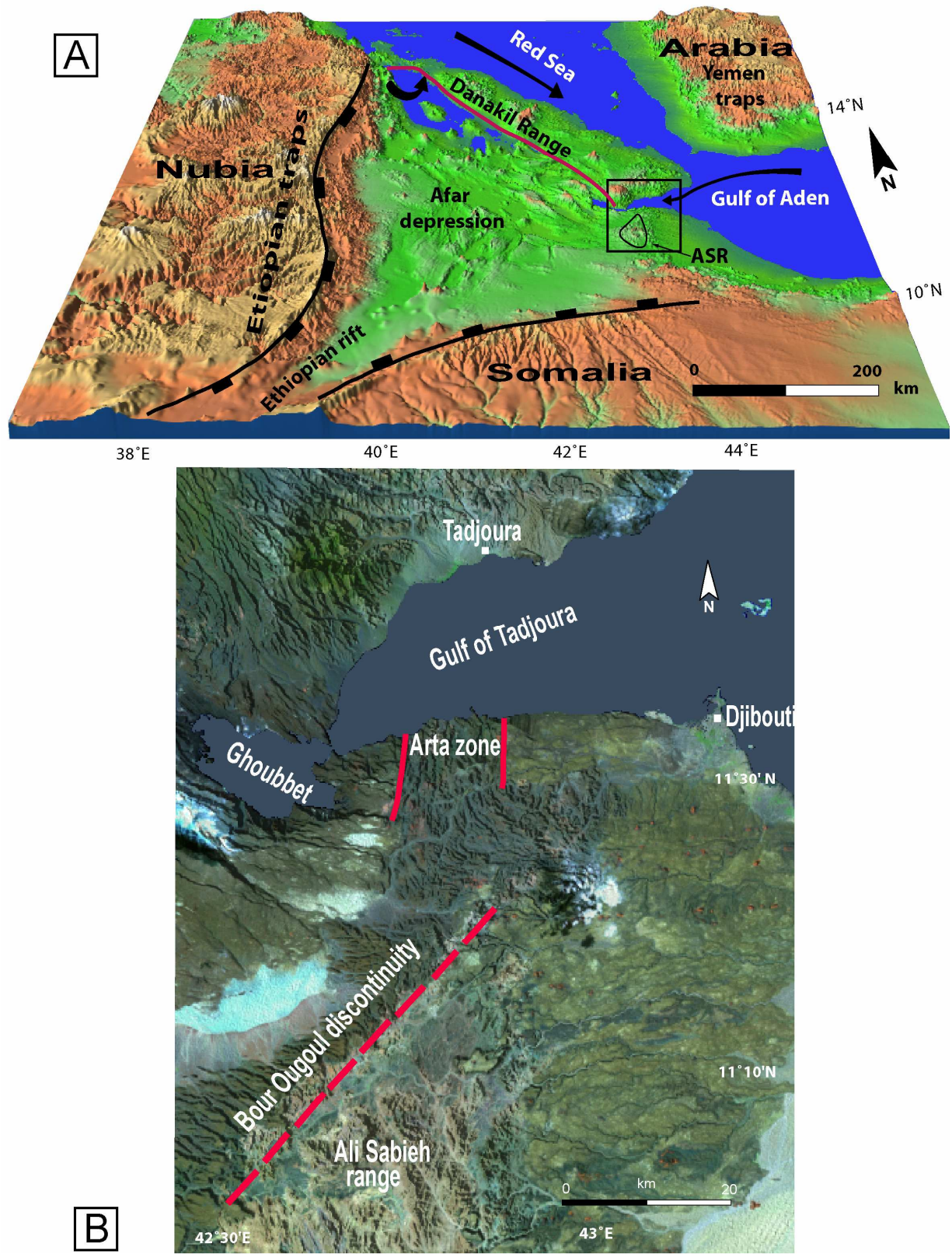

Figure 1 **:** (A) Modèle Numérique de Terrain (Gtopo 30) du Triangle Afar. Le trait rouge souligne la limite occidentale du « bloc » Danakil. Le carré noir indique la zone d'étude en République de Djibouti. ASR : Ali Sabieh Range. (B) Image Landsat Enhanced Thematic Mapper Plus (ETM+) de la zone d'étude.

(3a) A quel(s) champs de contraintes sont associées ces déformations et mouvements verticaux, et l'hypothèse de compressions, déjà évoquée à propos de la zone transverse d'Arta (Figure 1B) pour la période <3.6 Ma (Arthaud & Choukroune, 1976 ; Arthaud et al., 1980), s'applique-t-elle aux reliefs d'Ali Sabieh?

(3b) Quelle est la signification structurale de la discontinuité transverse (N50°E)(BOL) assurant le contact entre le domaine d'Ali Sabieh et le système en horst-grabens de la dépression Afar *sensu stricto* et dont la position actuelle, dans le prolongement SW de la faille transformante de Maskali (Figure 1B), pose le problème de l'importance de l'héritage synrift, voire antérieur, sur la cinématique de l'accrétion océanique.

(4) Quelles sont les modalités de mise en place des complexes magmatiques (effusifs et intrusifs) lors des premiers stades d'accrétion continentale ?

(5) Existe-t-il des analogies, d'ordres volcano-stratigraphique, pétro-géochimique, géochronologique, entre ces complexes magmatiques précoces et les traps basaltiques exposés au niveau des plateaux éthiopiens et yéménites ? Répondre à cette question équivaut à aborder le problème du caractère unique ou multiple du (des) panache(s) mantellique(s) à l'origine du magmatisme initial de la province Afar, *sensu lato* (George et al., 1998 ; Courtillot et al., 1999).

En complément de l'étude des séries anciennes des domaines Danakil et Ali Sabieh, il est apparu nécessaire de revoir aussi le contexte structural des basaltes récents (<3 Ma) qui les jouxtent vers l'E (Ali Sabieh) et au S (Danakil) afin d'avoir une vision globale de l'évolution cinématique du rifting enregistré au niveau de la partie SE du système Afar de 30 Ma à l'Actuel. En effet, les modèles récemment appliqués par Manighetti et al. (1997) à la propagation de la ride du GA au niveau du Golfe de Tadjoura ne considèrent qu'une partie des Basaltes du Golfe exposés sur les deux marges du golfe, et aboutissent à des hypothèses qui sont discutées dans ce travail, notamment à propos des mécanismes de transfert de l'extension entre le dispositif de rift oblique accommodé par l'extrémité occidentale du GA (Golfe de Tadjoura) et celui de rift orthogonal enregistré par le système Ghoubbet-Asal (Problématique 7).

L'étude géochimique approfondie de laves récentes (~1 Ma) provenant du volcan d'Hayyabley, à l'extrémité orientale de la marge sud du Golfe, a également été entreprise afin de mieux contraindre la nature des processus, et des sources, magmatiques mis en place à un stade plus évolué du rift Tadjoura, postérieurement aux Basaltes du Golfe. (Problème 6)

Les éléments de réponse apportés à ces questions font l'objet de quatre papiers qui seront soumis pour publication, et qui sont présentés selon le plan suivant :

- **Chapître 1**. Introduction. Problématiques
- **Chapître 2**. Méthodologie
- **Chapître 3**. Papier I : *Young rift kinematics in the western Gulf of Aden : the Tadjoura-Ghoubbet extensional linked system, Djibouti*. (in prep. to Tectonics). Daoud M.A., Le Gall B., Rolet J., Maury R., Guillou H & Jalludin M. Ce papier est focalisé sur la thématique (7).
- **Chapître 4**. Papier II : *Early rifting tectonics and magmatism in Eastern Afar: new evidence from the Danakil and Ali Sabieh ranges, Djibouti*. (in prep. to J. of Structural Geology). Le Gall B., Daoud M.A., Maury R., Rolet J. & Guillou H. Ce papier traite plus particulièrement des questions (1, 2, 3b, 4, 5).
- **Chapître 5**. Papier III : *Occurrence of a LREE-depleted component in the Afar plume: further evidence from Djibouti*. (in prep. to Lithos). Daoud M.A., Barrat J.A., Maury R., Taylor R.N., Le Gall B., Guillou H., Rolet J. Ce papier concerne la question (6).
- **Chapitre 6**. *Conclusions générales et prospectives.*
- **Références bibliographiques.**
- **Annexes.** Elles comprennent un certain nombre de documents, listés ci-dessous, en complément du Papier IV (en cours de rédaction) qui traite de **«** *Geodynamics of the Ali Sabieh antiform (Afar triple junction): new insights from paleostress analysis »*.(in prep. to Terra Nov). Sue C ., Daoud M.A, Le Gall B., Rolet J. Ce papier traite, entre autres, de la question (3a).

Afin de faciliter la lecture du manuscrit, en évitant des répétitions fastidieuses, les références bibliographiques spécifiques à chaque papier sont toutes regroupées en fin de mémoire. Concernant la méthodologie, les diverses étapes, ainsi que les protocoles, mis en œuvre pour l'approche géochimique-géochronologique (papiers I et II) sont regroupés au chapître 2, de même que les méthodes de l'analyse structurale qui concernent les papiers I, et II. Par contre, les principes de l'analyse microtectonique uniquement développée dans le papier IV, ainsi que les méthodes d'analyses isotopiques et géochimiques par ICP-MS (papier III), sont présentés dans les chapîtres correspondants.

La toponymie utilisée au cours de ce travail est synthétisée sur l'image Landsat Enhanced Thematic Mapper Plus (ETM+) en dépliant A3 à la fin du manuscrit

Des annexes complètent le manuscrit et contiennent un certain nombre de données et résultats non traités dans les papiers soumis à publication. Elles concernent les analyses géochimiques de certaines roches basiques de la zone d'étude, ainsi que 27 planches photos illustrant diverses structures (magmatiques et tectoniques) observées et mesurées lors des missions de terrain.

En préambule, il convient de préciser que ce travail de recherche s'inscrit dans le cadre du Programme scientifique MAWARI (**MA**nagement of **Wa**ter Resources in the East African **RI**ft System), financé par le M.A.E. (2001-09) et géré par le CIFEG (**C**entre **I**nternational pour la **F**ormation et les **E**changes en **G**éosciences). Ce programme, essentiellement hydrogéologique, est consacré à la gestion durable des ressources en eau sous-terraine de trois pays du Rift Est Africain, à savoir Djibouti, l'Ethiopie et le Kenya.

Notre contribution initiale à ce programme concernait l'étude structurale du substratum de la nappe aquifère de Djibouti, avec une attention particulière portée à l'analyse la fracturation des basaltes récents de la Plaine de Djibouti. La zone d'étude a ensuite été étendue, d'une part, au domaine symétrique sur le flanc N du Golfe de Tadjoura (secteur Obock-Tadjoura), et d'autre part, aux reliefs qui bordent la Plaine de Djibouti vers l'W (zones d'Ali Sabieh et d'Arta), afin de pouvoir aborder les questions scientifiques énumérées ci-dessus à propos de la dynamique du rifting Afar au cours des 30 derniers Ma.

Notre travail s'inscrit aussi dans le cadre d'une convention de coopération scientifique (signée le 17/06/06) entre l'UBO et le CERD de Djibouti.

Chapitre 2. Méthodologie et données

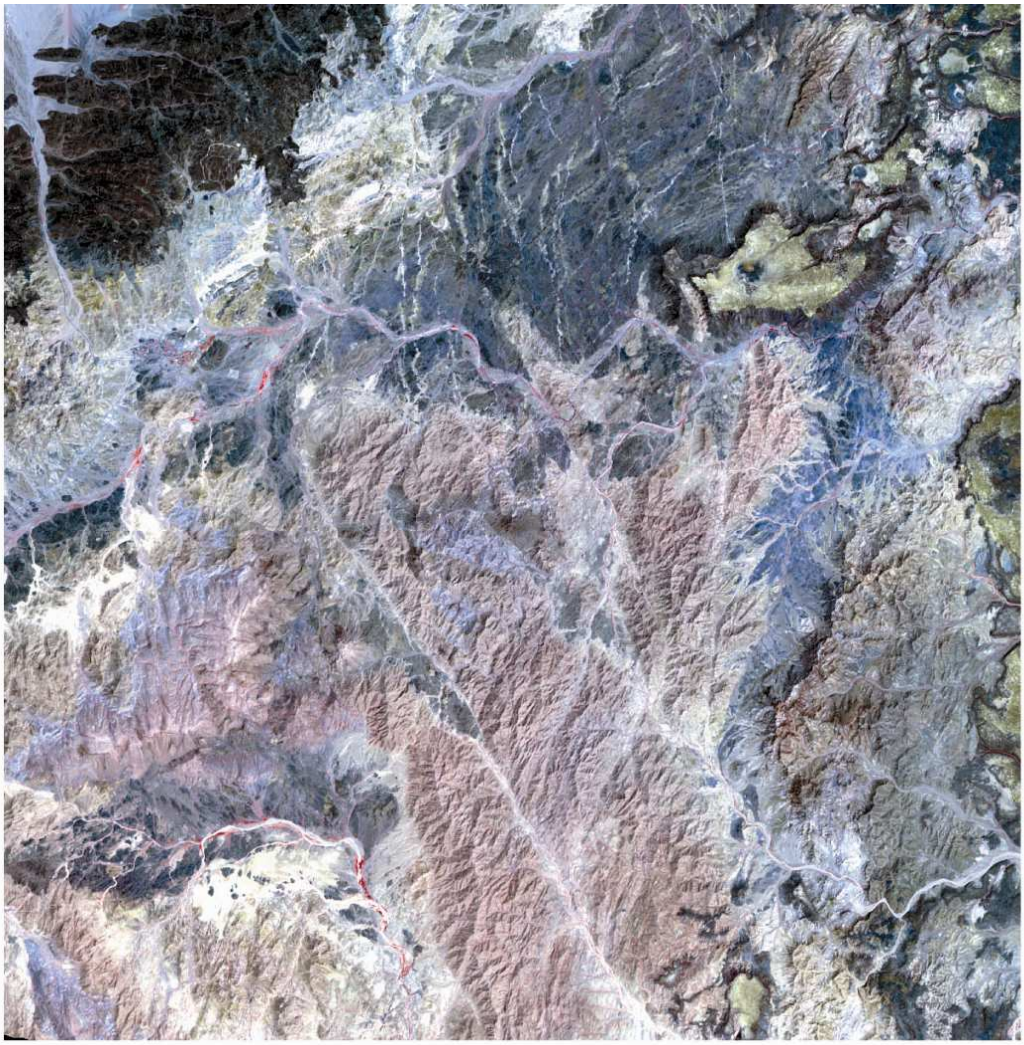

Extrait d’une image Aster (région d’Ali Sabieh)

Chapitre 2. Méthodologie et données.

Compte-tenu du caractère magmatique de la zone de rift étudiée, une approche pluridisciplinaire, combinant analyses structurales, géochimiques et géochronologiques, a été mise en œuvre afin de couvrir les divers aspects des complexes volcaniques en présence. Par rapport aux travaux antérieurs récemment consacrés au Rift Afar, notre travail se démarque, d'une part, en se focalisant sur les terrains synrift les plus anciens, largement délaissés par la plupart des travaux précédents, probablement en raison de leur déchiffrage plus complexe et aussi de leur modeste contribution à la meilleure compréhension des dispositifs actifs-récents, et d'autre part, en reposant sur une analyse structurale multi-échelle qui accorde une part prépondérante à l'approche 'terrain'.
Comme déjà énoncé en introduction sont présentées ici les méthodes de l'analyse structurale et de l'approche géochimie-géochronologie, communes à divers papiers constituant la thèse.

1. Approche structurale

L'étude structurale entreprise dans ce travail repose sur une approche multi-échelle intégrant des observations et mesures de terrain (environ 5 mois de mission), complétées par l'analyse et l'interprétation d'imagerie satellitale (ASTER) qui procure une vision élargie des structures dans le contexte plus global du rift.

1.1. Analyse de terrain

(1) Au cours de ce travail, l'accent a été mis sur l'analyse morpho-structurale des reliefs. Cette approche, très peu développée jusqu'à présent sur l'ensemble du Rift Afar, s'est révélée être fructueuse à la périphérie des zones de reliefs, et plus spécialement ceux d'Arta et d'Ali Sabieh. En effet, elle a permis de mettre en évidence des dispositifs de paléo-remplissage volcanique qui clotûrent des cycles de type 'soulèvement-érosion-incision-remplissage', plus particulièrement pour les époques récentes <3 Ma. Les nouveaux résultats ainsi acquis apportent des contraintes supplémentaires pour quantifier, et caler dans le temps, les mouvements verticaux de premier ordre accompagnant les déformations.

(2) La reconstitution du champs des paléo-contraintes à divers stades du rifting a été réalisée par le biais de l'analyse de plans striés, selon une méthode dont les principes sont présentés dans le papier IV (Cf annexe). Cette analyse a été mise en œuvre au niveau des terrains anciens (substratum et séquences synrift) de la zone d'Ali Sabieh dont la structure en dôme posait la question de l'existence et de l'importance de compressions à l'extrémité SE du rift Afar. Par contre, cette approche n'a pu être appliquée aux basaltes récents, présents sur la zone d'étude (Fm du Golfe, pour l'essentiel), par manque de marqueurs fiables.

1.2. Imageries satellitales

Notre étude morpho-structurale ainsi que l'analyse des relations géométriques entre les différentes séries volcaniques sont basées, pour l'essentiel, sur l'interprétation d'images satellites ASTER (*Advanced Spaceborne Thermal Emission and Reflection Radiometer*), combinée à l'analyse (1) de données topographiques (MNT et bathymétrie), (2) de cartes géologiques existantes (1:100 000, Ali Sabieh, Tadjoura et Djibouti) et (3) d'observations de terrain. Les deux types de MNT utilisés, SRTM 90 (*Shuttle Radar Topography Mission*) et ASTER, se distinguent par leurs résolutions spectrales et spatiales respectives, et fournissent ainsi une vision 3D plus ou moins fine et complète de la morphostructure des régions étudiées. Ces données ont permis, d'une part, d'élaborer de grandes coupes structurales à travers les principaux domaines volcaniques, et d'autre part, de quantifier les déplacements verticaux (minimum) le long d'escarpements de failles individuelles et permettre ainsi une estimation des taux d'extension cumulée le long de transects régionaux.

1.2.1. MNT SRTM

Les MNT SRTM 90, générés par la technique d'interférométrie radar, sont mis à la disposition du public par la NASA depuis mai 2004, en format numérique (*www2.jpl.nasa.gov/srtm*). Chaque MNT SRTM 90 couvre une zone d'un degré d'arc de côté, et résulte d'une projection *Transversale Universelle de Mercator* (UTM) suivant le système géodésique *Word Geodesic System* (WGS84). Ils présentent une résolution spatiale de 90m par pixel (équivalente en résolution latérale) et une précision de 16m (équivalente en résolution verticale). L'interférométrie radar image relativement mal les zones de rivage, ce qui se traduit, dans le cas présent, par la présence de zones 'blanches', non imagées le long de

la côte sud du Golfe de Tadjoura (Figure 1). L'autre limitation majeure des MNT SRTM réside dans leur résolution verticale relativement faible (16m), qui ne permet donc pas de repérer les structures (failles en particulier) dont la dimension verticale est <16 m, et conduit ainsi à une sous-représentation de l'échantillonnage effectué.

Ces limitations justifiaient donc la réalisation de MNT ASTER présentant une meilleure couverture ainsi qu'une résolution verticale plus fine.

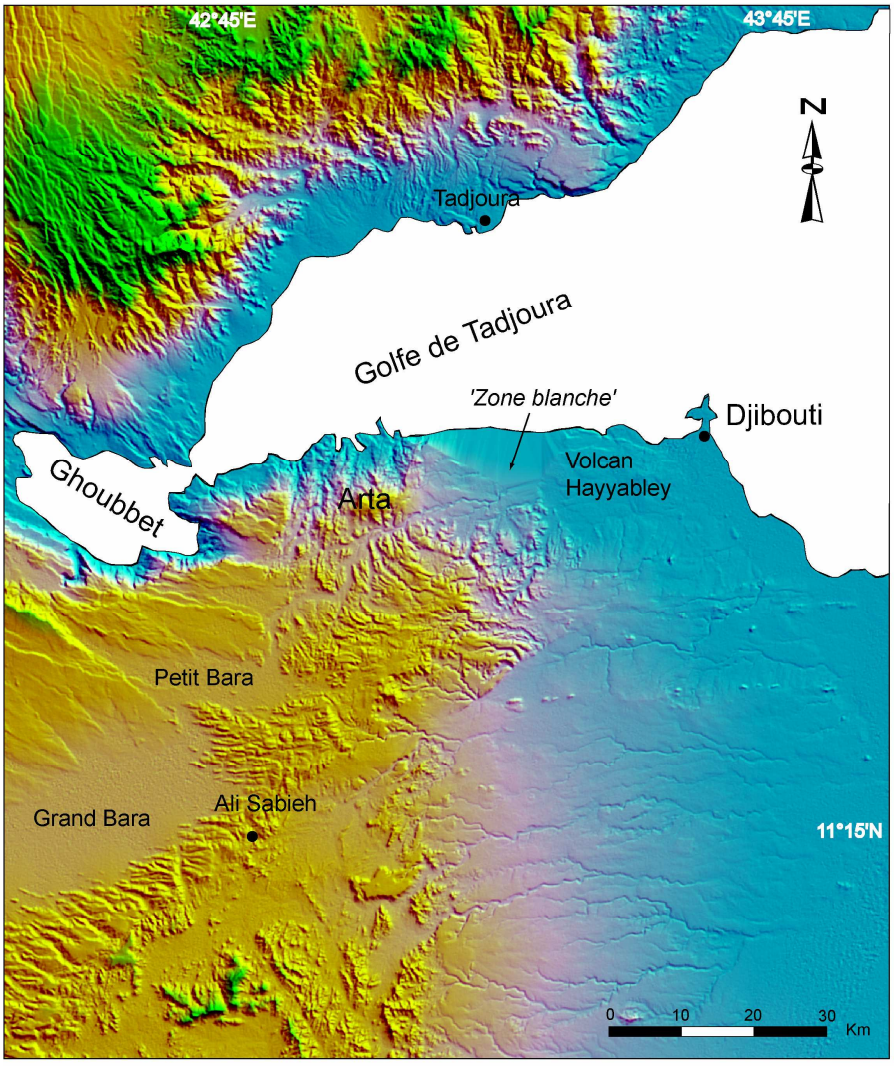

***Figure 1**:* MNT SRTM ombré. 'Zone blanche', zone non imagée par l'interférométrie radar

1.2.2. MNT ASTER

Les MNT ASTER ont été générés à partir d'un couple d'images ASTER par le module ORTHOENGINE du logiciel GEOMATICA9.1 de PCI. Deux images optiques ASTER à haute résolution couvrent l'ensemble de la zone d'étude (AST_L1B.003 :10102002074530, 2002/10/31 et AST_L1B.003 :10102002074539, 2001/10/31) (Figure 2). Les images satellitaires ASTER sont fournies par le capteur ASTER, embarqué à bord du satellite TERRA, qui fournit des scènes de 60 x 60 km.

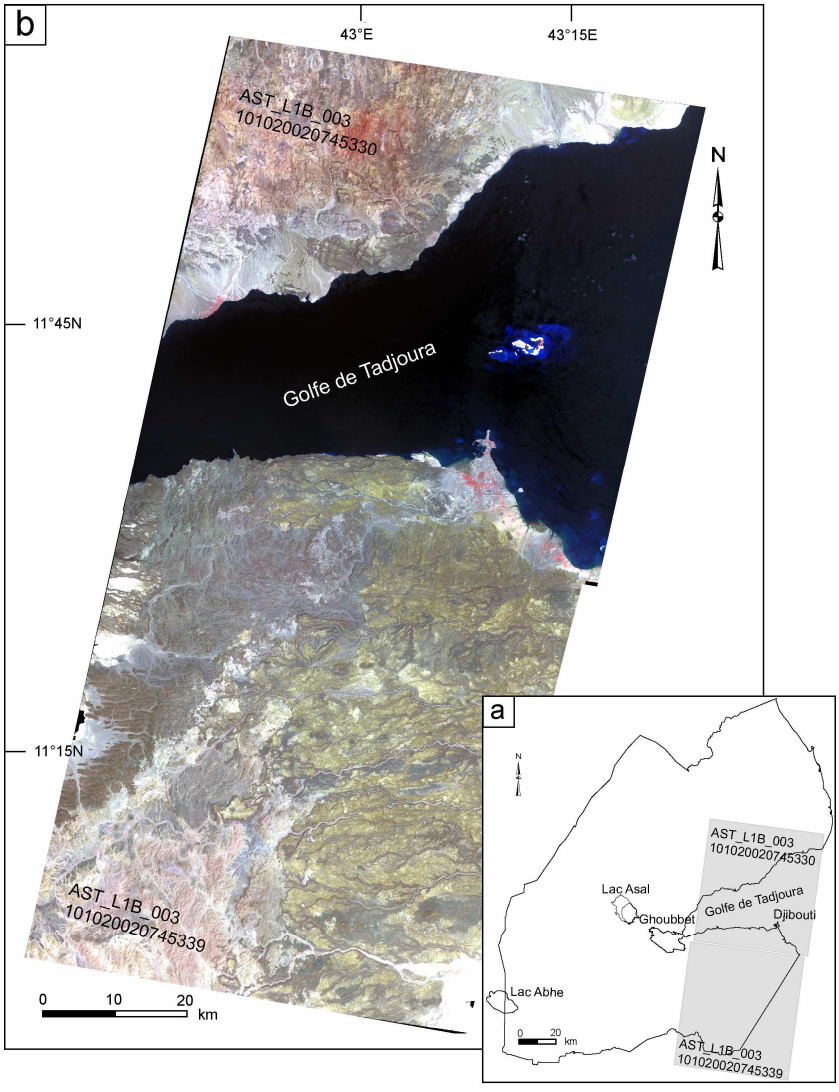

Figure 2 : Couverture des images ASTER : (a) Plan de position et référence des images. (b) Mosaïque de deux images utilisées pour cette étude. Composition colorée 132 (Vert-Proche-infrarouge-Rouge).

Il est équipé d'un mode d'acquisition stéréoscopique permettant d'extraire des MNT. Il contient 14 bandes ayant une étendue spectrale étalée de 0,52 à 11,65 µm. Le capteur ASTER est muni de trois radiomètres séparés, couvrant les trois spectres suivants : visible et proche infra-rouge (VNIR), moyen infrarouge (SWIR) et thermique (TIR) (tableau 1). La particularité du système VNIR (Visible et Proche-infrarouge) est d'être composé de deux télescopes : l'un pointant à la perpendiculaire vers la terre (3N, nadir), et l'autre pointant en arrière avec un angle de 28°(3B).

Caractéristiques	Visible et Proche-Infrarouge	Moyen-Infrarouge	Thermique
Bandes	**1** : 0,5 2 - 0,6 0 µm (Vert) **2** : 0,63-0,69 µm (Rouge) **3N:** 0,76-0,86 µm (Proche infra-rouge) **3B:** 0,76-0,86 µm (Proche infra-rouge)	**4** :1,60-1,70 µm **5** :2,14-2,18 µm **6** :2,18-2,22 µm **7** :2,23-2,28 µm **8** :2,29 2,36 µm **9** :2,36-2,43 µm	**1 0** : 8 ,1 2 - 8 ,4 7 µm **11** :8,47-8,82µm **12** :8,92-9,27µm **13** :10,25-10,95µm **14** :10,95-11,65µm
Résolution en m	15	30	90

Tableau 1: Résolutions spectrales et résolutions spatiales des images ASTER.

L'acquisition s'effectue dans la même bande du spectre de telle sorte qu'une scène est observée sous deux angles différents. ASTER peut ainsi produire des scènes stéréoscopiques, acquises en ligne (along-track) et espacées d'une minute (Figure 3a). Par rapport aux images SPOT dont l'acquisition des couples stéréoscopiques se fait à plusieurs jours d'intervalle et sur des orbites différentes (across-track), le système ASTER présente l'avantage de réduire les facteurs susceptibles de détériorer la qualité des images, tels que le changement de luminosité ou le déplacement des nuages. La résolution spatiale des scènes stéréoscopiques ainsi obtenues est de l'ordre de 15m. La réalisation de MNT ASTER repose ensuite sur l'utilisation du module ORTHOENGINE dont les principes de base sont régis par les équations de coplanarité et la méthode de corrélation linéaire automatique (Al-Roussan et al., 1998 ; Hirano et al., 2003 ; Stevens et al., 2004). Le principe consiste à procéder à la recherche automatique, par corrélation sur les deux images (3N et 3B), de points homologues (tie-points) pour produire des images épipolaires en s'appuyant sur la connaissance de la géométrie de deux prises de vue.

Après la création des images épipolaires, le module est capable de restituer le MNT par le procédé d'auto-corrélation (Figure 3b).

1.2.3. Traitement des images satellitales

Les images ASTER brutes comportent des déformations spatiales, liées aux capteurs et aux effets des reliefs, qu'il convient de gommer afin d'obtenir une image correcte des structures à analyser. Cette transformation spatiale de l'image nécessite des corrections géométriques et des rectifications de l'image. Par ailleurs, différents traitements sont aussi nécessaires pour améliorer l'apparence des images et optimiser leur interprétation.

- Correction géométrique et rectification de l'image

La correction géométrique consiste à supprimer les erreurs de mesures induites par les capteurs et les satellites afin que les données soient conformes au système de projection requis. Elle est réalisée en relocalisant chaque pixel dans le système cartographique utilisé, ce qui aboutit (1) à l'unification du système cartographique, (2) à la création d'ortho-images et (3) à la meilleure intégration de l'image dans des bases de données de type SIG. L'orthorectification est un procédé informatique qui permet de supprimer les distorsions horizontales et verticales de l'image, et améliore ainsi considérablement la qualité de l'image. Ces corrections sont effectuées à l'aide du module ORTHOENGINE du logiciel GEOMATICA9.1 de PCI.

Afin de procéder à l'orthorectification, il est indispensable de disposer d'un MNT (ASTER dans le cas présent) qui servira de source de projection. Aux termes de tous ces traitements, nous obtenons une image ortho-rectifiée et géoréférencée (ortho-image) dont la résolution spectrale comprend les bandes 1, 2 et 3N.

- Fusion des données

Les images ASTER utilisées comprennent trois bandes spectrales (Tableau 1). Chacune d'entre-elles procure une image en noir et blanc comportant 256 niveaux de gris. Pour produire une image en couleurs (composition colorée), il suffit de combiner trois bandes spectrales avec des filtres (bleu, vert et rouge). Concernant notre zone d'étude, la composition colorée optimale combine les bandes 1 (vert), 3 (proche infra-rouge) et 2 (rouge).

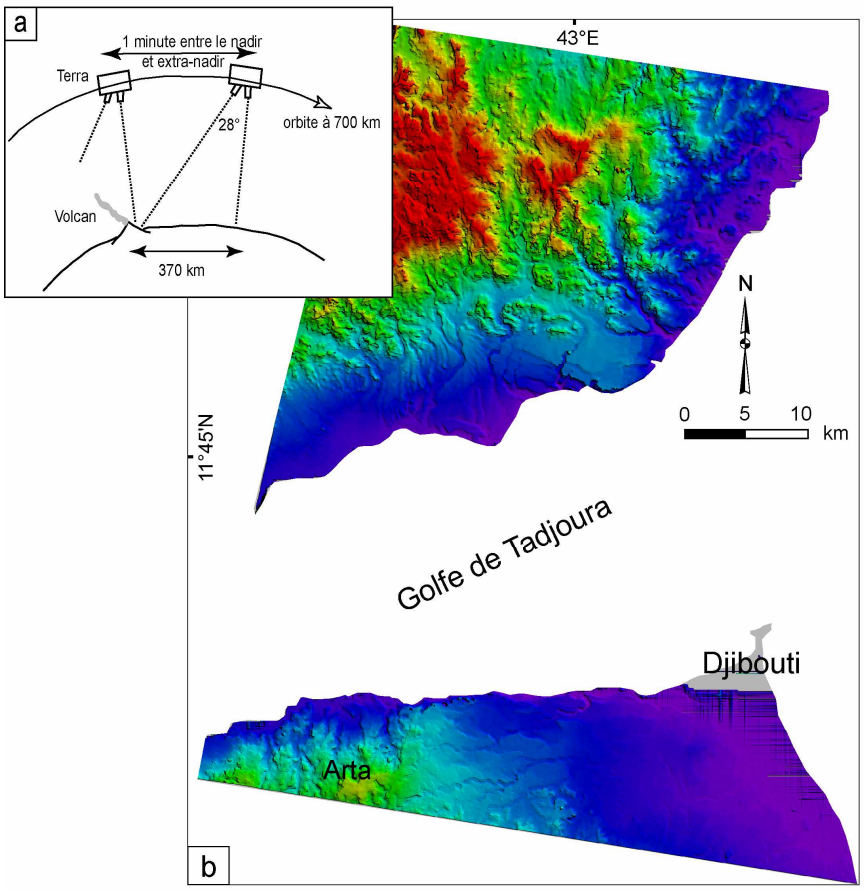

Figure 3: (a) Schéma simplifié montrant la prise de vue de deux images stéréo par le capteur ASTER NVIR. (b) MNT ASTER généré par le module ORTHOENGINE.

1.2.4. Extraction et analyse des réseaux de fractures

L'exposition exceptionnelle des structures dans les basaltes récents présents de part et d'autre du Golfe de Tadjoura était propice à conduire une analyse géométrique et statistique de la fracturation à partir des images satellites disponibles. L'extraction des structures, puis leur analyse et interprétation, se sont déroulées selon les étapes suivantes.

<u>- Numérisation des données</u>

Une carte de fracturation a été élaborée à partir de l'interprétation des images ASTER (dont la résolution spatiale de 15m ne permet de visualiser que les structures présentant un dénivellé vertical >15 m) (Figure 4b). En appliquant les critères géométriques adoptés par Clifton et al. (2000), la majorité des failles identifiées dans la zone d'étude apparaissent

constituées de segments, plus ou moins contigus, exprimés par exemple par des variations de la direction de la faille ou par des zones de relais inter-segments.

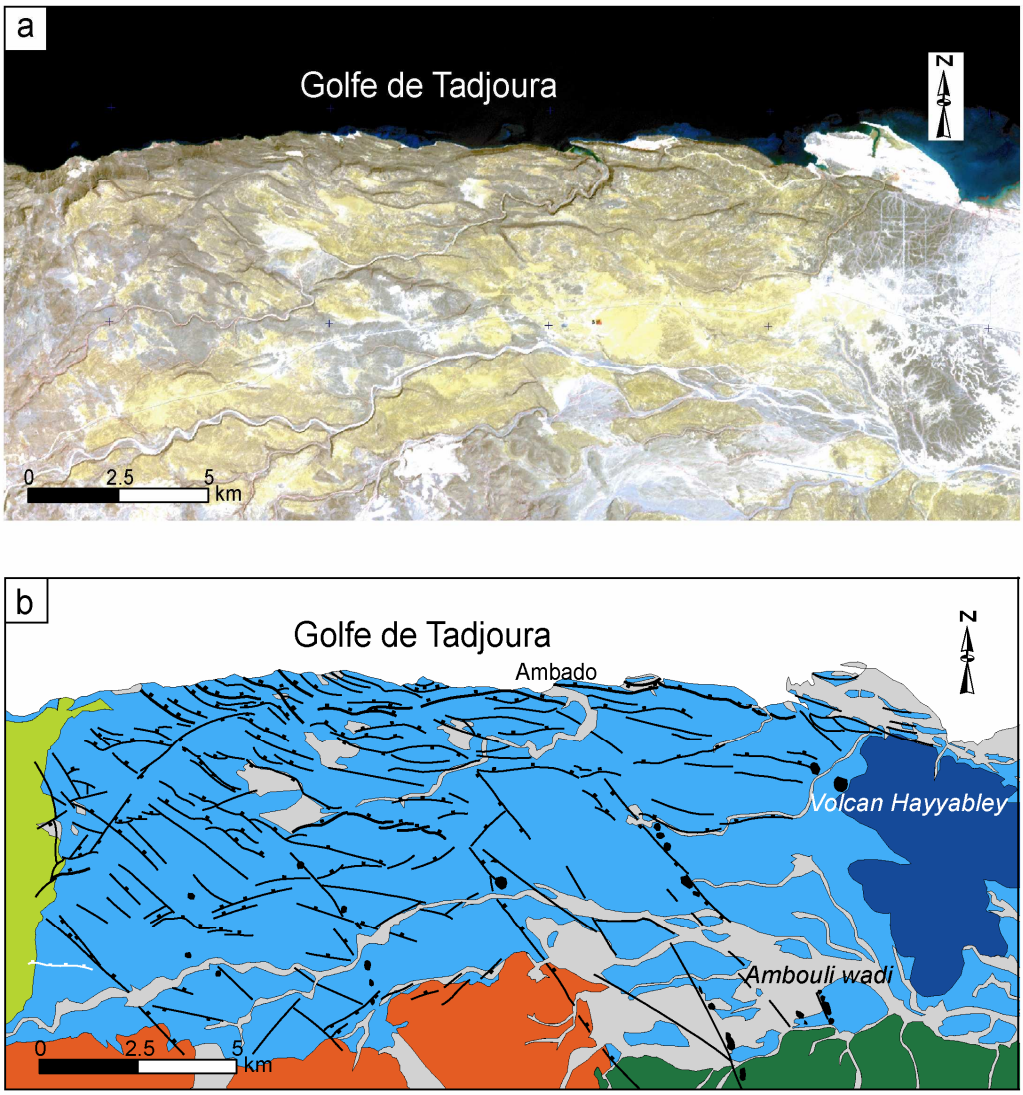

Figure 4: Réseau de failles de la Plaine de Djibouti. (a) Détail de l'image ASTER. (b) Carte de fracturation interprétée (cf figure 14 du chapitre 3 pour plus de détails).

Toutefois, l'une des caractéristiques du réseau de fractures étudié réside dans le faible espacement inter-faille qui ne permet pas, dans la plupart des cas, d'affirmer l'appartenance d'un segment à l'une ou l'autre des failles en présence. Afin d'éviter toute sur-interprétation, le caractère segmenté de l'ensemble du réseau de failles n'a donc pas été pris en compte. Le champs de fracture a été ensuite numérisé à l'écran à l'aide du logiciel ArcGis 8.3 qui

présente l'avantage de fournir directement des documents géoréférencés et autoriser ainsi un calcul automatique des longueurs et directions de failles. La plupart des paramètres géométriques des populations de faille (azimut, longueur, rejet, densité) peuvent être quantifiés à partir de l'interprétation des images ASTER.

- Traitement des données et quantification

- *Longueur et orientation des failles*. Compte-tenu du fait que la majorité des structures faillées identifiées sur l'image ASTER présentent des tracés courbes, intégrant plusieurs segments contigus, leur longueur et leur direction ont été assimilées à celles d'une ligne droite joignant leurs extrémités (Figure 5a) ; leur direction étant mesurée entre 0 et 180°. Le rapport entre la longueur ainsi mesurée ('tip-to-tip') et la longueur réelle caractérise la tortuosité de chaque structure faillée, paramètre non considéré dans cette étude.

- *Rejet des failles*. Le rejet apparent d'une faille est déduit des données topographiques du MNT Aster avec une résolution verticale de 7m. Les rejets apparents inférieurs à cette limite ne sont pas mesurables sur les coupes. La quantité d'extension associée à chaque faille est calculée par la relation :

$$e = T/\tan\mu,$$

où e représente l'extension, T le rejet vertical apparent, et μ le pendage du plan de faille (Figure 5b).

Le pendage des failles ne pouvant être directement mesuré, il est estimé entre 60° et 70° d'après l'allure des escarpements. Sur chaque transect étudié, l'extension cumulée est obtenue en sommant les extensions associées à chacune des failles intersectées par la coupe, selon la relation :

$$E = \sum e = \sum T/\tan\mu.$$

Le pourcentage d'extension enregistré le long d'une coupe est obtenu par la formule : Hi = (E/L)*100, L étant la longueur de la coupe.

- *Densité/Espacement des failles*. L'espacement inter-faille a été mesuré le long de coupes perpendiculaires à la direction générale des structures (3 et 6 coupes sur les flancs N et S du golfe, respectivement). Ce paramètre équivaut à considérer la densité de fracturation dont une meilleure appréciation a été obtenue à l'aide de « *l'outil de création et d'analyse par maille* » du logiciel ArcGis 8.3. Celui-ci permet de créer un maillage régulier (1 km de côté dans le cas présent) à partir (1) de la carte de la fracturation prise comme couche (fichier de forme) et (2) des failles considérées comme entités de cette couche. L'outil permet, dans un

premier temps, de créer et numéroter les mailles dans une nouvelle classe d'entités, puis de transférer sur chaque maille plusieurs valeurs statistiques (nombre de faille et somme de longueur de faille dans le cas présent) calculées à partir du champ de la couche 'faille'. Pour chaque maille, l'outil calcule deux valeurs, à savoir : (1) le nombre d'entités (failles) et (2) la somme brute des valeurs d'entités (longueur) que la maille intersecte. Ces résultats permettent de déterminer la densité de failles exprimée en km/km^2. La carte de densité est ensuite obtenue par interpolation en raster en considérant comme paramètre la valeur de densité dans chaque maille.

La variabilité géographique de la densité peut renseigner sur les variations du taux de déformation.

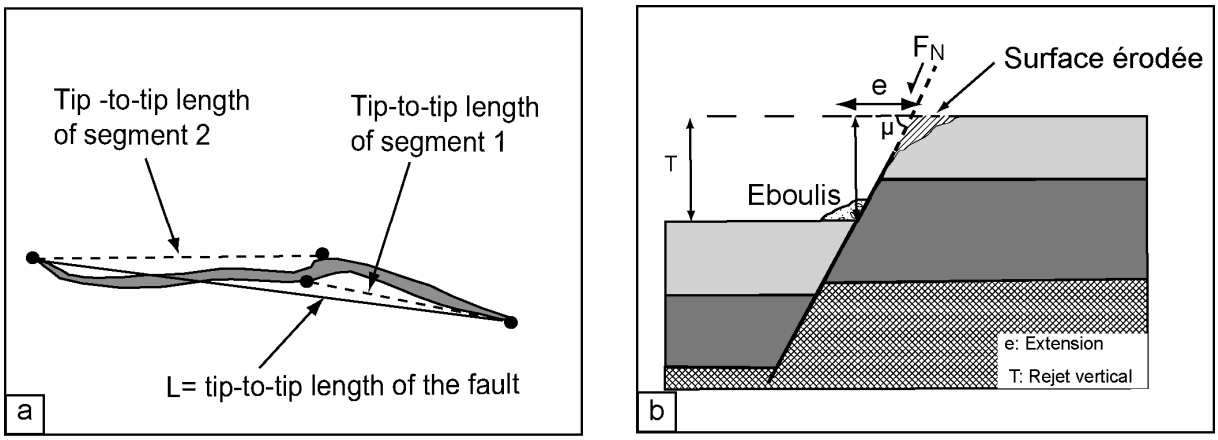

***Figure 5*:** (a) Méthode de mesure de la longueur d'une faille. (b) Paramètres pris en compte pour estimer l'extension le long d'une faille normale.

2. Approche géochimique

2.1.Préparation des poudres

Les roches analysées proviennent d'échantillons frais prélevés sur le terrain, montrant le moins de traces d'altération superficielle. Au laboratoire, ces échantillons ont été concassés manuellement pour obtenir des graviers qui seront débarrassés des minéraux d'altération secondaire (zéolites, carbonates…). Les graviers sont ensuite broyés, dans un premier temps, à l'aide d'un mortier à Abish permettant d'obtenir des broyats à granulométrie ≤ 1,5 mm, puis avec un mortier en agate pour finalement aboutir à des poudres fines de la Roche Totale. Le calcul de la perte au feu ou LOI (loss of ignition) nous informe sur le degré d'altération de la

roche. Pour cela, environ 500 mg de l'échantillon sont placés dans un creuset en céramique, puis calcinés dans un four à 1050°C pendant 30 minutes.

La LOI est calculée par la relation suivante :

$$LOI = [(P_{\text{creuset plein}} - P_{\text{creuset calciné}}) / (P_{\text{creuset plein}} - P_{\text{creuset vide}})] * 100,$$

où P représente le poids

Sur 144 échantillons récoltés (basiques pour l'essentiel), 24 présentent des valeurs de LOI > 2%. Ceux à LOI >4% ont été interprétés avec prudence, notamment à propos de leurs éléments mobiles (K, Rb). Les échantillons à fort LOI (>2%) proviennent pour l'essentiel des séries anciennes (Formations d'Ali Sabieh, x13 sur 23) et du Dalha (x2 sur 18). Cependant, les cuttings de basaltes récents (Golfe et Somalis) prélevés de sondages carottés présentent souvent aussi des LOI élevés.

2.2.La mise en solution

La mise en solution, nécessaire à la dissolution des constituants chimiques de la roche, est réalisée par rajout de réactifs chimiques liquides sur la poudre (Roche Totale) obtenue selon un protocole présenté en détail par Cotten et al. (1995). On prélève 250 mg de poudre qu'on place dans un bêcher d'attaque en Teflon ®, on y rajoute (1) 2,5 ml d'acide fluorhydrique (HF) pour briser les liaisons chimiques Si-O des silicates et (2) 0,5 ml d'acide nitrique afin d'obtenir les éléments solubles sous forme de sels. La solution est ensuite placée dans une étuve à 90°C pendant 2 à 3 heures, puis durant 15 minutes à une température de 110°C. Cette attaque à chaud provoque la formation de précipités issus d'éventuels minéraux réfractaires présents dans la roche. Afin de neutraliser l'excès de HF et de complexer les produits flurorurés formés durant l'attaque à chaud, on rajoute 97 ml de solution aqueuse d'acide borique (H_3BO_3) contenant 25 g/l de H_3BO_3 et de 0,5 g/l de CsCl. Ce dernier joue un rôle tampon pendant l'ionisation de la solution par ICP-AES. La solution de 100 ml finalement obtenue est laissée au repos durant deux jours pour permettre une totale complexation des fluorures en acide fluoborique (HBF_4) solubles dans l'eau. Cette solution contient, sous forme dissoute, tous les éléments chimiques susceptibles d'être mesurés par ICP-AES.

2.3.Mesure des éléments par ICP-AES

Le protocole analytique adopté pour cette approche est détaillé dans Cotten et al. (1995). On rappellera simplement que les concentrations en éléments majeurs et traces (excepté Rb) mesurées par l'ICP-AES (*Inductively Coupled Plasma-Atomic Emission Spectrometer*) ISA Jobin-Yvon® JY70 se font à partir de la solution obtenue précédemment. La teneur en Rb est déterminée grâce au spectromètre atomique à flamme de type Perkin-Elmer ®5000. L'ensemble des éléments (majeurs et traces) est déterminé à partir d'une même solution sans que celle-ci ait subit une quelconque extraction et pré-concentration sélective des éléments. Le bore est utilisé comme étalon interne dans les mesures par ICP-AES. La déviation standard relative est de 1% pour le SiO_2 et de 2% pour les autres éléments majeurs, à la condition que leur concentration soit ≥0,5%. La déviation est de 5% pour tous les éléments en trace, sauf pour Sr et Ba pour lesquels on obtient une déviation de 2%.

3. Approche géochronologique

La datation des roches volcaniques a été réalisée en collaboration avec Hervé Guillou au LSCE (Laboratoire des Sciences du Climat et de l'Environnement), UMR1572 CEA/CNRS à Gif-sur-Yvette. La méthode utilisée (^{40}K-^{40}Ar sans 'spike') a été appliquée à 27 échantillons de roches basiques (effusives et intrusives) appartenant à la presque totalité des diverses séries volcaniques présentes sur la zone d'étude (cf. Tableau 2).

3.1.Principe

La méthode de datation ^{40}K-^{40}Ar est fondée sur le principe de la désintégration radioactive de l'isotope père ^{40}K en isotopes $^{40}Ar^*$ et en $^{40}Ca^*$ radiogéniques avec une période de demi-vie de $1{,}25.10^9$ ans, en admettant que l'Ar* est absent au moment de la cristallisation des minéraux (t=0). La désintégration radioactive se fait suivant le relation suivante :

$N = No e^{-\lambda t}$ avec N : nombre d'atomes-parents au temps t

No : nombre d'atomes-parents au temps to

Le nombre d'atomes-fils formés (D) à l'instant t se définit comme suit :

$$D = No - N = N.(e^{-\lambda t} - 1)$$

qui permet de calculer t :

$$t = 1/\lambda Ln (1+D/N)$$

Dans le cas de la désintégration de ^{40}K en $^{40}Ar^*$ et $^{40}Ca^*$, on a :

$N = {}^{40}K$

$D = {}^{40}Ar^* + {}^{40}Ca^*$

$\lambda = \lambda\varepsilon + \lambda\beta$

où $\lambda\varepsilon$ représente la constante de désintégration de ^{40}K en $^{40}Ar^*$ et $\lambda\beta$ celle de ^{40}K désintégration en $^{40}Ca^*$.

$\lambda\varepsilon = 0{,}581.10^{-10}\ a^{-1}$, $\lambda\beta = 4{,}962.10^{-10}\ a^{-1}$ (Steiger et Jäger, 1977).

L'équation devient alors :

$t =[1/(\lambda\varepsilon + \lambda\beta)].Ln[1(^{40}Ar^*/ {}^{40}K)(\lambda\varepsilon + \lambda\beta)/ \lambda\varepsilon]$

Le temps t ainsi calculé a une signification géologique lorsque que les conditions suivantes sont remplies :

- $\lambda\varepsilon$ et $\lambda\beta$ ne varient pas dans le système formé par la roche ou le minéral (Garner *et al.*, 1975).
- La totalité de l'Ar dosé dans la roche ou le minéral est d'origine, soit atmosphérique, soit radiogénique. A l'instant initial (t = 0), le rapport $^{40}Ar^*/^{36}Ar^*$ équivaut au rapport mesuré dans l'atmosphère actuel (= 295.6 ; Nier, 1950).
- Depuis sa formation, le système est clos.
- L'âge de la roche est d'un ordre de grandeur bien supérieur à la durée de formation de la roche.

3.2.Préparation des poudres

Seules les roches montrant peu de traces d'altération sont sélectionnées pour datation. On utilise la LOI (< 2%) comme principal critère de sélection. Les échantillons récoltés sur le terrain sont d'abord découpés en petits morceaux à l'aide d'une scie diamantée. Les morceaux sont ensuite séchés dans une étuve à ~50-60°C, puis concassés dans un concasseur à mâchoires, et enfin finement broyés dans un concasseur à rouleau. On tamise entre 0,25-0,125 mm afin d'obtenir une fraction bien homogène, débarrassée des phénocristaux indésirables. La fraction tamisée est lavée à l'eau courante pour éliminer les dernières poussières, puis à chaud

(~ 60°C), pendant environ 1 heure, dans un bain d'acide acétique sous ultrason. Ce traitement permet d'éliminer les éventuelles phases d'altération (carbonates, sulfures) et les produits d'origine hydrothermale (zéolites, sels contenant du chlore). La fraction est de nouveau rincée à l'eau distillée afin d'éliminer l'acide acétique jusqu'à un pH 7, puis à l'éthanol absolu et à l'acétone pour faciliter le séchage, avant d'être enfin placé dans une étuve à ~50-60°C jusqu'au séchage complet. Après ce premier tri, l'examen à la loupe binoculaire permet d'identifier les phases restantes (phénocristaux, mésostase, verre, opaques) et sélectionner ainsi manuellement les éléments favorables à la datation.

3.3.Préparation des échantillons

Les dosages de K et Ar sont effectués sur la mésostase, qui est supposée représenter la phase cristallisée au moment du refroidissement de la lave. Les phénocristaux et xénocristaux susceptibles d'avoir piégé, soit de l'Ar en excès pendant la cristallisation précoce, soit de l'Ar hérité pouvant être incorporé dans le magma par les fluides, sont séparés de la mésostase. L'observation de la fraction 0,125< Ø <0,250 à la loupe binoculaire permet de trier les éléments à dater parmi les phases restantes (phénocristaux, mésostase, verre, opaques).

- Séparation magnétique : Ce tri se fait à l'aide d'un simple aimant. Dans les échantillons étudiés, les opaques magnétiques se trouvent essentiellement dans la mésostase, bien que certains phénocristaux en contiennent en inclusion. La séparation magnétique va permettre d'écarter, de la mésostase, tous les phénocristaux ne contenant pas de magnétite.

-Tri aux liqueurs denses : Ce tri permet de séparer les fractions minérales de densité différente. Pour cela, on utilise du diiodométhane (d=3,30) dilué avec de l'acétone (d=0,8) ou Bromoforme (d=2,87) dilué avec de l'éthanol (d=0,8) en fonction de la nature chimique des roches. Ce dernier tri va fournir une fraction minérale comprise dans un intervalle de densité connu.

3.4.Dosage du K et mesure de l'Ar

Le potassium a été mesuré au Laboratoire de Géochimie de l'UMR 6538 Domaines Océaniques par spectrométrie d'Emission Atomique de flamme Perkin-Elmer® 5000. La composition isotopique de l'Ar a été mesurée au LSCE (H. Guillou) par la méthode ^{40}K-^{40}Ar sans traceur (sans spike). Cette technique, développée par C. Cassignol, puis appliquée aux

roches récentes par P.Y. Gillot (Cassignol *et al.*, 1978 ; Cassignol et Gillot, 1982 ; Gillot et Cornette, 1986), est détaillée dans Charbit *et al.* (1998), Guillou (2001) et Guillou *et al.* (2004). La calibration manométrique de cette dose de référence, qui permet de déterminer l'équation de la courbe de calibration **,** est basée sur des mesures périodiques et reproductibles de standards internationaux, d'âge connu, dans les mêmes conditions que pour les échantillons (Charbit *et al.*, 1998). Ceci permet de déterminer la teneur totale en ^{40}Ar de l'échantillon avec une précision de ± 0,2% (2 σ). Les standards utilisés sont les biotites : LP-6 : 127,8 ± 0,7 Ma (Odin *et al.* 1982) et HD-B1 : 24,21 ± 0,32 Ma (Fuhrmann *et al.*, 1987 ; Hess et Lippolt, 1994 ; Hautmann et Lippolt, 2000).

Chapitre 3. Young rift kinematics in the western Gulf of Aden: the Tadjoura-Ghoubbet extensional linked system, (Djibouti).

Mohamed A. Daoud, Bernard Le Gall, René C. Maury, Joël Rolet[1], Hervé Guillou and Mohamed Jalludin

Graben d'Ambado (Sud du Golfe de Tadjoura)

Chapitre 3. Young rift kinematics in the western Gulf of Aden: the Tadjoura-Ghoubbet extensional linked system, (Djibouti).

(papier sera soumis après la soutenance à TECTONICS)

Mohamed A. Daoud[1,2], Bernard Le Gall[1], René C. Maury[1], Joël Rolet[1], Hervé Guillou[3] and Mohamed Jalludin[2]

[1] UMR 6538 Domaines océaniques, IUEM, Université de Bretagne Occidentale, place N. Copernic, 29280 Plouzané, France.

[2] IST, Centre d'Etudes et de Recherches de Djibouti, B.P. 486, Djibouti Ville, Djibouti.

[3] UMR 1572, LSCE/CEA-CNRS, Domaine du CNRS, 12 avenue de la Terrasse, 91118 Gif-sur Yvette, France.

Abstract

The so-called Tadjoura rift (TR) forms the westernmost extremity of the Gulf of Aden oceanic ridge which propagates westwards into the Afar depression. From structural, and remote sensing dataset, the TR is interpreted as an asymmetrical S-facing half-graben, about 20 km-wide, dominated by a large boundary fault zone to the N. It is partially filled with the 1-3 Ma-old Gulf Basalts which onlapped to the S older volcanics along its shallower flexural margin. The volcano-stratigraphical framework of the magmatic succession is refined from geochemistry and geochronology data. Major and trace elements features of the basalts further show enriched patterns typical of the Afar transitional basalts, whereas the overall magmatic pattern suggests a temporal evolution from enriched (margins) towards more depleted (axis) basalts in the TR. That is consistent with the proposed age progression of faulting which increases symmetrically away from the inner rift zone. Morphological and statistical analyses of onshore extensional fault populations exposed on the two opposite margins of the TR show marked changes of structural styles along-strike, in a direction parallel to the rift axis. These fault disturbances are assigned to the arrest of axial fault tip propagation against pre-existing discontinuities of the Arta transverse zone, displaying a NS (Red Sea-type) trend, nearly orthogonal to rift axis propagation. That resulted in the sinistral shift of extension into the Ghoubbet rift pattern to the SW. Some assumptions are also attempted at a greater scale about the kinematic development of the intricate rift axis pattern that propagated since 3 Ma throughout the trap basaltic series flooring the entire Afar depression.

Keywords: Afar, Tadjoura rift, active/recent extension, faults, rift propagation, inherited structures.

1. Introduction

The Tadjoura Gulf (TG) lies at the western tip of the nearly EW-trending Gulf of Aden (GA) which forms, together with the Red Sea and the Ethiopian rift, one of the three diverging branchs of the Afar Triangle (Figure 1A). According to aeromagnetic patterns, mid-oceanic segments and fractures zones were formed since 17-18 Ma along the eastern part of the GA, as far as 45°E (Shukra El Sheik transform) (Leroy et al., 2004), during a sea-floor spreading event propagating westwards, obliquely to the N30°E direction of separation between the Arabian and Somalian plates (Bellahsen et al., 2006) (Figure 1A). Further to the W, incipient rifting in the TG led to a thinned continental crust which was capped by the ca. 1-3 Ma-old Gulf Basalt series which extend laterally on the emerged opposite margins as two narrow faulted coastal strips in the Tadjoura-Obock (N) and Djibouti Plain (S) areas (Figures 2A, B, 3). This ~40 km-wide recent faulted volcanic belt is here referred to as the Tadjoura rift (TR). Its present-day tectonic activity is mostly restricted to its immerged central part along sismogenic fault structures lying to the W throughout the connection zone with the N130°E Ghoubbet-Asal rift (Figure 1B) (Lépine et al., 1980). This latter forms, together with the Manda Inakir, Manda Hararo and Erta Ale accretionary systems, emerged rift segments which penetrated onshore throughout the Plio-Pleistocene (2.3-1.0 Ma) Stratoid trap-like basaltic series covering most part of the Afar Depression (Figure 2B) (Varet, 1975; Zumbo et al., 1995). It is therefore clear that dramatic changes in rifting processes took place during the last 3 Ma between the narrow zone of localized strain along the Western GA (TR), and the >200 km-wide zone of diffuse extension and overlapping rift systems throughout the mantle plume-controlled Afar Depression (Manighetti, 1993; Manighetti et al., 1998). The way by which the two contrasted extended crustal domains are structurally linked is variously interpreted. According to Gaulier and Huchon (1991), a large-scale dextral fault zone following the NW side of the Ali Sabieh domain, in the onshore prolongation of the Maskali NE-SW transform network, played a prominent role in transferring strain from the TR towards southern Afar (Figure 2B) at an early stage of crustal extension. The Arta transverse zone, discussed later in this paper, was assumed by Arthaud et al. (1980a, 1980b) to be part of this transfer fault system. Alternatively, the connection between the Tadjoura and Ghoubbet rifts was assigned by Manighetti et al. (1997) to a soft linkage pattern involving en échelon fault structures at a later stage (~1 Ma ago) of extension (Figure 2A).

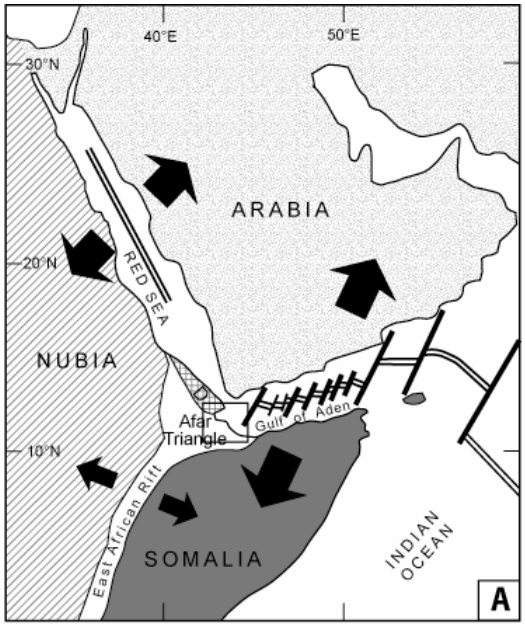

Figure 1: (A) Plate kinematic setting of the Afar Triple Junction. Thick arrows indicate plate motion vector, square is the studied area, D., Danakil. (B) Major physiographic features of the Tadjoura-Asal rifted domain from topography and bathymetry dataset, modified from Manighetti et al. (1997). The map trace of N130°E sismogenic fault structures is shown in the connection zone between the TG and the Ghoubbet-Asal rift system.

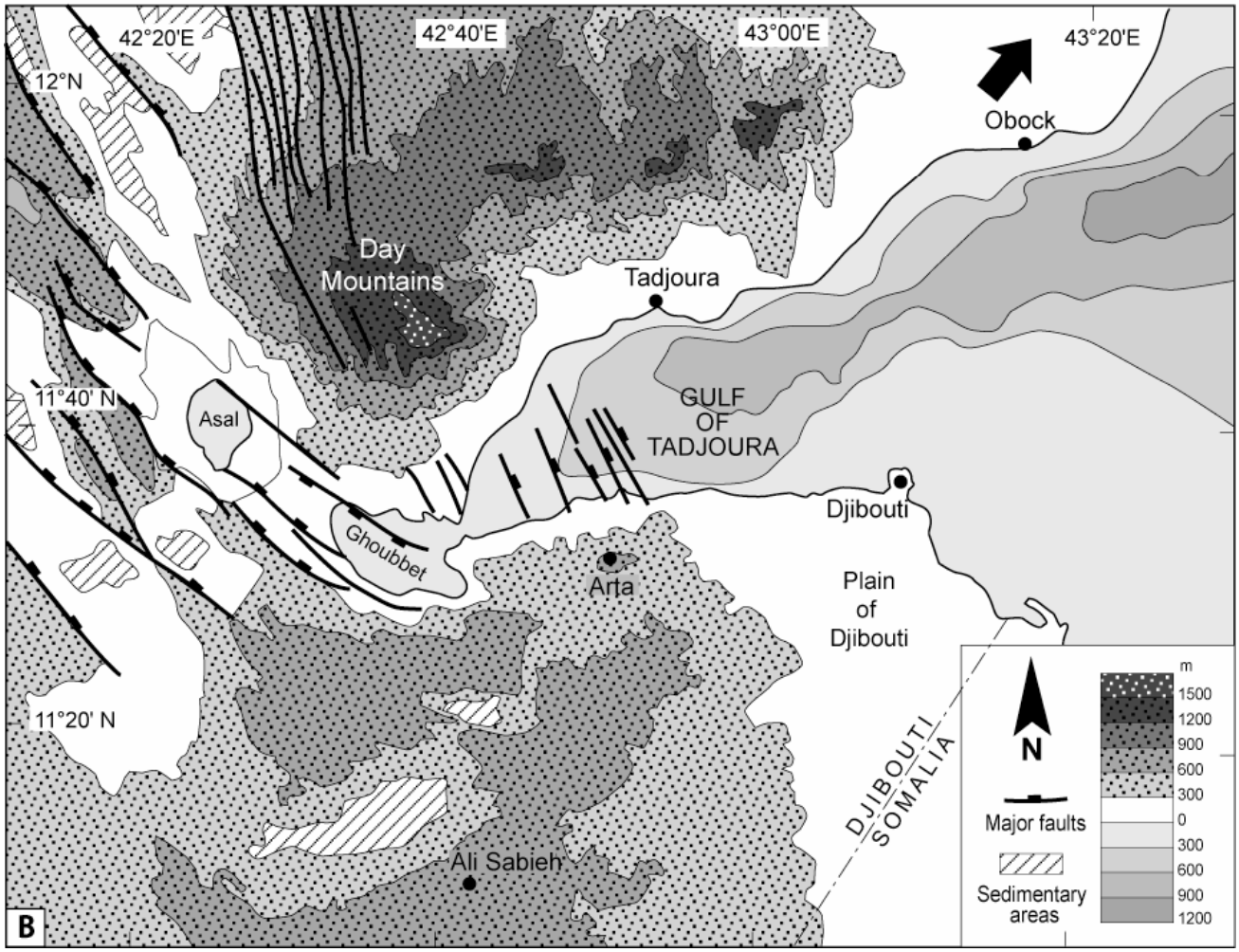

It is the aim of this work to precise kinematics of recent rifting in the Tadjoura-Ghoubbet rift linkage zone. Most of structural studies on this key-area have focused on dynamics of recent strain recorded by their inner active offshore troughs (Manighetti et al., 1997; 2001; Audin et al., 2001). Following the wide-scale 'bookshelf faulting' concept applied to the entire Aden-Red Sea rift pattern (Tapponnier et al., 1990; Manighetti, 1993), Manighetti et al. (1997; 2001) interpreted recent/active rift kinematics in the TG area in terms of small-scale and overlapping 'subrifts' which propagated diachronously towards the W throughout the northern margin of the TG, in response to northward strain jumps (Figure 2A).

These models are discussed here at a wider scale by integrating recent structures documented on the southern symmetrical TG margin, i.e. the Djibouti Plain (Figures 2A, B). Using the Gulf Basalts as a main structural marker for the tectono-magmatic history of the TR allows us to identify a typical half-graben which recorded a progressive axial (NS) shift of strain with time, during the last 3 Ma, towards its inner part. By further considering the structural history of older (>3 Ma) rift volcanics present in the poorly investigated Arta transverse zone (Figure 3), our study supplies some new insights about the key-role of inheritance from earlier and transverse structures on recent rift kinematics. According to the model applied here to the long-lived (~5 Ma) and multi-stage evolution of the western GA spreading system, it is assumed that (1) two diachronous rift systems, with oblique orientations, intersected in the W Tadjoura Gulf, and (2) offset and transfer of strain from the TR into the Ghoubbet rift was caused by the mechanical locking of the westerly-propagating extension against NS preexisting heterogeneities, related to an earlier tectono-magmatic rift setting with a Red Sea polarity.

2. Methodology

Our multi-disciplinary work is mainly based on the structural, geochemical and geochronological analysis of young volcanic rock sequences, using field dataset, complemented by interpretation of ASTER remote sensing data. Geochemical analyses (major and trace elements) and radiometric dating (K/Ar method) performed on poorly-known mafic volcanics from the Djibouti Plain, combined with new field data, led to improve the local volcano-stratigraphy in the southern flank of the TR.

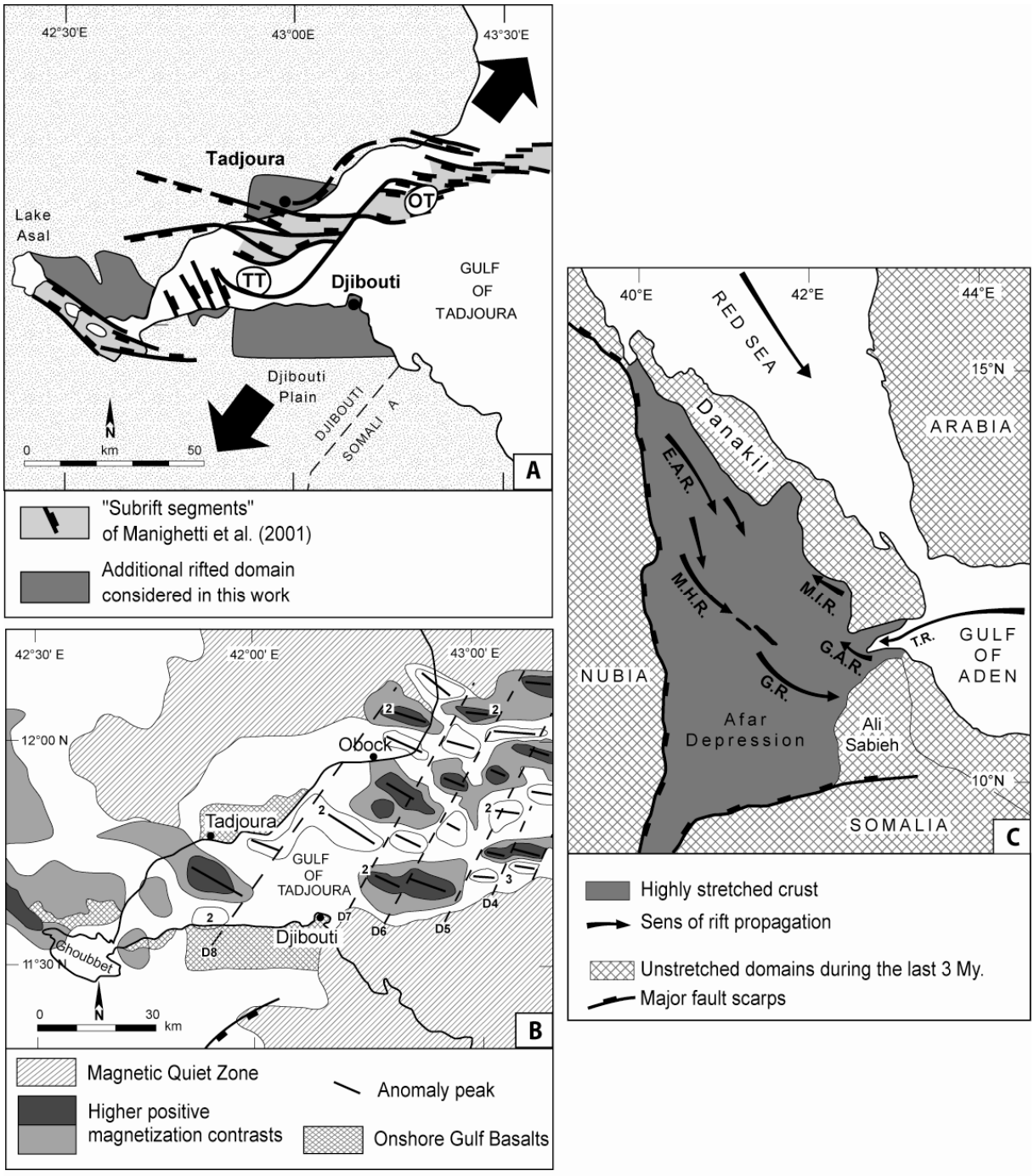

Figure 2 : Rift kinematic indicators in the Afar extensional system. (A) Rift kinematic model applied by Manighetti et al. (1997, 2001) to the Tadjoura-Ghoubbet area. The spatial extent of onshore Gulf Basalts is shown. A structural interpretation of the TG and its margins is proposed in figure 9A. OT., Obock trough; TT., Tadjoura trough. (B) Aeromagnetic map of the TG (in Manighetti et al., 1997). Dashed lines (D_1 to D_8) represent transform faults offseting magnetic segments; D_8 corresponds to the Maskali transform. (C) Sketch map of the Afar depression showing (i) the distribution of subaerial Quaternary magmatic segments and (ii) the sens of rift propagation proposed par Tapponnier et al. (1990), or Manighetti et al. (1998). EAR., GAR., GR., MHR., MIR., TR., Erta'Ale, Ghoubbet-Asal,, Gobaad, Manda Hararo, Manda Inakir, and Tadjoura rifts, respectively.

Whole-rock major and trace elements, except Rb, were measured at UMR 6538 Domaines Océaniques, Brest, using a Jobin-Yvon Inductively Coupled Plasma – Atomic Emission Spectrometer (ICP-AES) (see Chapter 2) Rb was measured by flame atomic emission using Perkin-Elmer 5000 spectrometer.

K contents and Ar isotopic compositions were measured at Brest (by ICP-AES) and at the 'Laboratoire des Sciences du Climat et de l'Environnement' of Gif-sur-Yvette, respectively (see Chapter 2).

Structural analysis was preferentially focused on onshore fault populations which were analyzed from a geometrical and statistical point of view in an attempt to establish the basic scaling properties of the fault system. Following criteria used by Clifton et al. (2000), the majority of fault structures in the TR are composed of segments identified principally by the presence of relay zones and abrupt changes in fault strike. Quantitative studies of a number of fault parameters (length, azimuth, spacing and density) were based on fault trace map interpretation. Estimates of vertical displacement along each fault structure were derived from fault scarp geometry observed on ASTER 3D-dataset. Seriated topographic profiles across each individual fault scarp gave the maximum value of displacement at the surface. When the top surface of the footwall uplifted block was degraded by erosion (Djibouti Plain), the summit-level envelop was used as a surface marker to restore the initial footwall geometry. In any case, vertical throws in this study are minimum estimates which do not account for possible fault displacement at depth. [A more detailed description of the methodology adopted in quantitative studies of faults can be found in chapter 2]. Markers for sense of displacement (striations) were rarely observed along exposed fault surfaces, hence precluding any accurate stress reconstructions to be performed. The offshore fault pattern extracted from published bathymetric contour-maps (Audin, 1999, Dauteuil et al., 2001) has a much lower resolution which does not permit quantitative comparisons with onshore fault parameters. Therefore, it has only been used to display the general structural arrangement of the TR (Figure 3).

3. Regional morphostructural pattern

The general morphostructural framework of the TR was obtained by merging both onshore (ASTER) and bathymetric dataset (Manighetti et al., 1997; Audin, 1999).

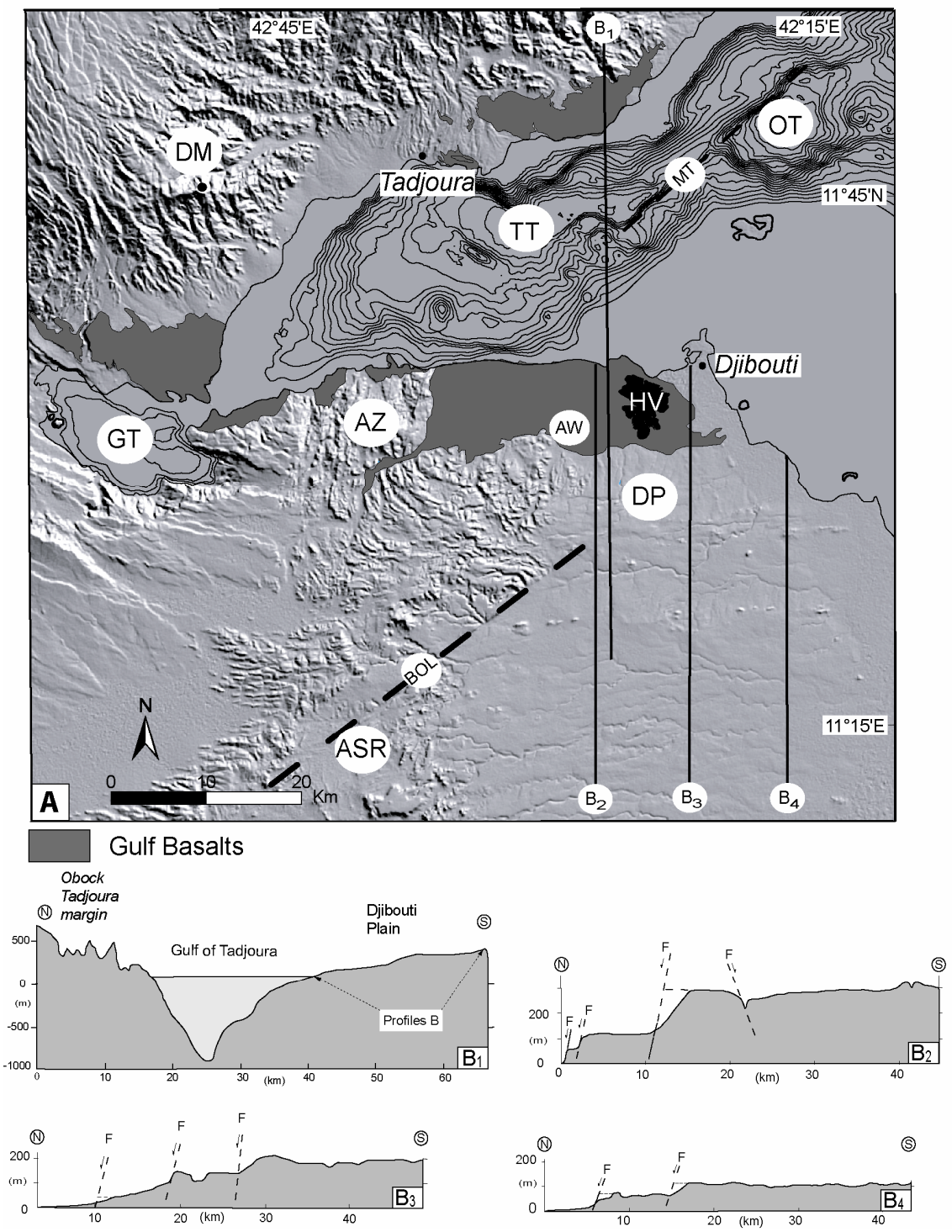

***Figure 3*:** Topographical framework of the Tadjoura rifted zone. (A) Shuttle Radar Topography Mission digital elevation model and bathymetric contour map (from Audin 1999). Thin lines (B_1, B_2, B_3 and B_4) are the trace of topographic profiles. Dashed lines represent the Maskali and Bour Ougoul transverse (transform) fault structures. ASR., Ali Sabieh range; AW., Ambouli Wadi; AZ., Arta zone; BOL., Boul Ougour lineament; DM., Day mountains; DP., Djibouti Plain; GT., Ghoubbet trough; HV., Hayyabley volcano; MT., Maskali transform; OT., Obock trough; TT., Tadjoura trough. (B) Topographic profiles across the TR (B_1) and the Djibouti Plain (B_2, B_3 and B_4). A structural interpretation of the cross-section B_1 is proposed on figure 9B.

The resulting digital elevation model and associated NS topographic profiles of figure 3 show the pronounced morphological asymmetry of the TG margins. The northern flank is dominated by EW-trending reliefs which decrease in altitude southwards from 1200 m to sea-level over a distance of 15-20 km. To the W, they swing into a NNW-SSE direction in the Day Mountains (1600 m), i.e. on the southern termination of the Danakil "block" (McKenzie et al., 1970; Barberi and Varet, 1977). The origin of these high reliefs, oblique to both the Tadjoura (N90°E) and Asal (N120°E) rift axes, still remains to be investigated. The topography of the southern margin is more subdued over the Djibouti Plain with mean altitudes <150 m which step down abruptly eastwards into a narrow N140°-trending strip of coastal lowlands. The seriated profiles of figure 3B show a marked inflexion of the topography along the Ambouli wadi, at the contact between the nearly horizontal Gulf Basalts (~3-1 Ma) and a northerly-tilted surface in the older Somali Basalts (~7.2-3.0 Ma) to the S. This monoclinal flexure evolves southwards into two successive stepping up monotonous plateaus, still involving the Somali Basalts, the altitudes of which increase gradually westwards towards the >1200 m Ali Sabieh relief. This elevated range, and the >700 m-high Arta zone located further to the N, both limit the Djibouti Plain to the W, and in turn are bounded westwards by the faulted Stratoid plateau basalt of southern Afar.

The offshore part of the TR comprises two adjacent structural units with distinct morphological features. To the NE, a narrow segment, striking NE-SW parallel to the trace of the Maskali transform fault (Lépine et al., 1976; Arthaud and Choukroune, 1976), links the Obock deep trough (>1100 m) and the Tadjoura rift segment sensu stricto. This latter forms a EW-oriented trough, about 20 km-wide, deepening towards a northern fault zone, with a bayonet map-trace involving N50°E, EW and N120°E fault-like segments, in contrast with its straight E-W-trending coastline to the S (Figures 3A, B_1). Its internal morphology is dominated by two sets of faults, at N50°E and N120-140°E (Maskali and Asal trends, respectively), which limit rhomb-shaped fault-blocks with inner floor depth decreasing westwards from ca. 1000 m to <300 m, via a system of NNW-oriented fault scarps. The morphostructural network of the TR and its surrounding domains is interpreted in terms of fault arrangement in Section 6.

4. Geological context

The geological setting of the TR is shown on the revised map of figure 4A which differs significantly from the geological maps of Djibouti, Tadjoura, and Ali Sabieh (Gasse et al., 1983, 1985, 1986). The modified volcano-stratigraphy of the Djibouti Plain is based on geochemical data, presented separately at the end of this section, and geochronological dataset integrating previously published and new radiometric age determinations.

The various geographical sub-units distinguished by previous authors within the Gulf Basalts (Gasse et al., 1983, 1985, 1986) have been grouped into a single volcanic unit. With the exception of the Gulf Basalts which form two narrow (<10 km) opposite coastal strips. The structural relationships between the TR and adjacent older rift domains have also been addressed, with emphasis on the Arta transverse zone which is here regarded as a key-structure for rift propagation throughout the Tadjoura-Ghoubbet linkage zone.

4.1. The Obock-Tadjoura northern flank of the TR

The ~1-3 Ma-old Gulf Basalts in the Obock-Tadjoura area (Richard, 1979) outcrop as a series of coastal tilted fault blocks limited to the N and the W by highlands involving older rift-related volcanics of the Dalha (8.6-3.8 Ma) and Mablas (18.8-11.8 Ma, in Gasse et al., 1985) units (Figure 4A). The main cartographic unit of the Gulf Basalts (the Roueli unit of Gasse et al., 1983, 1985) forms a 20 x 10 km faulted belt oriented N100°E (Gulf trend) which evolves to the NE into a narrower N50°E strip (Maskali trend). The total thickness of the Gulf Basalt volcanic pile is estimated to 350 m (Gasse et al., 1985). Its visible part is mostly made up of superimposed columnar-jointed subaerial lava flows, the individual thickness of which reaches up to 10 m. A few submarine lava flows have been described at the mouth of Sadaï-Tagarré wadi (Gasse et al., 1983). Most of the Gulf-parallel faults are blancketed to the W by 1.4-0.8 Ma-old Quaternary alluvium (Gasse, 1991), derived from the uplift of the surrounding mountains. The Gulf Basalts extend further S as discrete inliers beneath locally faulted Quaternary alluvial fans, possibly as young as Holocene (Manighetti et al., 1997). The significance of the two small-scale ‘subrifts’ identified by these authors in the alluvial deposits (Figure 2A) is questioned in the next section with respect to the overall rift architecture of the TR.

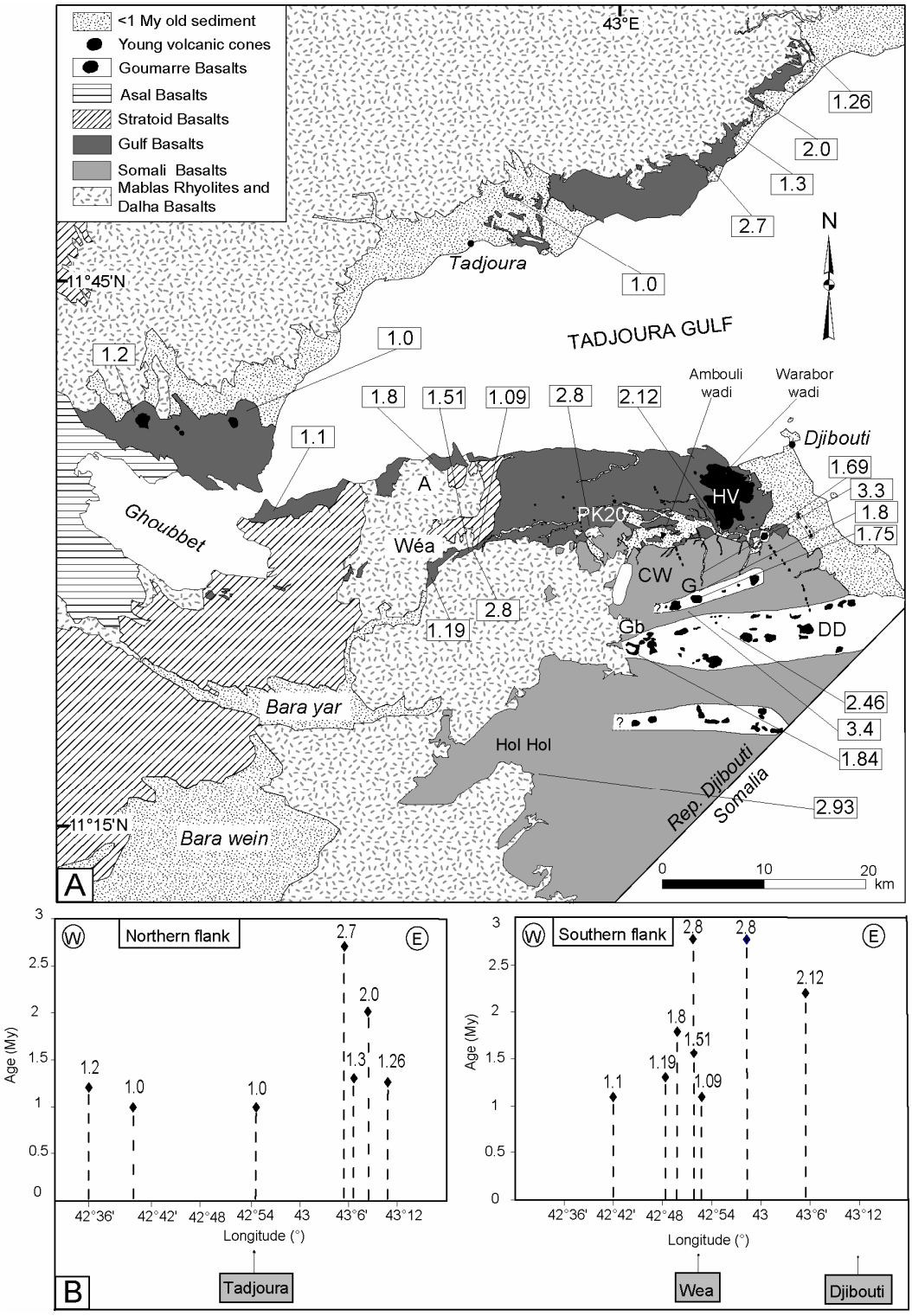

Figure 4: Radiometric age dataset about recent synrift volcanics on the onshore flanks of the Tadjoura rift. (A) Compiled age determinations (squares with number), from published (Richard, 1979; Gasse et al., 1983; Zumbo et al., 1995), and new (this study, see Table 1) data, shown on a revised geological map. The main improvements concern (i) the Goumarre Basalts, and (ii) the southern map boundary of the Gulf Basalts. A., Arta; CW., Chabelley wadi; DD., Dey Dey wadi; HV., Hayyabley volcano; G., Goumarre, Gb, Goubbetto. (B) Longitude *versus* age plot for the southern and northern coastal strips of Gulf Basalts. Linear age progression is not observed.

The rapid disappearance of Gulf Basalts W of 42° 50' is likely to be assigned to a nearly NS-trending paleo-high lying in the northern prolongation of the Arta eastern flank (Figure 4A). Vertical mafic dykes and associated sills and plug-type feeder magmatic structures identified through tilted lava successions NE of Tadjoura (Figure 4A) confirm the fissural origin of the entire Gulf Basalt series (Richard, 1979), but they also rule out its exclusive origin from vents located along the present-day offshore axis of the TR (Richard, 1979). The N110°E trend of the measured feeder dykes further indicates, in first approximation, a local direction of opening at N20°E, i.e. at a low angle with respect to the inferred regional applied extension (N30°E).

4.2. The southern flank of the TR

On the basis of geochemical criteria presented below, the map distribution of Gulf Basalts in the Djibouti Plain (Figure 4A) is assumed to be more restricted than previously assessed by earlier workers (Gasse et al., 1983, 1985). They are confined to a 10 x 30 km coastal faulted plateau bounded to the S, along the Ambouli wadi, by the older Somali Basalts. To the E, they are overlain by the ~1 Ma-old Hayyabbley ellipsoidal volcano (Gasse et al., 1983; Daoud et al., submitted), the main axis of which follows a major NW-SE fault scarp bounding the eastern coastal plain. From published aeromagnetic maps (Figure 2B) (Manighetti et al., 1997), the Gulf Basalts are likely to extend further E offshore, abuting rapidly against the Quiet Magnetic Zone, and being possibly offset to the NE by fault structures ($D_{7\text{-}5}$) of the Maskali transform network.

The Gulf Basalts pile consists of a succession of fluid lava flows of fissural origin, emplaced subaerially, contrary to the claim of Gasse et al. (1983) who identified pillow-type structures that have not been observed during the present work. Individual flows are generally less than 10 m thick, and their surfaces show typical pahoehoe features; their central part often displays columnar jointing patterns. Field emplacement criterions (e.g. deformation of pahoehoe "ropy" surfaces and flow patterns at their base, such as vesicle orientation and filling by late melts) indicate that they mostly flowed southwards in the Djibouti Plain. Their original vents have not been recognized, and therefore are presumably located in the submerged part of the TR. The Gulf Basalts pile reaches a maximum thickness of 220 m in boreholes drilled in the PK20 area to the W, in which it overlies the Somali Basalts (Figure 4A). Its basal contact with older underlying rift volcanics is locally visible along the Wea paleo-valley which deeply incises the Arta uplifted zone (Figure 4A).

There, the Gulf Basalts rest unconformably over highly weathered basalts of the 5.9-3.6 Ma-old Dalha series (Varet, 1975; Richard, 1979), along a SE-dipping surface which represents the initial slope of a NE-SW orientated paleo-valley (Figure 5B). Their present-day denivellation with respect to Gulf Basalts in the Djibouti Plain results from for recent vertical tectonics discussed in the last section. The uppermost sequence of Gulf Basalts exposed in the Ambouli-Chabelley southern area includes a succession of thin (<1 m-thick) subaerial lava flows, interdigitated with conglomeratic alluvial horizons (basaltic boulder-rich facies) which probably derived from uplifted reliefs in the Arta and Somali surrounding domains (Figures 4A, 5A). On the topographic profiles of figure 3B, these young and flat-lying Gulf mafic sequences seem to onlap over a previously tilted surface, facing the N, and involving the Somali Basalts.

Available K-Ar and Ar-Ar ages for Gulf Basalts from the Djibouti Plain range from 2.8 to 1.5 Ma (Richard, 1979; Gasse et al., 1983; Zumbo et al., 1995; Figure 4A). This range can be extended to 1.19 Ma (Table 1) taking into account our new results on Gulf lava flows from the Wea paleo-valley (see below). On the Warabor wadi cross-section, the Gulf lava pile is clearly overlain by the Hayyabley volcano lava flows which yield ages of 1.06 ± 0,09 Ma and 0.93 ± 0,06 Ma (Daoud et al., submitted). 3.3 Ma-old basaltic rocks lying SE of the Ambouli wadi have been assigned by Richard (1979) to the Gulf Basalts (Figure 4A), and are inversely attributed here the Somali series described below. As such, they can no longer be used to support the E-W progressive younging of Gulf Basalts previously assessed (Richard, 1979 ; Manighetti et al., 2001; Audin et al., 2004), and which is further contradicted by our longitude versus age plots for the southern and northern strips (Figure 4B).

The ca. 7.2-3.0 Ma old Somali Basalts (Chessex et al., 1975) cover most of the Djibouti Plain beyond the regional-scale flexure to the S (Figure 4A). They form two monotonous and weakly incised plateaus, separated by a 40-50 m-high fault scarp facing N (Figure 3B). Owing to their extensive map distribution on the southern flank of the TR (Figure 4A), the Somali Basalts are likely to have been emplaced as a trap-like series, similarly to the nearly contemporaneous (8.6-3.8 Ma) Dalha basaltic series located NW of the Djibouti Plain (Marinelli and Varet, 1973; Barberi et al., 1975). Because of their restricted exposure and difficult access conditions in SE Djibouti, the total thickness, as well as the internal organisation, of the Somali Basalts are poorly known. The 30-40 m high cross-sections exposed along the Dey Dey wadi (Figure 4A) show up to ten superimposed subaerial Somali basaltic flows (either columnar-jointed or showing lava tubes).

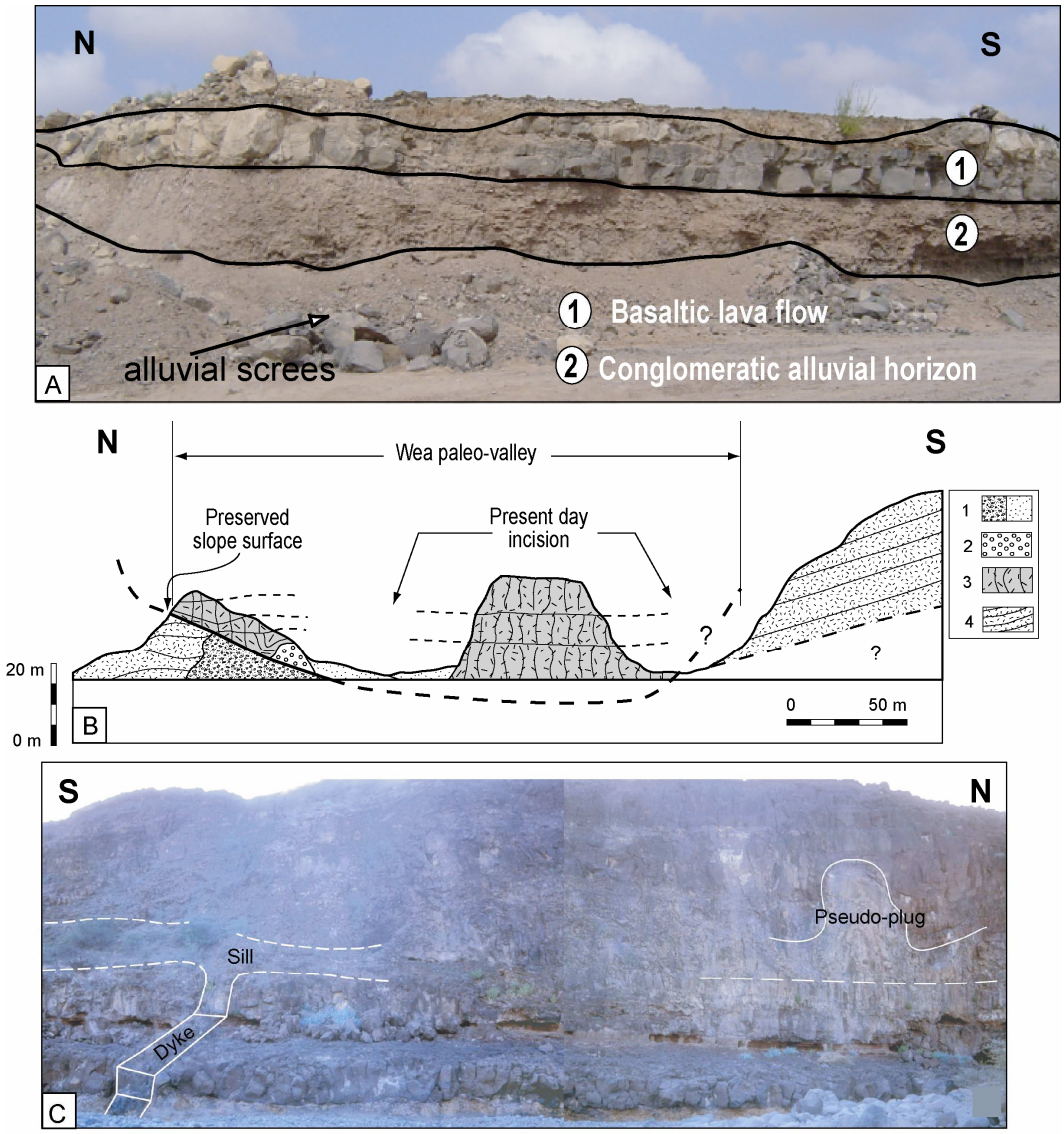

Figure 5: Magmatic features of recent volcanic series in the Djibouti Plain and Arta relief. (A) Alluvial conglomeratic horizon interdigitated with a thin basaltic lava flow of Gulf Basalts in the Ambouli-Chabelley area, i.e. close to the southern flexure with the underlying Somali Basalts. (B) Interpreted structural cross-section showing flat-lying Gulf Basalts filling a NE-SW-oriented paleo-valley incised into highly weathered and inclined Dalha Basalts (SW Wea village, see map in figure 6A for location and regional structural framework). 1. Recent alluvial deposits; 2. Paleo-valley deposits; 3. Gulf Basalts; 4. Dalha Basalts. (C) Mafic sill-dyke complex of the Goumarre series intruding a pile of flat-lying basaltic lava flows (Dey Dey wadi).

Sample	Loc. (GPS)	K (wt%) ± 1σ	Mass molten (g)	$^{40}Ar^*$ (%)	40Ar* 10^{-13} (mol./g) ± 1 σ	40Ar* 10^{-13} (mol./g) Weighted mean ± 1σ	Age (Ma) ± 2 σ
dj43/04b							
7454	11°28'26"N	0.371 ± 0.004	1.07191	2.434	7.003 ± 0.106	7.012 ± 0.008	**1.09 ± 0.03**
7470	42°49'49"E	« ..... »	1.00241	3.093	7.020 ± 0.105		
dj38/05							
7257	11°30'42"N	0.332 ± 0.003	1.09347	2.153	6.949 ± 0.109	6.882 ± 0.081	**1.19 ± 0.04**
7273	42°52'56"E	« ..... »	1.02438	3.088	6.796 ± 0.122		

Table 1: K-Ar ages for samples from Gulf Basalts (see figure 4A for location)

They range in thickness from 1 to 10 m and are often separated by autoclastic breccia levels and/or by strombolian lapilli horizons up to 1 m-thick. In the Holhol area (Figure 4A), the Somali Basalts rest unconformably over tilted and partially eroded rhyolitic sequences of the 15-11 Ma old Mablas series (Black et al., 1975; Zumbo et al., 1995). The 30 m-high Goumarre cross-section, located in the Chabelley wadi immediately to the N of the Goumarre strombolian cone (Figure 4A), exposes 7 superimposed subaerial basaltic flows, 2-8 m-thick each, emplaced from S towards N (i.e. in an opposite direction with respect to that of the Gulf Basalts), according to local field criterions. Their chemical composition, similar to that of the Dey Dey and Holhol basalts (Somali basalts), differs from that of the Goumarre cone pyroclastic deposits (see below). Mafic dykes cutting through Somali lavas in the Goubetto area to the W (Figure 4A) consist of ~1 m-thick vertical intrusions, oriented N80-90°E, i.e. parallel to the Gulf Basalts feeder dykes.

With respect to the intricate swarms of recent volcanoes which punctuate the Djibouti Plain (Figure 4A), special attention has been paid to three N80°E parallel arrays of basaltic vents crosscutting the Somali Basalts, and referred here as to the Goumarre Basalts (from their type-locality, the Goumarre strombolian lapilli/ash cone, dated at 1.75 Ma by Gasse et al., 1983). These volcanic corridors, each of them a few km-wide (their cartographic limits in Figure 4A, from remote sensing data, are tentative), are intersected to the E by the N140°E coastal scarp, whereas they disappear westwards before reaching the older Ali Sabieh range. In addition to numerous small strombolian or maar-type volcanoes, with maximum heights of ca. 100 m, the Goumarre Basalts sequence includes various types of intrusions (dykes, sills, plugs) often spatially connected with these volcanoes. The genetic relationships between Goumarre-type lavas and their inferred magmatic feeders are clearly depicted on interpreted aerial photographs from the Dey Dey central corridor in the Goumbourta Atar strombolian cone area (Figure 4A). There, lava flows, are seen to either radiate from small-scale vents, or diverge on both sides of N80°E trending fault/fissure structures which correlate in the field with narrow (1-2 m-thick) dykes and thicker (15 m) sills cutting through Somalis Basalts (Figure 5C). Most of the Goumarre Basalts are therefore likely to have been emitted from transverse fault/dyke corridors, nearly parallel to the present-day Gulf axis. Published radiometric ages from the Goumarre (2.46, 1.84, 1.8, 1.75 Ma) and Nagad (1.69 Ma) cones (Richard, 1979; Gasse et al., 1983) are younger than those obtained from the Somali Basalts (3.4, 3.3, 2.93 Ma) **(**Richard, 1979; Zumbo et al., 1995) (Figure 4A). They are here attributed to the so-called Goumarre Basalts which might have been emplaced during a short time

interval, concomitantly with the Gulf Basalts, but in a more southern, and external, position with respect to the TR.

4.3. The Arta transverse zone

The Arta zone is a 15 km-wide NS-trending elevated zone (maximum altitude of ca 720 m) made up of old rift-related volcanics. It is bounded on both sides by recent basaltic complexes that floor the Djibouti Plain to the E (Gulf Basalts), and occur as a series of tilted fault blocks in the Asal rifted domain to the W (2.3-1.0 Ma old Stratoid series) (Zumbo et al., 1995) (Figure 6A).

The Arta zone is cored by acidic effusive sequences of the Mablas formation, and overlying highly weathered Dalha Basalts, 5.9-3.6 Ma in age (Varet, 1975; Richard, 1979), which are both deformed into a large-wavelength anticline striking NS to N20°E (Figures 6A, B). Its deeply incised axial zone is a ~10 km-wide high-strain corridor composed of a dense set of NS-N20°E strike-slip faults with both dextral and sinistral senses of motion (Arthaud et al., 1980). The NS fault network is intruded by a swarm of 3.6 Ma-old acidic intrusions (Ribta series) (Richard, 1979) which disappear abruptly southwards at the latitude of the Koron acidic body, close to the eastern prolongation of the Ghoubbet axis. These highly-strained and fault-controlled volcanics are unconformably overlain to the NE by much less deformed basalts of the Lower Stratoid series (S_1), which probably extend laterally eastwards beneath the Gulf Basalts (Figure 6C). The eastern side of the Arta relief is incised by a NE-SW trending paleo-valley (close to the Wea village), partially filled up by Gulf Basalts subaerial lava flows (Figure 6A, B)that we have dated at 1.09 ± 0,03 Ma and 1.19 ± 0,04 Ma (Table 1). The maximal altitude of these lava flows increases from ~100 m in the Djibouti Plain up to ~500 m westwards in the Wea area, whilst field emplacement criterions (e.g. flow patterns at their base, such as vesicle orientation and filling by late melts) indicate that they flowed from the Djibouti Plain towards the Arta zone. Therefore, we consider that their present altitude difference results from vertical fault-related displacements, probably coeval to the narrow Gulf-parallel coastal extensional fault array which downthrows the northern edge of the Arta zone towards the Gulf axis (see below). To the W, the sharp and linear boundary of the Upper Stratoid Basalts (S_2) along the western side of the Arta relief probably follows a NS paleo-high which has subsequently acted as a mechanical barrier for the EW-trending extensional fault network of the Asal-Ghoubbet rift (see discussion in Section 7).

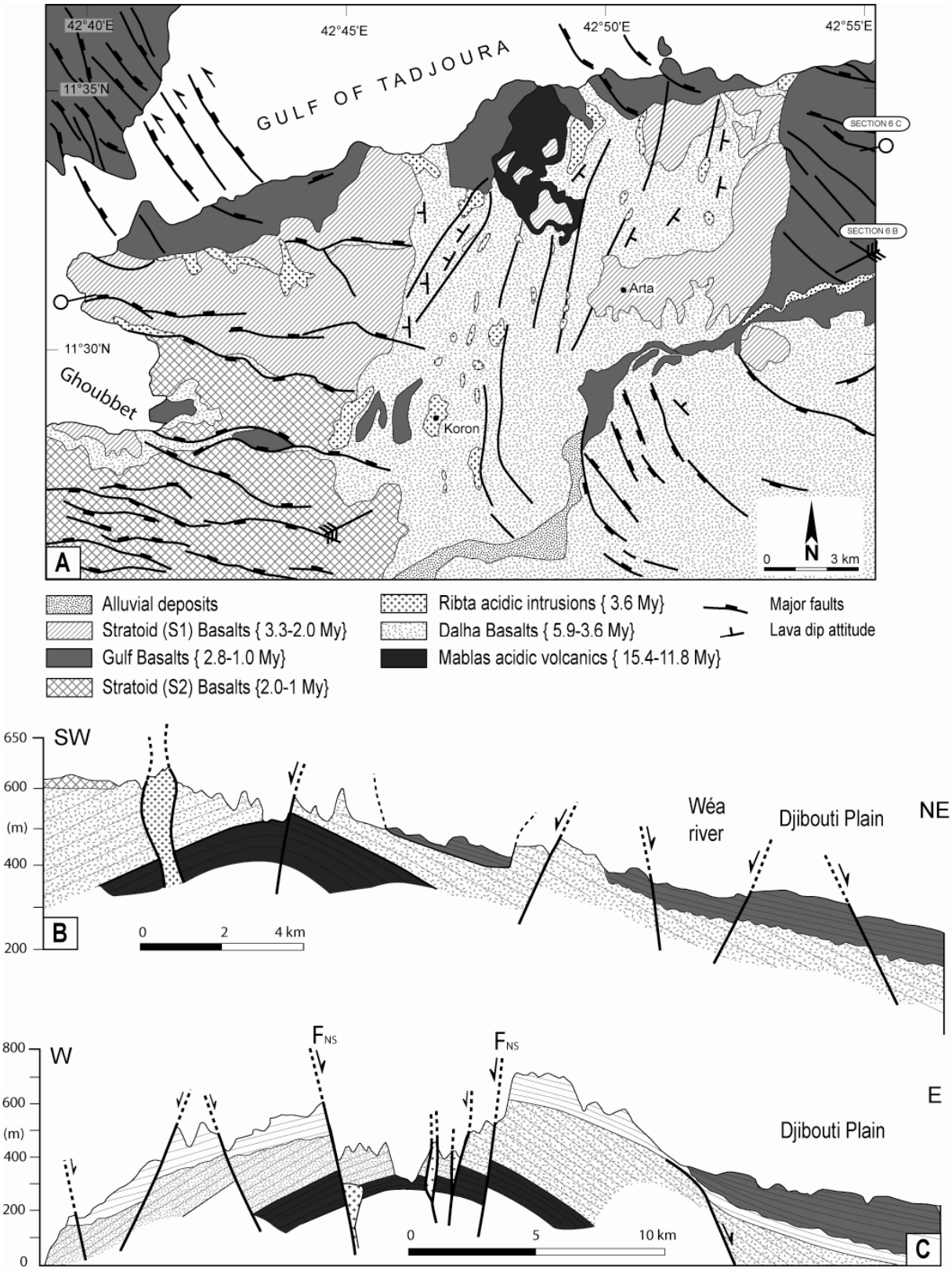

Figure 6 : Structure of the Arta transverse zone. (A) Structural map elaborated from revised published maps (Gasse et al., 1985), remote sensing interpretation, and field observations. (B, C) Structural cross-sections showing (i) the anticline structure of the Mablas-Dalha series, (ii) the close spatial association of Ribta acidic intrusions and NS faults, (iii) the angular unconformity of the Stratoid and Gulf Basalts, and (iv) the downthrow of the Djibouti Plain to the E, probably in response to fault-controlled flexuring (C). Vertical exaggeration ~ 10.

5. Geochemical data

5.1. Sampling, classification and petrographic notes

We have analyzed for major and trace elements 78 samples, among which 21 were collected from the Gulf Basalts series in the Djibouti Plain, 10 from the same unit N of the Tadjoura Gulf, 22 from the Somali Basalts series, 16 from the young volcanic cones and intrusions from the Goumarre Basalts series, and finally, 9 from the Hayyabley volcano (Figure 7A). The location of these samples are shown in figure 7A, except those of the Hayyabley Basalts which are described elsewhere (Daoud et al., submitted). Chemical analyses of representative samples are given in Table 2.

In addition to this sample set, we have shown, as envelops in figures 7 and 8, the fields of previously published analyses of (1) the Gulf Basalts (Initial Gulf Basalts: Richard, 1979; Joron et al., 1980a; Vidal et al., 1991; Deniel et al., 1994), (2) the Asal Basalts (Richard, 1979; Joron et al., 1980b; Vidal et al., 1991; Deniel et al., 1994), and (3) the basalts dredged along the Tadjoura Gulf axis (Barrat et al., 1990, 1993).

All the collected samples are basalts, according to the total alkalies-silica (TAS) classification scheme (not shown) of Le Bas et al. (1986). In the TAS plot of figure 7B, they lie on both sides of, but close to, the line separating the fields of subalkalic and alkalic basalts (Irvine and Baragar, 1971), with the exception of Hayyabley Basalts which are clearly subalkalic. The others can therefore be considered as transitional basalts with a dominant tholeiitic tendancy (Richard, 1979; Bizouard and Richard, 1980; Joron et al., 1980a,b; Vidal et al., 1991; Deniel et al., 1994). This terminology is consistent with the fact that most of them plot in the olivine tholeiite field in the CIPW normative plot of figure 7C, although a significant proportion of Somali Basalts are quartz-tholeiites. The various groups may be quite readily distinguished using the TAS plot (Figure 7B): the Somali Basalts are more silica-rich than the others (SiO_2: 48-52 wt%) while Hayyabley Basalts are consistently depleted in alkalies ($Na_2O + K_2O \sim 2$ wt%); and the Goumarre Basalts are, at equivalent SiO_2 contents, richer in alkalies than the Gulf Basalts. Among the latter, the compositions of samples collected on either sides of the Tadjoura Gulf overlap systematically, a feature already noted by previous authors (Richard, 1979; Bizouard and Richard, 1980; Gasse et al., 1983).

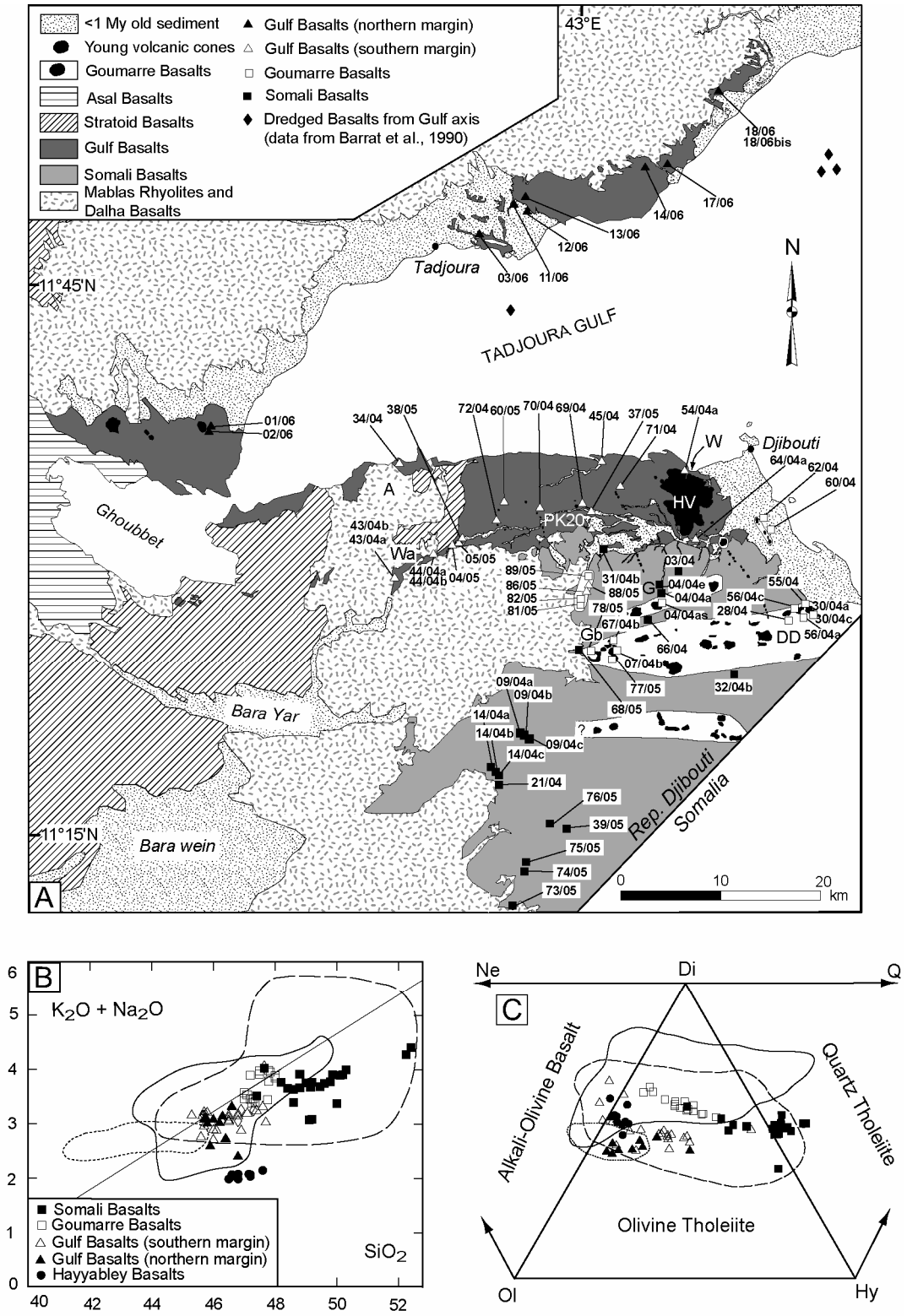

Figure 7: Geochemical dataset of recent mafic volcanics from the Tadjoura rift. (A) Location map of 78 rock samples studied in this work. (B) Total-alkalis-silica (TAS) diagram for the Gulf, Goumarre and Somali Basalts. Symbols refer as to our own analyzed samples, whereas the continued, dashed and dotted lines correspond to fields of Initial Gulf, Asal, and Gulf axis basalts, respectively, in published works (see corresponding references in the text). (C) Normative composition of the Gulf, Goumarre and Somali Basalts. Same symbols as in figure 4B. Fe^{3+} are calculated according to Middlemost (1989).

Groupe	Gulf Basalts(Northern margin)			Gulf Basalts(Southern margin)				Goumarre Basalts			Somali Basalts				Hayyabley Basalts
sample	dj18/06	dj03/06	dj18/06	dj45/04	dj38/05	dj 60/05	dj43/04b	dj07/04al	dj30/04al	dj04/04as	dj03/04	dj 39/05	dj14/04c	dj09/04b	dj54/04b
SiO_2	46.30	46.20	45.90	46.10	47.40	47.60	46.50	47.00	48.00	48.00	49.20	48.20	49.86	50.10	47.15
TiO_2	2.92	2.71	1.98	2.46	2.65	2.78	2.96	3.72	3.62	3.84	3.32	3.42	2.88	2.88	0.93
Al_2O_3	14.35	15.35	15.35	14.55	13.87	14.15	14.20	13.34	13.48	13.25	13.00	13.36	13.85	13.50	16.53
Fe_2O_3*	15.40	14.50	14.20	14.62	16.10	15.95	16.68	15.00	15.25	15.50	15.10	16.15	14.50	14.50	10.35
MnO	0.22	0.21	0.21	0.21	0.23	0.24	0.24	0.22	0.23	0.24	0.22	0.25	0.22	0.22	0.17
MgO	8.20	7.65	6.75	8.50	6.05	6.10	6.24	5.77	5.17	4.95	4.74	4.89	4.82	4.92	9.45
CaO	10.00	10.45	11.00	10.45	10.05	9.80	9.74	10.45	10.00	9.60	9.30	9.50	9.24	9.15	12.9
Na_2O	2.66	2.67	2.35	2.53	2.71	2.77	2.71	2.86	3.03	3.13	2.90	3.04	3.14	3.22	1.99
K_2O	0.47	0.34	0.23	0.34	0.53	0.54	0.44	0.71	0.81	0.75	0.86	0.72	0.76	0.67	0.08
P_2O_5	0.42	0.30	0.23	0.34	0.38	0.34	0.38	0.54	0.59	0.53	0.62	0.56	0.41	0.40	0.07
LOI	-0.83	-0.42	1.54	-0.28	-0.50	-0.46	-0.73	-0.38	-0.31	-0.48	0.41	-0.25	0.05	-0.12	0.46
Total	100.11	99.96	99.74	99.82	99.47	99.81	99.36	99.23	99.87	99.31	99.61	99.84	99.72	99.44	100.08
Rb	6.90	5.20	2.70	5.00	10.20	6.80	8.30	13.80	16.00	14.90	18.00	11.80	10.30	17.30	1.05
Sr	320.00	393.00	317.00	315.00	262.00	264.00	266.00	378.00	378.00	810.00	318.00	330.00	320.00	317.00	154.00
Ba	168.00	138.00	119.00	130.00	208.00	158.00	155.00	210.00	223.00	305.00	270.00	290.00	220.00	212.00	34.00
Sc	35.00	31.50	37.50	35.00	39.00	38.00	39.00	38.00	33.00	32.00	34.00	35.5	34.5	36.00	45.00
V	380.00	350.00	337.00	365.00	405.00	395.00	425.00	460.00	400.00	465.00	405.00	398.00	388.00	395.00	285.00
Cr	287.00	207.00	311.00	320.00	94.00	89.00	69.00	130.00	44.00	28.00	28.00	22.00	29.00	29.00	380.00
Co	56.00	53.00	57.00	58.00	56.00	51.00	54.00	44.00	43.00	43.00	44.00	43.00	44.00	43.00	51.00
Ni	150.00	135.00	153.00	175.00	79.00	71.00	78.00	76.00	48.00	35.00	38.00	24.50	42.00	41.00	198.00
Y	34.50	29.50	26.50	33.00	42.00	42.0	42.50	42.50	45.00	44.00	48.50	45.00	42.00	41.50	20.50
Zr	190.00	153.00	122.00	160.00	200.00	204.00	195.00	275.00	280.00	293.00	280.00	253.00	256.00	264.00	48.00
Nb	25.00	20.20	13.00	18.00	23.00	25.00	22.50	39.50	41.00	45.00	36.50	32.00	31.00	32.00	2.70
La	19.50	16.30	13.00	15.40	20.00	21.50	20.00	30.50	34.00	33.50	30.00	28.00	27.50	27.50	2.60
Ce	44.00	39.00	31.00	36.00	46.00	49.00	46.00	68.00	76.00	74.00	69.00	63.00	61.00	62.00	7.1
Nd	28.00	24.50	20.00	22.50	27.50	29.00	28.00	41.00	45.00	44.00	41.5	37.50	36.00	35.50	5.3
Sm	6.70	5.85	4.40	5.70	6.90	6.80	7.10	9.10	9.70	9.50	9.60	8.50	8.10	8.25	2,00
Eu	2.2	2.01	1.68	1.96	2.25	2.22	2.3	2.87	3.12	3.01	3.02	2.87	2.56	2.54	0.8
Gd	6.7	5.9	5.00	6.10	7.15	7.6	8.00	8.9	10.00	9.50	10.00	9.40	8.60	8.20	2.30
Dy	6.35	5.10	4.50	6.00	7.25	7.40	7.40	8.00	8.50	8.30	9.00	7.90	8.00	7.85	3.30
Er	3.30	2.70	2.50	3.10	4.00	4.00	4.10	4.00	4.40	4.10	4.70	4.20	4.00	4.00	2.10
Yb	3.05	2.55	2.29	2.85	3.73	3.80	3.80	3.47	3.80	3.62	4.00	3.90	3.68	3.66	2.18
Th	1.50	0.80	0.80	1.02	2.55	2.55	1.85	3.00	3.40	3.40	3.00	2.75	3.20	3.45	0.10

Table 2: Representative chimical composition (major in w% and trace element in ppm) of Gulf,, Goumarre, Somali and Hayyabley volcano Basalts

The studied basalts are subaphyric to moderately porphyritic, with 3 to 15 modal % phenocrysts which are mostly calcic plagioclase and magnesian olivine in a ~ 2:1 ratio (again with the exception of Hayyabley Basalts which display a reverse proportion).These phenocrysts are set in holocrystalline or moderately glass-rich groundmass showing microlitic to subdoleritic textures, with microcrysts of plagioclase, olivine, augite, titanomagnetite and hemoilmenite. Their crystallization order, typical of transitional and tholeiitic series, involves successively (1) magnesiochromite, usually found as inclusions within olivine phenocrysts, (2) olivine, (3) calcic plagioclase, (4) augite, and finally (5) iron-titanium oxides. The microprobe study of equivalent lavas (Richard, 1979; Bizouard and Richard, 1980) has documented a strong Fe enrichment in olivines and augites from the cores to the rims of phenocrysts and to groundmass crystals, as well as from relatively primitive basalts (with low FeO total/MgO ratios) to evolved ones, indicating their crystallization under low oxygen fugacities.

5.2. Major and transition elements

Selected plots of major and transition elements against total iron as FeO versus MgO ratios (FeO*/MgO) are shown in figure 8A**.** Once again, the Hayyabley Basalts differ from all the other groups by their more primitive character (lower FeO*/MgO ratios close to unity, higher Ni concentrations), and their much lower TiO_2 and P_2O_5 contents. Gulf Basalts from both the Djibouti Plain and the Tadjoura area tend to display lower FeO*/MgO ratios (1.5 to 2.5) than the Goumarre and Somali Basalts (2 to 3), as well as lower SiO_2 (45-48 wt%), TiO_2 ,P_2O_5 and K_2O contents. Regarding the transition element Ni and others not shown (Co, Cr), they are intermediate between the relatively primitive Hayyabley Basalts and the evolved Goumarre and Somali Basalts. The compatible behavior of Ni is consistent with olivine fractionation in the various series, whereas the incompatible behavior of TiO_2 and V (the latter not shown in figure 8A is consistent with the late crystallization of Fe-Ti oxides which incorporate selectively these elements (indicative of low oxygen fugacities; Bizouard and Richard, 1980).

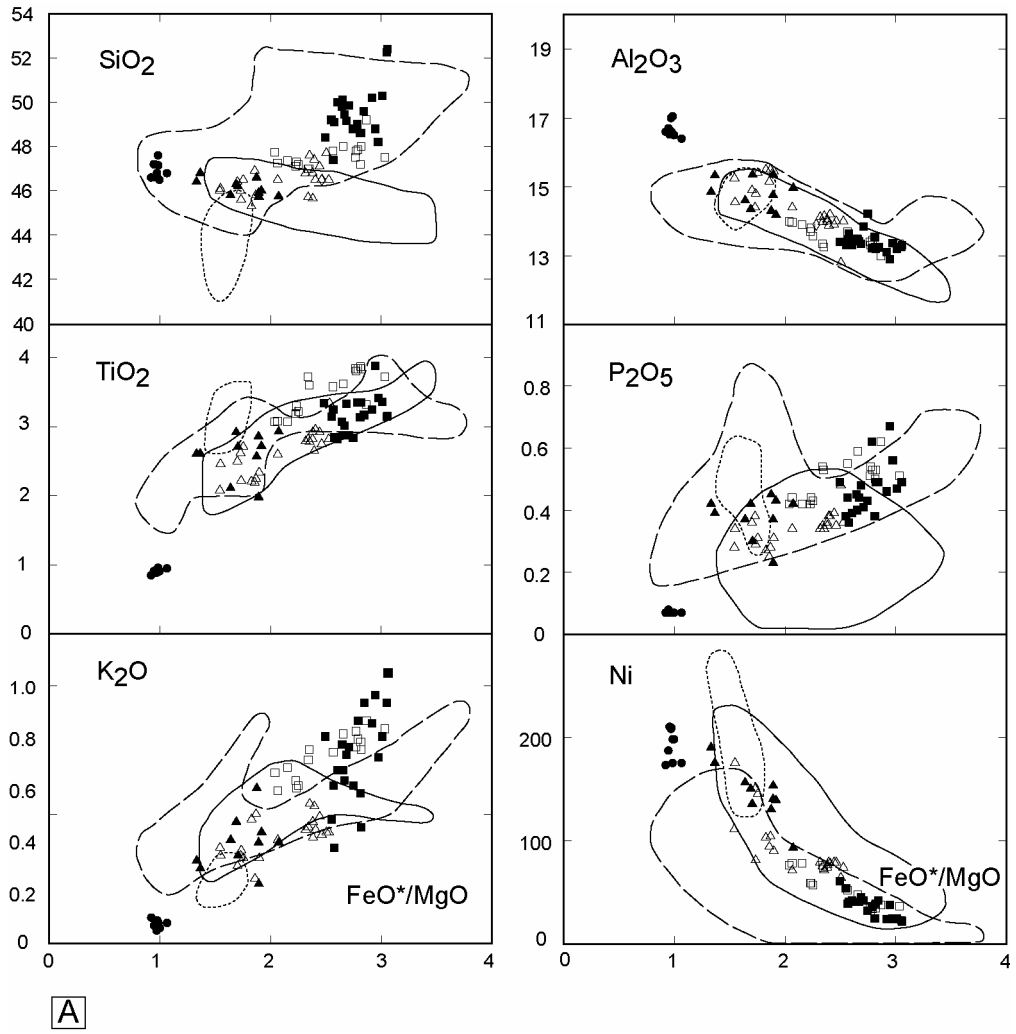

Figure 8: (A) Plots of SiO_2, TiO_2, K_2O, Al_2O_3, P_2O_5 and Ni against FeO*/MgO ratios of the studied basalts. Symbols are as in figure 7

5.3. Incompatible elements

The envelops of the incompatible multielement patterns of the studied basalts, normalized to the Primitive Mantle (Sun and McDonough, 1989) are shown in figure 8B. The Hayyabley Basalts have flat to slightly depleted patterns with low normalized concentrations which are obviously different from those of the other studied types (Gulf, Goumarre and Somali Basalts). The latter display moderately enriched patterns typical of Afar transitional basalts (Barrat et al., 1990, 1993; Vidal et al., 1991; Deniel et al., 1994; Rogers, 2006; Furman et al., 2006). However, several significant differences between the patterns of Gulf, Goumarre and Somali Basalts can be noticed on these plots. For instance, the Gulf Basalts are generally less enriched in incompatible elements (especially in the most incompatible ones, from Rb to Ce) than the Goumarre and Somali Basalts which display strong positive Th spikes. Furthermore, Somali Basalts display a larger range of heavy rare earth element (e.g. Dy and Yb) contents than the other types, including higher concentrations close to ten times the Primitive Mantle. Consequently, the rare earth element patterns (not shown) of the Goumarre Basalts are more fractionated than those of the Somali Basalts, and the two types can easily be distinguished by their different La/Yb ratios, calculated at 8-10 and 6-8, respectively.

An other discriminative method for distinguishing the Gulf Basalts from the Goumarre and Somali Basalts is provided by the incompatible element ratios plotted in rectangular diagrams in figure 8C that show no much overlap between the fields of these three groups. Basically, all ratios using an element plotting to the left or the middle of the multielement plot (e.g. Th, Ba, Nb, La, Zr or others not shown like Rb, K, Ce, Sr, P) versus an element plotting to the right (Y, Yb) will allow to distinguish the moderately enriched Gulf Basalts from the more enriched Goumarre and Somali Basalts. In addition, the two latter types may be distinguished using their different La/Yb ratios. Using these plots, together with geomorphological, structural and age data, led us to shift the map limit between the Gulf and Somali Basalts in the southern part of the Djibouti Plain 10 km further N than previously drawn on published map (Gasse et al., 1983, 1986). In addition, the abrupt chemical change observed at a depth of 220 m in basalts drilled in the PK20 borehole (Figure 5A) is consistent with the transition from the upper Gulf Basalts to the underlying Somali Basalts. However, the top of the Somali pile in this drilling is abnormally enriched in Y and heavy rare earth elements (e.g. Yb), and the corresponding point has thus not been shown in figure 8C plots.

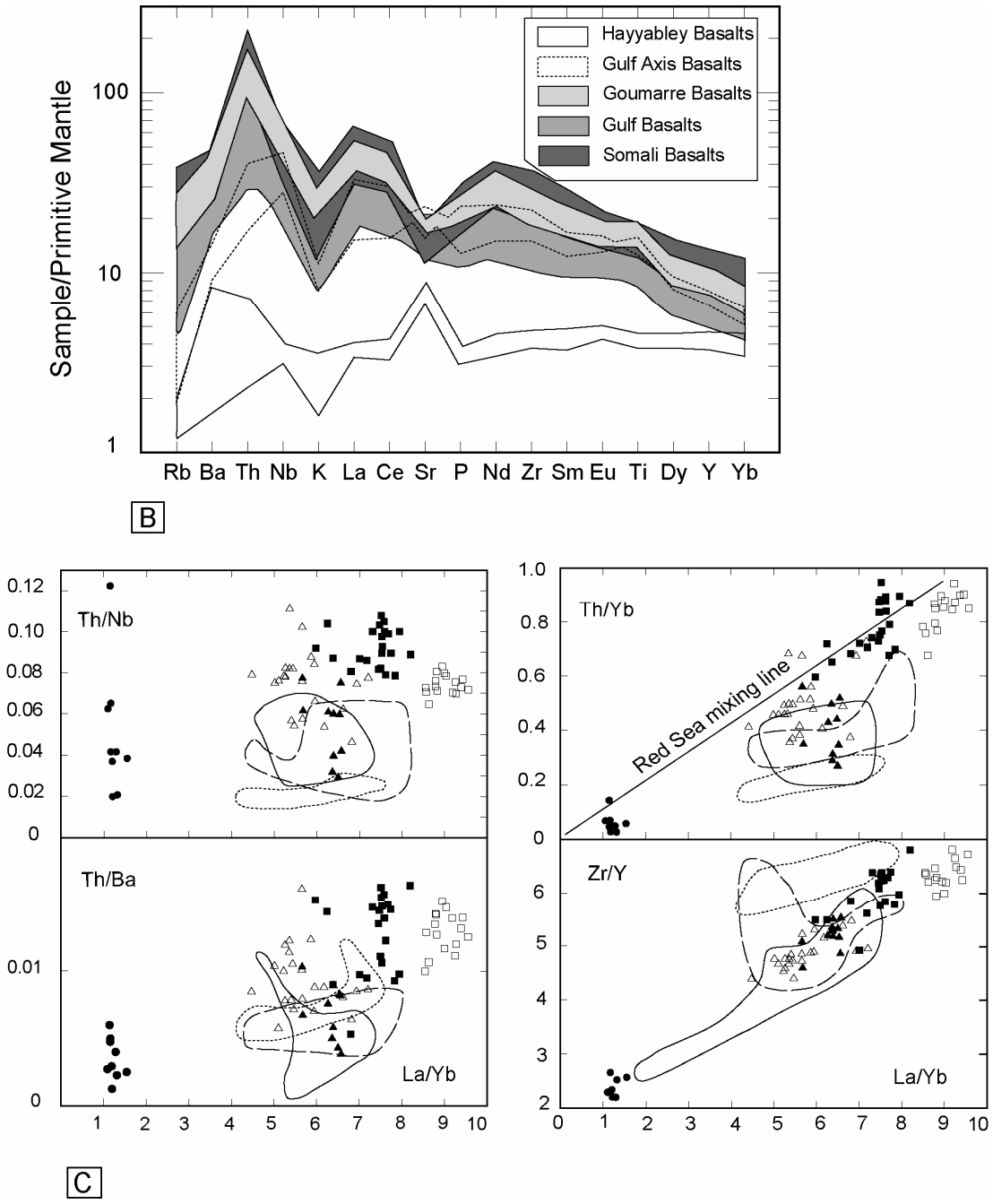

Figure 8 (continued): (B) Multielement patterns of the studied basalts. (C) Plots of Th/Nb, Th/Ba, Th/Yb, and Zr/Y ratios against La/Yb ratios. Symbols are as in figure 7.

Such abnormal enrichments are the consequence of the crystallization of the low-temperature REE-bearing rhabdophane during tropical pedogenetic alteration processes (Cotten et al., 1995), prior to the emplacement of the Gulf basaltic pile.

5.4. Magmatic patterns in the TR

The Hayyabley Basalts display flat incompatible element patterns obviously different from those of the other types. These relatively primitive basalts are interpreted as derived from a depleted component of the Afar mantle plume (Daoud et al., submitted), similar to that of the source of Manda Hararo basalts in Ethiopia (Barrat et al., 2003), and will not be discussed further in the present paper. Tholeiitic basalts dredged along the axis of the Tadjoura Gulf (Barrat et al., 1990, 1993) are also relatively primitive (high Ni contents and rather low FeO*/MgO ratios; Figure 8A) and depleted in the most incompatible elements Figure 8B). All the other types are transitional basalts, plotting close to the enriched component of the "Red Sea mixing line" (Figure 8C right diagram) which connects the depleted (depleted MORB mantle) and enriched (plume-type) components of the sources of the Red Sea basalts (Barrat et al., 1990). (However, the fact that most of the studied samples plot below this mixing line indicates that a third component is needed to explain their genesis (Barrat et al., 1990; Schilling et al., 1992; Chazot and Bertrand, 1993).
It could be either the Afar lithospheric mantle (Vidal et al., 1991; Barrat et al., 1990; Deniel et al., 1994) or alternatively, hydrothermalised gabbroic crust (Barrat et al., 1993).

Fractionation of olivine might account for some of the differences observed between the Gulf Basalts, on one hand, and the Goumarre and Somali Basalts, on the other hand, as the latter display higher FeO*/MgO ratios, lower Ni and other compatible transition element contents, and higher SiO_2, TiO_2, P_2O_5 and K_2O contents (Figure 8A). This process might also account for their higher incompatible element contents compared to the Gulf Basalts (Figure 8B)**.** However, as it does not fractionate appreciably ratios between highly incompatible elements (e.g. Th/Nb and Th/Ba, Figure 8C), nor strongly modifies the shapes of rare earth element patterns (and consequently the La/Yb ratios; Allègre et al., 1977), it cannot account for the differences shown in figure 8C plots. These differences could result from variations affecting partial melting degrees, mantle source heterogeneity, crustal contamination, or more likely a combination of these processes (Joron et al., 1980a, b; Barrat et al., 1990, 1993; Vidal et al., 1991; Deniel et al., 1994).

In addition, the different La/Yb ratios of the Goumarre and Somali Basalts, which display nearly equivalent enrichments in most incompatible elements, might indicate that the former derive from a deeper (i.e. garnet-bearing) mantle source than the latter, as garnet incorporates selectively heavy rare earth elements.

The occurrence of systematic spatial and/or temporal variations in basalt chemistry is far from obvious from our data set (which, however, does not include isotopes). E-W spatial trends have not been noticed, as the composition of the Gulf Basalts is rather constant throughout the studied zone. A progressive increase of incompatible elements away from the Tadjoura Gulf axis might be consistent with the enrichment pattern observed from the dredged basalts of the Gulf axis to the onshore Gulf Basalts and then towards the Goumarre and Somali Basalts in the S. However, one should note again that the Hayyabley Basalts do not fit in this pattern. A temporal trend from enriched (old) towards more and more depleted (young) basalts might also be envisioned. However, the enriched character of the Goumarre Basalts, emplaced more or less synchronously with the Gulf Basalts, is difficult to explain in this framework, except by postulating that partial melting degrees increased through time (especially near the axis of the Gulf) and that they affected mantle sources which are more and more enriched away from this axis (Deniel et al., 1994).

6. Rift fault pattern

The overall structure of the TR, as defined here, is first discussed in map-view and along selected cross-sections by merging available onshore and offshore datasets (Figure 9). Onshore fault networks cutting through the Gulf Basalts on either margins of the TR are deduced from ASTER satellite images (lateral resolution: 15 m), and ASTER 3D-topographic data (vertical resolution: 7 m). The classical parameters (azimuth, length, displacement, and spacing) of these extensively exposed fault populations can be analysed quantitatively, and their cross-cutting relationships with dated volcanic and sedimentary rift sequences further supply accurate timing constraints for elaborating an age progression framework of faulting within the TR. Much larger uncertainties exist about the offshore fault network extracted from bathymetric dataset (Audin, 1999) which are only used here to get a complete structural overview of the TR architecture.

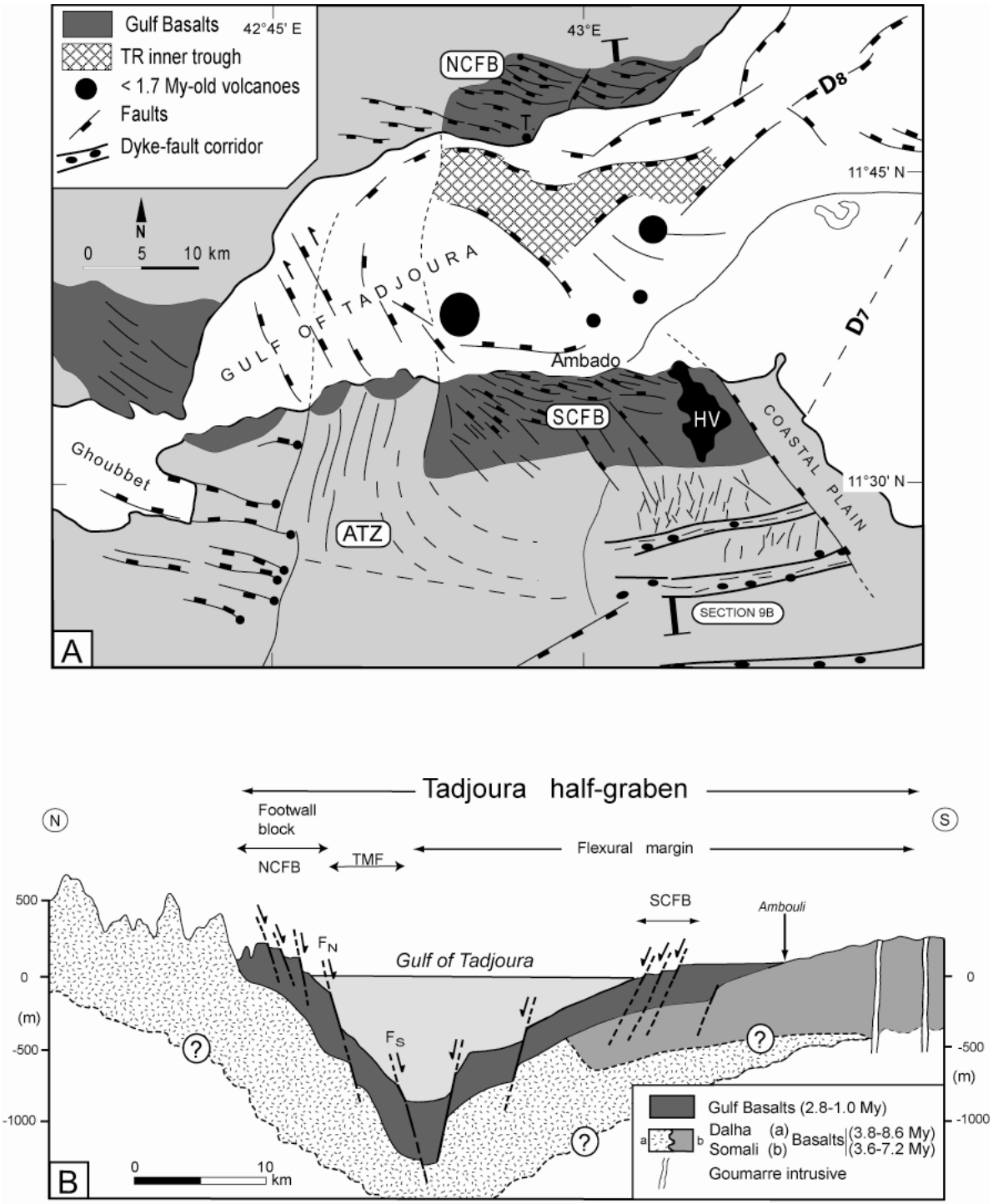

Figure 9: Overall structure of the Tadjoura rift. (A) Structural sketch map of the TR obtained (i) by merging onshore (ASTER 3D-topography) and offshore (bathymetry) dataset, and (ii) by using the Gulf Basalts as a rift marker. ATZ, Arta transverse zone; HV., Hayyabley volcano; NCFB., Northern coastal fault belt; SCFB., Southern coastal fault belt; D_7 and D_8 are transform structures. (B) Interpreted structural cross-section of the TR as a southerly-facing half-graben, partly filled with Gulf Basalts. The deep structure of TR is more conjectural; the geometrical relationships between the Somali and Dalha basalts are extrapolated from patterns observed onshore along the BOL (NW flank of the Ali Sabieh antiform). F_N and F_S represent two major synthetic extensional faults forming the Tadjoura master fault (TMF).

These results are then compared with those obtained on older surrounding units in the Arta transverse zone in an attempt to better constrain both the timing and the kinematics of recent faulting in the Tadjoura-Ghoubbet rift junction zone.

6.1. Overall rift fault network

As previously shown from topography and surface geology, the overall 2D-arrangement of faults in the TR is also asymmetrical, and typically characterizes a ~40 km-wide losange-shaped half-graben.

The so-called Tadjoura half-graben is bounded to the N by the Tadjoura master fault (TMF) and its associated faulted footwall (northern coastal fault belt). It extends southwards as a >20 km-long shallower flexural margin, partially exposed in the Djibouti Plain where it is locally disrupted by (1) an antithetic southern coastal fault belt, and (2) the Goumarre transverse fault-dyke corridors, close to the inflexion point of the Somali Basalts monocline. These latter form, together with the nearly contemporaneous Dalha basaltic series to the N, the substratum of the TR (Figure 9B). It is remarkable that recent faulting onshore is spatially restricted to the young volcanics (Gulf Basalts), dying out westwards before reaching the older 'substratum' series in the Arta-Ali Sabieh and Mablas ranges. Emphasis is placed here on the two exposed coastal fault belts which supply first-order structural data, despite their relatively restricted map dimensions. The deep structure of the Tadjoura half-graben is not yet well known due to the lack of any long-recorded seismic data. However, the location of the deepest inner fault-bounded trough along a NW-SE-oriented magnetic anomaly (Figure 2B) might indicate that it is underlain by a thinned (6 km) crust, of transitional type (Ruegg, 1975; Manighetti et al., 1997).

6.2. Geometrical and statistical fault analysis

6.2.1. The northern coastal fault belt

The Tadjoura Master Fault (TMF) system forms a ~5 km-wide faulted zone which involves at least two major synthetic extensional structures (F_N and F_S on figure 9B), bounding a narrow (<10 km-wide) inner trough to the N. Minimum vertical throws >200 m are estimated along each of these normal faults from the step-like bathymetric profile, a

feature which further indicates a bulk extension <20% along the TMF, assuming an average fault dip of 60°. In map-view, the TMF appears subdivided into numerous N50°E and N120°E segments (Figure 9A). However, the *en échelon* arrangement of individual second-order fault segments might result from a significant component of lateral (sinistral) shear along the N120°E course of the TMF.

The immediate footwall of the TMF forms the 20x10 km northern coastal fault belt (Figure 10A). The highly incised reliefs occurring further N in older substratum volcanic series are unlikely to be exclusively related to rift flank uplift. The coastal fault belt is dominated by two nearly orthogonal fault systems oriented at ca. N100°E (Gulf-parallel) and N20°E (Figure $11A_2$) in addition to N50°E (Maskali trend) faults to the E. Fault geometry is better expressed in the widely exposed unit to the N. There, the dominant N100°E fault set is composed of isolated and segmented structures with curved map traces (Figure 10A). The measured tip-to-tip length of the total fault dataset (N= 99) ranges from 0.4 to 6.0 km, with a peak at 1.2 km and 90% of length values <2.8 km (Figure $11A_3$). The prominent Gulf-parallel fault set is homogeneously distributed. Fault density (or spacing) calculated along five cross-sections (1 km apart) (Figure $11A_4$) and also as fault length per unit area (km/km^2) (Figure 13A) seems to decrease westwards. Individual fault structures are arranged into 4-5 major faults facing to the S, and causing the downthrow of the Gulf Basalts towards the Gulf axis. Very few antithetic structures exist with only minor displacement (for example F_{80} in Figures 10A, B). The morphotectonic expression of faults is depicted on four orthogonal cross-sections which also reveal marked variations of individual fault profiles along-strike (Figure 10B). The horizontal surface of most individual footwall blocks (F_4 and F_8) suggests non-rotational structures. The largest throw values (>50 m) strictly occur along the oldest (pre-alluvium) faults to the N. However, estimates of throws along the youngest (post-alluvium) fault structures to the S might be underestimated because of the occurrence of synfaulting alluvial screes at the foot of some fault scarps. Vertical throw in the northern fault array increases markedly southwards from 65m (F_6), 100 m (F_4) to >130 m (F_8). Comparing the four topographic sections shows the progressive westerly decrease of the total fault-induced elevation from 310 m (section 1) to 280 m (sections 2-4). These along-strike variations of cumulate fault displacement are illustrated by the distribution of throw along some individual structures, such as faults labelled $F_{1\text{-}7\text{-}19}$ or $F_{4\text{-}16}$ that die out towards a tip zone in the vicinity of the substratum contact to the W.

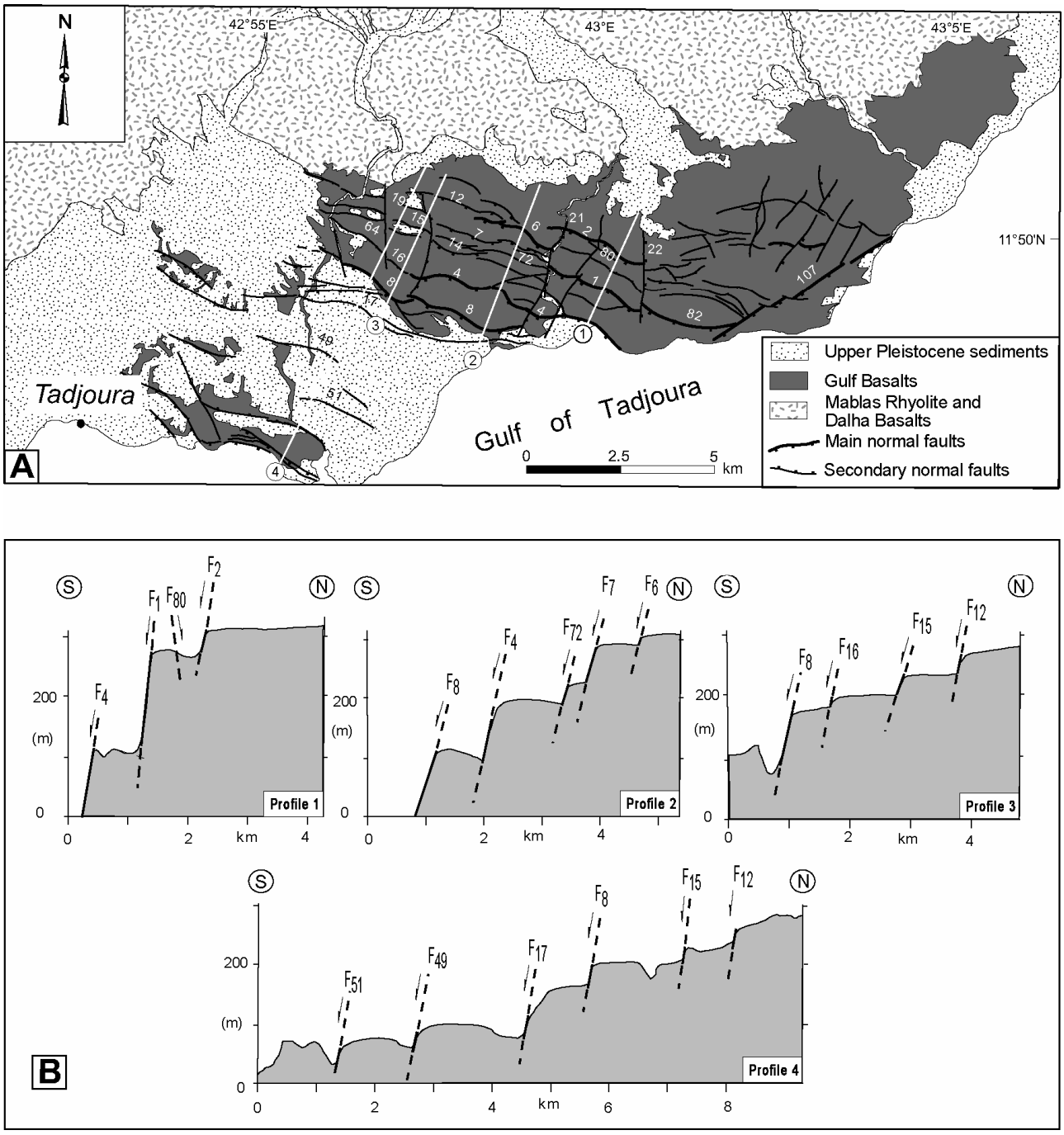

Figure 10: : Map distribution and morphological expression of extensional structures in the northern coastal fault belt (NCFB). (A) Structural map showing fault traces extracted from ASTER remote sensing dataset. Numbers refer to major individual structures. White lines indicate the trace of topographic profiles in figure 10B. (B) Four topographic cross-sections illustrating changes in fault geometry along-strike and perpendicularly to the N100°E rift axis.

The cumulate bulk extension is calculated along three regularly-spaced NS sections across the fault system (Figure $11A_1$) (see chapter 2 for the methodology). Fault dips applied for calculating cumulate bulk extension cannot be directly measured from ASTER 3D-topographic data, but previous studies suggested extensional fault dips ranging between 60°-70° in the Afar Depression (De Chabelier and Avouac, 1994). The bulk extension ranges from 1.60 to 3.40 %. These values are much lower than the 8-12% extension estimates applied by Gupta and Scholz (2000) to the Afar rift system. Concomitantly, the profile of each fault scarp changes significantly along-strike from a sharp and fresh step-like morphology to the E to a smooth topography with highly degraded upper surfaces to the W, hence suggesting the younging of Gulf-parallel fault structures eastwards.

Special attention is paid below to the throw-lenght ratio (T/L) which is known to supply interesting informations about fault growth processes (Cowie and Scholz, 1992; Dawers et al., 1993), as a function of either the restricted versus unrestricted nature of the faults (Gillespie et al., 1992; Marrett and Allmendinger, 1992), or the mechanical heterogeneity of the stressed medium (Trudgill and Cartwright, 1994; Wojta, 1994; Mansfield and Cartwright, 1996). T refers to maximum throw and L to fault trace length in map view.

Based on classical fault growth model (Cowie and Sholz, 1992b) predicting that displacement (referred here to as maximum throw) is generally greatest at or near the centre of fault and decreases toward the fault tips, Schlische et al. (1996) have defined, in log-log diagram of maximum fault displacement versus length, a field showing linear T-L scaling with a slope equal to 0.03. The T/L ratios calculated for N100°E Gulf-parallel faults (x 29 data) are in the range 0.0062-0.15 and fall within the field of the data of Schlische et al. (1996) (Figure 14A). This demonstrates the interdependence between horizontal and vertical dimensions of extensional Gulf-parallel faults in the northern coastal belt.

Two major submeridian extensional faults, facing E (F_{21} and F_{22}) (Figure 10A), with vertical displacements of 60 m and 50 m, respectively, are also identified. Their cross-cutting relationships with Gulf-parallel fault patterns (either interrupted or not, and with or without apparent offset) suggest their synchronous emplacement.

6.2.2. The southern coastal fault belt

The hangingwall of the TMF forms a shallower and longer flank along which seafloor depths decrease smoothly southwards towards the ca. 100 m-high plateau forming the Djibouti Plain (Figure 12B). This N-dipping flexure is locally disrupted by two discrete strained zones dominated by a series of north-facing (antithetic) fault structures. The outermost (coastal) faulted blocks in the Gulf Basalts give way southwards, *via* a ~10 km-long N-dipping monocline, to the much less deformed Somali Basalts plateaus which exhibit a NS-trending fracture network, clearly intersected by the three N80°E transverse dyke/fault corridors of the Goumarre intrusive series (Figure 9A). The entire Gulf-parallel tectono-magmatic structures in the Djibouti Plain are post-dated by the NW-SE fault-like lineament bounding the eastern coastal lowlands.

The antithetic fault network forming the southern coastal fault belt displays a much more intricate organisation than those described above for the Obock-Tadjoura conjugate margin (Figure 12A). Three sets of faults, striking N100-110°E, N130-140°E, and to a lesser extent N60-70°E, crosscut the Gulf Basalts pile (Figure $11B_2$). The dominant N100°E (Gulf-parallel) structures display a marked clockwise inflexion towards a N120-130°E trend westwards, in such a way that they parallel and connect into a ~5 km-wide swarm of N140°E faults which extend through the Somali Basalts, as far S as the Dey Dey transverse fault/dyke corridor (Figure 12A). Such map-scale relationships between the Gulf-parallel and N140°E fault networks are also documented from a few individual structures (Figure 12A), and may indicate the synchronous emplacement of the two systems. It is noteworthy that both Gulf-parallel and N140°E fault networks do not penetrate further W throughout the older volcanic terranes of the Arta plateau (Figure 12A). The map curvature of the Gulf-parallel fault pattern is accompanied by an increasing density of faults (Figure $11B_4$; 13B) which accordingly decrease in length. The majority of fault lengths (80%) are in the range 0.8-2.6 km, with a peak at 1.2 km (Figure $11B_3$), i.e. quite similar to the values obtained for the northern structures. Most Gulf-parallel fault structures are sigmoid or curved in map-view, and the *en échelon* arrangement of some of them (Figure 12A) might result from a significant component of sinistral shearing, as mentioned above for the TMF. However, their dominantly extensional nature is evidenced on the cross-sections of figure 12B. A majority of faults dip northwards, and display very little evidence for fault block rotation.

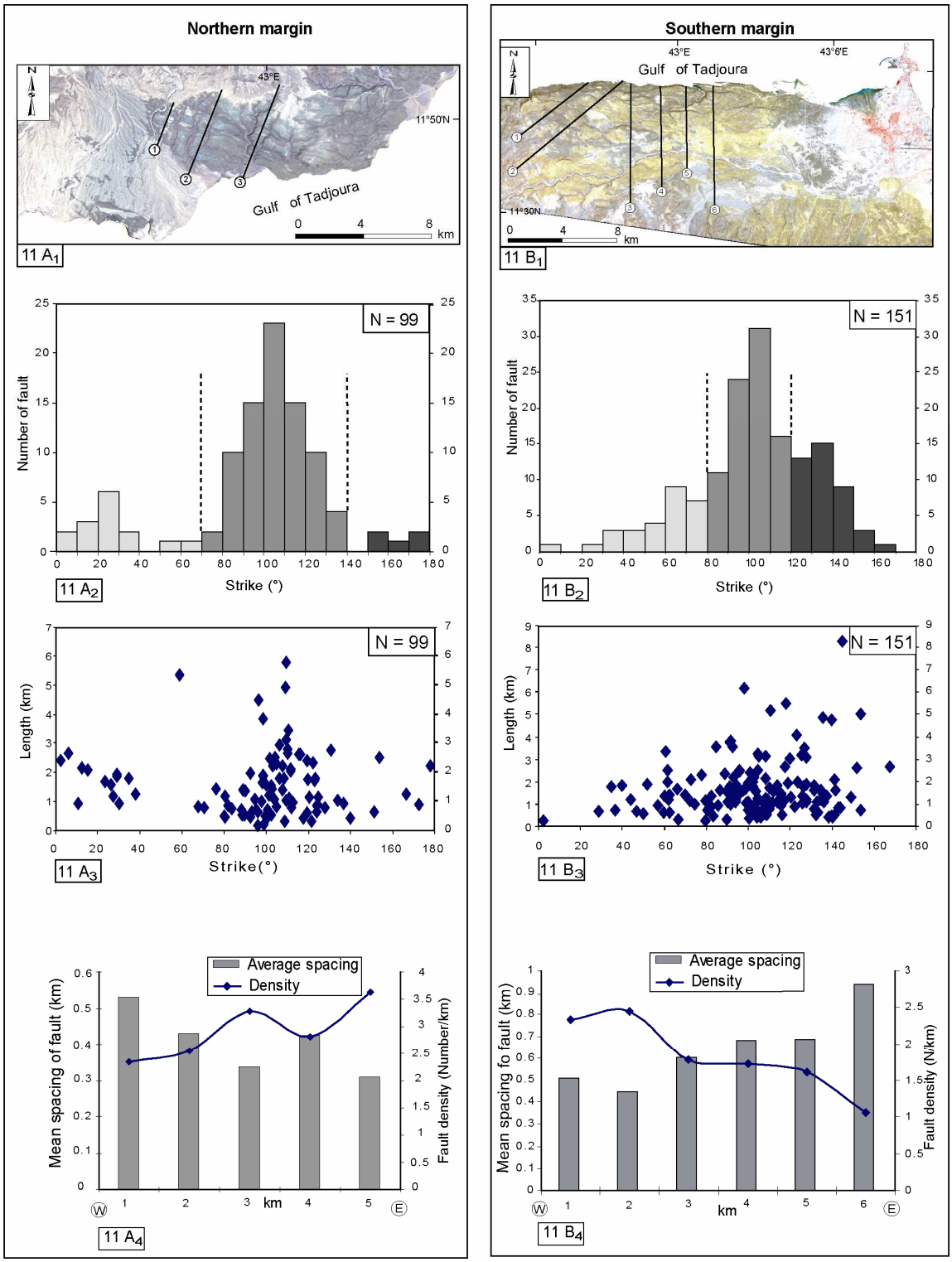

Figure 11: Geometrical and statistical characteristics of extensional fault networks in the northern (left column) and southern (right column) coastal fault belts of the Tadjoura rift. (A_1, B_1) General 2D-arrangement of faults on ASTER images. The traces of cross-sections used for calculating cumulate extension are drawn. (A_2, B_2) Histogram illustrating the frequency *versus* strike of faults. (A_3, B_3) Diagram of faults length *versus* strike. (A_4, B_4) Density and spacing of faults along five regularly-spaced (1 km apart) cross-section for Northern Coastal Fault Belt (See Figure $11A_4$ for cross-section location) and along six regularly-spaced (1 km apart) cross-section for Sourthern Coastal Fault Belt (See Figure $11B_4$ for cross-section location).

These faults are organized into a few (2-3) first-order tilted fault-blocks with an increasing structural complexity westwards which expresses from profiles 1 to 4 in figure 12B by (1) a larger number of N-dipping faults of reduced length, and (2) minor S-dipping faults, which together delineate second-order horst-graben patterns. For each structural section, maximum fault displacement is recorded along the coastal (innermost) structures, in a way symmetrical to that observed on the opposite (northern) side of the TR. Cumulate vertical fault displacement along each section perpendicular to fault system (Figure 12B) increases regularly westwards, from 100 m (profile 1), 250 m (profile 4), and 450m (profile 5), concomitantly with the structural complexity mentioned above. The cumulative extension calculated along six cross-sections (Figure $11B_1$) provides low values, ranging between 1.4 to 3.84 %, and increasing significantly westwards, in a similar way as mentioned above about the northern coastal fault belt. The T/L ratio for the Gulf-parallel structures (x 93 data) fall within a smaller range (0.0044-0.16) with respect to the published fault data of Schlische et al. (1996) (Figure 14B). The NW-SE transverse fault structures present in the western half of the belt are locally outlined by a dense swarm of small volcanic vents, ~1 Ma in age (Gasse et al., 1983). Similarly-trending, and probably deeply-rooted, faults likely controlled the emplacement of the ellipsoid-shaped Hayyabley volcano, as well as the downthrow of the Pleistocene coastal plain to the E (Figure 9A).

The N140°E fault network continues offshore, N of the Arta zone, and correlates with NW-SE left-lateral seismogenic structures (Figure 9A) (Lépine et al., 1980; Lépine and Hirn, 1992). The apparent contradiction with the dominant extensional component documented about their onshore counterparts (see morphological profiles in figure 12B) might be explained by the fact that strike-slip faulting usually results in a more intense seismic activity. Transverse faults are generally isolated and segmented structures with a more linear and longer map trace than Gulf-parallel faults (Figure 12A). Profiles 5-7 on figure 12B show the upper surfaces of the resulting ~1 km-wide fault blocks dipping consistently towards the Gulf, i.e. with a similar dip direction of that of the associated faults, hence suggesting a component of gravity-driven collapse along the transverse extensional structures. The cumulate displacement caused by transverse faulting increases regularly westwards towards the Arta zone, concomitantly with the ca. 300 m elevation of the topography (Figure 12B). Indeed, scarp heights measured along the 2-3 major NE-facing faults gradually increase from 20m and 50m (profile 7), to 70m and 80m (profile 6), and finally 70m, 30m and 90m (profile 5).

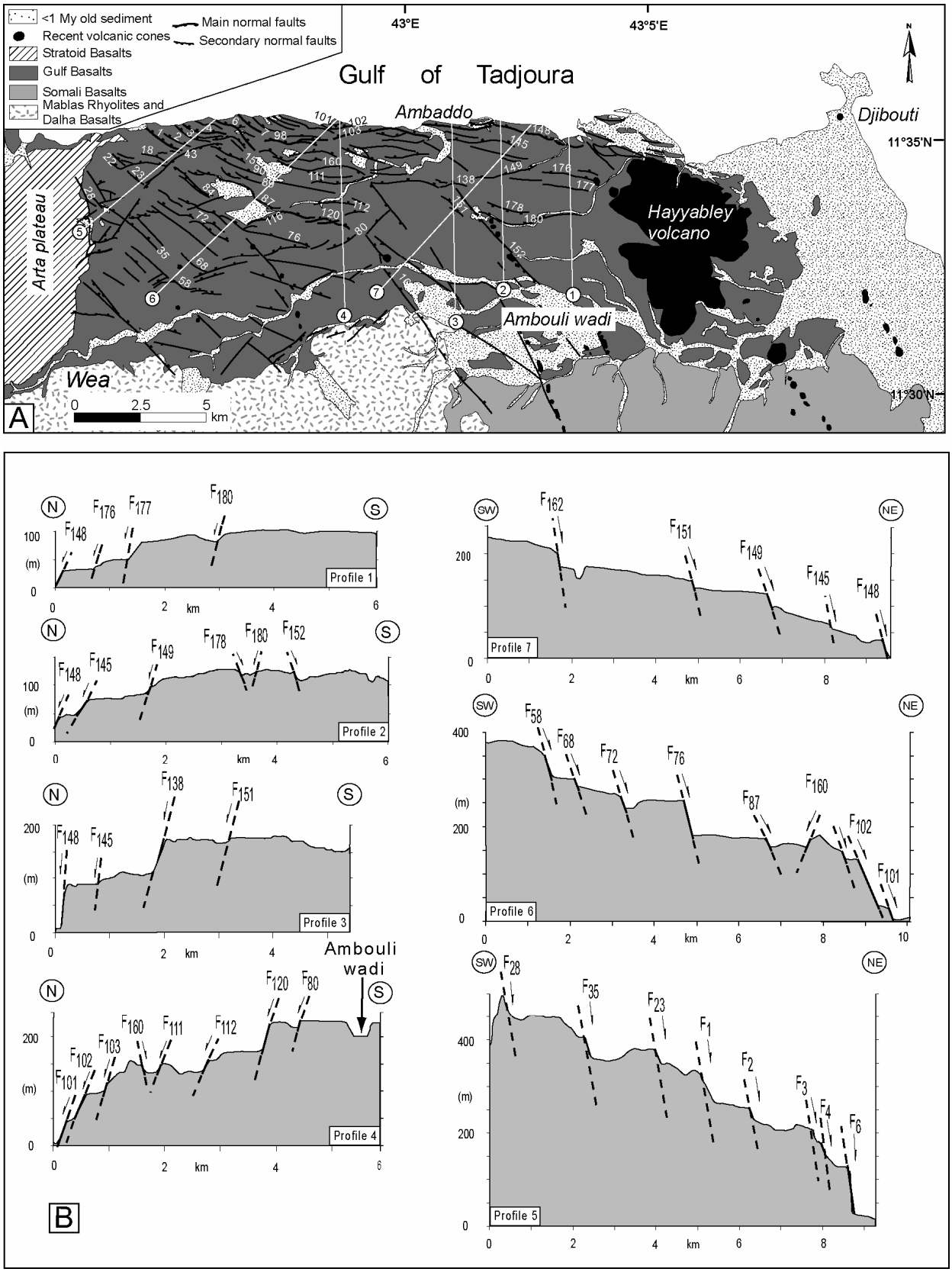

Figure 12: : Map distribution and morphological expression of the extensional fault pattern in the southern coastal fault belt of the Tadjoura rift. (A) Structural map of the SCFB from ASTER remote sensing interpretation. White lines are the traces of the topographic cross-sections of figure 12B. (B) Six morphostructural cross-sections showing (i) increasing structural complexity towards the Arta zone to the W.

The T/L ratios calculated for transverse faults (x 21 data) are in the range 0.0056-0.022, i.e. lower than those of the Gulf-parallel faults, but within the data of Schlische et al. (1996) (Figure 14B). The low T/L ratios reflect a deficit of vertical displacement with respect to fault length, as typically documented during fault growth processes dominated by linkage where fault length increases without increasing height (Cartwright et al., 1995). This is consistent with the isolated, linear and linked characteristics of the transverse faults cited above.

6.3. Timing of faulting in the TR

The compilation of published and new age determinations on both sedimentary and volcanic rift sequences exposed on the onshore margins of the TR supplies accurate temporal constraints about the sequential development of the Tadjoura half-graben during the past 3Ma. The Gulf-parallel extensional fault network in the two coastal belts shows a relatively clear age progression depicted on the NS cross-sectional diagram in figure 15. As already argued by Manighetti et al. (1997), two successive extensional fault sets are evidenced in the Tadjoura area. The most external faults are post-dated by 1.4-0.8 Ma-old alluvial fans in the footwall of the TMF (Gasse, 1991), while younger similarly-trending faults cross-cut Holocene conglomerates further S. A quite symmetrical age polarity is documented in the Djibouti Plain. Indeed, the oldest tectonic structures throughout the 20 km-wide onshore southern margin of the TR are the ~1.7 Ma-old Goumarre tectono-magmatic lineaments transecting the Somali Basalts, and tentatively assigned to extrados tensile stress on top of a regional flexure. This network is post-dated by onlapping Gulf Basalts (Ambouli section) which are in turn dissected by Gulf-parallel faults, necessarily younger than 1.7 Ma, and older than the ca. 1 Ma-old Hayyabley volcano to the E (Figure 9A; 12A). Younger (<1Ma) Gulf-parallel structures disrupted, in a more northern (inward) position, the northern edge of the Hayyabley volcano, and some of them might continue laterally westwards, up to the Ambaddo area (Figure 9A; 12A) where they are potential candidates for having caused the N-dipping tilt of 140-120 ky-old reef limestones (Gasse et al., 1983). As mentioned above, most of NW-SE transverse faults were probably active during Gulf-parallel fault emplacement. From the chronological dataset above, it appears that the age of Gulf-parallel faulting, on both sides of the TR, increases symmetrically away from the inner rifted zone (Figure 15).

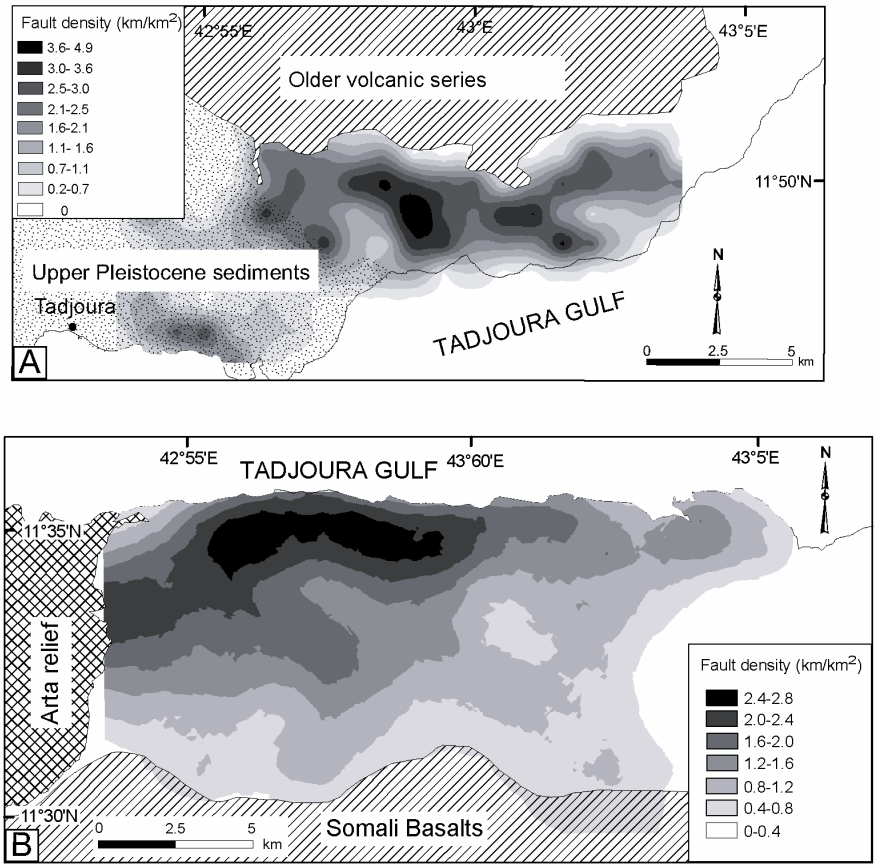

Figure 13: Fault density over the Northern (A) and Southern (B) coastal fault belts in the TR (see text for methodology). Note the pronounced increase of fault density westwards, towards the Arta relief, in the SCFB.

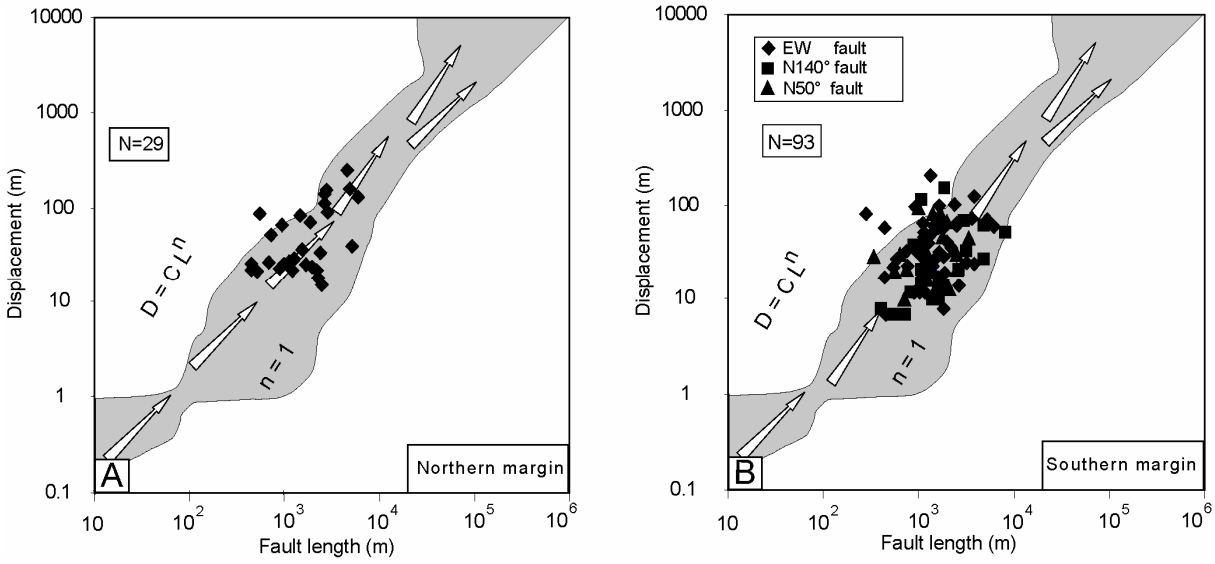

Figure 14: Log-log plot of maximum fault displacement *versus* fault length for structures in the northern (A) and southern (B) onshore margins of the TR. Shaded area outlines the field of published data from Schlische et al. (1996). White arrows indicate the fault growth path predicted by these authors. Note the tendency of EW-trending (axial) faults in the SCFB (B) to be 'over-displaced', suggesting that fault growth is only achieved by increase in fault displacement without increase in length when approaching the Arta transverse zone.

The current seismic activity in the Tadjoura trough (Lépine et al, 1980; Hofstetter and Beyht, 2003; Doubre et al., 2007) fits with the proposed age progression of faulting. Though uncertainties still subsist regarding the timing of development of the Tadjoura master fault to the N, major displacement (initial or reactivation) likely occurred along the TMF at ~1.7 Ma, assuming that the inward-facing flexure of the Somali Basalts to the S took place during the onset of half-graben development. The timing relationships between the sequential development of the TR and the intricate deformation recorded during the last 3-4 Ma by the Arta high-strained zone to the W are addressed in the general rift model proposed in the following section.

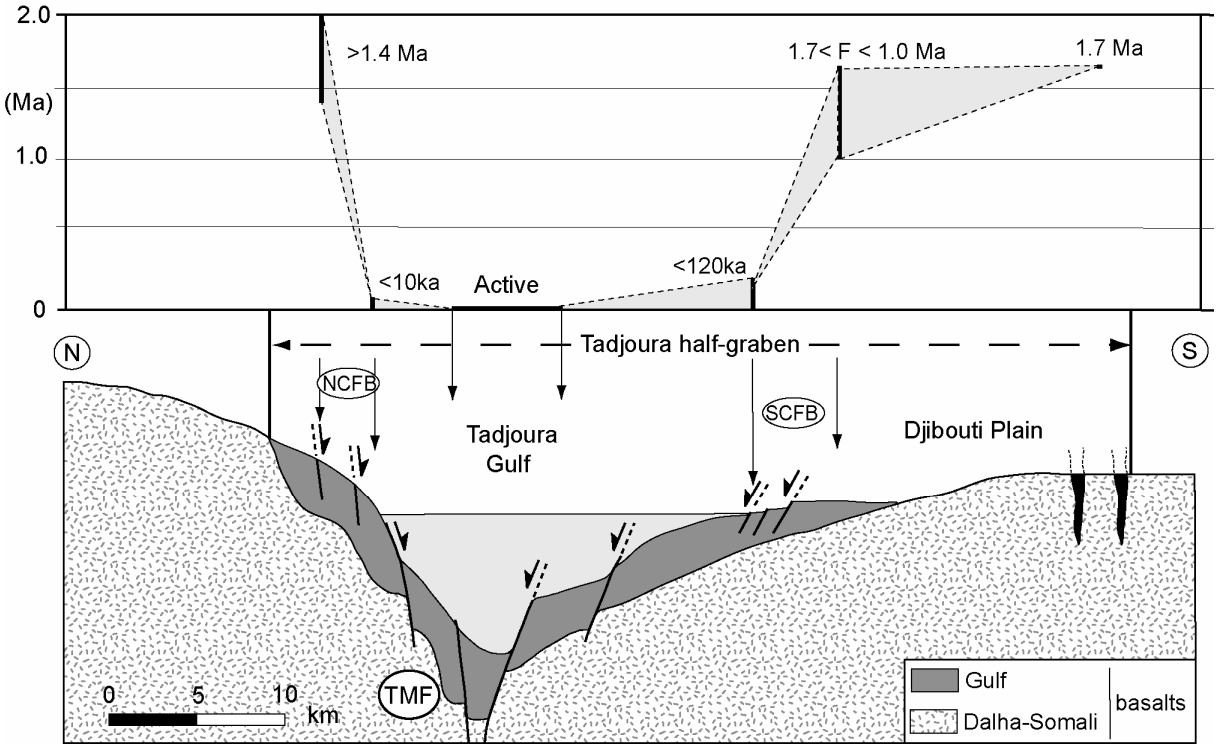

Figure 15: Timing of faulting along a cross-section in the Tadjoura asymmetrical rift. Despite age uncertainties, a rough younging of strain is clearly observed from the margins to the inner part of the TR, reflecting the progressive axial focusing of extension.

7. Proposed kinematic model for the Tadjoura Rift

A better understanding of the overall kinematic development of the TR during the last 3 Ma requires to address the nature of its relationships with the adjacent Ghoubbet-Asal rift segments to the W and, more generally, with the more extensive rift system that developed synchronously throughout southern Afar. Though timing of onset of faulting is poorly constrained along most of the rift axes in southern Afar (Gobaad, Hanlé, Gaggade), a two-stage kinematic model is attempted below from (1) our new results about the TR, and (2) a revised overview of published data about the Afar rift pattern. The two successive rift stages considered here, at 3-1 Ma and <1 Ma, roughly coincide with syn- and post-Gulf-Stratoid Basalts stages (Figures 16C, D). An earlier rift template (>3 Ma) is also shown in Figure 16 to illustrate the way pre-existing (synrift or older) structural fabrics might have controlled the locking or transfer or recent extension.

7.1. >3.0 Ma rift stage

The structural sketch map in Figure 16 is a restored picture of the Afar rift system at ~3.5 Ma, i.e. prior to Stratoid Basalts emplacement, and later than the 3.6 Ma-old Ribta Fm. At this stage, the entire area is assumed to be covered by the nearly synchronous Dalha (8.6-3.8 Ma) and Somali (7.2-3.0 Ma) trap-like basaltic series (Barbéri et al., 1975; Chessex et al., 1975). The presence of Dalha Basalts beneath the Afar depression is speculated from their present-day marginal distribution. The dimension of the Afar depression, as well as the corresponding position of the rotated Danakil ‘block’, are estimated by removing the ~12% of extension recorded by the Stratoid series during recent times (Gupta and Scholtz, 2000). The respective spatial distribution of the Dalha and Somali Basalts is partly controlled by NS (Asamo) and NE-SW (BOL) paleo-topographic and structural features related to the Ali Sabieh dome (Le Gall et al., submitted). At this stage, incipient continental rifting is chiefly accomplished via magmatic accretion, with no focussing of strain along axial ranges. The few mafic dykes feeding the Somali lavas in the Djibouti Plain consistently trend N80°E, and therefore indicate, at first approximation, a submeridian direction of extension during the onset of Somali basaltic activity. A quite similar N160°E-oriented extension is argued by Gaulier and Huchon (1991) about the tectonic regime that prevailed during eruption of the Dalha trap series further W.

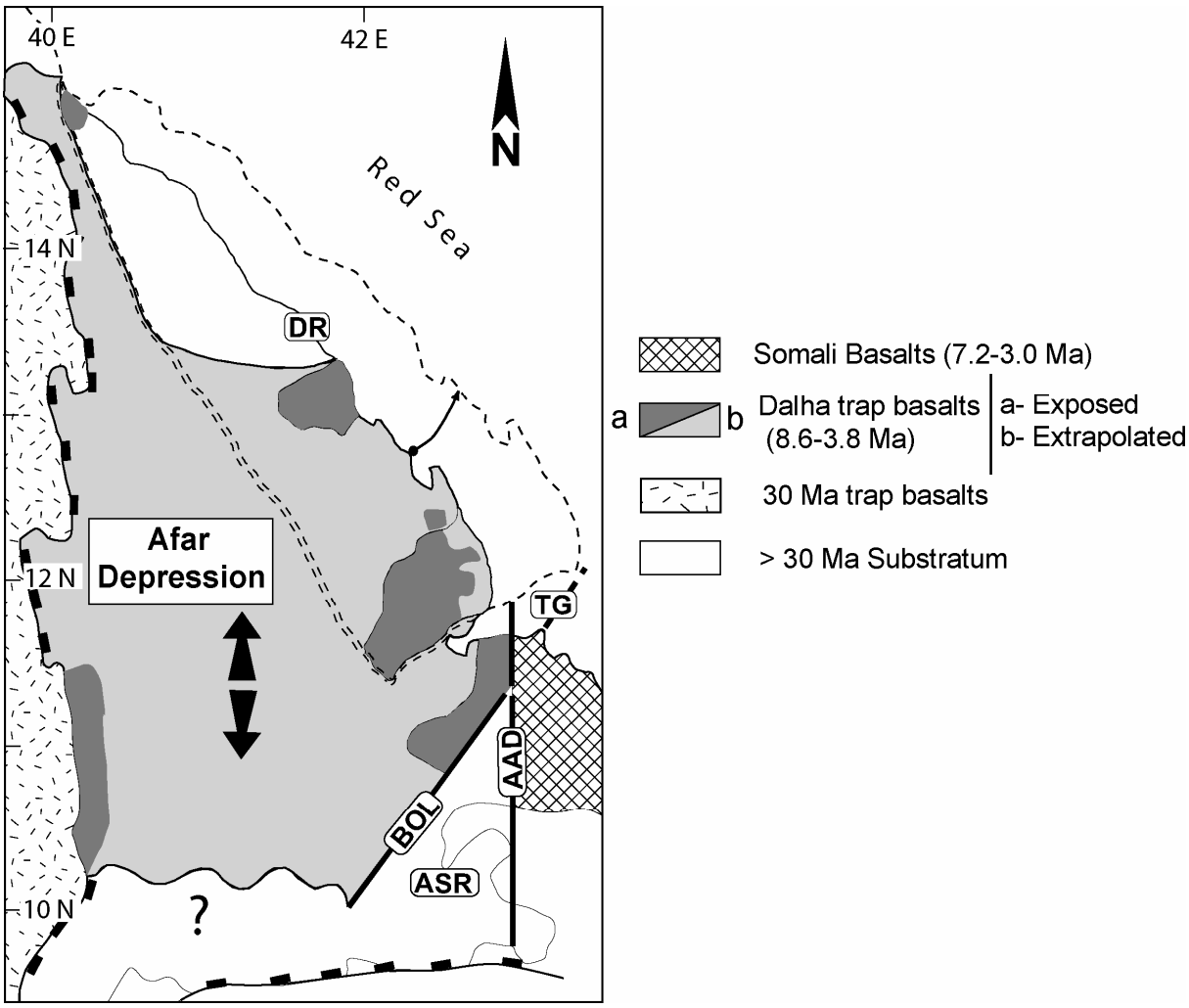

Figure 16: Major structural discontinuities assumed to have controlled the spatial distribution of Dalha and Somali trap-like basaltic complexes, prior to Stratoid emplacement, at < 3 Ma. The restored (clockwise) position of the Danakil range (DR) is obtained by removing 20% of estimated extension (and corresponding rotation) recorded during the last 3 Ma (see text for explanation). Dashed, and double-dashed, lines indicate the present-day, and restored, positions of the Danakil range, respectively. Black arrows show the direction of extension (<3 Ma), during the Dalha and Somali basaltic events. AAD., Asamo-Arta discontinuity; ASR., Ali Sabieh range; BOL., Boul Ougoul lineament; TG., Tadjoura Gulf.

The existence of a fundamental NS-trending discontinuity, the so-called Asamo-Arta structure, along the eastern flank of the Ali Sabieh dome, up to the Arta zone, is first documented to the S during emplacement of the Mablas acidic series at 15-11 Ma (Figure 17A, B). The *en echelon* map arrangement of four NE-SW intrusive segments (5 km-long each) is kinematically consistent with dextral shear along a NS deeply-rooted fault zone, reactivated in response to a transtensional regime (Gaulier and Huchon, 1991) (Figure 17C). The northern prolongation of this NS-oriented structure might have later guided the intense strike-slip shearing recorded by the Arta NS corridor synchronously to the intrusion of the 3.6 Ma-old Ribta acidic complex (see Section 4.3). The fact that only the northern part of the Arta-Asamo discontinuity, i.e. those strictly coinciding with the width of the TR, has been reactivated as a NS shear zone suggests local driving forces possibly related to the WNW-ESE-directed compression ahead of the rift propagator.

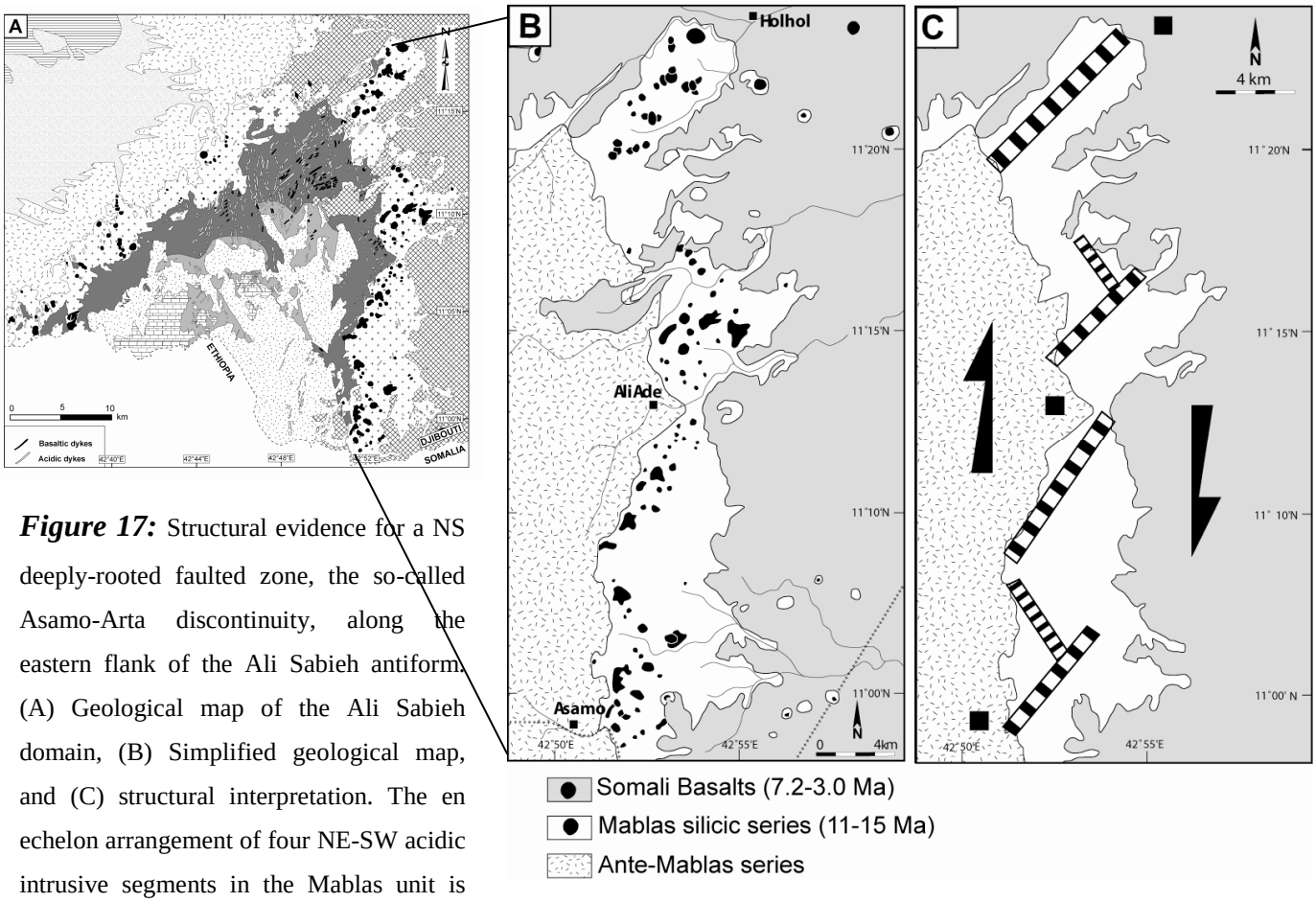

Figure 17: Structural evidence for a NS deeply-rooted faulted zone, the so-called Asamo-Arta discontinuity, along the eastern flank of the Ali Sabieh antiform. (A) Geological map of the Ali Sabieh domain, (B) Simplified geological map, and (C) structural interpretation. The en echelon arrangement of four NE-SW acidic intrusive segments in the Mablas unit is kinematically consistent with dextral shearing along a NS inherited deeply-rooted fracture zone.

In any case, the angle of 30-50° between the Arta submeridian shear zone and the NE-SW strike of the Maskali offshore transform system **(**Figure 18A) definitely excludes that these two features are part of a single transverse structure, in opposite with the model of Arthaud et al. (1980a ; b).

7.2. <3.0 Ma rift stages

As the result of the westerly propagation of the GA spreading system throughout the Dalha-Somalis magmatic province, radical changes in dynamics of rifting expressed by the synchronous activity of still ongoing magmatism (Gulf and Stratoid Basalts) and incipient extensional tectonics. The remarkably uniform left-stepping segmented geometry of the GA ridge (Tamsett and Searle, 1988; Manighetti et al. 1997) still occurred at its western extremity where extension is transferred southwestwards, via the Maskali NE-SW composite transform fault zone, from the Obock trough into the TR (Choukroune et al., 1988; Manighetti et al., 1998). During this early stage, extension might have been transferred further SW from the Obock-Tadjoura troughs into southern Afar along the so-called BOL which follows the NW flank of the Ali Sabieh dome (Acton et al., 1991; Audin, 1999). Sinistral transfer of strain along the Maskali offshore transform system, and subsidiary transverse fault structures, resulted in the development of a typical (30x25 km) S-facing half-graben (TR), partially filled with Gulf Basalt sequences, and bounded to the N by a highly segmented S-dipping master fault (TMF) which accommodated up to 15/20% of estimated extension. The inward-facing extensional fault network cutting through the uplifted footwall to the N, and the flexural margin to the S, have contributed to a minimum amount (~8%) of the 25-30% total extension. The general age migration of extensional fault networks in the TR, from oldest structures in an external position towards younger ones closer to the Gulf axis, resembles those typically observed along several parts of the Kenya rift (Cerling and Powers, 1977; Vétel and Le Gall, 2006). With regards to our proposed time-space rift model, which implies the progressive focusing of strain towards the axial zone, the small-scale ‘jumping rift segments’ identified by Manighetti et al. (1997) in the Tadjoura area, are considered as subsidiary structures on the northern flank of the Tadjoura half-graben. Half-graben basins, early Miocene in age, are also documented further E, in the Socotra margin (Fournier et al., 2007), hence suggesting that asymmetric extension is a common mechanism for accommodating continental rifting along most part of the GA system.

Initiation of the Ghoubbet-Asal active rifted zone to the SE, at around 900 ka (Manighetti et al., 1997; Audin, 1999), is here assigned to the transfer of extension from the Tadjoura half-graben system to the W in response to the lateral locking of axial structures against the Arta pre-existing heterogeneity (Figure 18A**).** Evidence for the arrest of tip fault propagation are supported at various stages of rifting by the following features :

- The spatial distribution of the synrift Gulf Basalts on the two opposite margins of the Tadjoura gulf appears to abut to the W along an inferred NS paleotopographic scarp following the eastern edge of the Arta zone.
- The normal fault network in the northern coastal fault belt (Tadjoura-Obock area) dies out westwards as approaching the volcanic substratum of the Gulf Basalts (Figure 18B).
- The conjugate fault pattern in the southern coastal belt neither penetrated further W into the Arta previously strained series. Instead, it is deviated counter-clockwise from EW to NW-SE for merging into a narrow corridor of N140°E fault structures (Figure 18B) with a dominant extensional downthrow to the NE. The map virgation of the Gulf-parallel fault network is accompanied by a marked increase of fault density westwards, concomitantly to a decrease of individual fault length, hence leading to a typical over-displaced fault pattern (cf. Figure 14B). Fault populations commonly show variable displacement-length ratios mainly because of changing strain regime (Gupta and Scholz, 2000), linkage processes (Cartwright et al., 1995), or variations in rock properties (Bai and Pollard, 2000), and layer thickness (Benedicto et al., 2003; Solvia et al., 2005). The high T/L values (>0.04) obtained here suggest that the horizontal growth of faults was limited or arrested by a mechanical barrier, in agreement with the model applied by Manighetti et al. (2001) to part of the Asal rift fault system from slip-length fault profiles. The Arta transverse faulted corridor is thus a good candidate for having acted as a major disturbance zone against which the Tadjoura westerly-propagating extensional structures are pinned and continued to accumulate vertical displacement without increasing their length.

Together with the Gulf-parallel normal fault system, the transverse extensional structures caused the general downthrow of the Djibouti Plain towards the Gulf axis. Using the flexed surface of the 1.0 Ma-old Gulf Basalts filling the Wea paleo-valley as a chronological and structural marker further supplies an average rate of 0.3 $mm.y^{-1}$ for the recent ~300 m vertical movement which occurred along the eastern edge of the Arta plateau.

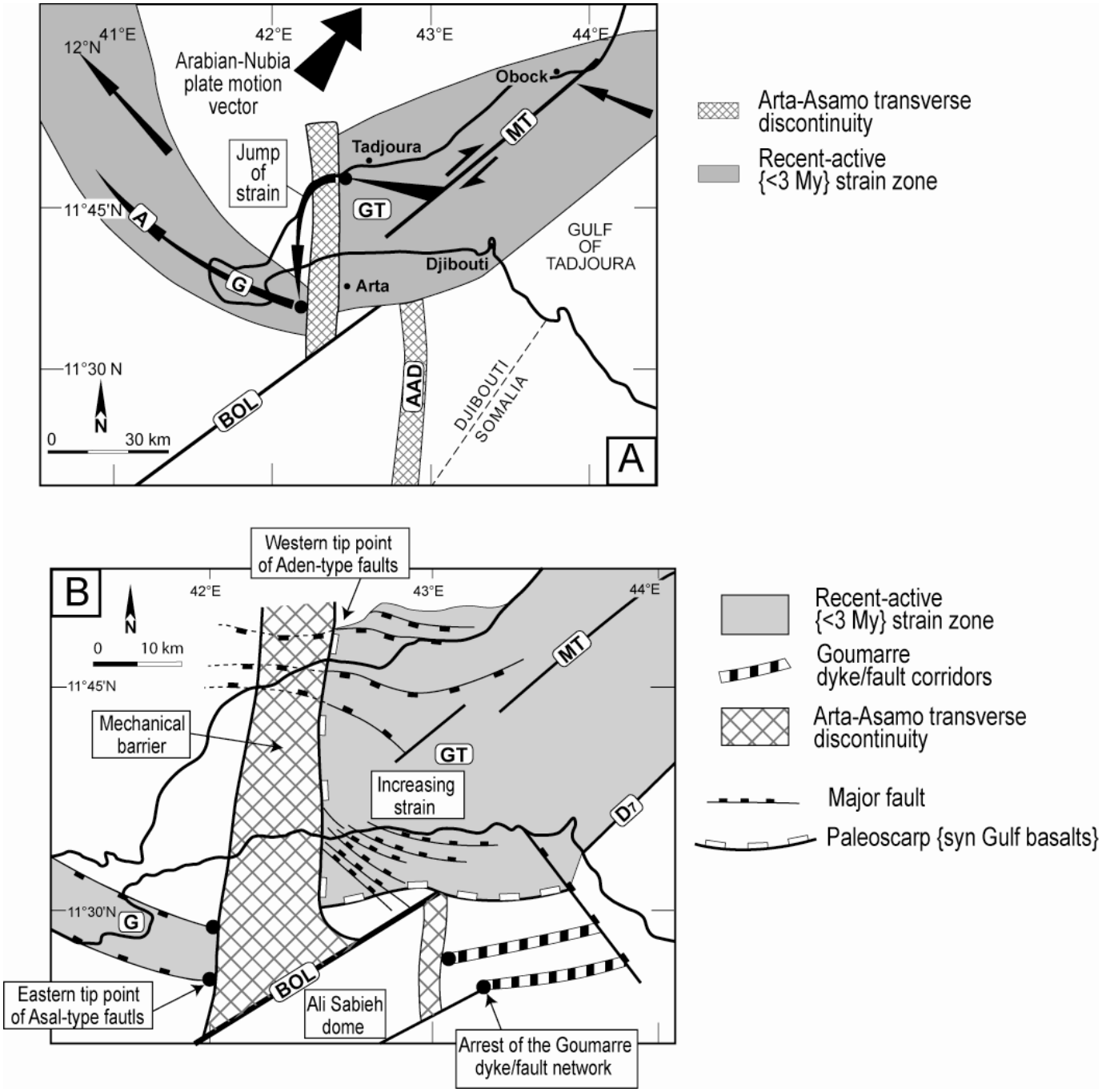

Figure 18: Kinematics of rift propagation throughout the Tadjoura-Ghoubbet connection zone. (A) Sketch model showing rift propagator path (elongated black arrows) in relation with both transfer structures (MT and BOL) and inherited transverse discontinuities (AAD). The key-role of the AAD is emphasized as causing (1) the lateral locking of axial fault propagation, and (2) the jump of rift axis in the Ghoubbet trough. A., Asal; AAD., Arta-Asamo discontinuity; BOL., Bour Ougoul lineament; G.,Ghoubbet; GT., Gulf of Tadjoura; MT., Maskali transform. (B) Structural evidences (cited in the text) for major disturbances of axial extensional strain along the AAD.

- A nearly symmetrical extensional rift fault pattern exists W of the 10 km-wide Arta shear corridor, throughout the Stratoid Basalts filling the Ghoubbet trough. There again, the early positive topographic expression of the Arta shear zone appears to have firstly controlled the distribution of the younger Stratoid Basalts, whilst tip propagation of extensional faults is also seen to stall abruptly against its western flank (Figure 18B). The restricted location of earthquakes and aftershocks linked to the 1978 seism in the Tadjoura Gulf (Lépine et al., 1980; Doubre, 2004) confirms the strong mechanical behaviour of the Arta transverse zone, whereas the locus of active movement along its eastern fault-controlled boundary is documented by the concentration of a swarm of earthquakes (>10) following the Arta-Asamo discontinuity (Hofstetter and Beyth, 2003).
- Lastly, two N80°E fault-dyke corridors of the Goumarre intrusive Fm cutting through the Somali Basalts, further SE in the Djibouti Plain, are seen not to penetrate laterally westwards into the oldest rift series of the Ali Sabieh reliefs, because being probably arrested along the Asamo-Arta discontinuity. Only the southernmost intrusive corridor (DeyDey) seems to merge to the W into the Hollol NW-SE normal fault, inferred to be part of the BOL transform fault system which thus likely accommodated a significant component of extension (Figure 18B).

It is thus pointed out here that strain transfer at the Tadjoura-Ghoubbet connection zone is the mechanical consequence of the lateral pinning of axial fault growth against the Arta NS inherited fabrics, probably in response to higher strength contrast, together with the orthogonal orientation of the preexisting discontinuity with respect to rift propagation. This inferred 'hard linkage' pattern differs from the *en echelon* fault model of Manighetti et al. (1997), and it might be the first structural expression of NS-oriented Red Sea-type fabrics overprinting on younger westerly-propagating GA rift structures. This sub-meridian preexisting fault-fracture network is likely to have nucleated at depth along prominent ancient (Proterozoic) lithospheric weakness zones, which are long known to have played a major role in the opening and tectonic/depositional development of the Red Sea since at least late Oligocene (Dixon et al., 1987; Mitchell et al., 1992).

With respect to the overall Afar extensional system, the Tadjoura rifted trough is known to lie in a transition zone where radical changes occurred in terms of (1) width of the stretched domains which increases dramatically from the localized TR trough to the widespread southern Afar rifted depression, and (2) orientation of the rift fabrics which deviates from EW (oblique rifting) to NW-SE (orthogonal rifting). These changes in rift styles are likely to be

primarily linked to contrasted lithospheric mechanical properties from a cold and amagmatic lithosphere beneath the GA system to a thermally-weakened lithosphere beneath the Afar plume-related volcanic province (Mohr, 1983; White and McKenzie, 1989). Since the 'bookshelf fault' model of Tapponnier et al. (1990), the two major rift axes extending throughout the Afar depression, i.e. the Erta Ale-Manda Hararo (W) and Ghoubbet-Asal-Manda Inakir (E) tectono-volcanic ranges, are generally assumed to represent the frontal parts of the GA and RS systems, respectively, which overlapped and propagated with opposite senses (Figure 2C). These concepts are based on a number of assumptions dealing with (1) the sens of propagation of the Manda Hararo rift axis, (2) the timing of its emplacement with respect to the Ghoubbet-Asal-Manda Inakir rift axis to the E, and (3) the causative mechanisms responsible for the location of these two rift ranges at the periphery of the Afar depression. However, most of these evidences are not satisfactorilly argued with regards to the following features which rather support an alternative kinematic rift model.

(1) The large-scale 'overlapping' rift model (Tapponnier et al., 1990; Manighetti et al., 1997) implies that the Manda Hararo axial range forms the southern offset part of the Red Sea southerly-propagating accretionnary system, up to the Gobaad (frontal) rifted segment to the S (Figure 2C). However, the inferred old age (2.7 Ma) of faulting along the Gobaad volcano-tectonic axis (Gasse et al., 1987), relatively to the much younger Erta Ale axial range further N, does not fit within the proposed southerly-propagating rift model, unless admitting an hypothetical jump of at least 4-500 km from the RS main rifted domain to a discrete nucleation cell S in the Gobaad area. The earlier extension recorded in Central Afar with respect to those in Northern Afar (Barbéri et al., 1972a, 1972b) further disagrees with the fault age progression expected with an extensional system migrating southwards. The more intense extensional tectonics displayed by the southernmost rift segments in the Manda Hararo-Erta Ale range as a whole (Barbéri and Varet, 1977) rather favours a northerly-propagating rift kinematics. One should note that the recent dating of basalts from the Dadar (~350 ka) and Manda Hararo (32±4 ka) tectono-magmatic ranges (Lahitte et al., 2001) only testify to the young volcanic activity of these rift axes, without advocating their origin as either part of the RS or GA propagating systems.

From the finite rift arrangement depicted on Figure 19, it is thus suggested, in agreement with previous authors (Audin, 1999), that extension has been transferred southwestwards from the Obock-Tadjoura troughs into the Gobaad, Hanlé and Gaggade rifted axes, *via* the so-called BOL NW-SE discontinuity.

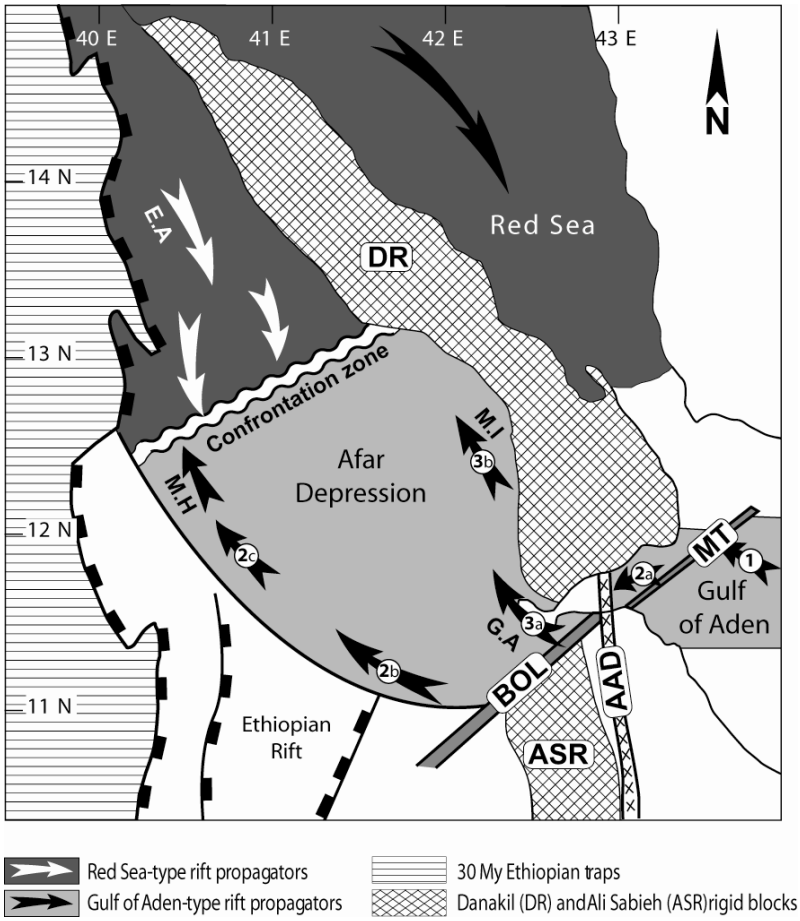

Figure 19: Alternative kinematic model for rift propagation throughout the Afar Depression over the last 3 Ma. The western (Manda Hararo) and eastern (Ghoubbet-Asal and Manda Inakir) marginal rift axes in southern Afar are inferred (i) to propagate northwards, and (ii) to be integral parts of the Gulf of Aden-Tadjoura spreading system, resulting from both sinistral transfer *via* the MT, BOL transform, and rift jump along the AAD. Therefore, a confrontation rift zone might exist further N with the Erta Ale southerly-migrating (Red Sea-type) rift axes. ASR., Ali Sabieh range; DR., Danakil range. Numbers refer to as relative timing of rift propagation.

These latter, as well as the Ghoubbet-Asal axis to the E, are thus assumed to be parts of the GA accretionnary system. Consequently, only the northernmost extremity of the western rift arm, i.e. the Erta Ale segment, should represent the frontal part of the RS extensional system in the Afar depression (Figure 19).

(2) Dating of acidic sequences interlayered with the Lower Stratoid Basalts in the Gobaad, Hanlé, Gaggade, and Asal yield ages younging gradually from 2.7, 2.5, 2.0, and <1.0Ma, respectively, concomitently to younging of the Upper Stratoid basaltic sequences (Gasse et al., 1987). That led some authors to assess the age progression of extension towards the NE, in contradiction with a southerly-migrating strain. From available age dataset, it thus seems likely that the southern parts of the two external rift branches (Manda Hararo and Ghoubbet-

Manda Inakir) were never active synchronously, as already reported by Gaulier and Huchon (1991), and that they both propagated in the same direction towards the N.

(3) According to Manighetti et al. (1998), the location of the Manda Hararo-Erta Ale and Goubbhet-Manda Inakir rift axes along two narrow linear marginal zones, following the edges of the Afar depression, is directly controlled by lithospheric necking, in turn associated to recent (<3.0 Ma) volcanic areas with lesser volume of erupted Stratoid Basalts. However, recent gravimetry modelling conversely shows the crust to be much thinner in the heart of the Afar depression (Seber et al., 2001). In addition, the Stratoid magmatism is thought to have migrated from the center of the depression to its margin since ~1.75 Ma (Lahitte et al., 2003), hence reducing the time period (3.0-1.75 Ma) during which Stratoid magmatism might have influenced lithospheric thickness. Instead, the main controlling factors for the Afar recent rift pattern arrangement should rather be linked to the earlier, and much longer (>27 Ma), magmatic history recorded by the Afar depression, prior to the Stratoid activity. Though only constrained from lateral correlation with the Ali Sabieh range (Le Gall et al., submitted) and the West Afar margin (Wolfenden et al., 2005), initial rift evolution might have been dominated by the emplacement of volcanics, coeval to the Ali Sabieh (mafic) and Mablas (acidic) series, along inferred magmatic cells with a NS orientation, orthogonal to the EW applied extension (see annexe A). It is suggested that the resulting NS-oriented thermally weakened portions of crust might have later guided the propagation path of the two recent marginal rift axes.

Chapitre 4. Early rifting tectonics and magmatism in Eastern Afar: new evidence from the Danakil and Ali Sabieh ranges, Djibouti

Bernard Le Gall, Mohamed A. Daoud, René C. Maury, Joël Rolet, Hervé Guillou

Dykes acides en échelon (région d'Ali Sabieh)

Chapitre 4. Early rifting tectonics and magmatism in Eastern Afar: new evidence from the Danakil and Ali Sabieh ranges, Djibouti

(papier sera soumis, après la soutenance, à *Journal of Structural Geology*)

Bernard Le Gall[1], Mohamed A. Daoud[1,2], René C. Maury[1], Joël Rolet[1], Hervé Guillou[3]

[1] UMR 6538 Domaines océaniques, IUEM, Université de Bretagne Occidentale, place N. Copernic, 29280 Plouzané, France.

[2] IST, Centre d'Etudes et de Recherches de Djibouti, B.P. 486, Djibouti Ville, Djibouti.

[3] UMR 1572, LSCE/CEA-CNRS, Domaine du CNRS, 12 avenue de la Terrasse, 91118 Gif-sur Yvette, France.

Abstract

The <3 Ma-old Stratoid basaltic cover in the Afar depression is bounded to the E by older synrift volcanics and substratum terranes forming the Danakil and Ali Sabieh ranges (DR and ASR). The structural study of the DR and ASR, from remote sensing interpretation and field calibration, supplies new insights about (i) the volcano-stratigraphic framework of initial synrift magmatism in Eastern Afar, and (ii) the causal mechanisms of uplift processes. The Ali Sabieh antiform is assumed to result from magma-driven doming caused, at ca. 27-20 Ma, by the uprise of a shallow-depth mafic laccolith and its intricate network of sill-dyke that in turn possibly fed higher level effusive products. Isolated fragments of Mesozoic country-rocks within the mafic magma are regarded as roof-pendants of the Jurassico-Cretaceous enveloping cover formed during a block-stopping process. Vertical movement in the DR is assigned to a much younger tectonic event, probably in relation with rift shoulder uplift along the Tadjoura and/or Asal rift system(s). The lack of 30 Ma-old basaltic trap complexes in the DR and ASR contradicts the generally accepted model of a single and continuous flood magmatic province in Afar at 30 Ma. The postulated amagmatic crustal domain, involving the ASR and DR, between the Ethiopian and Yemen sub-provinces, will later record a specific tectono-magmatic evolution during the 30 Ma-long Afar rifting process. Emphasis is also put on (i) the structural significance, and the timing of individualisation, of the Danakil 'block', and (ii) the role of its eastern margin, on either sides of which mechanisms of crustal extension vary dramatically during Afar rifting, since being exclusively accommodated by either magmatic accretion to the W (Afar *sensu stricto*), or fault-basin development to the E (Red Sea).

Keywords : Afar rift, Danakil and Ali Sabieh ranges, Lower Miocene, Mafic laccolith, Uplift, Doming, Extension.

1. Introduction.

Most of the Afar rift system extends within a ca. 12.10^4 km^2 fan-shaped depression resulting from the downwarping of the early (30 Ma) plume-induced dome (Baker et al., 1996 ; Hoffman et al., 1997) during a major extensional faulting event initiated at 29-26 Ma, in relation with the long-lived tectono-magmatic development of the western Afar margin (Wolfenden et al., 2005). The corresponding early synrift volcanics, i.e. the 30 Ma-old plume-related flood basalts currently exposed in the Ethiopian faulted plateau, as well as the narrow belt of 29-7 Ma-old volcanic complexes fringing the western Afar margin at the foot of the Ethiopian scarp, are likely to extend further E, beneath much younger extensive trap-like basaltic sequences, namely the 3-1 Ma Stratoid Basalts, flooring the Afar depression. However, the extent of Oligo-Miocene synrift volcanics, as far E as the Yemen traps, within a unique plume-induced magmatic province (Figure 1), generally postulated by previous authors (White & McKenzie, 1989 ; Courtillot et al., 1999)**,** is not firmly argued. New insights about this key-question, also dealing with the number and 2D-map dimension of mantle plume(s) responsible for initial flood continental volcanism in the Afar rift, can be obtained from old rift-related volcanics in the Danakil and Ali Sabieh ranges (referred to as the DR and ASR). Indeed, given their marginal position to the E, separating the Afar depression from the Red Sea-Gulf of Aden oceanic accretionary system (Figure 1), they represent key-markers between the Ethiopian and Yemen trap provinces. These two NS elevated ranges might have initially formed a single domain during much of the history of the Afar, at least until the opening of the westerly-propagating Tadjoura rift (Garfunkel and Beyth, 2006). The synrift volcanics, as old as 11 Ma and 25 Ma in the DR and ASR, respectively (Black et al., 1975; Zumbo et al., 1995), are likely to have recorded most of the ~3-30 Ma relevant geological history of the Afar rift. They show contrasted tectonic styles with respect to the surrounding, and generally less strained, younger trap-like basaltic complexes (the Stratoid, Somali and Dalha Fm) onlapping their flanks. This overall structural arrangement undoubtedly results from a positive inversion process which still remains to be precised in terms of (i) origin of the driving forces, (ii) evolution of the corresponding stress regimes, and (iii) relative timing of associated uplift.

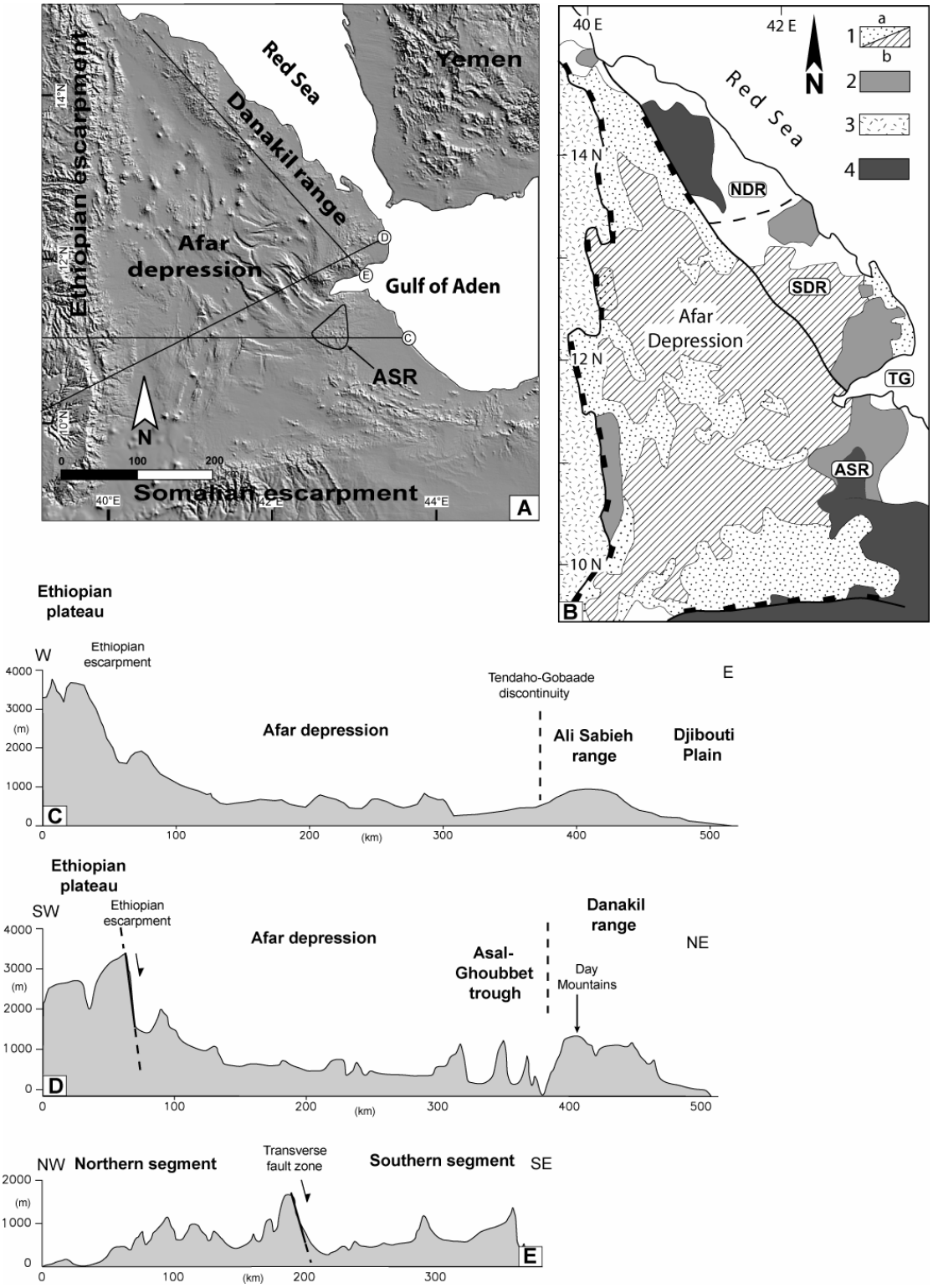

Figure 1: Major topographical and geological structures in the Afar Triangle. (A) Digital elevation model based on Gtopo 30 dataset. (B) Main geological units. 1. <3 Ma series in the Afar depression, a. lacustrine deposits, b. Stratoid basalts; 2. 29-3 Ma-old synrift volcanics; 3. 30 Ma trap complex; 4. >30 Ma substratum. (C, D) Topography of the Afar Triangle along two complete profiles crossing through the Ali Sabieh (C) and Danakil (D) ranges. Vertical exaggeration ~30. (E) Axial topographic profile along the two segments of the DR. Vertical exaggeration ~30.

The lack of consensus about the structural significance of the DR and ASR resulted in various kinematic interpretations involving (1) microplates (Sichler, 1980 ; Manighetti et al., 1998 ; Collet et al., 2000), (2) rigid blocks (Barberi and Varet, 1977; Acton, 1991; Hofstetter and Beyth, 2003; Audin et al., 2004), (3) horsts (Sichler, 1980; Clin, 1991 ; Eagle et al., 2002), (4) antiforms/anticlines (Clin and Pouchan, 1970), or finally (5) dômes (Dreyfuss, 1932). New structural results, primarilly obtained from the ASR, suggest that large-scale doming in the Ali Sabieh area is genetically linked to a component of magma-driven stress during emplacement of a laccolith-like intrusion, i.e. the so-called Ali Sabieh mafic complex, in Lower Miocene times. Detailed structural investigations along the contact between this laccolith and its Meso-Cenozoic country-rocks further supply new insights about dynamics of magma emplacement during early rifting. Comparing tectonic styles and timing of strain recorded by the DR and ASR allows us to discriminate distinct uplift processes along the eastern margin of the Afar depression. Although our results are based on restricted observation windows (DR and ASR), they bear evidence on processes expected to involve a much larger rifted region (the present-day Afar depression). The lack of lateral correlation between the volcano-stratigraphical and timing frameworks of the Ali Sabieh intrusive-extrusive mafic complex, and those of the Ethiopian and Yemen flood basalts, usually regarded as its lateral counterparts (Courtillot et al., 1984), leads us (i) to question the 'single-plume' model classically applied to the Afar magmatic province at 30 Ma, and (ii) to envisage its partitioning into two disconnected sub-provinces, on either sides of an intermediate crustal domain cored by the ASR and DR. The existence of a fundamental crustal-scale bounding this domain to the E is further suggested by considering the various ways crustal extension is achieved during Mio-Pliocene times in western Afar and throughout the Red Sea basinal area to the E.

2. Geological context.

The Danakil relief is a N150°E-oriented range, about 500 km-long, widening regularly southwards from <50 km in the Zula Gulf, where it encroaches the Ethiopian plateau, to >100 km close to the Tadjoura Gulf. It comprises two distinct morpho-tectonic segments separated by the Bidu-Dubbi volcanic transverse zone (Barberi et al ., 1974), usually regarded as a proto-transfer zone connecting the Red Sea (RS) and Asal-Manda Inakir active rift systems (Manighetti et al., 2001; Lahitte et al., 2003) (Figures 1B, E).

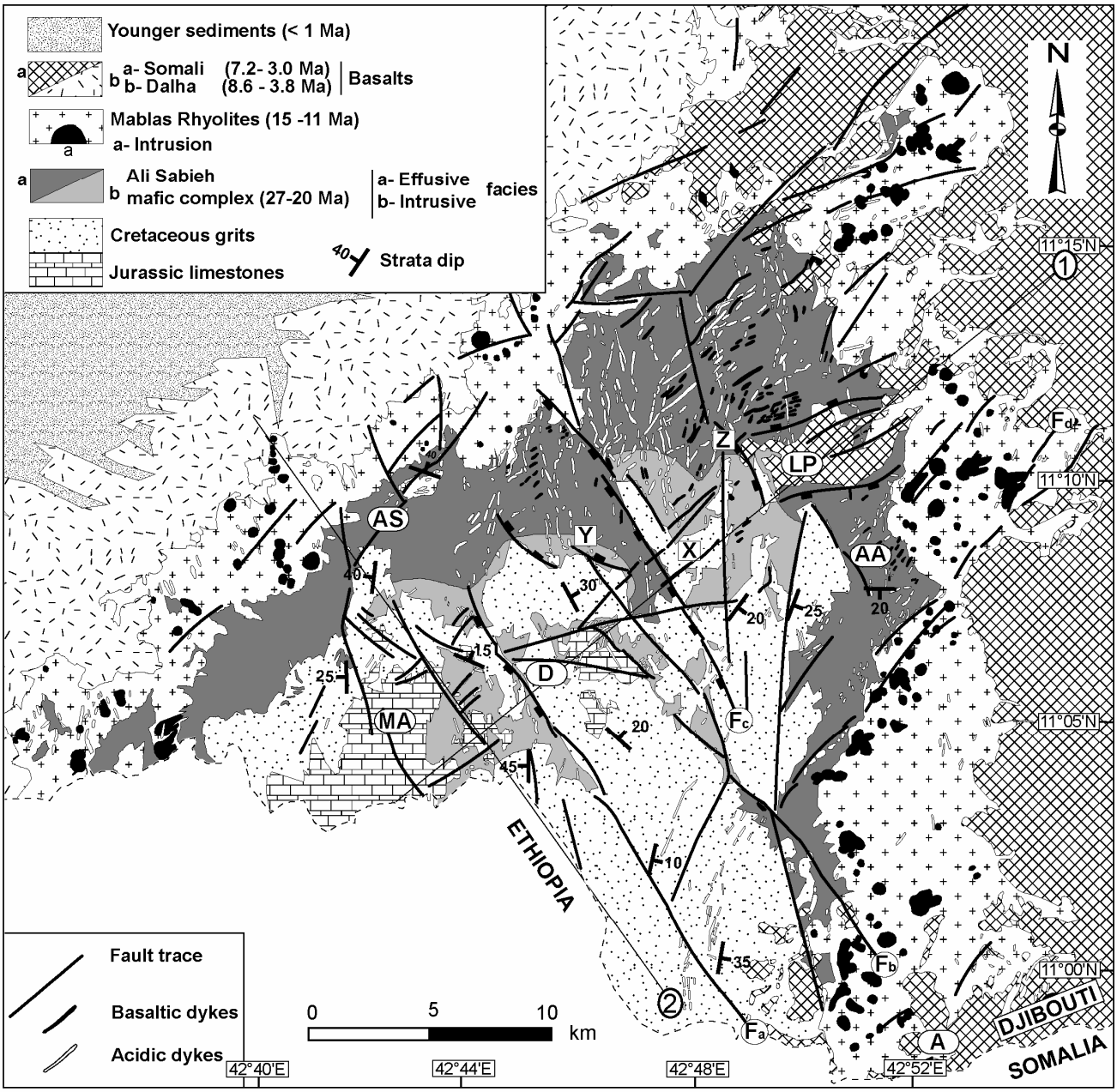

Figure 2: Geological map of the Ali Sabieh antiform elaborated from published documents (Barrère et al., 1975; Gasse et al., 1986), further revised by remote sensing data (ASTER) interpretation, and field observations. For ease of reading, the Ali Sabieh dyke swarm is not entirely drawn. AA., Ali Adde; AS., Ali Sabieh; D., Dadin ; LP., Lougag Plateau ; MA., Mount Array. (1, 2) and (X, Y) are the traces of structural cross-sections drawn in figures 3, 4, 5, and 10B, respectively. F_{a-d} refer to as main fault structures discussed in the text.

The pronounced topographical asymmetry of the two segments is shown on the axial profile in figure 1E with increasing altitudes southwards. The northern segment is exclusively composed of Proterozoic metamorphic terranes of the Nubian shield, overlain by Jurassic and Cretaceous sedimentary strata (Hutchinson and Engels, 1970). These series probably extend laterally beneath younger rift volcanics in the southern segment. There, dominantly acidic sequences of the 15-11 Ma-old Mablas unit are overlain by a >1000 m-thick pile of Dalha flood basalts, 8.6-3.8 Ma in age (Marinelli and Varet, 1973 ; Barberi et al., 1975 ; Gasse et al., 1985), which culminate at ca. 1600 m in the Day Mountains to the S (Figures 1A, D). The flanks of the DR are onlapped by (i) the 2.3-1.0 Ma Stratoid Basalts which floor most of the Afar depression to the W, and (ii) the Ribta series and Gulf Basalts occupying the lowlands along the Red Sea shore, to the E.

The Ali Sabieh range is a 250 km^2 triangle-shaped highland extending further S into the Aisha 'horst' (Figure 1A) (Muller and Boucarut, 1975). Its overall cartographic arrangement evokes a N-plunging antiform-like structure (Figure 2). It is composed of a mafic intrusive core mantled by an outward-dipping envelope, including a Jurassic-Cretaceous sedimentary cover overlain by (i) initial mafic effusive sequences, and (ii) younger acidic series of the 15-11 Ma-old Mablas Fm (Zumbo et al., 1995). These latter form two narrow NS and NE-SW topographic lows (western flank), or crests (eastern flank), onlapped by the younger Dalha (8.6-3.8 Ma) and Somali (7.2-3.0 Ma) trap-like basalts which floor part of the Afar depression and the Djibouti plain, respectively. The ASR thus occurs as a residual antiformal relief not affected by the Asal-type tilted fault block pattern involving the Stratoid and Dalha basalts to the W. Due to a severe erosion, the oldest rocks coring the Ali Sabieh antiform are exceptionnaly well exposed. The Upper Jurassic limestones and Cretaceous grits, which both constitute the oldest substratum rocks of the Afar rift system as a whole, typically form high reliefs culminating at 1290 m in Mt Array to the S (Figure 2).

The Jurassic limestones consist of dominantly shallow platform carbonates, with a total thickness estimated at ~350 m (Gasse et al., 1986). Their base is not observed in the ASR, but further S, in Somalia, they rest unconformably over crystalline Proterozoic basement rocks (Black et al., 1972). They are overlain, along erosive contacts (see Plate 2A), by a >500 m-thick sequence of Cretaceous fluviatile grits (Gasse et al., 1986). The Meso-Cenozoic sedimentary succession is spatially associated with highly weathered mafic material, variously referred to as the Galile (Chessex et al.,1975), the ßi (Black et al., 1975), the Adolei (Barberi et al., 1975), or the Ancient (Gasse et al., 1986) basalts. These early

volcanics are here interpreted as the mafic intrusive part of the so-called Ali Sabieh complex which also includes a sub-aerially emplaced mafic effusive sequence, previously assigned to the Mablas younger acidic series (Gadalia, 1980 ; Gasse et al., 1986), and with a subdued topographic expression, N of the Cretaceous grits reliefs (Figure 2). There, they are cut by a dense network of NS and NE-SW basaltic-acidic dykes which might have fed, at one stage, younger extrusive deposits, later removed by erosion in the core of the antiform. The youngest intrusions in the ASR are probably the dense swarm of km-scale radius rhyolitic plugs, typically arranged in en echelon magmatic lineaments throughout the Mablas acidic series on the eastern flank of the ASR. The arched series of the Ali Sabieh antiform are dissected by a network of fault-like structures with a dominant N150°E trend.

3. Methodology.

Previous studies, and corresponding published maps, of the ASR show no uniform volcano-stratigraphical (see above) and structural interpretations of the pre-Dalha-Somali rift series (Barrère et al., 1975 ; Gasse et al., 1986). The multidisciplinary approach performed in this study, which combines structural, geochemical and radiometric analyses of ASR volcanic rocks and their substratum, allows us (i) to apply a new nomenclature to the early Ali Sabieh mafic complex, and (ii) to establish a revised dynamical model for the origin of the ASR. Geochemical analyses **(**x 15) and K/Ar radiometric datings (x 7) have been focused on both effusive and intrusive facies of the Ali Sabieh complex, with the exception of its intensely weathered basaltic dyke swarm. Previous mapping works only quoted the presence of a dyke-sill system, but without any detailed description of its contacts with the country-rocks, whereas the occurrence of numerous sedimentary xenoliths within the magmatic intrusive was totally neglected.

We provide a 3D-structural picture of the Ali Sabieh intrusive-extrusive complex, the interpretation of which raises a number of issues pertinent to the mechanism of emplacement of mafic magma with respect to regional tectonic setting in early rift evolution. The tectono-magmatic model applied here to the ASR is further supported by new structural dataset from remote sensing (ASTER) interpretation, calibrated by extensive field observations and measurements at various scales. The microtectonic analysis carried out on substratum and synrift volcanic series in order to restore the corresponding paleo-stress fields is presented in Annexe A . Much less detailed work has been devoted to the DR in the present study, but our

results, once compiled with revised existing data, allow comparisons with the structural development of the ASR, in terms of timing and nature of causal mechanisms.

4. The Ali Sabieh mafic complex.

4.1. Overall organization.

4.1.1. The mafic pluton-sill system.

A map-scale (a few km^2) mafic hypovolcanic intrusion occurs in the SW part of the Ali Sabieh antiform (Figure 2). It is entirely surrounded by Jurassic-Cretaceous sedimentary country-rocks which form the highest reliefs in the ASR. Its homogeneous and aphyric structure, with no clear magmatic flow fabrics, typically evokes an intrusive body. Owing to the present erosion level, it forms the lowermost outcropping structural unit in the ASR, the maximum thickness of which is estimated at ca. 400 m from the observed vertical sections (Figure 3). No floor is exposed, leaving the total thickness of the intrusion uncertain, whilst its origin as either a deeply-rooted pluton, a flat-bottomed laccolith, or even a thick sill, cannot be ascertained (see discussion below). The roof of the main mafic unit is largely exposed in the core of the antiform, as a large wavelength arched surface. In its central part, it seems concordant with the overlying Jurassic limestone succession, while to the W, it clearly cross-cuts the northwesterly-dipping sedimentary strata (Figure 3A).

From map and field evidences showing mafic material discordant with respect to tilted Cretaceous grits (Figures 2, 3), the mafic intrusion is assumed to have ascended through higher stratigraphic units *via* magmatic ramp-like structures which correlate with narrow belts of mafic material extending in the prolongation of NW-SE lineaments throughout Cretaceous grits. These fault-like structures, with no (or little) topographic expression, are likely to represent pre-rift structures which have later guided younger magma uprise, as commonly reported in sill-dyke patterns (Francis, 1982). On the basis of field diagnostic features (cross-cutting relationships, presence of sedimentary ‘klippes’ discussed below), the southernmost part of the mafic unit, previously mapped as extrusive sequences (‘Basaltes fissuraux’ of Gasse et al., 1986) N of Cretaceous grits reliefs, is here conversely regarded as the highest sill body of the Ali Sabieh mafic complex (Figure 2).

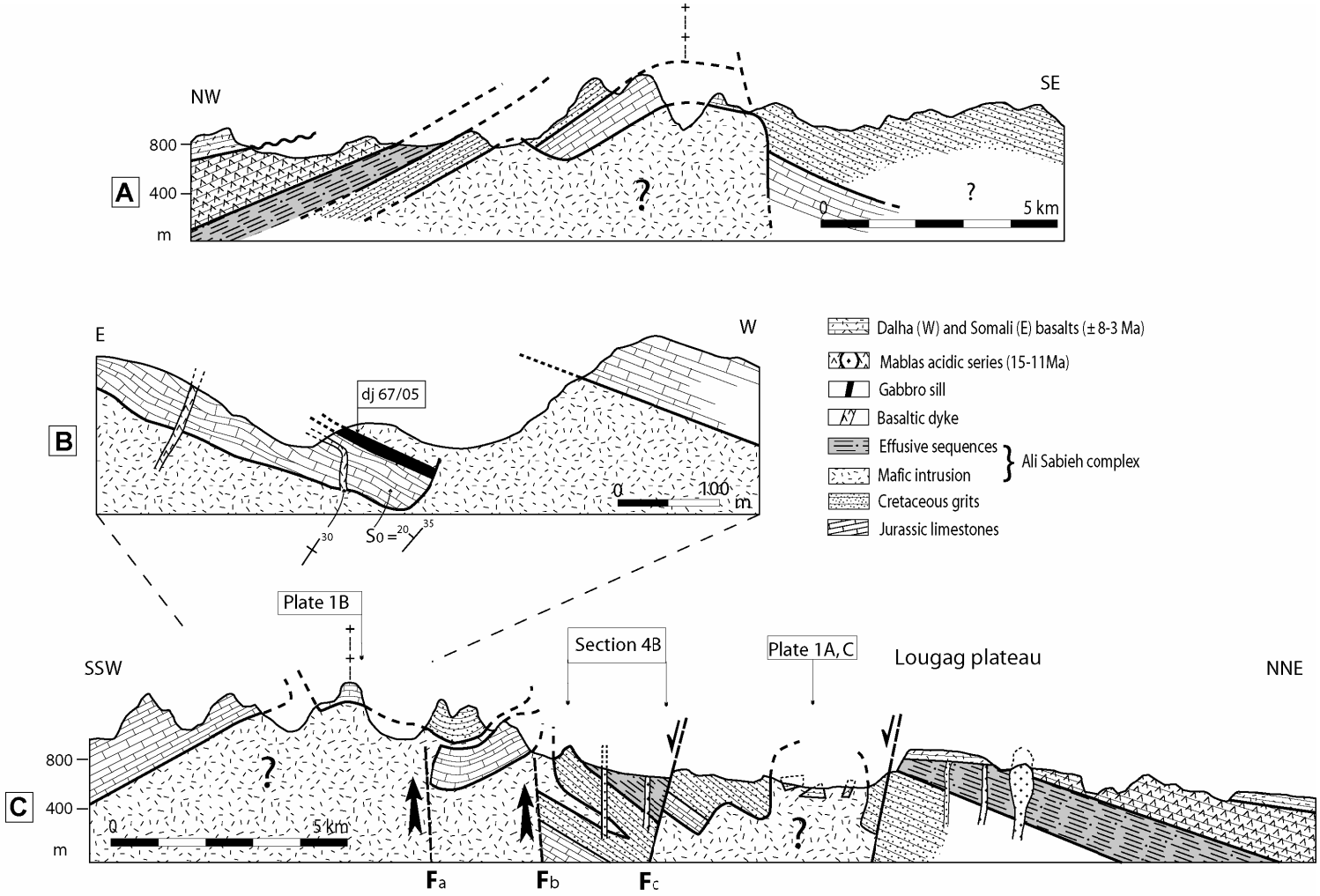

***Figure 3*:** Interpreted structural cross-sections of the Ali Sabieh antiform (see traces in figure 2). (A) NW-SE-oriented section showing a major EW-trending magmatic ramp-like structure along which magma migrated upwards into high stratigraphic country-rock levels. (B) Evidence for the transgression of a sill-dyke network into a Jurassic limestone succession in the core of the antiform (western side of the mafic laccolith). Note the polyphase emplacement of the intrusive bodies from mutual cross-cutting relationships (gabbros-basalts, for example). Location on the cross-section C. (C) General NE-SW-oriented cross-section supporting the origin of the Ali Sabieh antiform as a laccolith-induced domal structure. Faults labelled F_{a-b} are regarded as inherited structures, probably Cretaceous in age. Vertical exaggeration ~2.5.

Because of poor exposures and intense weathering, its northern extent, and consequently its relationships with the Ali Sabieh extrusive unit, are extrapolated from restricted field observations. As such, its corresponding limits on the map of figure 2 are only tentative.

4.1.2. The effusive basaltic sequences.

On the revised geological map in figure 2, the Ali Sabieh effusive basaltic sequences extend largely at the northern termination of the antiform, N of the Cretaceous grit reliefs, narrowing markedly along the two flanks of the structure. To the N, they are poorly exposed with a negative weathering topography, in contrast with the dense dyke swarm that emerges as NS and NE-SW narrow ridges. Therefore, its overall internal organisation, total thickness, and exact map extent are poorly constrained. Despite these limitations, the reference section described below, as well as the totality of sampled volcanic rocks, are located in this topographically subdued area. Evidences for its subaerial origin are locally supplied by typical fluid lava flow features, but in most of cases, the discrimination between extrusive and intrusive (sills) mafic facies is not possible, given the strong alteration. Our reference cross-section is continuously exposed over ~0.5 km, between two N150°E ridges of Cretaceous sandstones, close to the mid-point between Ali Sabieh and Ali Adde towns (Figures 2, 4B). It exhibits a monoclinal succession of bedded mafic material, dipping consistently at 25-30° to the ENE, on top of Cretaceous grits with a similar dipping attitude. Owing to the lack of significant fault structures, the total thickness of the exposed section is estimated at 200 m.

Despite intense alteration, a number of specific volcanic facies have been recognized, including (1) porphyric picrobasaltic lava flows (x4, see age determination below), (2) fine-grained tuff/tuffites forming the bulk of the section, and (3) mafic boulder-bearing conglomerates (3 levels), assimilated to laharic deposits. The exposed extrusive succession is cut by a number of acidic (x2, >10 m-thick) and mafic (x3, <1.0 m-thick) vertical dykes, trending either N10°E or N140°E. The structural interpretation of the complete section, including the ridges of Cretaceous grits at the two extremities of the transect, is discussed below (Figure 4A).

The hydrothermal origin of the alteration experienced by the Ali Sabieh effusive series is supported by the epidote/chlorite-rich facies observed, in association with a dense array of quartz-filled open fractures, within layered tuff materials lying close to Ali Adde, further E.

Numerous porphyric picrobasaltic lava flows have been identified elsewhere, and more especially on top of numerous discrete hills in the Ali Sabieh town area (Figure 2). They consist of typically a few m-thick flows, dipping gently (~25°) towards the N. Five of them have been analyzed and dated (see following section). From its map extent, and assuming a general strata dip <20°, the total thickness of the Ali Sabieh effusive sequence might approximate 1-2 km.

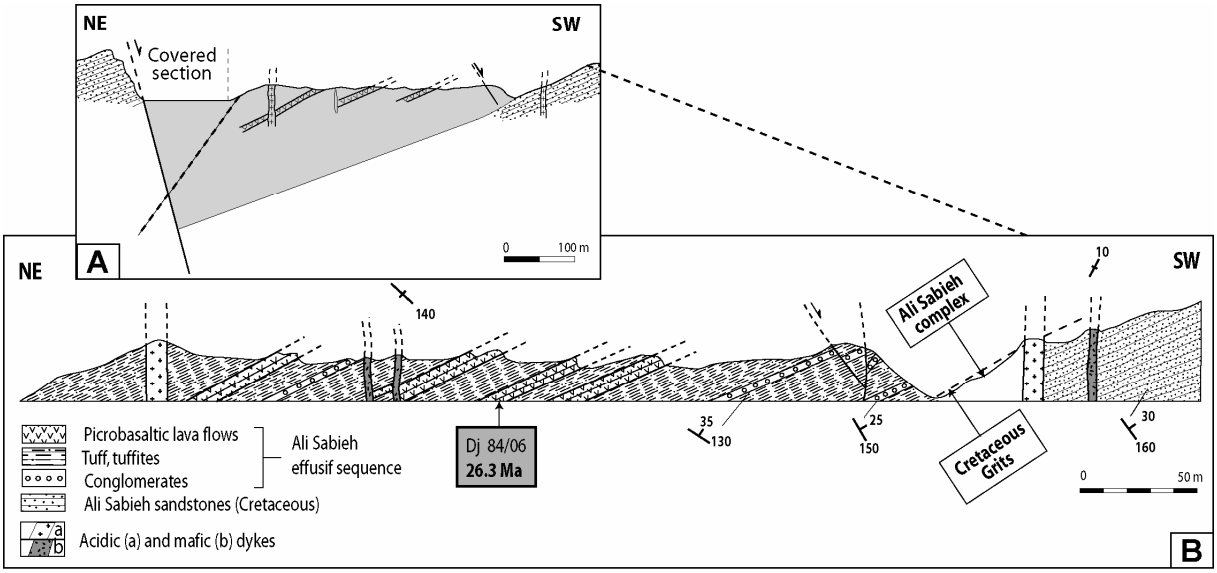

Figure 4: Reference cross-section of a Lower Miocene half-graben structure, partly filled with effusive mafic sequences of the Ali Sabieh complex (27-20 Ma). (A) Interpreted structural section in terms of NE-facing half-graben geometry. (B) Exposed section showing the concordant dipping attitude of both the underlying Cretaceous grits to the SW, and the Lower Miocene volcanic horizons. Sample Dj84/05 is a picrobasaltic lava flow which yielded a K/Ar age of 26.3 Ma (see paragraph 4.3.4). Location as X on figure 2, and on the regional cross-section in figure 3C.

4.1.3. The dyke swarm.

The pre-Mablas series in the ASR are densely crosscut by a composite basaltic-acidic dyke swarm (Figure 2).This swarm can be arbitrary attributed to either the Mablas and/or Ali Sabieh volcanic formations, according to their respective geochemistry and the few available age dataset (Chessex et al., 1975; Zumbo et al., 1995), since no confident age inference can be made from their cross-cutting map relationships. Two types of dyke geometries, with specific spatial distributions, are observed as a function of the country-rock types. To the N, a dense mafic-acidic dyke network is exceptionally well-exposed throughout the Ali Sabieh effusive

series. The larger abundance of acidic intrusions shown on published maps was probably overestimated because of the subdued topographic expression of the altered mafic dykes on aerial photographs. The Ali Sabieh mafic dykes are typically 20 m-thick and show two main orientations at NS and N70°E (Figure 5A). The 'dyke-in-dyke' system exposed on the cross-section of figure 5B, with four steeply-dipping basaltic dykes trending N45-60°E, and dated at 25±0.5 Ma (see below), suggests that the Ali Sabieh intrusive complex formed by multiple injection of mafic magmas.

Much narrower (<1.0 m-thick in average), and dominantly mafic dykes cut with quite similar strikes through the Meso-Cenozoic tilted strata to the S. They are also tentatively regarded as feeder intrusions of the Ali Sabieh effusive complex. Their changing geometry might reflect either their specific location with respect to suspected underlying magma bodies, or/and contrasted mechanical properties of their respective country-rocks during magma injection.

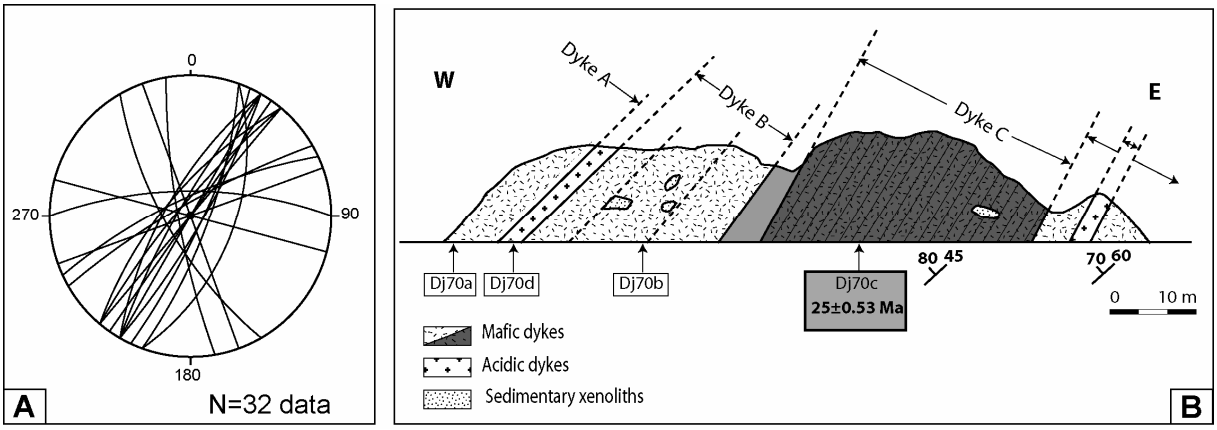

Figure 5: Structure of the Ali Sabieh mafic dyke swarm. (A) Stereonet of dyke orientations (x 32 data measured in the field), clustering around 45-60°E. Mafic (x 26 data) and acidic (x 6 data) intrusions undifferenciated. (B) Steeply-dipping geometry (70-80° to the NW) of four mafic dykes (>10 m-thick in average), arranged in a 'dyke-in-dyke' structure, and cut by parallel and narrower acidic intrusions, probably related to the Mablas series. (See paragraph 4.3.4 for comments about the dated dyke Dj70c). Location of the section as Y in figure 2.

4.2. Pluton/country-rocks relationships.

The contacts between the Ali Sabieh mafic igneous intrusion and its country-rocks, whatever the latter occur as autochtonous terrains or isolated large xenoliths, are almost invariably sharp. Evidences for host-rock assimilation have not been observed. Locally, the intruded rocks are thermally metamorphosed, as examplified by silicified grits, but rarely more than one meter apart, hence indicating magma of low heat.

One major new insight of our study is to recognize the presence of numerous isolated masses of sedimentary rocks, totally surrounded by igneous material of the Ali Sabieh mafic complex (Figure 6).

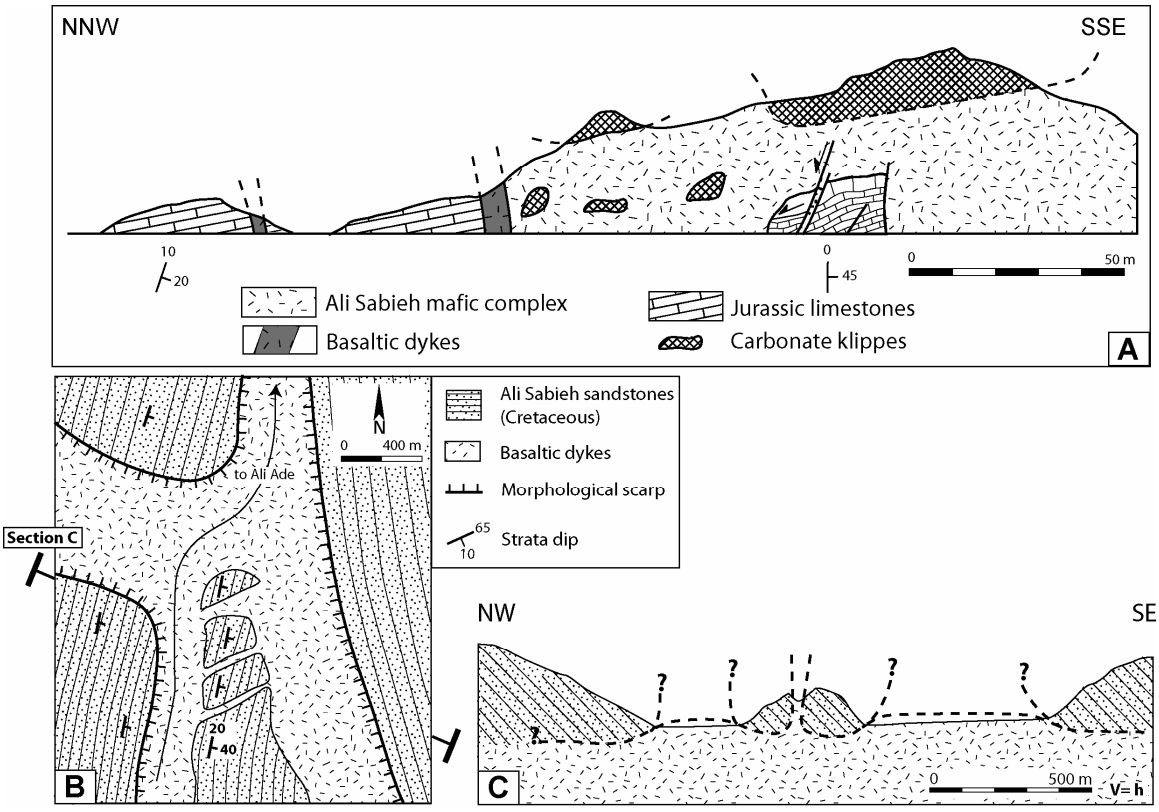

Figure 6: Various types of sedimentary country-rocks inliers within the Ali Sabieh mafic intrusive complex. (A) True xenoliths (m-scale) and raft or klippes (>10's m) of Jurassic limestones surrounded by mafic magma. The steeply-dipping basaltic dyke to the NNW, along the contact between the main intrusive body and a gently inclined (probably authochtonous) limestone succession, is likely to follow a ramp-like structure (see text for details). Location W of the laccolith coring the antiform. (B, C) Map and cross-section showing examples of country-rock masses (Cretaceous grits) totally disconnected, but with still preserved and parallel bedding attitude, by an intricate sill-dyke network. Dadin wadi area, (see figure 2).

Their sizes range from a few m^3 to tens of m^3, and their local origin is attested by lithological similarities with the generally adjacent autochtonous Jurassic (limestones) and Cretaceous (grits) successions. With respect to the overall structural organization of the Ali Sabieh dome, these sedimentary 'klippes' are located within, or close to, the (eroded) roof zone of the main mafic intrusion. Various types of cover inliers can be distinguished, and attest of varying dynamical conditions during magma emplacement .

- True xenoliths with relatively modest sizes, typically less than a few m^3, show irregular shapes. They generally occur as randomly oriented slabs with a preserved sedimentary layering totally discordant from one xenolith to another, and also with respect to those of adjacent autochtonous strata (Figure 6A, Plates 1A, B).

- By contrast, much larger sedimentary bodies (up to tens of m^3) display sharp and linear contacts with their igneous host material. Many stratified sedimentary enclosures exhibit a remarkable uniformity of strike and dip, as if reflecting an original structural attitude with no significant differential movement between blocks (Plate 1C). Locally, they occur as closely-spaced masses, separated by an intricate mafic dyke-sill network, as illustrated on figures 6B, C. In such cases, they undoubtedly form *in situ* rafts originating from the progressive disruption of an initially homogeneous sedimentary cover by a propagating and inflating magma-filled fracture network. Depending on the width of the fracture/sill/dyke system, the resulting blocks of country-rocks occur either as isolated, or still connected masses.

Plate 1: Field evidence for Mesozoic sedimentary xenoliths embedded within mafic magma of the Ali Sabieh Lower Miocene complex. (A) A ~10 m-scale block of Cretaceous grits within the structurally highest sill intrusion of the complex. Note the autochthonous ridge of inclined grits to the E. (see location on the cross-section in figure 3C). (B) Meter-scale inliers of both Jurassic limestones and Cretaceous sandstones in the axial part of the laccolith coring the antiform. The easterly-inclined limestone strata in the back of the photograph represent the structurally highest country-rock units in the axial part of the Ali Sabieh antiform. (see location on the cross-section in figure 3C). (C) Closely-spaced masses of Cretaceous grits, disconnected by a mafic sill-dyke network. Note the sharp and linear intrusive contacts. (Same location as figure A).

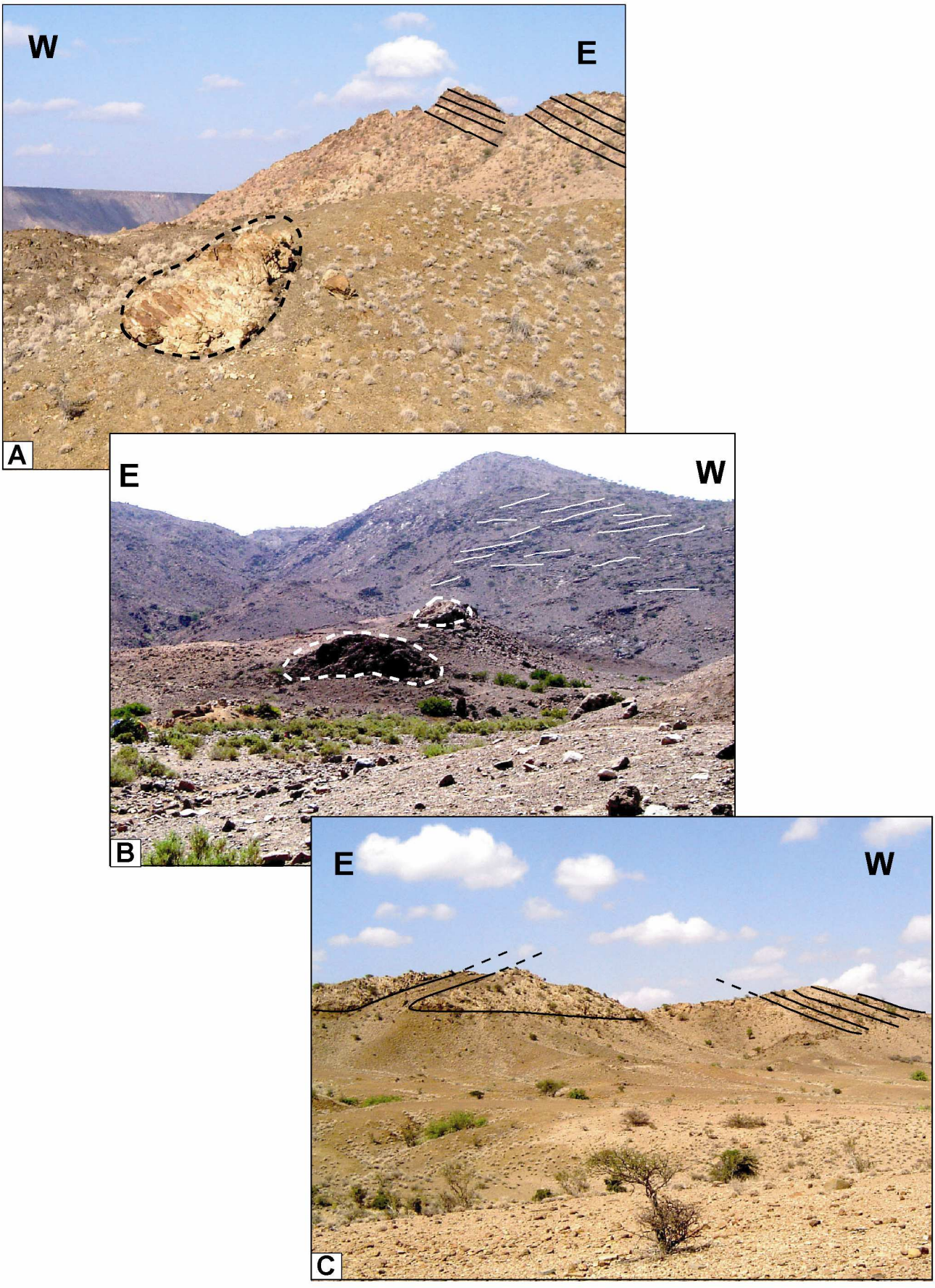
W
E
A
E
W
B
E
W
C

4.3. Geochemical data and age determinations.

4.3.1 Major elements and classification.

Whole rock major and trace elements, except Rb, were measured on 15 Ali Sabieh basalt samples (9 intrusions and 6 lava flows, see location map on figure 7) at UMR 6538 Domaines Océaniques, Brest, using a Jobin-Yvon Inductively Coupled Plasma – Atomic Emission Spectrometer (ICP-AES). Rb was measured by flame atomic emission using a Perkin-Elmer 5000 spectrometer.

Chemical analyses of representative samples are given in Table 1. With the exception of one intrusive microgabbro (sample dj67/05), the collected ASR samples are picrobasaltic and basaltic lavas, according to the total alkalies-silica (TAS) classification scheme (not shown) of Le Bas et al. (1986). In this diagram, they plot on both sides of, but close to, the line separating the fields of subalkalic and alkalic basalts (Irvine and Baragar, 1971), although most of them plot within the subalkalic field. They can therefore be considered as transitional basalts with a dominant tholeiitic tendancy (Barberi et al., 1975; Gasse et al., 1986; Vidal et al., 1991, Deniel et al., 1994). This terminology is consistent with their normative composition which is mostly that of olivine tholeiites.

Plots of major element oxides (not shown) against total iron as FeO *versus* MgO ratios (FeO*/MgO) indicate that the five picrobasalts differ consistently from the 10 other samples, the compositions of which are rather homogeneous, (i) by their much lower FeO*/MgO ratios, close to unity, (ii) by lower SiO_2 and Na_2O, and (iii) by higher CaO. These features are consistent with mechanical accumulation of diopside and olivine phenocrysts in these lavas, in agreement with their petrographic features. Most of the basalts and picrobasalts display TiO_2 contents higher than 2 wt% (Table 1).

4.3.2. Petrographic notes and mineral chemistry.

The five studied picrobasalts (SiO_2 <45 wt%; $Na_2O + K_2O$ <3 wt%) are highly porphyritic, with 35-50 modal% phenocrysts which are mostly diopsidic clinopyroxene, magnesian olivine and calcic plagioclase in a ~3:2:1 ratio. The other ASR basalts are moderately porphyritic with 5-15 modal% among which calcic plagioclase dominates over olivine and clinopyroxene.

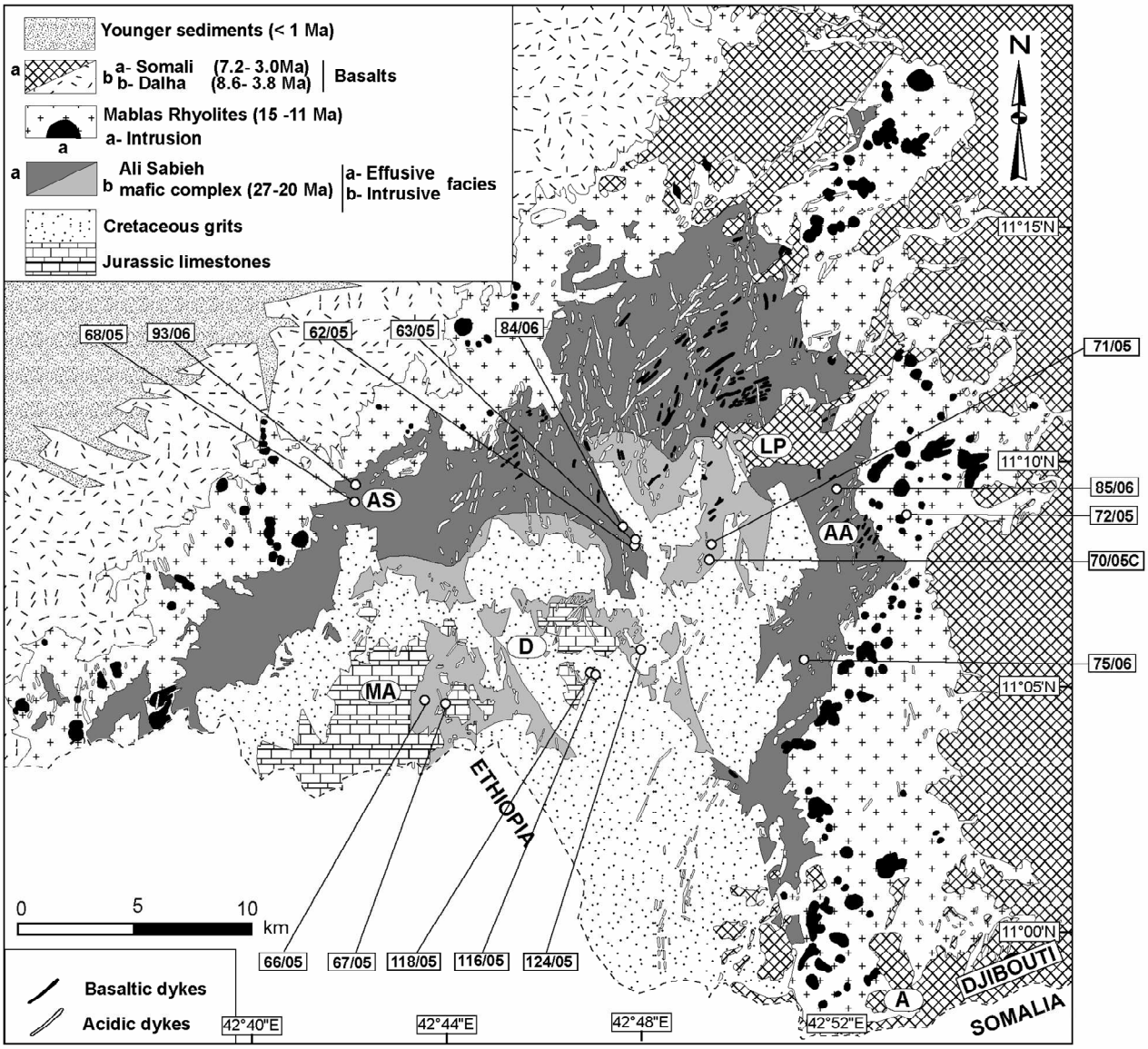

Figure 7: Map location of volcanic rock samples analyzed in the present study.

In both types, these phenocrysts are set in holocrystalline or moderately glass-rich groundmass showing microlitic to subdoleritic textures, with microcrysts of plagioclase, olivine, augite, titanomagnetite and hemoilmenite. Their crystallization order, typical of transitional and tholeiitic series, involves successively (1) magnesiochromite, usually found as inclusions within olivine phenocrysts, (2) olivine, (3) calcic plagioclase, (4) augite, and finally (5) iron-titanium oxides.

Microprobe analyses of phenocrysts and groundmass minerals were performed on three picrobasalts, (dj68/05; dj62/05 and dj118/05). Analyses were obtained with a Cameca SX50 five spectrometer automated electron microprobe (Microsonde Ouest, Plouzané, France). Representative analysed samples are given in Table 2. Analytical conditions were 15 kV, 10-

12 nA and a counting time of 6 sec. (see Defant et al., 1991, for further analytical details). Olivine compositions range from Fo_{88-64} for the phenocryst cores to Fo_{58-56} for their rims. Groundmass olivine composition is Fo_{58-56}. The plagioclase phenocryst cores are labradoritic and bytownitic (An_{89-66}) and contain negligible amounts of Or component (<1.6%). The corresponding rims are similar (An_{88-62}) to the cores, whereas the small laths from the groundmass are less calcic (An_{79-34}). Pyroxenes from the picrobasalts are mostly diopside (Wo_{50-44} En_{44-38} Fs_{14-8}). The groundmass clinopyroxenes (Wo_{49-45} En_{40-36} Fs_{15-14}) are quite similar to the phenocrysts, although slightly more Fe-enriched.

sample	dj118/05	dj63/05	dj62/05	dj68/05	dj93/06	dj72/05	dj70/05c	dj116/05	dj71/05	dj75/06	dj85/06	dj 66/05	dj124/05
SiO_2	44.4	44.7	44	42.3	43	51.9	52.1	48.4	51.5	47.8	50.4	48	51
TiO_2	2.8	3.07	2.63	3.09	2.95	2.61	3.32	2.67	3.46	1.62	2.62	3.63	3.44
Al_2O_3	10.45	13.55	9.27	11.77	11.75	13.3	12.35	13.75	12.65	16.32	13.9	13.2	12.5
$Fe_2O_3^*$	14.55	14	13.52	14.8	14.3	12.44	13.95	13.9	14.3	12	15.3	14.5	14.15
MnO	0.19	0.18	0.17	0.18	0.18	0.21	0.21	0.24	0.21	0.16	0.2	0.22	0.19
MgO	13.45	8.65	12.9	9.35	10.25	5.05	4.66	4.1	4.83	4.02	3.15	5.23	4.63
CaO	11.15	10.1	13.45	15.05	14.5	9.5	8.65	8.65	9.1	10.2	6.7	6.4	8.8
Na_2O	1.89	2.02	1.01	1.68	1.61	2.66	2.44	2.81	2.67	2.52	2.39	3.15	2.56
K_2O	0.47	0.98	0.53	0.46	0.41	0.83	0.7	0.81	0.4	0.64	1.87	0.87	0.79
P_2O_5	0.25	0.35	0.21	0.27	0.23	0.37	0.56	0.64	0.6	0.22	0.7	0.56	0.55
LOI	0.48	2.31	1.86	0.69	0.61	1.42	0.91	3.89	0.26	4.35	1.83	3.84	0.97
Total	100.08	99.91	99.55	99.64	99.79	100.29	99.85	99.86	99.98	99.85	99.06	99.6	99.58
Rb	20.2	20.3	13.2	22	15.1	19.7	9.9	14.8	14.7	7.4	26.6	31	17
Sr	470	543	445	458	436	242	445	394	518	355	363	386	440
Ba	225	332	240	250	212	184	323	325	468	300	770	280	290
Sc	35	30.5	40.5	43	46.5	34	29	22	30	29	23.5	29	28
V	335	346	390	490	457	348	396	255	428	291	281	404	405
Cr	565	200	820	330	405	156	53	2.5	57	21	12	47	54
Co	74	60	78	70	61	38	42	37	45	41	37	42	43
Ni	286	130	270	138	132	79	31	3	33	55	20	30	31
Y	19.5	24.5	16	19.7	18.5	51	34	36.5	35.5	28.5	51.5	33	35
Zr	153	215	138	156	145	294	250	177	255	116	282	226	255
Nb	26	37	22.5	28.2	25	31	22	30	23	8	28	23	22
La	23	31	19.5	21	20	28.5	22.5	27	22.5	13.6	56	23	22.5
Ce	53	68	43	48	46	64.5	53.5	60	53.5	31.5	118	51	53
Nd	29	38.5	25	27.5	27.5	37	34.5	35	34.5	18.3	62	35.5	34
Sm	6.2	7.4	5.6	6.25	5.65	8.75	7.9	7.6	8.1	4.45	12.1	7.9	8
Eu	1.96	2.37	1.7	1.94	1.8	2.59	2.57	2.54	2.65	1.54	3.1	2.57	2.6
Gd	5.1	6.7	4.45	5	4.85	9.3	7.6	7.4	7.8	5.3	10.8	7.8	7.1
Dy	4.1	5	3.3	4	3.75	9.1	6.2	6.6	6.45	4.9	8.6	6.4	6.4
Er	1.8	2.1	1.4	1.7	1.7	4.8	3	3.6	3.1	2.6	4.6	3.1	3.2
Yb	1.5	1.85	1.15	1.44	1.41	4.45	2.69	3.4	2.72	2.38	3.93	2.56	2.91
Th	2.25	3.15	1.8	2.2	1.9	3.3	2.1	2.85	2.15	1.1	3.25	1.95	2.35

Table 1: Representative analyses of Ali Sabieh mafic rocks.

Sample	dj68/05 Groundmass	dj62/05 core	dj118/05 core
SiO_2	35.86	40.86	38.16
TiO_2	-0.012	-0,03	0.06
Al_2O_3	0.01	0.05	0.03
Cr_2O_3	0.00	0.04	0.00
FeO	35.34	11.09	18.87
MnO	0.74	0.15	0.35
MgO	28.05	47.57	42.49
CaO	0.46	0.35	0.19
Na_2O	0.00	0.02	0.02
K_2O	-0.01	-0.02	-0.01
P_2O_5	0.02	0.00	0.01
NiO	0.01	0.15	0.06
Total	100.53	100.32	100.29
Fa%	3.00	2.99	3.02
Fo%	58.59	88.43	80.05

Olivine

Sample	dj68/05 Groundmass	dj62/05 core	dj118/05 core
SiO_2	58.76	45.74	51.24
TiO_2	0.15	0.09	0.18
Al_2O_3	25.15	34.06	30.98
Cr_2O_3	0.00	-0.03	0.05
FeO	0.50	0.56	0.48
MnO	-0.04	-0.01	-0.03
MgO	0.05	0.00	0.00
CaO	7.26	18.19	14.09
Na_2O	7.05	1.23	3.72
K_2O	0.78	0.01	0.16
P_2O_5	-0.01	0.02	-0.02
NiO	-0.0206	-0.0696	-0.0444
Total	99.74	99.93	100.94
An	34.65	88.98	67.04
Ab	60.86	10.94	32.04
Or	4.48	0.07	0.91

Feldspar

Sample	dj68/05 Groundmass	dj62/05 core	dj118/05 core
SiO_2	48.11	46.48	49.58
TiO_2	2.11	2.30	0.35
Al_2O_3	5.02	7.02	4.72
Cr_2O_3	-0.00	0.12	0.06
FeO	8.38	8.13	5.41
MnO	0.16	0.12	0.19
MgO	12.40	13.15	14.46
CaO	22.76	22.11	24.89
Na_2O	0.52	0.28	0.30
K_2O	-0.00	0.05	-0.04
P_2O_5	0.00	0.03	0.02
NiO	-0.03	-0.06	-0.06
Total	99.4914	99.8519	100.04
Wo	48.75	47.17	50.39
En	36.96	39.06	40.73
Fs	14.28	13.76	8.86

Pyroxene

Table 2: Representative analyses of phenocrysts from picrobasalts.

In addition to their Mg-rich character, the picrobasalt clinopyroxenes also display high Al_2O_3 and TiO_2 contents typical of alkalic and transitional basalts (Leterrier et al., 1982). Olivine-liquid and clinopyroxene-liquid (FeO/MgO) equilibrium distribution coefficients are close to $K_D = 0.33$ (Irvine, 1979) and $K_D = 0.23$ (Grove and Bryan, 1983), respectively. Therefore, the (FeO/MgO) ratios of olivine and clinopyroxene phenocrysts in equilibrium with picrobasaltic whole rocks should be close to 0.3. Most of the measured (FeO/MgO) ratios are higher (0.35 to 0.80) and the corresponding phenocrysts are therefore in desequilibrium with respect to the corresponding whole rocks. This feature, together with the highly porphyritic character of the picrobasalts, suggests that the FeO*/MgO ratios of these rocks have been controlled by the accumulation of Mg-rich phenocrysts.

4.3.3. Incompatible elements.

The incompatible multielement patterns of the studied basalts, normalized to the Primitive Mantle (Sun and McDonough, 1989) are shown in figure 8A. They display moderately to fairly enriched patterns typical of Afar transitional basalts (Barrat et al., 1990, 1993; Vidal et al., 1991; Deniel et al., 1994; Rogers, 2006; Furman et al., 2006). Their strong positive spikes for Th, in addition to negative K anomalies and relatively low Rb and Ba contents are typical of magmas derived from an enriched plume-related mantle source. The patterns of the non-porphyritic basalts are rather similar to those of the HT1 flood basalts from Ethiopia (Pik et al., 1998) and those of the younger Guguftu and Choke shield volcanoes (Kieffer et al., 2004). The five picrobasalts are consistently more depleted in Y and Heavy Rare Earth Elements (HREE) than the non-porphyritic basalts; accordingly, they display higher La/Yb ratios (14-18) than normal basalts (5-10). Their patterns are quite similar to those of the HT2 flood basalts from Ethiopia (Pik et al., 1998), except for the HREE which are more depleted (Figure 8A, left column).

Several rectangular diagrams using selected element concentrations and ratios plotted against FeO*/MgO are shown in figure 8B. Besides the variations linked to the different Y and HREE contents of the picrobasalts and basalts, respectively, they show that the two groups have equivalent La/Nb, Th/La and Th/Yb ratios, and should therefore originate from the melting of a single type of enriched (plume-related) mantle source. The studied basalts differ from the low-Ti flood basalts from Ethiopia (Pik et al., 1998) by their higher La/Yb and

Th/Yb ratios. The differences in HREE and Y contents between the two groups might be ascribed to different depths of genesis, deeper (in the garnet lherzolite field) for the picrobasalts. Once again, the non-porphyritic basalts plot within or near the fields of the HT1 flood basalts and that of the younger shield volcanoes. The picrobasalts plot within the field of HT2 flood basalts in all these diagrams (Figure 8B, right column).

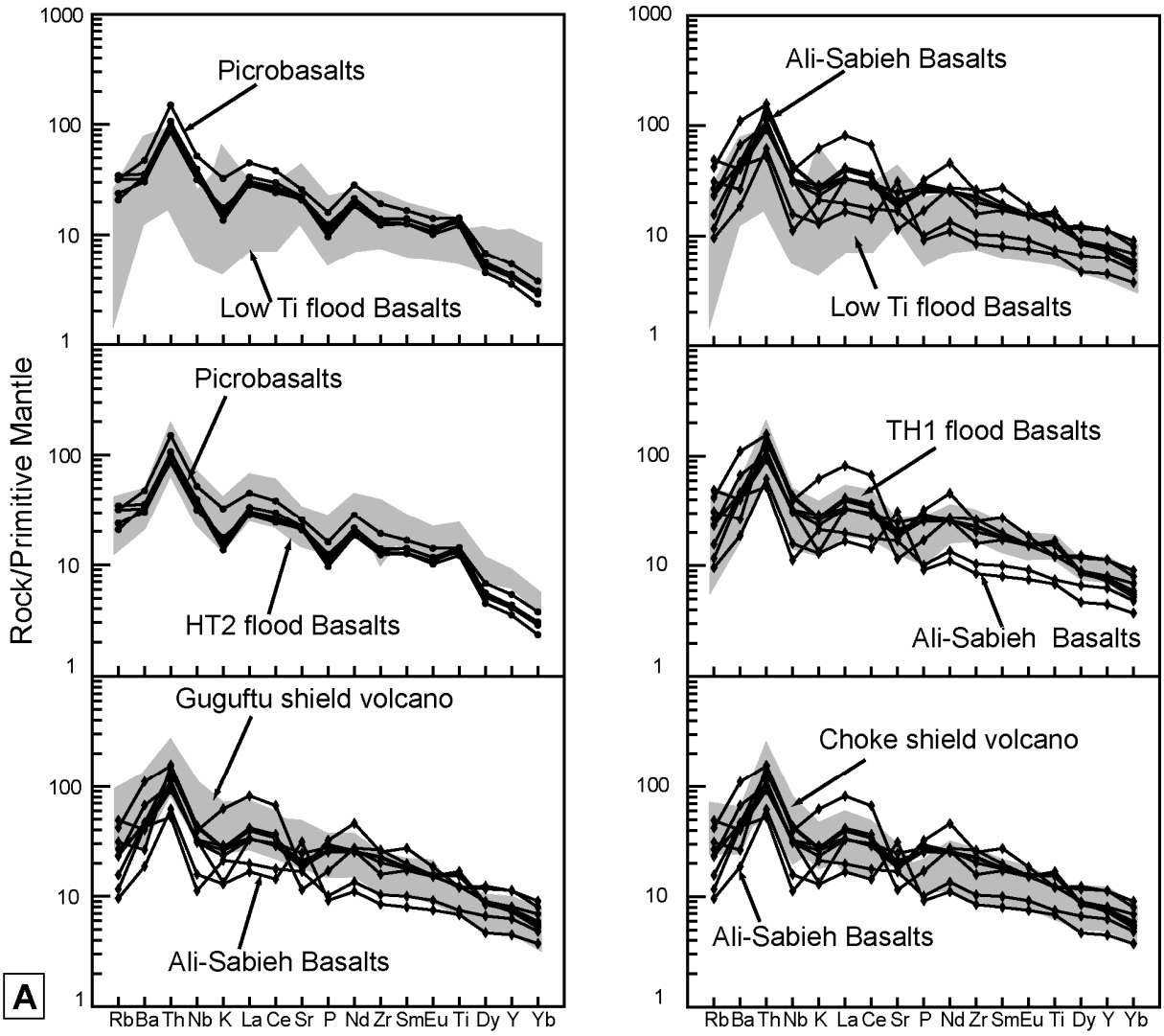

Figure 8: Data about (i) Ali Sabieh Basalts, and (ii) Low Ti, HT1 and HT2 flood basalts from Ethiopia (Pik et al., 1998; Kieffer et al., 2004.) in multielement normalized patterns of Sun and McDonough., 1989.

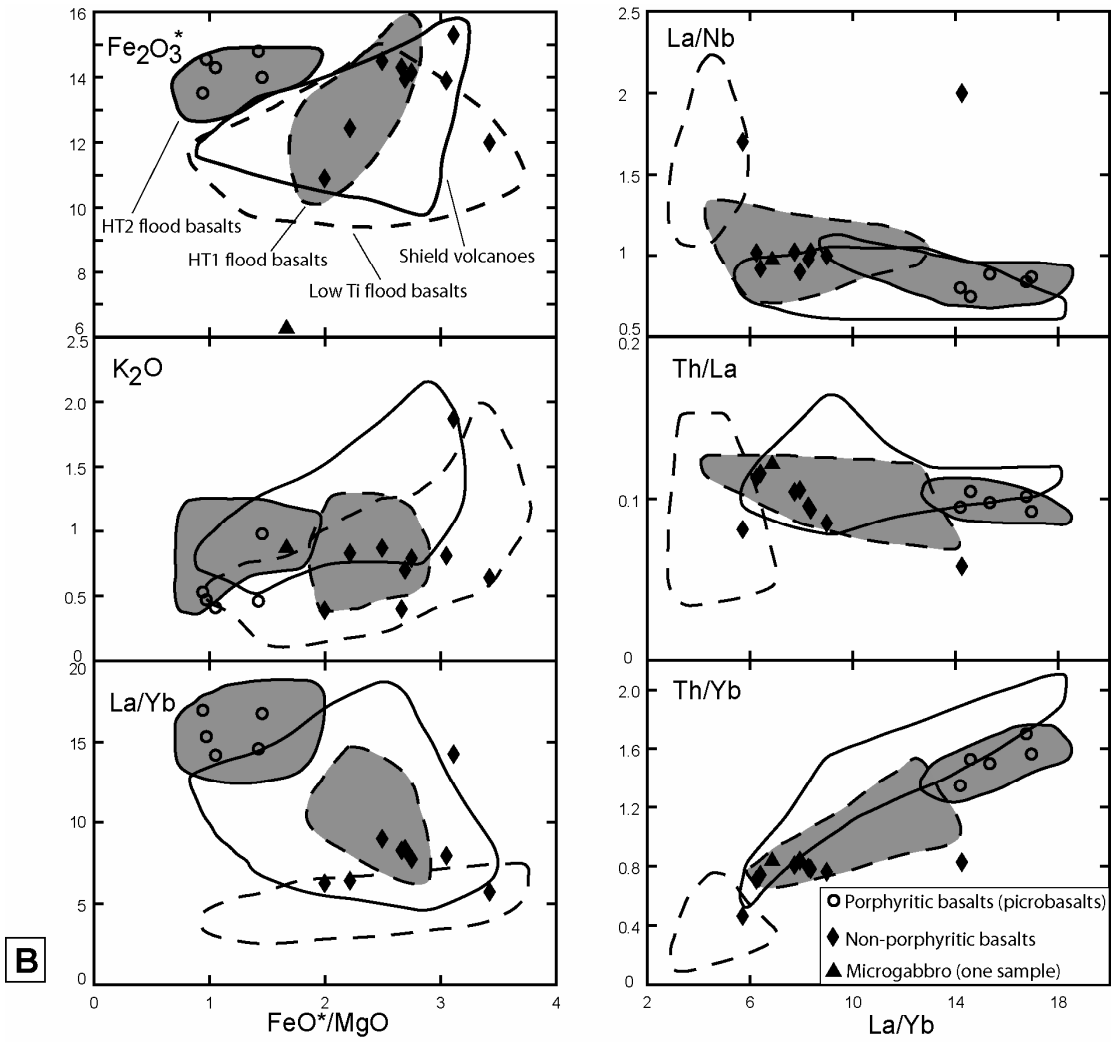

Figure 8 (continued): Plots of Fe_2O_3, K_2O, La/Yb against Fe*/MgO ratios (left column) and La/Nb, Th/La and Th/Yb against La/Yb ratios (right column). The significance of the different envelops is precised in the Fe_2O_3 diagram (left up).

4.3.4. Unspiked K-Ar radiometric datings

Seven ASR mafic rocks have been dated (see map location in figure 9), and yielded ages ranging from 27.71±0.58 Ma to 16.45±0.50 Ma (Table 3). However, the youngest of them has been obtained on a micro-gabbroic sill (dj67/05), crosscutting the Jurassic limestones in the core of the Ali Sabieh antiform (Figure 3B), and displaying hydrothermal minerals (chlorite, epidote, pyrite). Given its relatively high LOI (4.38 wt%), the corresponding date of 16.45±0.5 Ma may not be regarded as an emplacement age. The six other ages range from 27.71±0.58 Ma to 20.04±0.42 Ma, and those of intrusions (dykes, sills, x 3) and lava flows (x 3) clearly overlap.

These new data are consistent with the previously proposed time range of emplacement of Ali Sabieh basalts between 26.7 ± 1.0 and 20.0±0.6 Ma (K-Ar method on whole rocks: Barberi et al., 1975; Black et al., 1975; Chessex et al., 1979). Zumbo et al. (1995) have measured a $^{40}Ar/^{39}Ar$ plateau age of 23.6 ± 0.5 Ma on a basaltic flow which also fits this range. However, they also obtained younger ages ranging from 17.3 ± 0.2 Ma to 16.7 ± 0.4 Ma on the basaltic and rhyolitic dyke swarms.

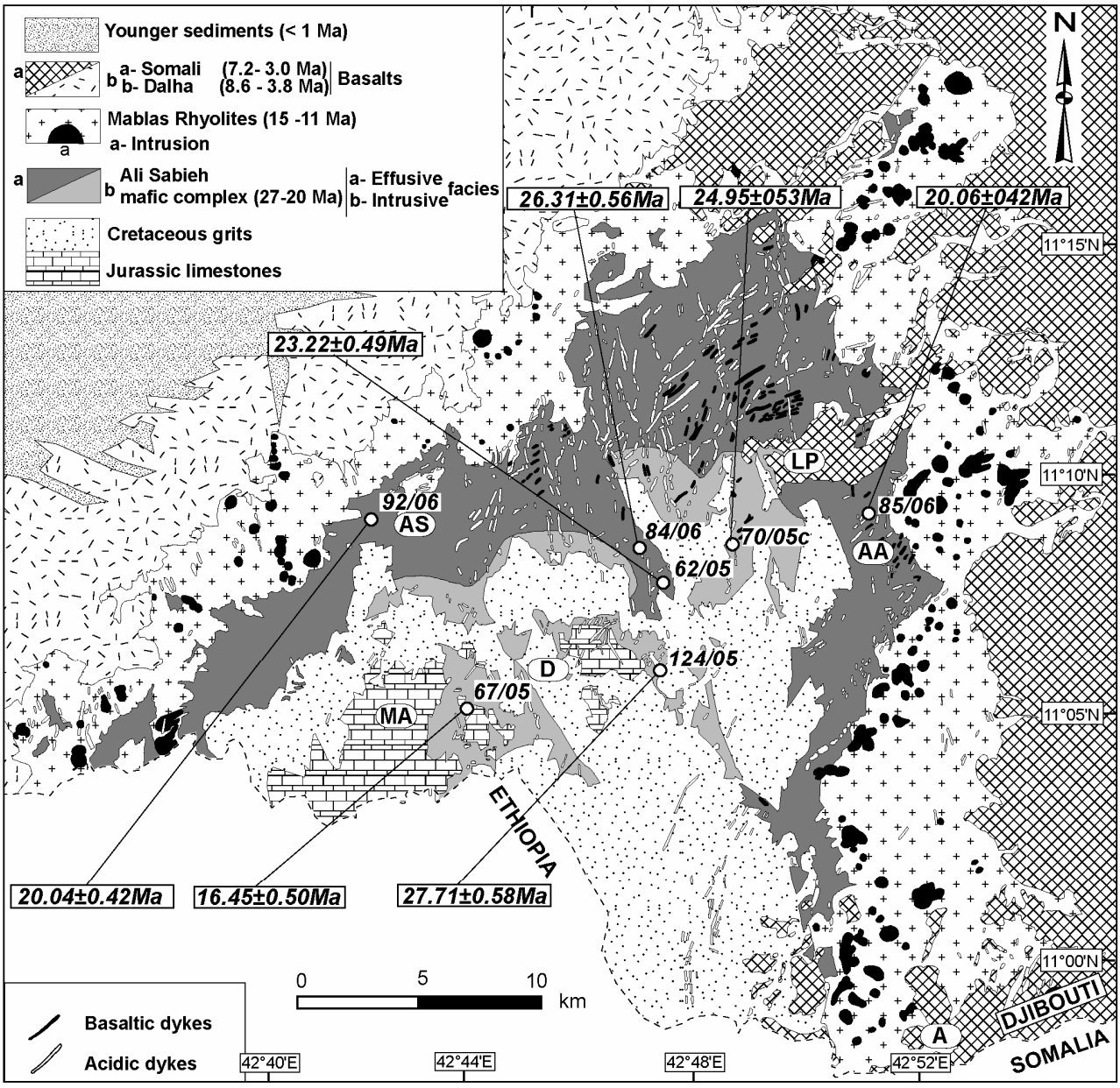

Figure 9: Map location of seven mafic rock samples from the Ali Sabieh complex dated in the present study (x4 intrusive and x3 effusive rocks).

The above age datasets firmly demonstrate that the ASR mafic lavas are significantly younger than the Ethiopian traps (~30 Ma: Zumbo et al., 1995; Hofmann et al. 1997; Backer et al., 1996; 30.6 to 29.6 Ma: Coulié et al., 2003) and the Yemen traps (30.9 to 29.2 Ma: Backer et al., 1996). Their emplacement seems concomitant with that of the large Ethiopian shield volcanoes at ~ 22 Ma (Kieffer et al., 2004).

Sample Experiment	Split K (wt%) ± 1σ	Mass molten (g)	^{40}Ar*%	40Ar* 10^{-11} (mol./g) ± 1 σ	Weighted mean 40Ar* 10^{-11} (mol./g) ± 1 σ	Age (Ma) ± 2 σ
dj 92/06						
7419	0.672 ± 0.007	1.14897	59.555	2.342 ± 0.012		
7435	« …… »	1.03413	54.852	2.356 ± 0.012	2.348 ± 0.008	***20.04 ± 0.42***
dj 85/06						
7486	1.515 ± 0.012	1.02570	59.789	5.208 ± 0.026		
7519	« …… »	0.53711	56.960	5.400 ± 0.027	5.301 ± 0.019	***20.06 ± 0.42***
dj 62/05						
7258	0.728 ± 0.007	0.44500	37.935	2.932 ± 0.015		
7274	« …… »	0.48997	39.211	2.969 ± 0.015	2.950 ± 0.011	***23.22 ± 0.49***
dj70/05c						
7251	0.623 ± 0.006	0.97913	30.598	2.692 ± 0.014		
7267	« …… »	1.18979	32.084	2.738 ± 0.014	2.715 ± 0.010	***24.95 ± 0.53***
dj 84/06						
7453	0.132 ± 0.001	1.01047	12.897	0.605 ± 0.032		
7469	« …… »	1.04650	12.251	0.609 ± 0.033	0.607 ± 0.022	***26.31 ± 0.56***
dj 124/05						
7276	0.666 ± 0.007	1.16157	48.359	3.231 ± 0.016		
7292	« …… »	0.60841	49.543	3.218 ± 0.016	3.225 ± 0.011	***27.71 ± 0.58***

Sample Experiment	K (wt%) ± 1σ	Mass molten (g)	^{40}Ar*%	40Ar* 10^{-11} (mol./g) ± 1 σ	Age (Ma) ± 2 σ
dj67/05 7268	0.360 ± 0.004	0.62562	4.843	1.032 ± 0.011	***16.45 ± 0.50***

Table 3: K-Ar age determinations on basaltic samples from the Ali Sabieh volcanic complex (see figure 9 for location). The younger age of the gabbroic sample dj67/05 is probably due to weathering process, and is not discussed in the text.

5. Fault pattern and domal structure.

5.1. The Ali Sabieh domal structure.

The general cartographic arrangement, and dipping attitude (x 77 field data), of the pre-Dalha-Somali series typically characterize an asymmetrical N-plunging domal structure, with a much wider eastern flank (Figure 10). Strata dip values range between 0-45°, and cluster at ca. 20° (Figure 10A). The highest values correspond to easterly-dipping strata from the eastern flank, though strata dip as high as 45° are locally observed on the western flank, in close association with drag-folds along strike-slip faults. Since no discrepency exists between strata dips measured in the four stratigraphic units involved in the domal structure, they are all assumed to have suffered similar amount of tilt.

5.2. Regional fault pattern.

The Ali Sabieh domal structure is crosscut by a relatively dense network of faults expressed at various scales (Figure 10B). Four regional-scale brittle-style fault-like features (referred to as F_{a-d} on the map of figures 2, 10B) are easily seen on ASTER dataset as linear structures exerting a strong control on river drainage in the central part of the ASR. Although the age, magnitude and throw of these fault structures are obscure because of the lack of relationships to elements of the country-rocks, a few assumptions can tentatively be made regarding their kinematic development from field and map-scale structural evidences. Two sets of faults are discriminated with quite distinct structural meanings.

Figure 10: Main structural features in the Ali Sabieh antiform. (A) Stereographic projection (Wulff projection, lower hemisphere) and histogram of strata dips in synrift volcanic series and pre-rift (Mesozoic) sequences involved in the Ali Sabieh antiform (77 data, undifferenciated). Poles and cyclographic traces of strata typically suggest a domal structure with dip values <25-30° in average. (B) Structural section showing the geometry (i) of dipping Cretaceous grits, and (ii) of a network of extensional fault, with conjugate dip, and post-dating the mafic sill-dyke intrusions. (See location as Z on figure 2). (C) Structural sketch map of the Ali Sabieh antiform, showing the main fault pattern and the distribution of stratal dips, and suggesting its control by two oblique, probably inherited, discontinuities, i.e. the Bour Ougoul (BOL) and Arta-Asamo (AAD) structures.

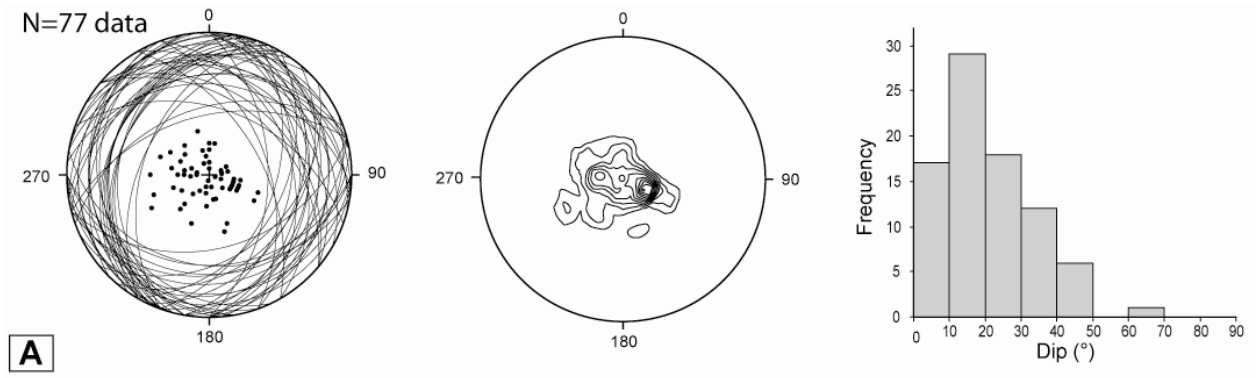
N=77 data
0
90
180
270
Frequency
Dip (°)
A

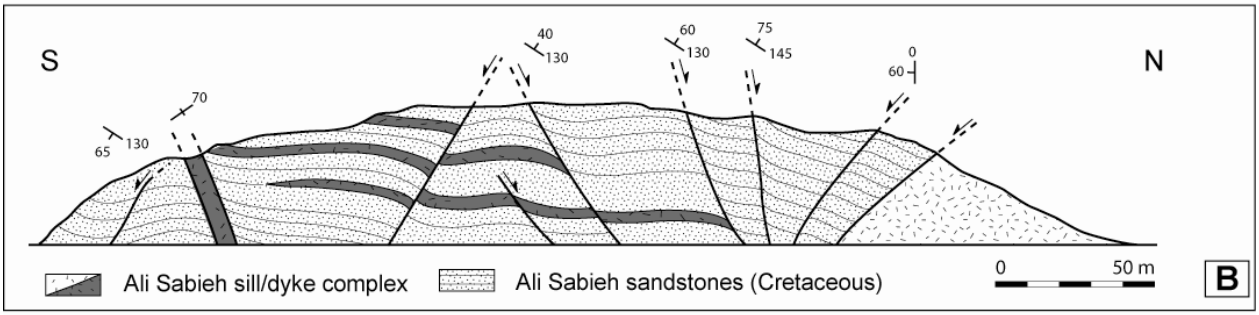
S
N
40
130
60
130
75
145
0
60
70
65
130
Ali Sabieh sill/dyke complex
Ali Sabieh sandstones (Cretaceous)
0
50 m
B

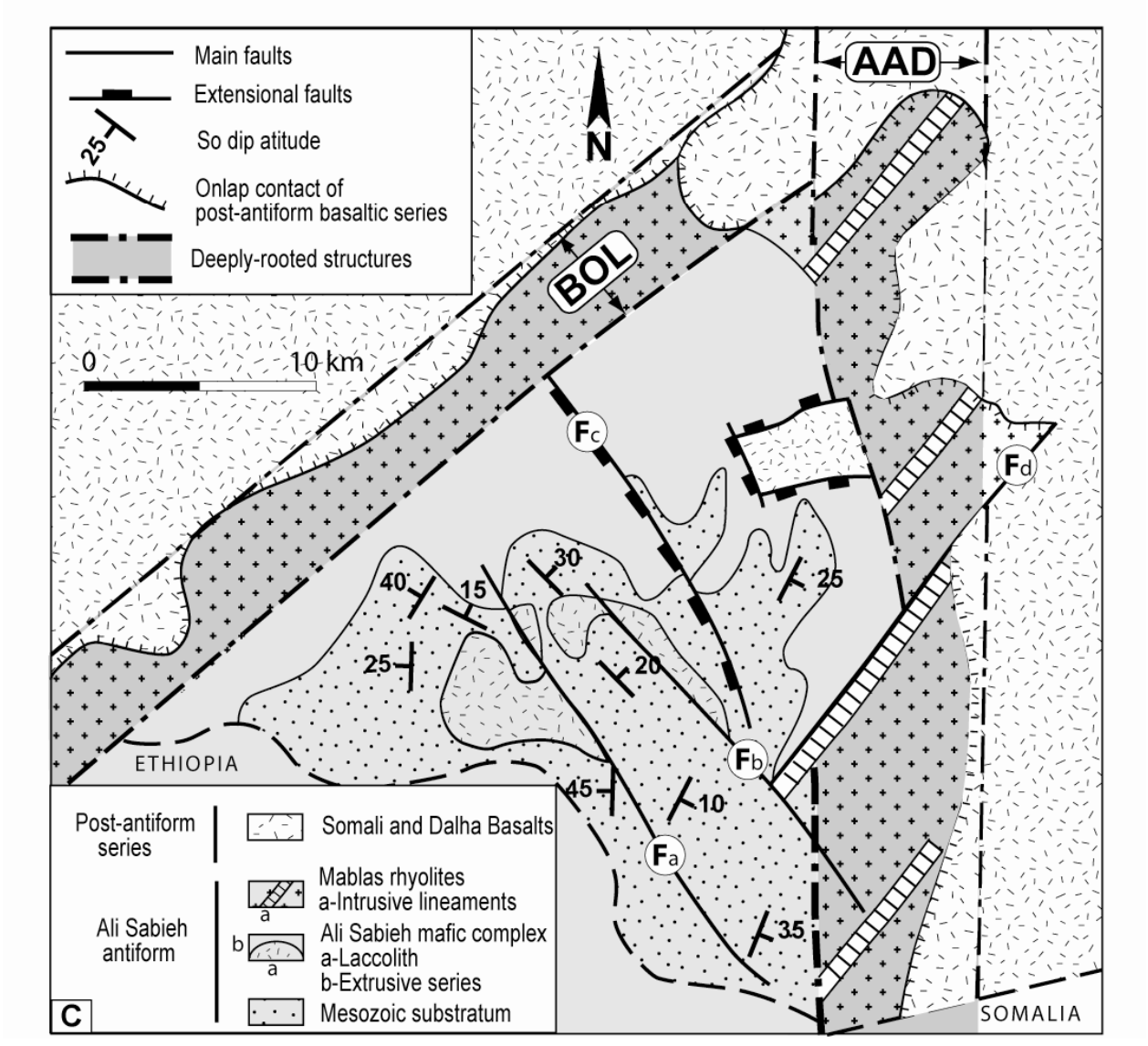
Main faults
Extensional faults
So dip atitude
Onlap contact of post-antiform basaltic series
Deeply-rooted structures
N
AAD
BOL
0
10 km
Fc
Fd
Fb
Fa
ETHIOPIA
SOMALIA
Post-antiform series
Somali and Dalha Basalts
Ali Sabieh antiform
Mablas rhyolites
a-Intrusive lineaments
Ali Sabieh mafic complex
a-Laccolith
b-Extrusive series
Mesozoic substratum
C

- The NE-SW fault labelled F_d is outlined by a swarm of rhyolitic plugs intruding the Mablas acidic series, similarly as three parallel, but shorter, en echelon tectono-volcanic lineaments on the eastern flank of the antiform (Figure 10C). The origin of these syn-Mablas faults, as either subsidiary structures to the Bour Ougoul NW-SE-oriented proto-transform to the N, or en echelon fractures linked to dextral shearing along the Arta-Asamo NS discontinuity (see Chapter 3), is not firmly established.
- Three NW-SE oriented fault-like structures, named $F_{a,b,c}$, extend nearly exclusively throughout pre-Mablas series. Two of them ($F_{a,b}$) primarilly crosscut the Cretaceous grits without any topographic expression (see sections on figure 3), and are therefore likely to represent pre-rift structures.

Similarly-trending inherited faults, probably Cretaceous in age, are assumed to have been partly rejuvenated in Miocene times, during the onset of the Ali Sabieh mafic event. They might have first behaved as ramp-like discontinuities, guiding the upward transgression of magma through the sedimentary cover (Figure 3), and then, at higher structural levels, as a master W-directed normal fault (F_c) bounding to the E a westerly-facing half-graben partly filled with the Ali Sabieh effusive mafic sequences (Figures 3, 4A). The extensional scarp morphology of this Miocene fault structure is still preserved with elevations up to 100's m in footwall uplifted Cretaceous grits (Figure 4B). A dense network of similarly-trending normal faults disrupted, at a smaller scale, the Mesozoic strata and the mafic dyke-sill pattern (Figure 10B). These inherited, or newly-formed, dominantly extensional structures probably recorded a significant component of dextral shearing under the EW-oriented extension inferred to have prevailed during the onset of the Ali Sabieh magmatic activity (see annexe A). Very few evidence support younger extensional faults (post-Mablas), excepted those bounding Somali Basalts in the Lougag uplifted plateau to the E (Figures 3C, 10C). On an other hand, the Asal-type extensional fault network, disrupting both the Dalha and Stratoid basaltic series to the NW, dies out abruptly eastwards along the Bour Ougoul transverse lineament (BOL), along which it veers anti-clockwise (Figure 12A). This overall fault arrangement reflects the stable behaviour of the ASR over the last 3 Ma with respect to the highly stretched Afar depression to the NW.

Lastly, the existence of large-scale inherited discontinuities in the ARS area is supported by the triangular map-geometry of the Ali Sabieh antiform, with two linear flanks probably controlled at depth by a NS (Arta-Asamo) and a NE-SW (BOL) deeply-rooted structures. The

origin of the Arta-Asamo accident as a Proterozoic (Marda-type) structure is likely (see Chapter 3), whereas those of the BOL is much more questionable.

6. Tectono-magmatic model.

6.1. Kinematics of mafic intrusion emplacement.

The Ali Sabieh mafic complex is here considered as a single and nearly continuous volcano-plutonic association, emplaced over 6-7 Ma, and to which is assigned the magma-driven origin of the Ali Sabieh domal structure, though it is often difficult to discriminate the effects of an intrusion from regional deformation. First, elevated basement highs in the ASR are not spatially linked to clear fault rift shoulders, and more generally to any extensional map-scale fault structures, hence ruling out the 'horst' hypothesis proposed by earlier workers (Clin, 1991 ; Eagles et al., 2002). A few significant normal faults exist, such as those bounding the Ali Sabieh effusive-filled half-graben, or the Lougag Somali plateau (Figure 10C), but they have a restricted and local significance. Secondly, the fact that the Jurassico-Cretaceous sedimentary cover is arched at the apex of the Ali Sabieh mafic pluton lends supports to the magmatic origin of doming process. Indeed, diapir uprise of mafic magmas is known to produce, at the final time of their entrapment in the upper crust, dome-like structures in the overburden (Roman-Berdiel et al., 1995). The uplift of the roof, usually accompanied by removal of material by erosion, provides a possible explanation for the 'space' problem, classically linked to pluton emplacement (Hutton, 1996). From the 3D-geometry of the overlying sedimentary envelope, which strictly mimics the shape of the pluton, the Ali Sabieh mafic body is suggested to have been emplaced as an asymmetrical cryptodome plunging gently towards the N. The maximal width and elevation of the Ali Sabieh eroded antiform can be deduced from the restored geometry of its most external envelop, i.e. the Mablas effusive sequences (Figure 11A). On an other hand, the flat-lying attitude of Mablas acidic lava flows in the Goubetto area, 5 km NE of Mablas dipping series in the eastern flank of the antiform, indicates that the Ali Sabieh structure does not extend laterally far beyond its present map exposure, beneath the onlapping Somali Basalts. Assuming a nearly symmetrical dip pattern on its western flank indicates a total width of approximately 50 km for the Ali Sabieh antiform, whereas its coring mafic intrusion should be around 20 km-wide (Figure 11A).

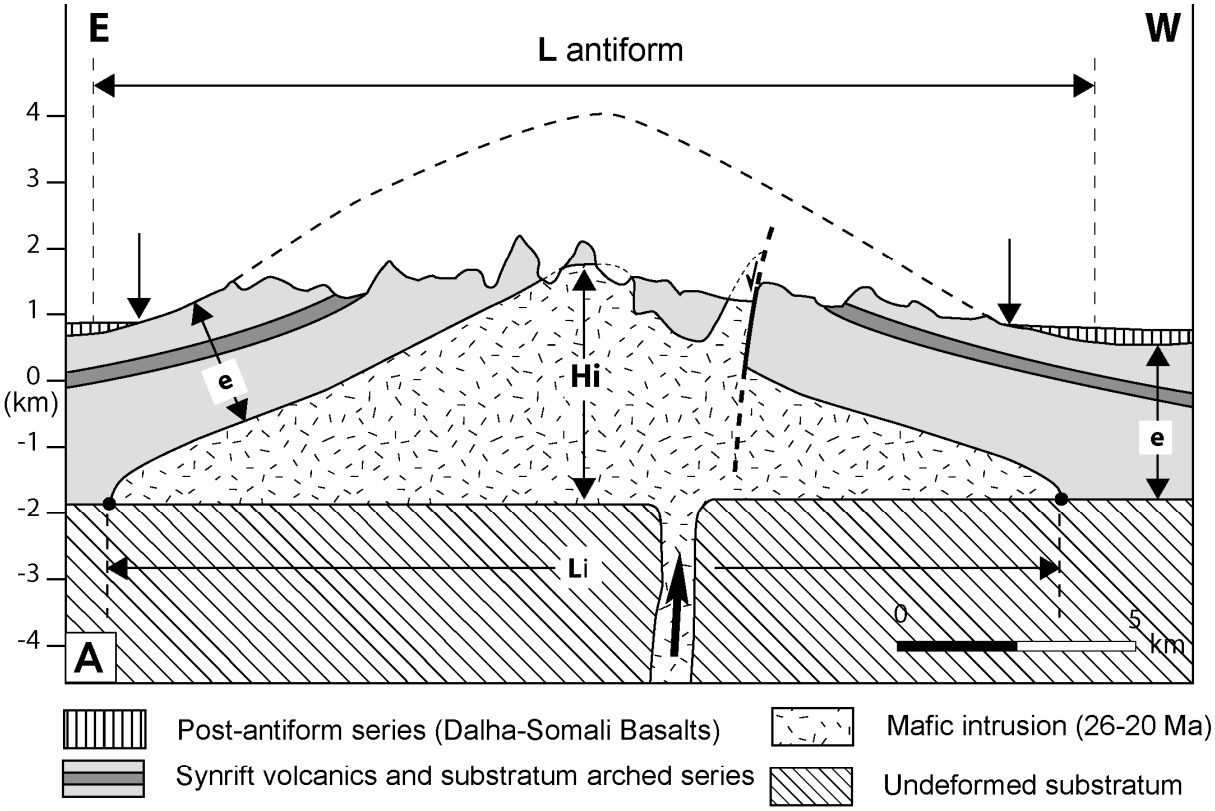

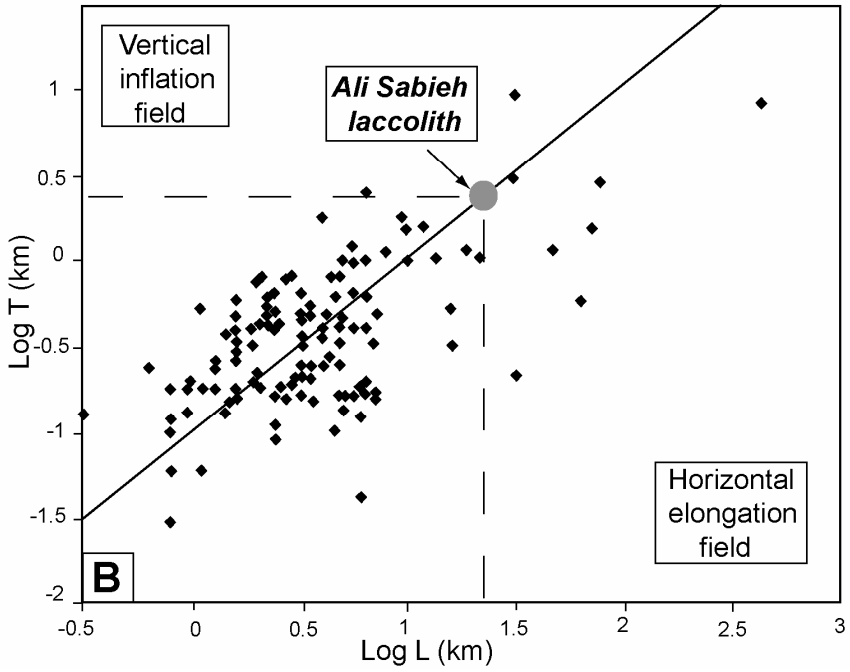

Figure 11. Structural and geometrical characteristics of the Ali Sabieh (Lower Miocene) mafic laccolith. Diagrammatic cross-section illustrating the restored geometry of the antiform and its coring laccolith (Hi, height and Li, length). Geometrical constraints are supplied by thickness data of Mesozoic and synrift sequences (e) forming the external envelop of the antiform. The depth of the base of the laccolith (at ca. 2.5 km) is deduced from its map length when plotted on the log-log diagram of figure B (in Galland, 2004). Vertical exaggeration ~1.5.

Further assuming a regular dome-shaped geometry for its envelop suggests that nearly 4 km of dome-related uplift occurred, and that ca. 2 km of sedimentary overburden has been partly removed by erosion since Upper Miocene (post-Mablas) in the axial part of the antiform. Theoretical and experimental models predict linear relationships between the maximum length of laccoliths and the depth of their inferred basal contact (equivalent to their heigth or thickness) (Roman-Berdiel et al., 1995). Plotting the estimated length of 20 km on the log-log diagram of figure 11B (in Galland, 2004) indicates a depth of 2.5 km for the base of the laccolith, i.e. nearly coincident with the base of the undeformed sedimentary cover beyond the antiformal area (Figure 11A). These values indicate an aspect ratio (amplitude/diameter) close to 0.1, as typically displayed by natural laccoliths (Dixon and Simpson, 1987). The basal contact of the intrusion probably exploited a major weakness zone that might occur, either within the Jurassic sedimentary section, or along the the top of the metamorphic basement exposed further S in Somalia (Black et al., 1972).

The spatial distribution of cover xenoliths clearly shows that they are more abundant close to the roof of the pluton, in position up to hundreds m below the restored attitude of the roof (Figure 11A). The existence of recognizable locally-derived fragments, with dimensions ranging typically from a few to hundreds of meters, in addition to the lack of any metasomatism replacement, generally argue for magma emplacement by stoping mechanism (Best, 2003). Such a dynamical process is supported by either the study of natural examples (especially granitic intrusions), or by analog modelling (e.g. McColl, 1964; Pitcher, 1979, Zak & Patterson, 2006, and references therein). Isolation of cover blocks might thus result from the downward collapse of the brittly fragmented roof above the central part of shallow magma chambers, in agreement with the classical experimental models of Ramberg (1967, 1970). Limestones xenoliths are thus likely to have sunk a few hundreds meters downwards into the ascending magma.

The Ali Sabieh cryptodome would have risen through the upper crust, up to the Jurassic-Cretaceous cover where it was probably forced to spread into a sill/dyke network during successive pulses of magma. Similar laccolith/sill associations are commonly reported (Jackson and Pollard, 1990), and in the present case, a series (at least 2) of steeply-dipping ramps, following pre-existing NW-SE Cretaceous faults, are assumed to have guided the ascent of mafic magmas filling up the sill-dyke system to the surface. There, effusive mafic sequences were deposited within a half-graben also initiated along reactivated Cretaceous ault structures, under an inferred EW-oriented extension (see Annexe A).

6.2. Timing of strain and magma-induced doming.

The lithologies exposed in the ASR bracket a long period of time from the Jurassic substratum up to the Miocene-Quaternary rift volcanics. The contact relationships between these series record distinct phases of strain, and therefore allow to constrain the timing of the dome-induced uplift. First, extensive 3-D exposures in the Dadin area (location on figure 2) clearly show that the Jurassic and Cretaceous tilted strata have concordant attitude, with no evidence for any angular unconformity (Plate 2A). However, Cretaceous grits locally filled up paleo-depressions resulting from a major pre-Cretaceous erosional event. It is thus suggested that both Jurassic and Cretaceous series have been rotated by the same amount, in contradiction with previous models implying an early (late Jurassic) compressive event in the ASR area (Barrère et al., 1975).

Secondly, the conformity of the Cretaceous grits and the overlying Ali Sabieh effusive sequences on the 'reference' section of figure 4 indicates that initial synrift volcanics in the ASR erupted at the surface as horizontal flows flooding over a flat-lying pre-rift land surface.

Lastly, the quite similar dipping attitude of the Ali Sabieh mafic layered series and the overlying Mablas acidic sequences (Figure 10A) suggests that the onset of doming took place after 15-11 Ma, but prior to the emplacement of the Somali (7.2-3.0 Ma) and Dalha (8.6-3.8 Ma) basaltic units, which later onlapped the unroofed series on the flanks of the Ali Sabieh antiform (Plates 2B, C).

In agreement with the timing constraints discussed above, it is therefore suggested that doming in the Ali Sabieh area was a ca. 10 Ma long-lived process. It initiated as early as 26 Ma (Late Oligocene) in response to the uprise of the Ali Sabieh mafic complex, and then continued growing during the extrusion of its associated sub-aerial effusive sequences. The emplacement of younger and high-level sill bodies, discordant with respect to already arched Cretaceous strata, typically characterized a multiple mafic injection process. The ascent of acidic melts from hidden magma chamber(s) in the time range 15-11 Ma later resulted in the extrusion of the Mablas rhyolites which, in turn, recorded the still ongoing doming process.

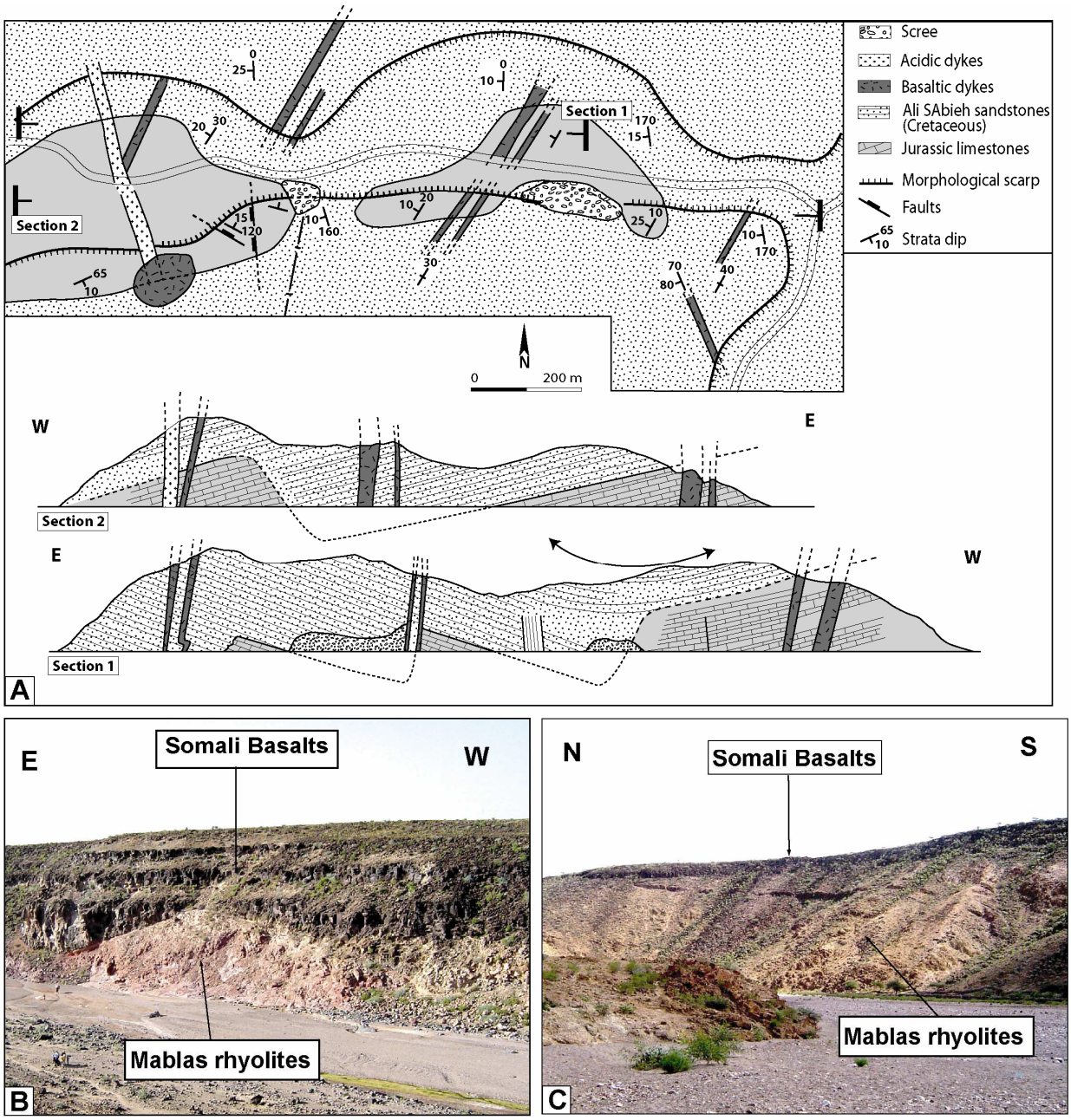

Plate 2: Timing constraints for the onset of doming in the Ali sabieh range from structural relationships between stratigraphical units. (A) Geological map and structural sections showing similar dipping attitude of both Jurassic and Cretaceous sedimentary piles in the core of the antiform (Dadin area, see location on figure 2). Note pre-Cretaceous erosional structures in the Jurassic series. (B, C) Flat-lying Somali Basalts resting unconformably over inclined Mablas acidic sequences, and thus post-dating the edification of the Ali Sabieh antiform, on its eastern flank (Hollol area (B) and NE of Ali Adde (C), see location on figure 2).

7. The Danakil range.

Only the southern segment of the DR, involving synrift volcanics coeval to the Miocene series in the ASR, is considered here since it supplies structural and timing constraints for comparing dynamics of uplift processes in the two ranges.

The overall structure of the southern DR first resulted from the early arching of the Mablas acidic series into a few km-wavelength anticline, oriented at N150°E, with diverging strata dip up to 15-20° (Figure 12C). NW-SE extensional faults, of possibly extrados-type, accommodated a limited amount of extension. The Mablas deformed sequences are unconformably overlain by gently-inclined (<15°) trap basalts of the Dalha Fm. (Figure 12D). When considering the thickness variations of the Dalha basalts at a regional scale, it appears that the thickest pile (>800 m) currently culminates in the Randa Mountain, S of the DR, whereas much thinner Dalha successions systematically occupy subdued areas, in the lowland plain fringing the DR to the E, or along the NW flank of the ASR (Figure 12A). Such a rough 'isopach' map undoubtedly reflects positive inversion of the 8.6-3.8 Ma Dalha depositional pattern in the southern part of the DR. The inferred vertical uplift is likely to have been initiated prior, or synchronously, to the eruption of the Stratoid Basalts flooring the Asal-Manda Inakir rifted zone to the W, since the resulting reliefs are assumed to have directly restricted their spatial distribution to the E (Figure 12A). The ongoing vertical uplift of the DR during, or even later than the emplacement of the Stratoid cover is supported by the elevated structural position of marginal Stratoid Basalts on the western flank of the DR, i.e. hundreds of meters higher than initially deposited over the floor of the Asal-Manda Inakir rifted zone (Figure 12B). This recent vertical movement could be linked to rift shoulder uplift along the Tadjoura and/or Asal active extensional frameworks. At a greater scale, the elongate map structure of the two uplifted segments of the DR, parallel to the RS axis, might be linked to a linear rift-induced process probably following preexisting structural trends, in agreement with recent gravimetry modelling which excludes the origin of the DR topography as a plume thermal effect (Redfield et al., 2003), in contrast with the broad circular magma-driven doming applied to the ASR.

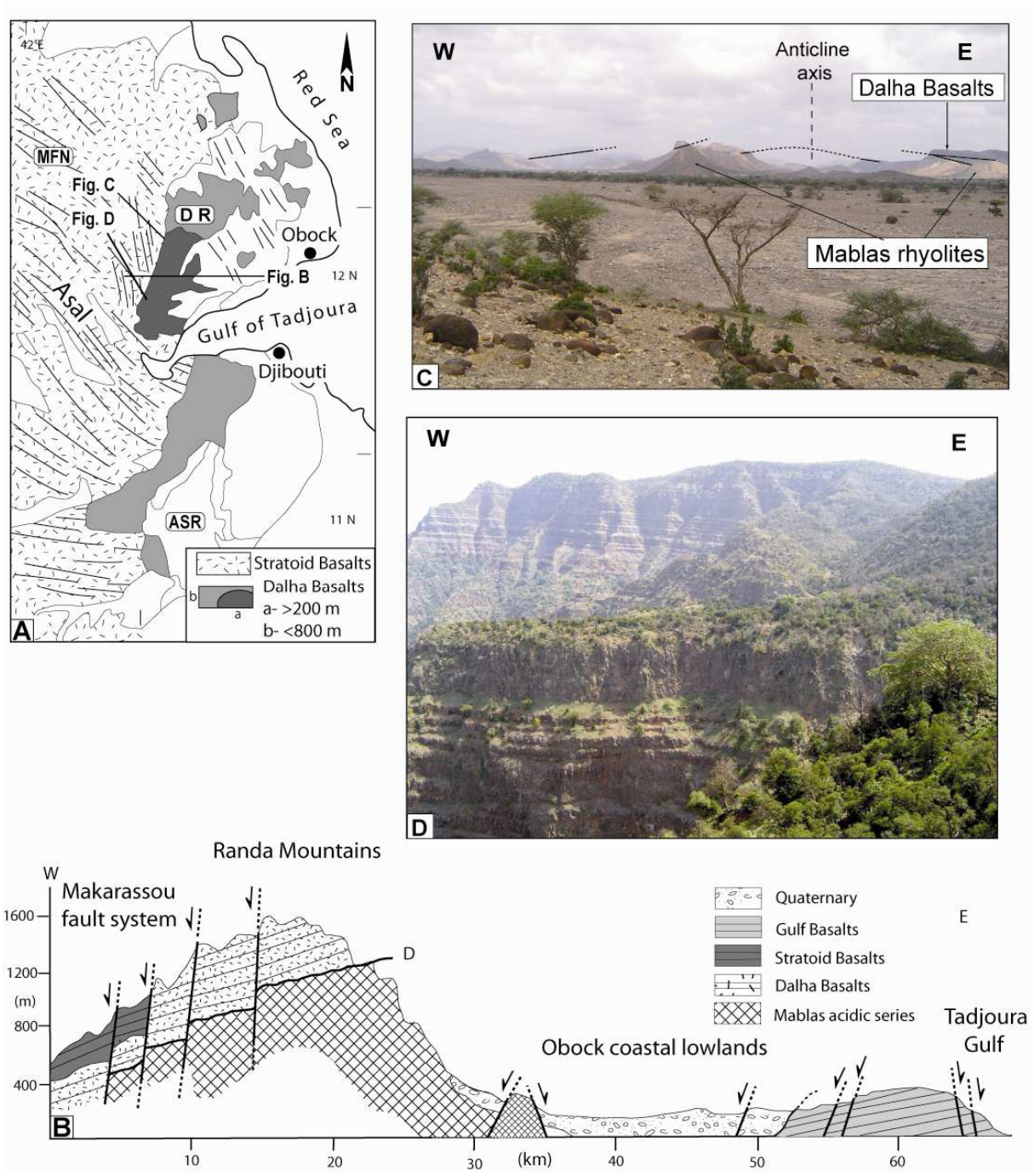

Figure 12: Structural evidence for the polyphase tectonic history of the Danakil range. (A) Simplified geological map of Eastern Afar illustrating regional thickness variations of the Dalha basaltic trap complex. Note also the nearly undisturbed character of the DR and ASR with respect to the Asal-type extensional fault pattern. MFN., Makarrasou fault network. (B) Geological cross-section of southern DR, in the Randa region, showing (i) the culmination of the Dalha basalts shown in figure D, and (ii) the elevated topographic position of Stratoid Basalts on the western flank of the DR. (C) Field view from the Sandai river showing sub-horizontal Dalha Basalts resting unconformably over arched acidic sequences of the Mablas series (see location in figure A). (D) A thick (>800 m) succession of Dalha flood basalts, slightly tilted to the W, forming the highest reliefs in the Randa Mountains.

8. Kinematical model. Implications.

8.1. Trap correlations and plume models.

It is generally accepted that the Ethiopian and Yemen flood basalts initially formed a single contigous magmatic province, ~30 Ma ago, prior to the opening of the RS and GA (Figure 13A) (Gass, 1970 ; White and McKenzie, 1989; Courtillot et al., 1999). However, the unclear temporal relationships between flood volcanism in Yemen and Ethiopia led some authors to question these models (Ukstins et al., 2002), which are further challenged here from additional volcano-stratigraphical dataset about Early Miocene volcanics in the ASR and DR intermediate domains.

It should be first noticed that evidence for Early Miocene synrift volcanics in the DR do not exist. They are totally missing in the exposed sections in the northern DR, whereas the pre-Mablas stratigraphy is not currently exposed in southern DR.

Secondly, the Early Miocene magmatic series in the ASR differ dramatically from the classical trap succession, in terms of age, volcano-stratigraphy and mode of emplacement. The 1-2 km-thick dominantly volcano-sedimentary facies forming the effusive part of the Ali Sabieh mafic complex are younger than, and contrast with, the 3-4 km-thick pile of flood lavas forming the Ethiopian plateau. Together with its intrusive laccolith, the 27-20 Ma-old Ali Sabieh complex rather resembles the ca. 22 Ma-old Choke and Guguftu shield volcanoes caping the Ethiopian traps (Kieffer et al., 2004), in agreement with their similar High-Ti affinities (Pik et al., 1998, 1999). It is thus firmly demonstrated that initial trap-like basaltic series are lacking in both the DR and ASR, i.e. close to the expected center of the Afar plume, between the Ethiopian and Yemen flood basalt provinces. Therefore, the map distribution of the 30 Ma flood basalts is undoubtedly much smaller than the ca. 2000 km radius magmatic province generally inferred since White and McKenzie (1989) (Figure 13A). If excluding the unlikely hypothesis of traps totally removed by erosional processes, two scenario can be proposed, both with major geodynamical implications.

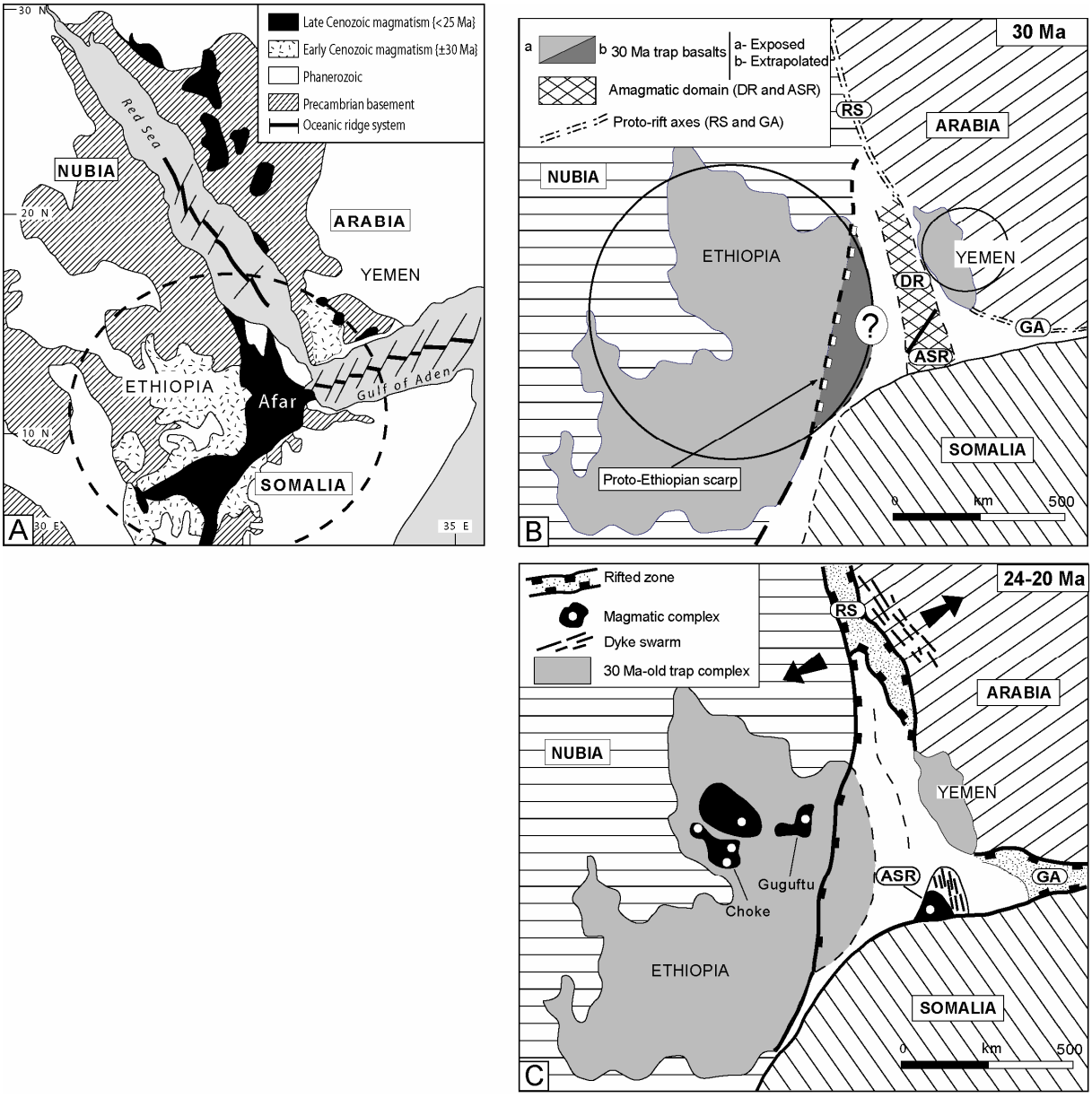

Figure 13: Dynamical evolution of the Afar rift system over the past 30 Ma. (A) Distribution of Cenozoic magmatism in the Red Sea-Gulf of Aden extensional system. The circle in dashed lines is the generally accepted surface trace of the Afar plume. (B) Alternative magmatic zonation of the Afar flood province at 30 Ma, into two disconnected volcanic sub-provinces (Ethiopia and Yemen) on both sides of an intermediate sliver of continental crust (encompassing the ASR and DR), totally devoid of magmatism. GA., Gulf of Aden; RS., Red Sea. (C) Plate reconstruction at 24-20 Ma showing the position of the Ali Sabieh magmatic area (i) at the eastern periphery of the (earlier) Ethiopian flood province, and (ii) in the southern continuation of the incipient Red Sea rift and its associated axial dyke swarm, modified from Bosworth et al. (2005).

(i) The Danakil and Ali Sabieh areas occurred within the single Afar plume-induced flood province (Gass, 1970), and formed structural highs where the 30 Ma trap basaltic cover was absent. However, structural evidence do not exist for a post-Cretaceous tectonic event which could have generated significant topographic reliefs, disturbing the widespread distribution of flooding basalts, prior to the intrusion of the Ali Sabieh mafic complex at 27 Ma.
(ii) The most likely hypothesis is to assess that during trap emplacement at 30 Ma, the ASR and DR both occurred beyond the sphere of influence of the Ethiopian plume (Figure 13B). The earliest magmatic event in these areas took place ca. 3 Ma later, at 27 Ma, during the intrusion of the Ali Sabieh mafic complex (Figure 13C), i.e. coeval with the eruption of discrete shield volcanoes on top of the Ethiopian traps (Kieffer et al., 2004).
At 30 Ma, the Yemen trap province was therefore disconnected from the time-equivalent flood province in Ethiopia by a amagmatic intermediate domain, at least 150-200 km-wide, enclosing the DR and ASR, the dimension of which could have been greater depending on the position of the eastern and buried edge of the Ethiopian flood area beneath the Afar depression (Figure 13B). According to this model, the discrete Yemen traps to the E might have been fed either by vertically-displaced magma from a subsidiary plume, or by magma derived laterally from the Ethiopian plume, and guided at depth by topographical discontinuities at the base of the lithosphere. It is thus assessed that flood basalt extrusion at 30 Ma operated over two separate magmatic provinces - the proto-Afar depression and Yemen - on either sides of an intermediate submeridian crustal domain which appears to lie in the exact southerly prolongation of the future Red Sea rift axis (Figure 13B). It is further assessed that, during the 30 Ma-long Afar rift evolution, this postulated sliver of continental crust will later undergo an intricate tectonic and magmatic history with regards to the extensional development of the Red Sea and western Afar adjacent domains.

8.2. The heterogeneous rift structure of the Afar Triangle.

The cross-sectional cartoons of figure 14 illustrate three successive kinematic stages of the Afar extensional system since 30 Ma, along a WNW-ESE transect drawn at its widest, perpendicular to the rift axes.
- The initial stage at 30 Ma (Figure 14A) is restored by cancelling the bulk anticlockwise rotation of nearly 23° in paleomagnetic reconstructions (Sichler, 1980).

The out-of-plane strain inherent to more intricate strike-slip (sinistral) kinematic models (Collet et al., 2000) has no implications on the amount of extension roughly estimated for each rift stage. Very little (if any) tectonic extension accompanied the eruption of plume-related trap volcanism at 30 Ma (Barberi et al., 1972, 1975).

- Mechanims of extension during the rift stage 29-3 Ma are extrapolated from the corresponding structural frameworks currently exposed along the western and eastern sides of the Afar depression. To the E, there is no evidence for major faults within the volcano-stratigraphy of the Ali Sabieh (26-19 Ma) and Mablas (15-11 Ma) series (excepted those bounded the Ali Sabieh effusive-filled half-graben), neither significant fault control and coeval sedimentary sequences have been recognized on the distribution of the younger Dalha and Somali trap-like basalts in the ASR and DR. Similar conclusions are applied by Wolfenden et al. (2005) about most of the 29-7 Ma polyphased tectono-magmatic evolution of the western Afar margin which exclusively recorded a magma-driven extension through dyke injection and intrusions.

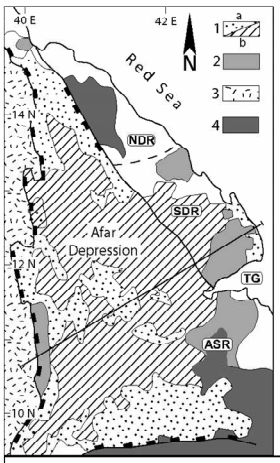

Figure 14 **:** Cross-sectional cartoons illustrating a 3-stage kinematic model of the Afar rift through the past 30 Ma. The trace of the cross-section in the widest part of western Afar is drawn on the map inset. Restored stages A and C are relatively well constrained (i) by removing recent (<3 Ma) extension, and (ii) from plate reconstructions, respectively. Note that the 'structural' individualisation of the Danakil domain, as a separate and rotated micro-block, is assumed to have occurred in recent times (<3 Ma).

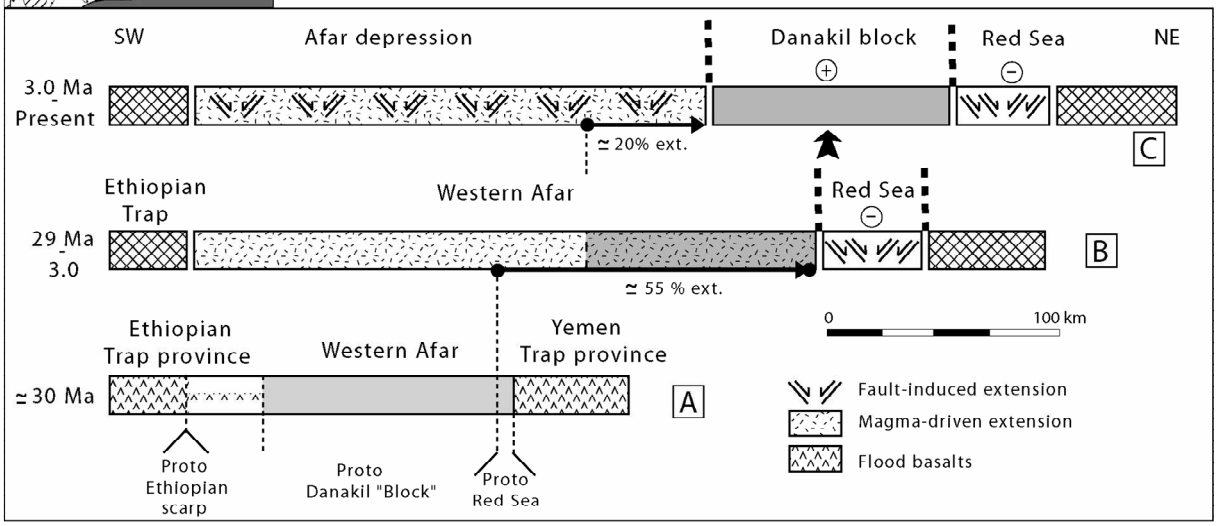

It is thus emphasized that during Miocene-Pliocene time (<3 Ma), (i) crustal extension throughout the entire Afar domain was primarilly achieved by magmatic accretion, and (ii) the Danakil area was integral part of the magmatically-extended Afar crustal domain, and it did not behave as a discrete and passively rotated continental 'micro-block' until recent times, in contradiction with most paleomagnetic reconstructions (Sichler, 1980; Acton et al., 2000; Collet et al., 2000; Eagles et al., 2002, and references therein). On the restored stage 24-20 Ma drawn on figure 13C, it is noteworthy that the position of the ASR, and its Lower Miocene NS-trending dyke swarm (Ali Sabieh intrusive complex), strictly correlates with the southern extent of the coeval, and nearly parallel, tholeiitic dyke network accompagnying the onset of continental rifting along the proto-RS axis (Sebai et al., 1991). It is thus likely that initial magmatism in SE Afar resulted from the interference of (i) a fundamental ~NS fracture zone of Red Sea affinity, in turn, probably part of the inherited Marda fault system (Purcell, 1975; Boccaletti et al., 1991), and (ii) marginal plume-related magma supply. The 50-55% magma-induced crustal inflation assigned to Afar in the time period 29-3 Ma (Figure 14B) is undirectly deduced from comparisons with the preceeding and following, better constrained, restored rift templates (Figures 14A, C). The magma-induced extension assumed to have been recorded by the Danakil crust at this stage, i.e. during the Mablas and Dalha volcanic event, might better account for the continental overlap shown in a number of paleomagnetic reconstructions (Le Pichon and Francheteau, 1978) than postulating oceanic-type crust in the Afar depression (McKenzie et al., 1970).

During most of this >25 Ma-long rift stage, mechanisms of crustal extension vary dramatically E of the Danakil domain, in the RS, where initial rifting at 25-30 Ma conversely resulted in a subsiding depositional area which was the locus of extensional tectonic strain and sedimentary basin development. There, earliest rift sedimentation is of Oligocene to early Miocene age (Mitchell et al., 1992), and graded upwards into a thick (>3000 m) fault-controlled sedimentary fill, mainly Miocene in age (Hempton, 1987; Bohannon et al., 1989), with volumetrically minor volcanism (Crossley et al., 1992).

We therefore come to the conclusion that, in the time span 29-3 Ma, the magmatically-dilated Afar crustal domain to the W might have formed a broad thermal-induced domal uplifted domain, devoid of any (documented) sedimentary depositional areas, and further decoupled to the E from the tectonically-extended fault-basin system in the Red Sea (Figure 13C). The inferred decoupling zone might coincide with the eastern edge of the present-day Danakil

submeridian range, probably guided at depth by preexisting Precambrian shear zones which are known to have also exerted structural control on the locus of rifting along the RS framework (Dixon et al., 1989; Drury et al., 1994).

With regards to the classical issue about strain location *versus* thermal profile of extended materiel, it is remarkable to note that propagation path of the RS axis extends exactly throughout the crustal domain previously devoid of magmatism at 30 Ma, i.e. where the crust/lithosphere was thus colder and more brittle, when recording tensile stress, than those of the flood basaltic sub-provinces in Ethiopia and Yemen. These rift/plume relationships are at odd with those applied by Manighetti et al. (1997) to the GA ridge with respect to the Afar plume, and they also contradict the general concept of 'strain softening', based on analog and numerical modelling, which rather predicts the more deformable state of crustal material weakened by thermal events (Callot et al., 2001; Corti et al., 2003).

- The <3 Ma rift stage (Figure 14C) is restored by removing (i) the 10-12 % extensional strain caused by block faulting in the Stratoid basaltic cover (Gupta and Scholtz, 2000), and (ii) the much less constrained dyke-related dilatation, inferred to have accompagnied at depth the Stratoid flood event, and expected not to be <10-20%, given the huge volume and spatial extent of erupted flood lava at the surface.

This rift stage is overall dominated by the starting isolation of the DR as a discrete and passively rotated microblock with respect to the highly-strained western Afar where extension expressed, on the opposite, *via* both ongoing magmatism (Stratoid) and initial (Asal-type) block faulting. The only clear evidence of young deformation in the DR is the <3 Ma-old vertical uplift, responsible for the elevated topographic position of marginal Stratoid Basalts, and likely caused by Tadjoura and/or Asal rift shoulder uplift.

Chapitre 5. Occurrence of a LREE-depleted component in the Afar plume: further evidence from Djibouti.

Daoud M.A., Barrat J.A., Maury R., Taylor R.N., Le Gall B., Guillou H., Rolet J.

Cratère d’un volcan récent (marge sud du Golfe de Tadjoura)

Chapître 5. A LREE-depleted component in the Afar plume: further evidence from recent basalts of Djibouti

(papier sera soumis après la soutenance à Lithos)

Mohamed A. Daoud[a,b], René C. Maury[a], Jean-Alix Barrat[a], R.N. Taylor[c], Bernard Le Gall[a], Hervé Guillou[d] and Joël. Rolet[a]

[a]CNRS UMR 6538 Domaines océaniques, IUEM, Université de Bretagne Occidentale, Place N. Copernic, 29280 Plouzané, France.

[b]Centre d'Etudes et de Recherches Scientifiques de Djibouti, B.P. 486, Djibouti.

[c]SOES, SOC, University of Southampton, Southampton SO14 3ZH, UK.

[d]LSCE/CEA-CNRS UMR 1572, Domaine du CNRS, 12 avenue de la Terrasse, 91118 Gif-sur Yvette, France.

.

Abstract

Major, trace element and isotopic (Sr, Nd, Pb) data and unspiked K-Ar ages are presented for Quaternary (0.90-0.95 Ma old) basalts from the Hayyabley volcano, Djibouti. These basalts are LREE-depleted (La_n/Sm_n= 0.76-0.83), with $^{87}Sr/^{86}Sr$ ratios from 0.70369 to 0.70376, and rather homogeneous $^{143}Nd/^{144}Nd$ (ε_{Nd} = +5.9 - +7.3) and Pb isotopic compositions ($^{206}Pb/^{204}Pb$= 18.47-18.55, $^{207}Pb/^{204}Pb$= 15.52-15.57, $^{208}Pb/^{204}Pb$= 38.62-38.38.77). They are very different from the underlying enriched Tadjoura Gulf basalts, and from the N-MORB erupted from the nascent oceanic ridges of the Red Sea and the Aden Gulf. Their compositions are closely similar to those of (1) depleted Quaternary Manda Hararo basalts from the Afar depression in Ethiopia and (2) one Oligocene basalt from the Ethiopian Plateau. Their trace element and Sr, Nd, Pb isotope systematics suggest the involvement of a discrete but minor LREE-depleted component, which is possibly an intrinsic part of the plume.

1. Introduction.

The study of basalts from intra-oceanic islands and plateaus as well as from trapps and rifts has shown not only the existence of different types of mantle plumes and associated hotspots (e.g. Courtillot et al., 2003), but also the considerable chemical heterogeneity of plume materials (e.g., Hart, 1988), which might indicate very complex plume structures and dynamics (Lin and van Keken, 2006). However, this complexity may not only result from the initial chemical heterogeneity of mantle plumes but also from the entrainement of surrounding mantle materials (Hart et al., 1992). In addition, a lithospheric component is clearly recognised in some intracontinental basalts, for instance in the Afar area, but its origin has been debated. Some authors have suggested that melting of the Afar lithospheric mantle explains a significant proportion of the erupted lavas (Hart et al., 1989; Vidal et al., 1991; Deniel et al., 1994) whilst others point out that continental crust contamination can account for the isotopic signature of these basalts (Barrat et al., 1993; Baker et al., 1996; Pik et al., 1999).

Although there is no doubt that the vast majority of plume-related basalts derive from a dominant chemically and isotopically enriched component, the occurrence of subordinate components characterised by a light rare earth element (LREE) depletion has been suggested from the study of basalts from major mantle plumes in: (1) Iceland (Zindler et al., 1979 ; Hémond et al., 1993; Chauvel and Hémond, 2000; Skovgaard et al., 2001; Fitton et al., 2003; Thirlwall et al., 2004; Kokfelt et al., 2006); (2) Hawaii (Chen and Frey, 1985; Yang et al., 2003; Frey et al., 2005); (3) the Galapagos (White et al., 1993 ; Hoernle et al., 2000; Blichert-Toft and White, 2001); and (4) the Kerguelen Archipelago (Doucet et al., 2002). However, the characterisation of this reservoir is difficult because its signature may be obscured by the dominant enriched plume component or by the lithospheric reservoirs. Therefore, the presence at depth of an intrinsic depleted component in the plume is still an open question.

LREE-depleted basalts associated to the Afar mantle plume have been recognised in the Quaternary Manda Hararo volcanic chain, Ethiopia (Treuil and Joron, 1975; Joron et al., 1980; Barrat et al., 2003). A single LREE-depleted Oligocene Ethiopian Plateau basalt has also been so far analysed (Pik et al., 1998, 1999).

The purpose of this paper is to describe another newly discovered occurrence of such basalts, the Hayyabley Quaternary volcano in Djibouti, i.e. on the SE part of the Afar triangle rift system, and to discuss its bearing on the composition and heterogeneity of the Afar mantle plume.

2. Analytical procedures

2.1. Phase compositions

Major element compositions of the phases were determined using a Cameca SX50 five spectrometer automated electron microprobe (Microsonde Ouest, Plouzané, France). Analytical conditions were 15 kV, 10-12 nA and a counting time of 6 sec. (see Defant et al., 1991, for further analytical details).

2.2. Major and trace element abundances

Major and trace element data were first obtained by Inductively Coupled Plasma-Atomic Emission Spectrometry (ICP-AES). The samples were finely powdered in an agate grinder. International standards were used for calibrations tests (ACE, BEN, JB-2, PM-S and WS-E). Rb was measured by flame emission spectroscopy. Relative standard deviation are ±1 % for SiO_2 and ±2 % for other major elements except P_2O_5 and MnO (±0.01 %), and ca. 5% for trace elements. The analytical techniques are described in Cotten et al. (1995). In addition, complementary concentrations of trace elements were measured at the Institut Universitaire Europeen de la Mer (IUEM), Plouzané, by ICP-MS (inductively coupled plasma-mass spectrometry) using a Thermo Element 2 spectrometer following procedures adapted from Barrat et al. (2000). Based on standard measurements and sample duplicates trace element concentration reproducibility is generally better than 5 % (Barrat et al., 2007), and are in good agreement with the ICP-AES results.

2.3. Sr-Nd-Pb isotopes

Isotopic compositions of Sr and Nd were determined at IUEM. Conventional ion exchange techniques were used for separation of Sr and Nd and isotope ratio measurements were carried out by thermal ionization mass spectrometry using a Thermo Triton spectrometer. Sr and Nd isotopic ratios were normalized for instrumental mass fractionation relative to $^{86}Sr/^{88}Sr = 0.1194$ and $^{146}Nd/^{144}Nd = 0.7219$, respectively. The results are reported relative to $^{87}Sr/^{86}Sr = 0.710240$ for the NBS 987 standard and $^{143}Nd/^{144}Nd = 0.511860$ for the La Jolla standard.

Isotopic compositions of Pb were determined at Southampton Oceanic Center using the SBL 74 double spike.

2.4. K-Ar dating

K contents and Ar isotopic compositions were measured at Brest and Gif-sur-Yvette, respectively. The samples were crushed, sieved to 0.25-0.125 mm size fraction and ultrasonically washed in acetic acid. Potassium and argon were measured on the microcrystalline groundmass, after removal of phenocrystals using heavy liquids of appropriate densities and magnetic separations. This process improves the K yield as well as the percentage of radiogenic argon, and removes at least some potential sources of systematic error due to the presence of excess ^{40}Ar known to occur in olivine and feldspar phenocrystals. Ar analyses were performed using the Cassignol technique (Cassignol and Gillot, 1982; Gillot and Cornette, 1986). The volumetric calibration of the spike-free introduction line was refined by the cross calibration of GL-O (Odin et al., 1982; Charbit et al., 1998), Mmhb-I (Samson & Alexander, 1987), LP-6 (Odin et al., 1982), and HD-B1 (Fuhrmann et al., 1987). This calibration (Charbit et al., 1998) allows Ar content to be determined with a precision of 0.2% ($\pm 2\sigma$).

3. Geological setting and K-Ar ages

3.1. Geological and tectonic framework

The geology of the Republic of Djibouti records the effects of the activity of the Afar mantle plume since 30 Ma (Schilling, 1973; Barberi et al., 1975; Barberi and Varet, 1977; Furman et al., 2006). Plume-related basaltic and derived magmas, variably enriched in incompatible elements (e.g., Joron et al., 1980 ; Deniel et al., 1994) cover ca. 90% of its surface, and range in age from at least 23.6 ± 0.5 Ma to Present (Barberi et al., 1975; Courtillot et al., 1984; Zumbo et al., 1995). Since the Miocene, the most salient tectono-magmatic process observed in the area was the penetration of the Gulf of Aden (GA) oceanic ridge between the Arabia and Somalia plates, hence leading to the opening of the Tadjoura Gulf (TG) (Courtillot et al., 1980; Manighetti et al., 1997), at the southwestern edge of which the Asal Rift shows spectacular tectonic and magmatic activity (Stieltjes et al., 1976; Needham et al., 1976).

On land, the principal marker of the Pliocene opening of the TG was the emplacement of a basaltic lava flow pile, referred to as the "initial basaltic series from the borders of the TG" (Fournier et al., 1982; Gasse et al., 1983), which will be named hereafter the Tadjoura Gulf Basalts (TGB). These very fluid subaerial lava flows are generally assumed to have been emitted from now submerged fissures in the Gulf, and emplaced rather symetrically towards S between Djibouti and Arta, and towards NE on the Tadjoura side of the tear (Figure 1, inset) (Richard, 1979). Additional feeder dykes, and associated neck-like features, have been identified onshore, along the northern flank in the Tadjoura area (see Chapter 3). TGB range from olivine tholeiites to ferrobasalts, and in thin section are subaphyric to sparsely phyric, with 3-6 modal% calcic plagioclase, and 1-3 modal% olivine set in a microlitic groundmass. They display mild, but significant, enrichments in light rare earth elements (LREE) and other highly incompatible elements (Joron et al., 1980; Barrat et al., 1990, 1993; Deniel et al., 1994). Reviewing published age dataset, further completed by our own age determinations, contradicts the model applied by Richard (1979) to the TGB in the southern margin, which implies age emplacement of the TGB decreasing linearly to the W, towards the Arta relief (Figure 4 in chapter 3).

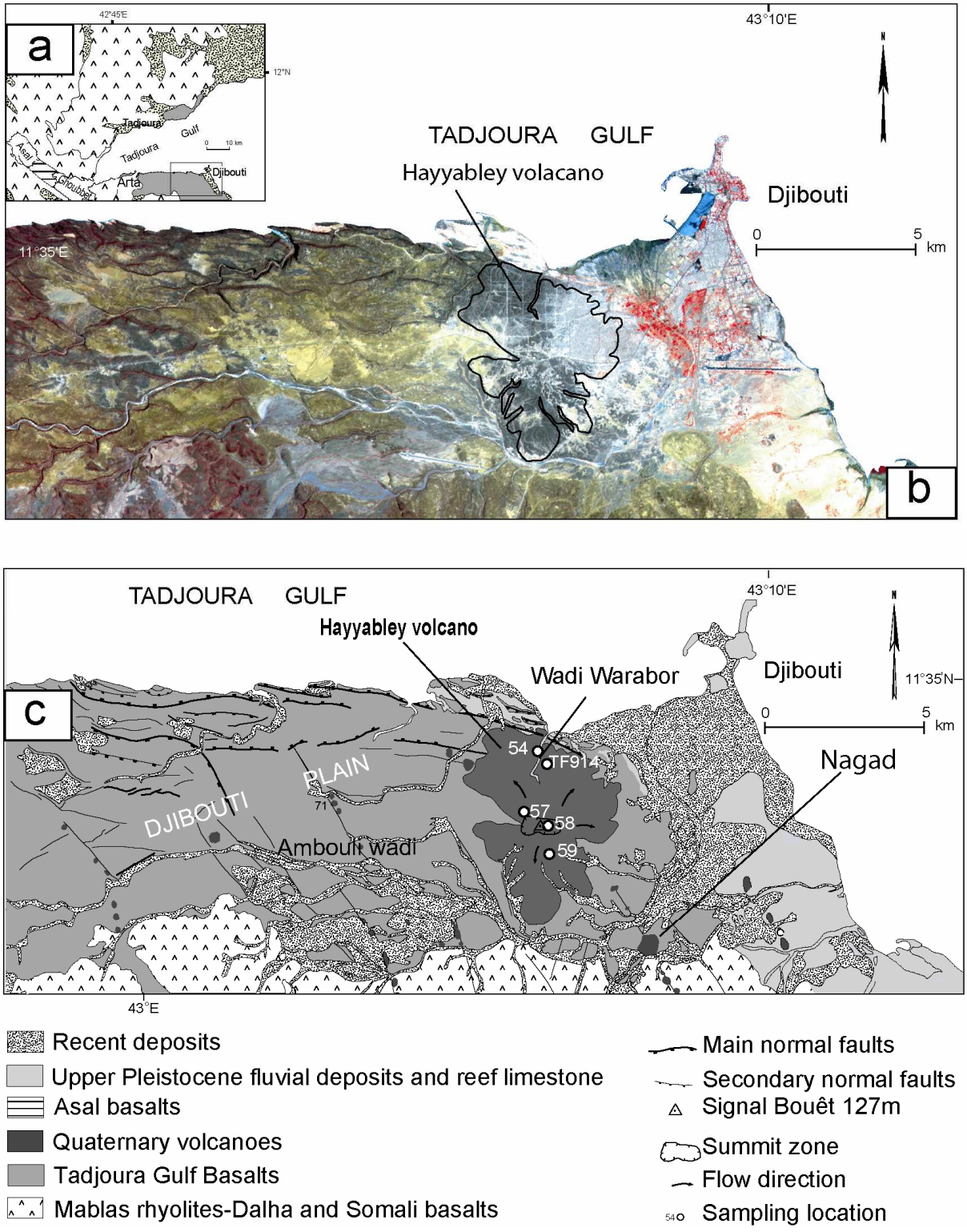

Figure 1:(a) Location of the study area**.** (b) Satellite image showing the Hayyabley volcano. (c) Geological map of Djibouti Plain

In the Djibouti plain, the TGB are involved into a network of Gulf-parallel tilted fault blocks, bounded by dominantly extensional faults, facing to the N, in association with N140°E normal fault structures outlined by a swarm of small cinder cones (Figure 1).

To the E, they are post-dated by the Hayyabley elongated volcano, the long axis of which also strikes NW-SE, parallel to the regional fault scarp bounding the eastern coastal plain further SE.

3.2.The Hayyabley volcano

The youngest volcanic units of the Djibouti plain are a set of generally small ash and cinder strombolian-type cones with associated basaltic flows (e.g. the Nagâd volcano, Figure 1), aligned along NNW-SSE trends (Fournier et al., 1982) corresponding to a very young fracture network. They overlie the TGB and have been dated to 1.75-1.70 Ma (Gasse et al., 1983). The largest of these post-TGB volcanic centers is the Hayyabley volcano (Figure 1), to the E. Although it was shown on the 1:50 000 geological map of Djibouti (Fournier et al., 1982), and further well-described and dated in the corresponding notice (Gasse et al., 1983), it has apparently never been investigated later despite the obviously unusual characteristics of its basaltic lavas.

The Hayyabley volcano forms in map-view a 5x10 km elliptic edifice, with a NNW-SSE-oriented long axis. It has a shield-like and rather flat morphology, culminating at 147 m at Signal Bouêt. It overlies the TGB lava flows outcropping W and N of wadi Ambouli valley (Figure 1), and seals the EW to WNW-ESE normal fault pattern related to the Tadjoura rift. Despite its great surface dimension, we estimate its volume to ca. 0.6-0.8 km^3 only. Its eruptive vents are no longer identifiable, possibly because of the strong anthropic imprint and constructions of the Djibouti suburbs: they are thought to be located in its summit zone, and aerial photograph data suggest radial emplacement of the lava flows away from this summit (Fournier et al., 1982).

The total thickness of the Hayyabley lava flow pile is estimated at 120 m. The best section is exposed in Wadi Warabor, along the northern coast (Figure 1), along

which we sampled seven superimposed basaltic lava flows (Dj54-04), resting conformably upon a 15 m-thick columnar-jointed lava flow belonging to theTGB sequence. These flows are vesicle-rich, and their thickness decreases upwards from ca. 4 m to 40 cm. Only the thickest lava flows show columnar jointing, and the uppermost ones, less than 20 cm-thick, are highly vesicular and often scoriaceous (Gasse et al., 1983). A sample (TF 914) collected from a possible eruption vent in the summit area has been dated by the K-Ar unspiked method to 0.98 ± 0.10 Ma and 0.83 ± 0.08 Ma (Gasse et al., 1983), the youngest K-Ar dates obtained in the area. We have checked the previous results by dating two basaltic flows from the Oued Warabor section (Figure 1). The results are shown in Table 1. The two ages obtained, 0.93 ± 0.06 Ma and 1.06 ± 0.09 Ma, are mutually consistent, and compatible as well with those previously published (Gasse et al., 1983). Indeed, the four results overlap at around 0.90 – 0.95 Ma, and are remarkably convergent considering the very low concentration of potassium in the studied samples and the young age range.

Sample id Experiment #	Split K (wt%) ± 1σ	Mass molten (g)	^{40}Ar*%	40Ar* 10^{-13} (mol./g) ± 1 σ	Weighted mean 40Ar* 10^{-13} (mol./g) ± 1 σ	Age (Ma) ± 2 σ
DJI-54B						
7040	0.09 ± 0.005	2.10972	1.254	1.430 ± 0.057		
7056	« …… »	2.07428	1.213	1.468 ± 0.058	1.449 ± 0.041	***0.93 ± 0.06***
DJI-54F						
7039	0.04 ± 0.004	2.77642	0.577	0.642 ± 0.046		
7063	« …… »	3.01844	0.699	0.745 ± 0.040	7.000 ± 0.030	***1.06 ± 0.09***

Table 1 : Age determinations of Hayyabley volcano Basaltes

4. Petrologic and geochemical results

4.1. Petrographic and mineralogical notes

The Hayyabley basalts are rather homogeneous from a petrographic point of view, and also quite different from the underlying TGB. They are moderately to highly vesicular (10 to 30 modal% vesicles in thin section). These vesicles are usually void, or sometimes partly filled by calcite, especially in the summit part of the volcano. They are also sparsely to moderately phyric, with 5 to 15 modal% phenocrysts, the size of which ranges from 0.5 to 3 mm. They include olivine (dominant) and calcic plagioclase (subordinate), in a roughly 2:1 ratio. These phenocrysts are set in an holocrystalline groundmass, showing doleritic or intersertal textures. It contains, by order of decreasing abundance, plagioclase laths, olivine microcrysts (the periphery of which is often iddingsitized), calcic pyroxene grains and titanomagnetite.

Olivine compositions range from Fo_{84-82} for the phenocryst cores to Fo_{78-54} for their rims and the microcrysts, the smallest ones being the most Fe-rich. The plagioclase phenocryst cores are bytownitic (An_{86-77}) and contain negligible amounts of Or component (<0.3%). The corresponding rims are less calcic (An_{70-32}) and the small laths from the groundmass are clearly enriched in alkalies (up to $An_{27-15}\ Ab_{70-80}\ Or_{2-5}$). Groundmass clinopyroxenes are augitic ($Wo_{45-41}\ En_{43-40}\ Fs_{12-16}$) and their low TiO_2 (<1 wt%) and Na_2O (<0.3 wt%) contents are typical of tholeiitic clinopyroxenes.

4.2 Major and trace elements

9 samples taken from different flows from four different locations (Figure 1) were analysed, and the results are given in Table 2. Their major and trace element abundances are uniform. These lavas display high Al_2O_3 (16.4-17.05 wt%) and CaO (12.5-13.8 wt%) abundances, low Na_2O (1.9-2.1 wt%) abundances and FeO*/MgO ratios close to 1. Although not primitive, these lavas are amongst the least evolved basalts collected so far from the Republic of Djibouti. Indeed, they exhibit the highest compatible trace element abundances (e.g., Ni, Co, Cr) measured in samples from this area (e.g., Joron et al., 1980; Barrat et al., 1990, 1993; Deniel et al., 1994).

Sample / Comp.	DJ54B ICP-AES	DJ54B ICP-MS	DJ54C ICP-AES	DJ54D ICP-AES	DJ54F ICP-AES	DJ54G ICP-AES	DJ54H ICP-AES	DJ54H ICP-MS	DJ57 ICP-AES	DJ57 ICP-MS	DJ58 ICP-AES	DJ58 ICP-MS	DJ59 ICP-AES	DJ59 ICP-MS
SiO_2	47.15		47.00	46.8	46.6	46.8	46.5		47.2		46.6		47.6	
TiO_2	0.93	0.91	0.95	0.95	0.89	0.89	0.91	0.99	0.92	0.90	0.85	0.88	0.96	0.97
Al_2O_3	16.53		16.55	16.40	17.00	16.60	16.50		16.52		16.60		17.05	
Fe_2O_3	11.33		11.50	11.33	11.16	11.22	11.29		11.41		10.29		11.07	
MnO	0.17	0.16	0.17	0.17	0.17	0.16	0.16	0.17	0.17	0.16	0.15	0.14	0.16	0.15
MgO	9.45		8.92	8.75	9.46	9.47	9.30		9.80		9.18		9.25	
CaO	12.90		13.25	13.50	12.50	12.85	13.10		12.90		13.80		12.90	
Na_2O	1.99		2.00	1.90	1.98	1.98	1.92		1.96		1.96		2.08	
K_2O	0.08		0.07	0.08	0.05	0.09	0.06		0.07		0.1		0.06	
P_2O_5	0.07		0.07	0.07	0.07	0.07	0.07		0.07		0.07		0.07	
LOI	0.46		0.6	0.72	0.63	0.49	0.92		0.05		1.36		-0.38	
Total	101.06		101.08	100.67	100.51	100.62	100.73		101.07		100.96		100.82	
Li		*2.77*						*3.09*		*2.81*		*2.67*		*3.05*
Be		*0.24*						*0.26*		*0.25*		*0.27*		*0.29*
Sc	45	*43.9*	46	46	44	44	44	*47.4*	45	*45.5*	38	*39.6*	40	*41.1*
V	285	*266*	290	290	275	280	275	*291*	285	*279*	245	*244*	270	*253*
Cr	380	*362*	340	340	350	359	355	*351*	405	*388*	362	*352*	370	*364*
Co	51	*52*	52	50	53	52	52	*55*	53	*53*	48	*51*	51	*51*
Ni	198	*192*	175	175	208	209	198	*208*	210	*201*	173	*179*	175	*174*
Rb	1.05	*0.82*	0.8	1	0.5	1	0.85	*0.32*	0.5	*0.42*	1.15	*1.24*	0.5	*0.45*
Sr	154	*149*	156	157	155	153	155	*160*	147	*144*	174	*174*	170	*168*
Y	20.5	*20.89*	21	20.5	19.5	20	20.5	*21.08*	20	*19.99*	17.5	*18.49*	19	*19.57*
Zr	48	*44.91*	48	47	43	46	47	*44.09*	44	*42.81*	45	*46.87*	48	*47.77*
Nb	2.7	*2.28*	2.5	2.4	2.5	2.45	2.3	*2.26*	2.4	*2.37*	2.6	*2.59*	2.4	*2.56*

Sample / Comp.	DJ54B ICP-AES	DJ54B ICP-MS	DJ54C ICP-AES	DJ54D ICP-AES	DJ54F ICP-AES	DJ54G ICP-AES	DJ54H ICP-AES	DJ54H ICP-MS	DJ57 ICP-AES	DJ57 ICP-MS	DJ58 ICP-AES	DJ58 ICP-MS	DJ59 ICP-AES	DJ59 ICP-MS
Ba	34	*32.19*	41	55	40	50	30	*29.81*	25	*24.11*	40	*40.01*	22	*20.49*
La	2.6	*2.37*	2.5	2.4	2.5	2.4	2.5	*2.34*	2.7	*2.40*	2.7	*2.53*	2.5	*2.44*
Ce	7.1	*6.34*	7.0	6.5	6.3	6.4	6.7	*6.38*	6.5	*6.47*	7.3	*6.81*	7.0	*6.73*
Pr		*1.00*						*1.02*		*1.00*		*1.06*		*1.08*
Nd	5.3	*5.39*	5.5	5.3	4.8	5.2	5.4	*5.43*	5.4	*5.34*	5.4	*5.73*	5.8	*5.89*
Sm	2.0	*1.82*	2.0	1.7	1.9	1.7	1.8	*1.85*	1.9	*1.82*	1.8	*1.99*	1.9	*2.02*
Eu	0.8	*0.75*	0.78	0.78	0.73	0.76	0.77	*0.79*	0.74	*0.76*	0.75	*0.81*	0.82	*0.83*
Gd	2.3	*2.45*	2.3	2.4	2.5	2.05	2.4	*2.52*	2.3	*2.43*	2.5	*2.48*	2.5	*2.53*
Tb		*0.47*						*0.47*		*0.45*		*0.46*		*0.47*
Dy	3.3	*3.26*	3.4	3.3	3.1	3.15	3.25	*3.40*	3.25	*3.21*	2.9	*3.10*	3.25	*3.18*
Ho		*0.73*						*0.76*		*0.72*		*0.67*		*0.68*
Er	2.1	*2.19*	2.1	2.1	2	2.1	2.15	*2.23*	2	*2.14*	1.8	*1.93*	1.9	*2.02*
Yb	2.18	*2.23*	2.29	2.2	2.08	2.1	2.15	*2.28*	2.1	*2.20*	1.75	*1.84*	1.9	*1.95*
Lu		*0.33*						*0.33*		*0.32*		*0.27*		*0.28*
Hf		*1.23*						*1.23*		*1.21*		*1.34*		*1.34*
Ta		*0.17*						*0.18*		*0.18*		*0.19*		*0.19*
Pb		*0.26*						*0.23*		*0.26*		*0.24*		*0.26*
Th	0.1	*0.25*	0.2	0.15	0.05	0.3	0.15	*0.22*	0.1	*0.23*	0.1	*0.25*	0.05	*0.22*
U		*0.06*						*0.06*		*0.05*		*0.07*		*0.03*

Table 2. Major and trace element abundances of the Hayyabley basalts (oxides in wt%, traces elements in µg/g).

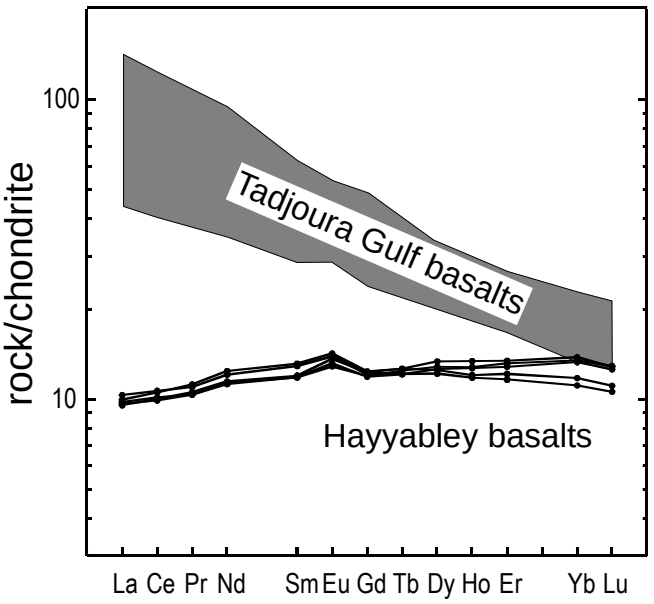

Figure 2. REE patterns of the Hayyabley basalts. The field of the patterns defined by the older Tadjoura Gulf basalts is shown for comparison. The reference chondrite is from Evensen et al. (1978).

More importantly, their incompatible trace element abundances are low, and these samples are characterized by light REE depletions (La_n/Sm_n=0.76-0.83), and small but significant positive Eu anomalies (Eu/Eu*=1.08-1.12, Figure 2). These features unambiguously distinguish the Hayyabley basalts from the Tadjoura Gulf basalts (TGB) and the older post-TGB basalts, which are always light REE enriched (Joron et al., 1980; Barrat et al., 1990, 1993; Deniel et al., 1994)..

The unusual features of the Hayyabley basalts are strengthened by their primitive mantle normalized patterns that exhibit large positive Ba (Ba_n/Rb_n=2.9-8.6) and Sr (Sr_n/Ce_n=1.8-2.1) anomalies (Figure 3).

Although light REE depleted, the Hayyabley basalts are clearly distinct from typical N-MORBs and the basalts actually emitted by the nearby nascent oceanic ridges. For example, basalts with N to T-MORB affinities are known from the E of the Tadjoura Gulf (Barrat et al., 1990; 1993). Although a positive Sr anomaly has been observed in a single light REE depleted basalt, positive Ba and Eu anomalies are missing (Barrat et al., 1990, 1993 and unpublished results).

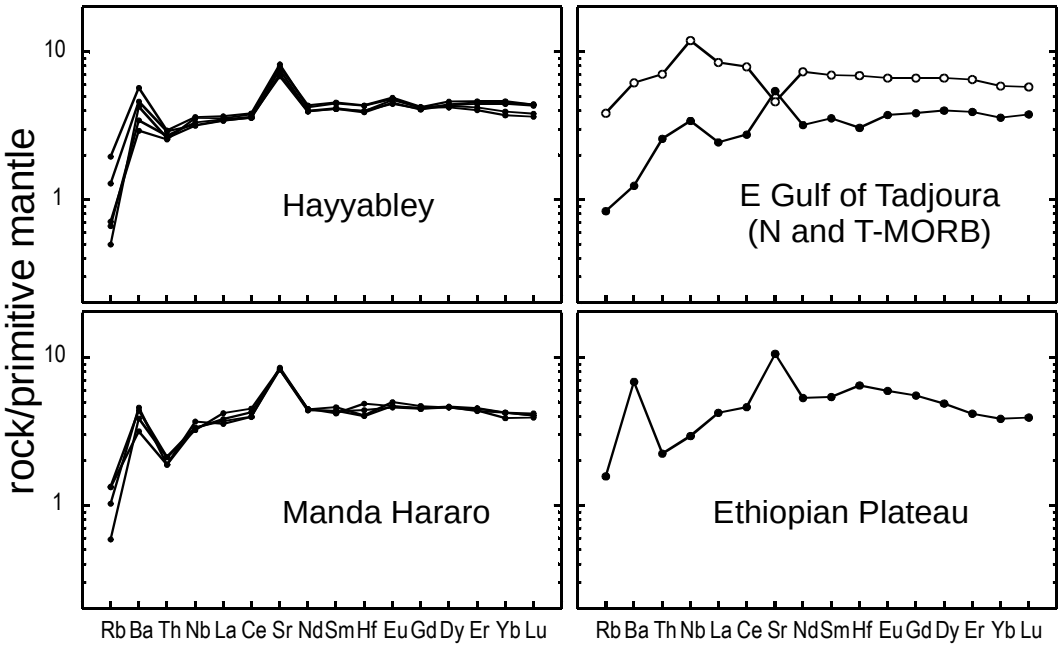

Figure 3. Primitive mantle normalized element patterns for Hayyabley basalts, the LREE-depleted Manda Hararo basalts (Barrat et al., 2003), the MORBs from the East of the Tadjoura Gulf (Barrat et al., 1990, 1993), and the LREE-depleted sample from the Oligocene Ethiopian Plateau (Pik et al., 1999). The primitive mantle values are from Sun and McDonough (1989).

Interestingly, the Hayyabley basalts are remarkably similar to the scarce light REE depleted basalts which were sporadically emitted by the Manda Hararo rift (Barrat et al., 2003): the light REE-depleted basalts from Manda Hararo display incompatible element abundances and distributions a like the Hayyabley basalts ones (Figure 3). The noticeable differences are unimportant. The Manda Hararo basalts are somewhat more evolved than the Hayyabley basalts and display for example lower Ni and Cr concentrations (Table 3). In addition, an Oligocene flow with the same features was reported by Pik et al. (1999) in the Ethiopian Plateau.

	Hayyabley (n=5)	**Manda Hararo** (n=4)	**Ethiopian Plateau** (n=1)	**Tadjoura Gulf** (n=1)
SiO_2	47.01	48.50	48.05	48.40
TiO_2	0.91	1.04	1.08	0.83
Al_2O_3	16.64	15.50	16.05	15.50
Fe_2O_3	11.08	11.94	11.63	9.78
MnO	0.16	0.18	0.17	0.13
MgO	9.40	8.47	8.67	8.83
CaO	13.12	11.32	10.58	12.90
Na_2O	1.98	2.33	2.38	2.06
K_2O	0.07	0.08	0.16	0.09
P_2O_5	0.07	0.08	0.10	0.05
total	100.93	99.44	98.87	98.57
Sc	43.5	36.7		37.9
V	267	260	229	
Cr	363	64	182	
Co	52.4	54.80		47.7
Ni	191	101	152	139
Rb	0.65	0.68	1.0	0.53
Sr	159	177	224	114.5
Y	20.0	23	21	
Zr	45	41	61	
Nb	2.41	2.43	2.1	
Ba	29.32	28.01	48	8.68
La	2.42	2.63	2.9	1.68
Ce	6.55	7.41	8.2	4.90
Nd	5.56	6.03	7.2	4.33
Sm	1.90	1.94	2.40	1.58
Eu	0.79	0.80	1.00	0.63
Gd	2.48	2.73	3.30	2.30
Dy	3.23	3.40	3.60	2.96
Er	2.10	2.14	2.00	1.88
Yb	2.10	2.04	1.90	1.77
Lu	0.31	0.30	0.29	0.28
Hf	1.27	1.34	2.0	0.95
Ta	0.18	0.18	0.1	0.14
Th	0.23	0.17	0.19	0.18
U	0.05	0.06	0.06	0.28
(La/Sm)n	0.80	0.85	0.76	0.67
Eu/Eu*	1.11	1.06	1.09	1.01
(Ba/Rb)n	4.10	3.75	4.36	1.49
(Sr/Ce)n	2.04	2.01	2.30	1.97

Table 3. Compositions of light REE depleted basalts from Hayyabley (average of the samples analyzed by ICP-MS), Manda Hararo (average from data given by Barrat et al., 2003), Ethiopian Plateau (sample E88, Pik et al., 1999), and of a N-MORB from Tadjoura Gulf (sample A3D3, Joron et al., 1980; Barrat et al., 1993). (oxides in wt%, traces elements in µg/g).

4.3. Sr, Nd, Pb isotopic data

The isotopic compositions of 5 samples are given in Table 4, and are uniform, excepted for Sr isotopes. The $^{87}Sr/^{86}Sr$ ratios vary significantly, and range from 0.70369 to 0.70396 (Table 4).

Although fresh, the Hayyabley basalts display restricted evidence of weathering. One may suspect that the $^{87}Sr/^{86}Sr$ ratios are not pristine, and have been affected by secondary processes. Indeed, we note that DJ 59, the least radiogenic sample displays a negative LOI value (LOI=-0.38 wt%). Conversely, the LOI value of DJ54H, the most radiogenic sample is much higher (LOI=0.92 wt%), and in a $^{87}Sr/^{86}Sr$ vs. LOI plot (not shown), a weak positive correlation is apparent. In order to check if the Sr isotopic composition of the samples were modified by alteration, 150 mg of sample DJ54B was leached for 2 hours in hot (150-180°C) 6N HCl, and rinsed in deionized water prior to dissolution. Its $^{87}Sr/^{86}Sr$ ratio is significantly lower than the value obtained on the unleached powder, and demonstrates that the Sr isotopic compositions have been modified by secondary processes. Similar observations were made by Deniel et al. (1994) on other Djiboutian samples.

	DJ54B	DJ54H	DJ57	DJ58	DJ59
$^{87}Sr/^{86}Sr$	0.703909±3	0.703962±5	0.703869±4	0.703871±4	0.70 3693±5
$^{87}Sr/^{86}Sr$ (R)	0.703762±9				
$^{143}Nd/^{144}Nd$	0.512961±4	0.513001±3	0.512965±4	0.512942±3	0.51 3010±4
ε_{Nd}	+6.3	+7.1	+6.4	+5.9	+7.3
$^{206}Pb/^{204}Pb$ (R)	18.4856±15	18.4776±15	18.5502±27	18.4842±17	18.4979±21
$^{207}Pb/^{204}Pb$ (R)	15.5478±14	15.5421±14	15.5662±25	15.5407±16	15.5292±20
$^{208}Pb/^{204}Pb$ (R)	38.6917±43	38.6658±44	38.7692±78	38.6217±50	38.5842±61
$\Delta 7/4$	5.3	4.8	6.4	4.6	3.3
$\Delta 8/4$	71.6	69.9	71.5	64.7	59.3

***Table 4*:** Sr, Nd and Pb isotopic compositions for Hayyabley basalts (R: residue after leaching).

Indeed, we suggest that $^{87}Sr/^{86}Sr$ ratios obtained on unleached samples from this area should be discussed only with an extreme caution, even those obtained on apparently fresh basalts. Here, we believe that only two $^{87}Sr/^{86}Sr$ ratios can be safely used in the discussion: the least radiogenic one (DJ59), and the value obtained on the residue of DJ54B.

The isotopic compositions of the Hayyabley basalts and other volcanics from the NE of Africa are compared in figures 4 to 6. The Sr, Nd, and Pb isotopic compositions of the Hayyabley basalts lie significantly outside the fields defined by the basalts erupted from the nascent oceanic ridges of the Red Sea, the East of Tadjoura Gulf, and the Aden Gulf, again demonstrating that these light REE-depleted lavas are unlike MORB (Figure 5 to 6). They display for example $^{87}Sr/^{86}Sr$ ratios more radiogenic than N- MORB, and ε_{Nd} values significantly lower (Ito et al., 1987). In contrast, the ε_{Nd} vs. $^{87}Sr/^{86}Sr$ plot (Figure 4) shows that the Hayyabley basalts and light REE depleted basalts from Manda Hararo are isotopically very close.

The Hayyabley basalts display uniform Pb isotopic compositions ($^{206}Pb/^{204}Pb$= 18.47-18.55, $^{207}Pb/^{204}Pb$= 15.52-15.57, $^{208}Pb/^{204}Pb$= 38.62-38.38.77) well above the NHRL (Hart, 1988). In the Sr-Nd, Pb-Pb, or Nd-Pb plots (Figure 4 to 6), the Hayyabley basalts extend the range of the compositions displayed by the recent (< 4Ma) basalts from Djibouti. They might reflect the contribution of a distinct light-REE component in their petrogenesis.

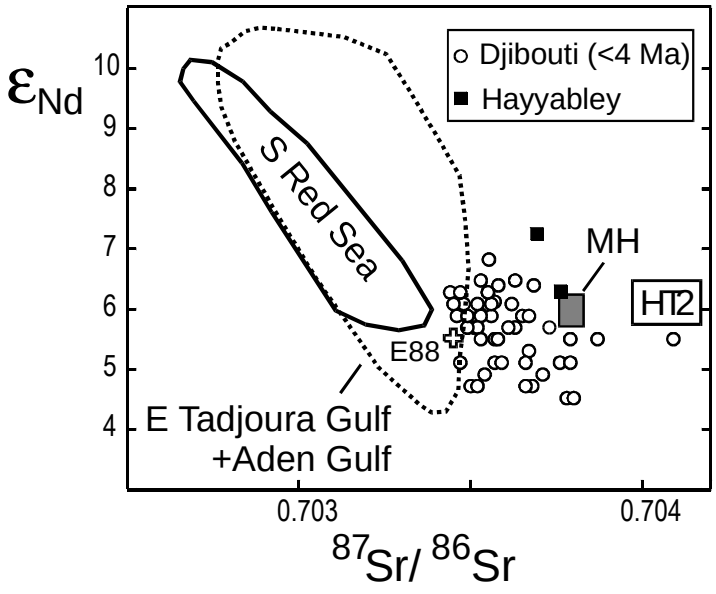

Figure 4:. ε_{Nd} vs. $^{87}Sr/^{86}Sr$ in recent basalts from Djibouti (Deniel et al., 1994, and this study). Older basalts have been omitted because of possible contamination by continental crust. The fields for the S Red Sea basalts (Volker et al., 1993, 1997), the East Tadjoura Gulf and Aden Gulf (Barrat et al., 1990, 1993 ; Schilling et al., 1992), for the light REE depleted basalts from Manda Hararo (MH, Barrat et al., 2003), and for some Ethiopian samples (E88 : depleted basalt ; HT2 : high Ti basalts, Pik et al., 1999) are shown for comparison.

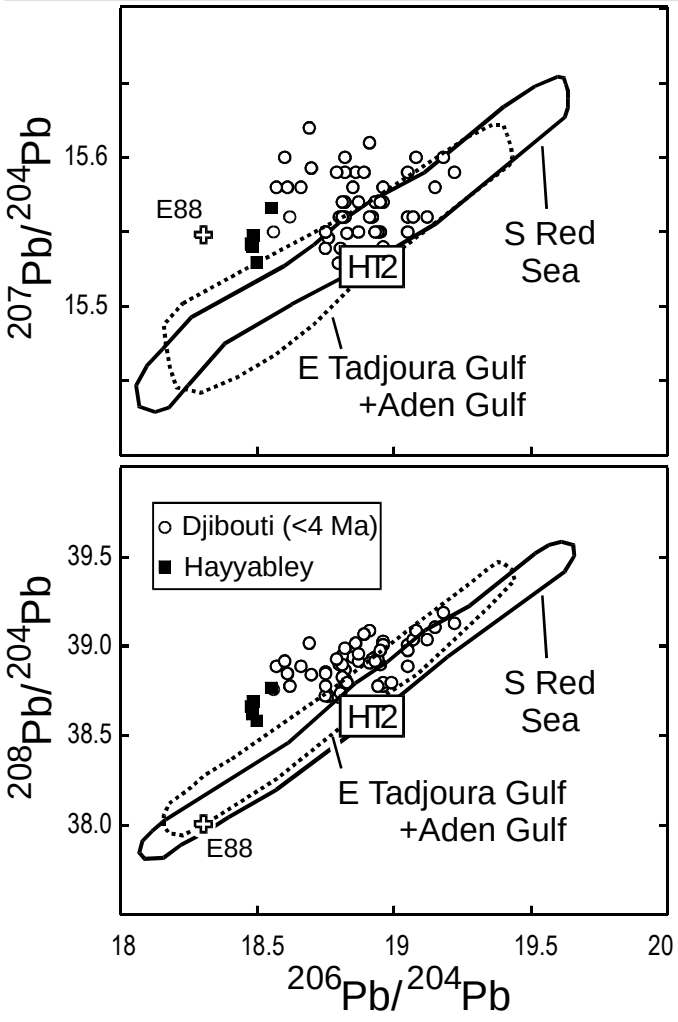

Figure 5: $^{207}Pb/^{204}Pb$ and $^{208}Pb/^{204}Pb$ vs. $^{206}Pb/^{204}Pb$ in recent basalts from Djibouti (Deniel et al., 1994, and this study). Older basalts have been omitted because of possible contamination by continental crust. The fields for the S Red Sea basalts (Volker et al., 1993, 1997), for the East Tadjoura Gulf and Aden Gulf (Schilling et al., 1992), and for some Ethiopian samples (E88 : depleted basalt ; HT2 : high Ti basalts, Pik et al., 1999) are shown for comparison.

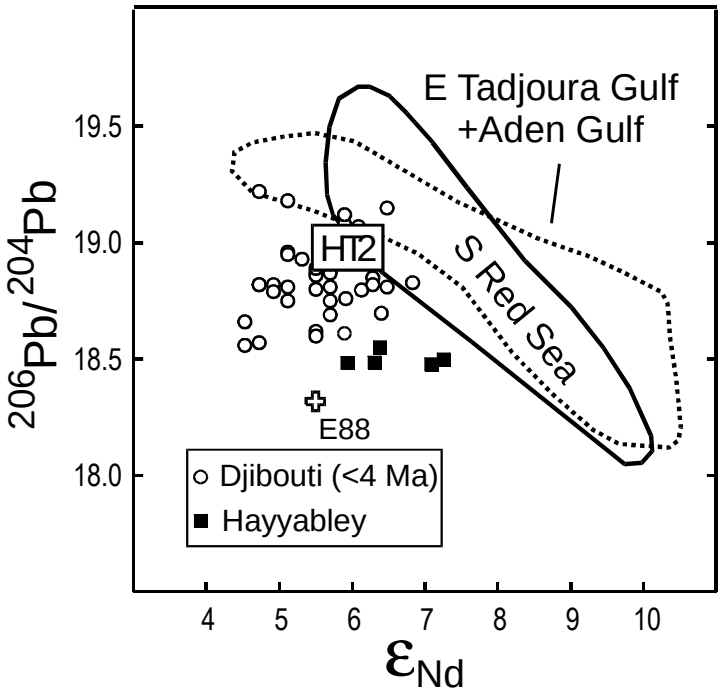

Figure 6. $^{206}Pb/^{204}Pb$ vs. ε_{Nd} in recent basalts from Djibouti (Deniel et al., 1994, and this study). Older basalts have been omitted because of possible contamination by continental crust. The fields for the S Red Sea basalts (Volker et al., 1993, 1997), for the East Tadjoura Gulf and Aden Gulf (Schilling et al., 1992), and for some Ethiopian samples (E88 : depleted basalt ; HT2 : high Ti basalts, Pik et al., 1999) are shown for comparison.

5. Discussion

Previous geochemical studies of Ethiopian Plateau basalts (Pik et al., 1999; Meshesha and Shinjo, 2007), and Afar basalts (e.g., Barrat et al., 1993, 2003) have demonstrated that depleted components were involved during their petrogenesis. The discovery of a new occurrence of light REE depleted basalts in Djibouti can provide important constrains on their origin. Two important points will be discussed below: (1) the origin of the Ba, Sr and Eu positive anomalies observed in the Hayyabley basalts, and (2) the occurrence of a specific light REE depleted component in the sources of the Afar basalts.

5.1. The Ba, Sr and Eu positive anomalies in the Hayyabley basalts

The origin of Ba, Sr and Eu in light REE depleted basalts have been previously discussed in details in the case of some Icelandic basalts (e.g., Kokfelt et al., 2006 and references therein) and of the Manda Hararo basalts (Barrat et al., 2003). The light REE depleted basalts such as those erupted by the Hayyabley volcano, may be related to common MORB, with the chief differences being due to secondary processes, such as hot-desert weathering, crystal accumulation, or contamination by a crustal component. Alternatively, they could be derived from an unusual mantle source, located in the lithospheric mantle or in the plume.

In a hot-desert environment, secondary processes are perfectly able to generate these Ba and Sr positive anomalies in a very short time. The studies of meteorites from Sahara have demonstrated that some of them, and not only the most weathered ones, exhibit marked Ba and Sr enrichments that are sensitive indicators of the development of secondary calcite, gypsum, or barytine (e.g., Barrat et al., 1998, 2003). Such processes would have generated a range of Ba and Sr abundances from low values typical of unweathered N-MORB (about 10 µg/g Ba, and 100 µg/g Sr) to much higher concentrations. To the converse, Ba and Sr abundances in the Hayyabley basalts are uniform, and strikingly similar to the concentrations measured in the distant Manda

Hararo basalts. Furthermore, the development of secondary phases is unable to increase the Eu/Eu* and to generate positive Eu anomalies, ruling out this explanation.

Positive Ba, Sr and Eu anomalies in basaltic rocks, are usually explained by plagioclase accumulation or digestion. However this process is unable to produce Sr anomalies as high as those displayed by the Hayyabley or Manda Hararo basalts without increasing drastically the Al_2O_3 contents of the resulting rocks. The Al_2O_3 abundances of the LREE-depleted basalts are not anomalously high, which immediately rules out this explanation.

The Hayyabley basalts show elevated Sr isotopic compositions and low ε_{Nd} values relative to Aden Gulf or Red Sea MORB (Schilling et al., 1992; Volker et al., 1993; Hase et al., 2000). The assimilation of a continental component could explain this shift from usual N-MORB values, but incompatible trace element ratios give no support to this interpretation. Contamination of MORB-like melts with continental crust would produce significant changes in incompatible trace element ratios. The Hayyabley basalts, like the Manda Hararo LREE-depleted basalts, lack the classical negative Nb or Ta anomalies observed in crust-contaminated basalts, and show a limited range of Ce/Pb ratios from 24 to 28, similar to values measured in oceanic basalts (e.g., Sun and McDonough, 1989). Thus, there is no indication for assimilation of significant amounts of material derived from the crust in the LREE-depleted basalts. In the case of the Manda Hararo basalts, this conclusion is strengthened by their $\delta^{18}O$ values close to 5.5 ‰, which are typical of mantle composition (Barrat et al., 2003).

As previously pointed out for the Manda Hararo basalts (Barrat et al., 2003), the positive Sr, Ba and Eu anomalies and the particular Sr-Nd-Pb displayed by the Hayyabley basalts are more likely a genuine feature inherited from their mantle sources. The same conclusions have been reached for depleted basalts with similar positive anomalies from Iceland. As an alternative mechanism, Chauvel and Hémond (2000), Skovgaard et al. (2001), and Kokfelt et al. (2006) have suggested that the sources of Icelandic lavas contained an old recycled oceanic lithosphere component and that melting of the gabbroic portion of this lithosphere led to the formation of basalts that exhibit large positive Ba, Sr and Eu anomalies. At first glance, such an explanation is attractive because if this recycled gabbroic component has been hydrothermally altered, one may expect much more radiogenic $^{87}Sr/^{86}Sr$ ratios than those of typical MORB.

Hence, the involvement of such component could account for the relatively high $^{87}Sr/^{86}Sr$ ratios of the Manda Hararo and Hayyabley depleted basalts. However, an old light REE depleted gabbroic component would be certainly characterized by high ε_{Nd} values. To the converse, the Manda Hararo and Hayyabley lavas display ε_{Nd} values unexpectedly low (ε_{Nd}= 5-7) for depleted basalts. We conclude that this model fits at best only partially the observations.

5.2. The depleted components in the sources of the basalts from Ethiopia and Djibouti

Previous geochemical studies have emphasized the participation of a depleted component during the genesis of the NE Africa basalts. In the case of basalts emitted by the young oceanic ridges from the Red Sea or the Aden Gulf, major involvement of MORB-related sources has been proposed (e.g., Barrat et al., 1990, 1993; Schilling et al., 1992; Volker et al., 1993). On land, in Afar and Ethiopia, where enriched basalts have been massively erupted, the geochemical and isotopical features of the depleted reservoirs which have been involved during the genesis of the lavas, are very difficult to constrain. Sometime, rare lavas display the signatures of such components or some mixing trends permit to deduce some of their features. Two distinct light REE depleted components have been unambiguously detected: (1) a MORB-like component is involved in the genesis of Quaternary basalts from Northern Afar; the Sr-Nd-Pb isotopic relationships displayed by the Erta'Ale basalts point to the participation of two mantle end-members, namely a HIMU component and a depleted component undistinguishable of the source of the Red Sea MORB (Barrat et al., 1998); furthermore, a similar depleted component has been detected in the sources of the Oligocene lavas from the Northwestern Ethiopian volcanic province (Meshesha and Shinjo, 2007); the entrainment of depleted mantle during plume ascent is a plausible explanation for the contribution of this component in the sources of some of the basalts erupted in Afar and Ethiopia. (2) the light REE depleted basalts from Manda Hararo and Hayyabley point to a depleted endmember chemically and isotopically distinct from the previous one; in addition, a single light REE depleted basalt that displays the same chemical features as the depleted basalts from Afar has been collected

in Ethiopia (Pik et al., 1999); although, its isotopic compositions are not exactly the same as the Hayyabley basalts (see figures 4 to 6, sample E88), this sample indicates that a depleted component distinct from the MORB source was involved in this area at this time. We suggest that a depleted component, intrinsic to the plume, has contributed to these young and old lavas related to the Afar hot spot.

6. Conclusions

The Hayyabley volcano, which formed 1 Ma ago near Djibouti, has emitted unusual light REE depleted basalts (La_n/Sm_n=0.76-0.83) that display unusual chemical features (positive Ba, Sr and Eu anomalies). These lavas are chemically distinct from the N-MORB erupted from the nearby oceanic ridges of the Red Sea and the Aden Gulf and more closely resemble the LREE-depleted basalts from the Manda Hararo rift located in Central Afar (Barrat et al., 2004). Another similar occurrence, Oligocene in age, has been reported from the Ethiopian Plateau by Pik et al. (1999). These results confirm the involvement in the genesis of the Ethiopian and Afar basalts of an unusual depleted component within the plume, that is isotopically distinct from depleted asthenospheric compositions.

CONCLUSIONS ET PERSPECTIVES

Chapitre 6 : Conclusions générales et perspectives

1. Conclusions générales.

L'objectif de ce travail consiste à compléter les modèles cinématiques appliqués au rift Afar par l'étude de deux chantiers, et leurs thématiques correspondantes, largement délaissés jusqu'à présent, et situés à la périphérie orientale de la dépression Afar ; celle-ci ayant, à l'inverse, fait l'objet de nombreux travaux, bien que n'exposant que des dispositifs relativement jeunes (<3 Ma) par rapport à la longue histoire du rift Afar, étalée sur environ 30 Ma. Ces deux chantiers, situés dans la partie orientale de la République de Djibouti, concernent :

- Les basaltes récents exposés sur les deux marges du Golfe de Tadjoura, à savoir, la Plaine de Djibouti, au S, et le secteur Tadjoura-Obock, au N, qui appartiennent à l'extrémité la plus occidentale du système d'accrétion du Golfe d'Aden.
- Les séries initiales synrift, et leur substratum, des domaines Danakil et Ali Sabieh.

Notre travail repose sur une approche multi-disciplinaire, combinant (i) une analyse structurale multi-échelle, basée sur l'interprétation d'imageries satelittales (ASTER) calibrée par des observations de terrain, et (ii) l'étude géochimique/géochronologique de roches volcaniques synrift (pour l'essentiel les facies effusifs, et exclusivement les séries basiques).

(1) En prenant les Basaltes du Golfe (2.8-1.1 Ma) comme marqueurs tectoniques du rift Tadjoura, et en combinant les données morphologiques disponibles (topographiques et bathymétriques), la structure générale du rift Tadjoura est assimilée à celle d'un hémi-graben à vergence sud, d'environ 20 x 30 km, bordé au N par un système de failles bordières et passant au S à une marge flexurée impliquant un substratum volcanique (séries des traps du Dalha et Somalis). Sur la base de données géochimiques et géochronologiques (méthode K-Ar), l'organisation volcano-stratigraphique ainsi que les caractéristiques géochimiques des séries basaltiques de la marge sud ont été affinées, avec notamment la mise en évidence d'un nouveau complexe intrusif (dyke-sill), l'ensemble de Goumarre, daté à 2.4-1.7 Ma, qui alimente trois chapelets d'édifices volcaniques alignés au N80°E, parallèlement à l'axe du Golfe. Les séries basaltiques concernées (Golfe, Somali, Goumarre et volcan Hayyabley) présentent une signature géochimique de basaltes transitionnels à affinité thôleiitique, exceptés ceux du volcan Hayyabley, plus appauvris et aux caractéristiques géochimiques

particulières. Les basaltes du Golfe sont moins enrichis en alcalins et en éléments les plus incompatibles par rapport aux basaltes Somali et Goumarre. Ces derniers se distinguent des basaltes Somali par leur fort enrichissement en terres légères (LREE) par rapport aux terres lourdes (HREE), tandis que le fractionnement des terres rares observé pour les basaltes Goumarre suggére une origine mantellique plus profonde (zone stabilité de grenat) que celle des basaltes Somali.

L'hémi-graben de Tadjoura est la première expression tectonique du rifting (à polarité Golfe d'Aden) à travers la province magmatique Afar, et il correspond à une extension cumulée estimée à 25-30%. Le rajeunissement progressif des structures extensives vers la partie centrale de l'hémi-graben témoigne de la concentration de la déformation dans l'axe, sismiquement actif, du dispositif.

L'analyse morphostructurale, géométrique et statistique des systèmes de failles extensives exposées sur les marges du rift, au niveau de la zone Tadjoura-Obock au N, et de la Plaine de Djibouti au S, permet en particulier de démontrer la plus grande complexité du dispositif faillé méridional qui se marque par (i) la présence de structures extensives transverses N140°E et (ii) de grandes variations latérales du style tectonique. Celles-ci témoignent d'un gradient croissant de la déformation vers l'W, en direction d'une discontinuité transverse, la zone d'Arta. A l'inverse des modèles cinématiques précédents qui interprétaient ce couloir décrochant subméridien comme partie intégrante du système transformant de Maskali, la zone d'Arta est considérée dans ce travail comme une structure héritée, à polarité Mer Rouge, qui entrave la propagation axiale, vers l'W, des structures extensives du système Golfe d'Aden. Ce blocage frontal de la déformation provoque le saut du rift vers le SW, depuis le Golfe de Tadjoura vers la zone du Ghoubbet, selon un modèle de type 'hard linkage', en opposition avec les conceptions précédentes qui favorisaient un transfert du rifting par l'intermédiaire de structures néo-formées disposées en échelon ('soft-linkage').

(2) L'étude structurale et pétro-géochimique des séries synrift des domaines Danakil et Ali Sabieh fournit de nouvelles contraintes (i) sur la nature des mécanismes responsables de l'édification des reliefs bordiers à l'E du domaine Afar, et (ii) sur la distribution spatiale des complexes volcaniques lors des stades initiaux du rifting Afar.

Les séries mafiques les plus anciennes présentes au cœur de l'antiforme d'Ali Sabieh (ex séries d'Adolei) sont réinterprétées en termes de laccolithe basaltique et complexe filonien associé (dyke-sill), alimentant lui-même des séquences effusives datées entre 27 et 19 Ma.
L'analyse géochimique de ces séries (intrusives et effusives) révèle l'existence de deux groupes de basaltes : (i) les basaltes porphyriques (picrobasaltes), moins évolués et dont la teneur en éléments majeurs est contrôlée par l'accumulation de phases minérales précoces (olivines et diopsides) et (ii) les basaltes non porphyriques, plus enrichis en alcalins. De nature transitionnelle à tendance tholeiitique, les basaltes porphyriques et non porphyriques se distinguent aussi par leurs teneurs en terres rares lourdes. Le rapport élèvé La/Yb des picrobasaltes suggère leur origine profonde (domaine de stabilité de grenat) par rapport aux basaltes non porphyriques. Les picrobasaltes montrent des caractéristiques géochimiques similaires à celles (i) des HT1 (flood basalts enrichis en TiO_2 de type 1) et (ii) des volcans boucliers situés sur les plateaux éthiopiens. Par contre, les basaltes non porphyriques sont géochimiquement plus proches des HT2 (flood basalts enrichis en TiO_2 de type 2).
Sur la base d'arguments structuraux, l'antiforme d'Ali Sabieh est attribué à la mise en place du laccolithe à travers une couverture mésozoïque (Jurassico-crétacée), selon un mécanisme de 'block stoping' exprimé, notamment, par la présence d'un abondant cortège d'enclaves d'encaissant à proximité du toit de l'intrusion. De simples considérations géométriques permettent de préciser les dimensions 3D du laccolithe dont le contact basal doit se situer vers 2.5 km de profondeur, probablement à proximité du toit du socle protérozoïque. D'un point de vue chronologie de mise en place de l'intrusion, les dernières étapes du doming sont intervenues postérieurement à l'événement acide Mablas (15-11 Ma), dont les séquences sont impliquées dans la structure, et antérieurement à l'éruption des traps Somali (7.2-3.o Ma) et du Dalha (8.6-3.8 Ma) qui reposent en discordance sur les deux flancs de l'antiforme.

Les résultats obtenus à propos du rift récent de Tadjoura, d'une part, et des dispositifs plus anciens des domaines Danakil et Ali Sabieh, d'autre part, fournissent de nouvelles contraintes qui permettent de discuter, à plus grande échelle, de certains aspects des modèles cinématiques appliqués au rift Afar pour la période Miocène-Actuel.
- (a) Concernant la cinématique des deux axes de rift jalonnant les marges E et W de la dépression Afar, une synthèse critique de données publiées ne nous paraît pas confirmer le modèle généralement accepté depuis Tapponnier et al. (1990) ; modèle qui implique deux

propagateurs migrant, l'un vers le S le long de l'escarpement occidental - le système Erta Ale-Manda Hararo – interprété comme la partie frontale, émergée, du système Mer Rouge, et l'autre vers le N, longeant l'escarpement oriental – le système Ghoubbet-Asal-Manda Inakir – à l'avant du système Golfe d'Aden ; les deux dispositifs déterminant une zone de recouvrement dominée par des déformations de type 'bookshelf faulting'.

Un modèle alternatif consiste à interpréter la totalité des segments de rift recoupant la moitié méridionale du système Afar, cad. le segment Manda Hararo à l'W et l'ensemble des segments Ghoubbet-Manda Inakir à l'E, comme la partie frontale du dispositif d'accrétion 'Golfe d'Aden', se propageant vers le N, suite à leur transfert le long du système transformant Maskali-BOL, auquel se rajoute les complications (saut de rift) liées à la discontinuité d'Arta. Seuls les segments de rift de l'Erta Ale au N se propageraient vers le S, à l'avant du dispositif 'Mer Rouge' ; la vergence opposée des deux systèmes de propagateurs déterminant ainsi, non pas une zone de recouvrement, mais une zone de confrontation.

- (b) L'absence de magmatisme de type trap, équivalent aux complexes à 30 Ma d'Ethiopie et du Yemen, au niveau des domaines Danakil et Ali Sabieh démontre le caractère discontinu et composite de la province magmatique Afar à cette période initiale ; celle-ci étant composée de deux sous-provinces, déconnectées de part et d'autre d'un domaine crustal intermédiaire, amagmatique, de direction subméridienne, centré sur les domaines Danakil et Ali Sabieh. Cette distribution de surface du magmatisme trap pose le problème des modalités des processus mantelliques en profondeur (nombre de panache(s) ou sous-panache(s), types de connection entre-eux, ….) .

- (c) La limite orientale du domaine intermédiaire (bordure du proto-bloc Danakil) est considérée comme l'une des discontinuités fondamentales du dispositif Afar, le long de laquelle va s'initier, vers 24 Ma, l'axe du rift Mer Rouge. Au cours du Miocène, les mécanismes de l'extension vont être totalement différents de part et d'autre de cette discontinuité, étant exclusivement associés, soit à de l'accrétion magmatique à l'W (Afar), soit à des structures tectoniques (failles/bassins) à l'E (Mer Rouge).

- (d) D'après le scénario cinématique envisagé, le domaine Danakil ne se comporte en bloc indépendant, soumis à une rotation anti-horaire, qu'à partir de 3Ma, postérieurement à l'événement magmatique Dalha qu'il partage en commun avec le domaine Afar, et non pas dès le Miocène inférieur comme généralement admis.

La plupart des nouvelles hypothèses énoncées ci-dessus à propos de la cinématique Afar dans son ensemble devraient être maintenant vérifiées et argumentées par de nouvelles

études structurales, en complément de celles proposées ci-dessous sur des thématiques plus 'locales' concernant des chantiers situés à proximité de la zone d'étude de ce travail de thèse.

2. Prospectives

Projet A : La structure profonde des dépressions de type 'Baras', République de Djibouti.

Intervenants : MA. Daoud (CERD), B. Le Gall, M. Maia et S. Hautot (UBO, IUEM).

Il s'agit d'imager la structure profonde (quelques km) d'une discontinuité transverse de 1er ordre du Rift Afar, séparant un domaine à déformation récente-active au N - la dépression Afar *sensu stricto*) -d'un domaine fixe au S. Il s'agit du linéament NE-SW de Bour Ougoul (BOL), qui souligne le flanc occidental de l'antiforme d'Ali Sabieh, dans le prolongement à terre de la transformante de Maskali (Figure 1) (cf. Chapître 4).

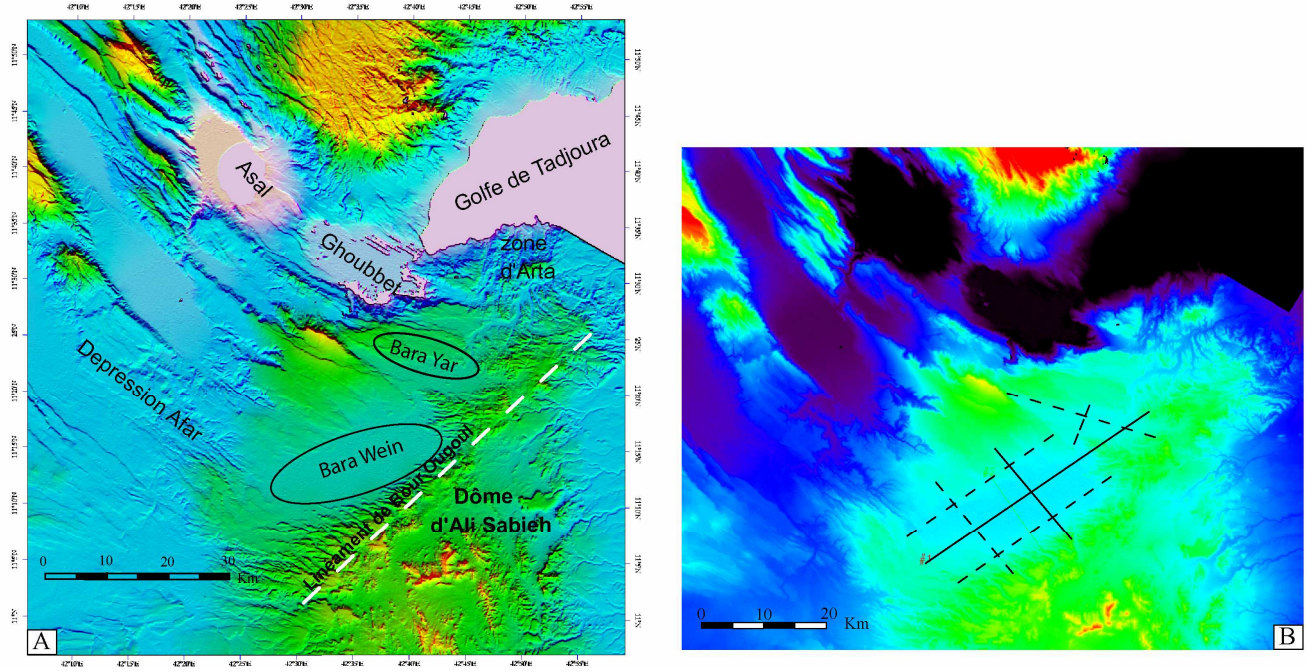

Figure 1: (A) MNT ombré de la zone de contact entre les domaines Asal et Ali Sabieh (données SRTM, résolution verticale de 16 m). On remarque l'organisation en échelon des dépressions (baras) le long de la bordure NW des reliefs d'Ali Sabieh. (B) MNT de la même zone montrant la trace des profils gravimétriques (pointillés) envisagés dans ce projet au niveau des 2 principaux baras (Weyn et Yar).

L'un des moyens de préciser la géométrie et la cinématique de cette zone de découplage, assimilable à une proto-transformante, est de vérifier si son fonctionnement s'est accompagné du développement de bassins sédimentaires, ce qui permettra d'estimer le caractère extensif

et/ou décrochant de cette structure ainsi que sa période d'activité. La géologie de surface, en particulier l'existence de trois dépressions sédimentées 'baras', de dimension 10 x 30 km pour la plus grande d'entre-elles, et disposées en échelon dextre le long de BOL (Figure 1), suggère la présence de bassins cachés dont la présence pourrait être vérifiée par le biais d'une approche couplée Gravimétrie-MagnétoTellurique, la MT permettant d'obtenir des images mieux contraintes que celles obtenues par gravimétrie. La gravimétrie a l'avantage quant à elle d'être de mise en œuvre rapide et relativement peu coûteuse et c'est donc la méthode idéale pour une première campagne de prospection dont l'objectif sera d'obtenir un premier modèle de distribution des densités en profondeur (de l'ordre de 10 km) à la verticale des baras. Les résultats escomptés devraient aussi permettre de mieux contraindre les modèles de rotation de blocs appliqués jusqu'à présent au dispositif Afar sur la base de données paléomagnétiques.

Les deux méthodes géophysiques complémentaires, effectives à l'UMR 6538 de Brest, consistent, dans un premier temps (année 2008), en enregistrements gravimétriques, puis, dans un deuxième temps (année 2009) et en fonction des résultats de l'approche gravimétrique, de prospections magnéto-telluriques.

L'approche gravimétrique consistera à enregistrer un certain nombre de profils au travers de chacun des baras retenus grâce à un gravimètre SCINTREX CG5. Avec une bonne topographie et des corrections précises (marées terrestres, dérive instrumentale, surcharge), la résolution peut atteindre de 10 à 20 mGal. Pour chacun des baras, nous réaliserons quatre profils gravimétriques selon (1) une direction parallélle à leur axe d'élongation (x 2, environ 20 km de long chacun) et (2) une direction perpendiculaire à l'axe (x 2, environ 15 km de long chacun) (Figure 1A). Cette approche nous permettra d'avoir une image 3D de la structure en profondeur. Sur chaque profil, les points d'enregistrement seront espacés de 500 m, ce qui permettra d'imager les structures avec une bonne résolution. Après acquisition et correction, les données seront modélisées afin d'obtenir une image 2D et 3D de la structure en profondeur des baras étudiés. Notre équipe dispose de différents codes de modélisation, soit par méthode directe, soit par méthode inverse.

Dans l'hypothèse où des anomalies négatives, susceptibles d'être associées à des remplissages sédimentaires en profondeur, seraient mises en évidence, il conviendrait alors de préciser la géométrie 3D des bassins correspondants en complétant l'approche géophysique par des enregistrements magnéto-telluriques, similaires à ceux réalisés au niveau de la Plaine de

Djibouti dans le cadre du Projet 'Nappe de Djibouti' (Responsable S. Hautot, IUEM). Ce second volet de notre projet de recherche ne sera réalisé qu'en 2009.

Projet B : Transformantes océaniques et héritage structural : la structure de Bia Anot (escarpement sud éthiopien).

Intervenants : MA Daoud, B. Le Gall, + un géologue éthiopien (à préciser).

Le modèle cinématique appliqué par Audin (1999) au rift Afar implique que la plupart des structures transformantes intra-océaniques (dextres), décalant l'axe d'accrétion du GA, se prolongent à terre le long d'accidents synrift (Figure 1). Si cette hypothèse est argumentée à propos de la faille Maskali et de son extension à terre le long de la structure transverse BOL (cf. Chapître 3), dont l'âge et la structure profonde restent toutefois à préciser (cf. Projet A), elle est beaucoup moins argumentée à propos du système Shukra El Sheik-Bia Anot (Figure 1). Cette hypothèse ne repose sur aucun argument structural, si ce n'est la reconnaissance cartographique d'une structure morphologique à terre dont le tracé prolonge au SW la transformante de SES. Il s'agit de la structure de Bia Anot qui recoupe (i) des terrains métamorphiques précambriens, (2) leur couverture jurassique (carbonates), et (3) des ensembles volcaniques mio-pliocènes, avant de se connecter vers l'W à l'escarpement somalien.

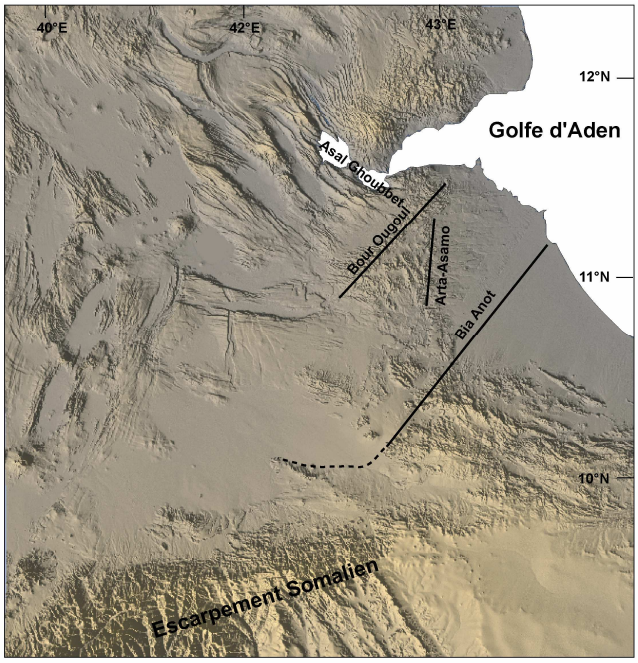

Figure 1 : MNT ombré montrant les accidents transverses BOL et Bia Anot ainsi que la discontnuité NS d'Arta-Asamo (données SRTM, résolution verticale de 16 m).

Ce modèle est envisageable, compte tenu de l'importance de la discontinuité océanique SES le long de laquelle la propagation de l'accrétion est restée bloquée pendant 13 Ma, de 17 à 4 Ma (Audin, 1999). On propose de tester sa validité par le biais d'une étude structurale détaillée du secteur situé au S d'Aisha, au N de l'escarpement somalien. Une première étape consistera à élaborer un schéma morphostructural précis à partir de l'interprétation d'images satelittales (ASTER et/ou SPOT), puis de réaliser, dans un deuxième temps, une étude structurale de terrain au niveau des éventuelles structures précédemment repérées. L'objectif sera (1) d'identifier des indices de déformation compatibles avec le fonctionnement d'accidents NE-SW à forte composante dextre, (2) de préciser si ceux-ci sont contrôlés par des structures pré-existantes, et (3) de contraindre la chronologie de ces déformations afin de vérifier si elle est compatible avec l'activité intra-miocène de la discontinuité SES, puis de la comparer avec celle de son équivalent plus 'interne' au N, cad. la BOL (Figure 1). L'une des implications de cette étude sera de vérifier si le domaine d'Ali Sabieh a subi une rotation et/ou une translation dextre au cours du Miocène

Projet C : Le complexe filonien (Miocène inférieur) d'Ali Sabieh : structure, géochimie, géochronologie, conditions de mise en place.

Intervenants : MA. Daoud et N. Moussa (CERD), JA. Barrat, C. Delacourt, B. Le Gall, P. Nonnotte (UBO-IUEM), Y. Fouquet (IFREMER), C. Aubourg (Cergy), H. Guillou (CEA Gif).

Le complexe filonien (acide-basique) recoupant, de façon spectaculaire, l'extrémité nord de l'antiforme d'Ali Sabieh (Figure 1) est, à notre connaissance, le plus important de l'ensemble du rift Afar. La distribution spatiale ainsi que la densité de ce complexe à travers les séquences effusives du Miocène inférieur et leur substratum sédimentaire mésozoïque sont relativement bien définies sur les documents cartographiques existants (Feuilles d'Ali Sabieh au 1 :100 000, Barrére et al., 1974 ; Gasse et al., 1985). Par contre, peu d'études structurales de détail leur ont été consacrées, probablement en raison du taux d'altération important de l'ensemble des séries occupant la dépression nord de l'antiforme.

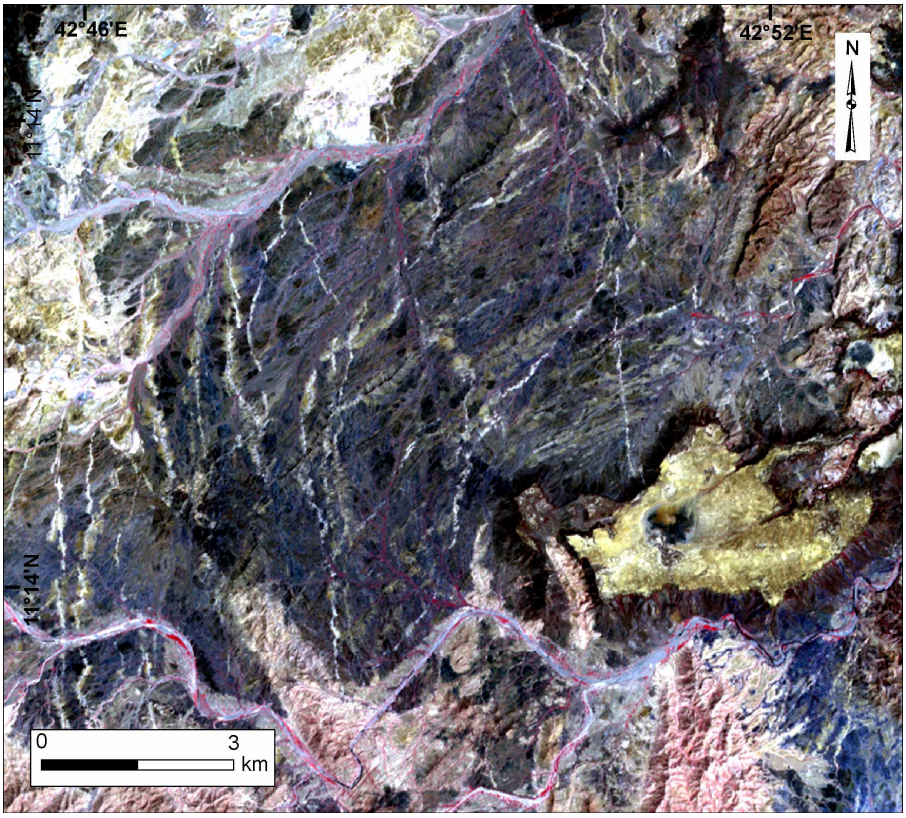

Figure 1 : Extrait de l'image ASTER (résolution latérale 15 m) à la verticale du complexe filonien d'Ali Sabieh.

Compte tenu de l'importance des complexes filoniens comme marqueurs tectoniques et magmatiques, il serait intéressant de préciser les principales caractéristique structurales, pétro-géochimiques et géochronologiques du complexe d'Ali Sabieh par une étude multi-disciplinaire.

- De récentes datations (K-Ar) ont fourni âge de 25 Ma pour un dyke basaltique, démontrant ainsi qu'une partie des intrusions basiques doit appartenir au complexe magmatique d'Ali Sabieh (Miocène inférieur) (cf. Chapître 4). Par contre, l'appartenance (probable) des filons acides à la série (plus jeune) des Mablas reste à confirmer. On propose donc de réaliser des datations systématiques de l'ensemble du complexe filonien (termes acides et basiques) par méthode K/Ar (H. Guillou), en fonction de l'état de fraicheur des roches. Cette approche sera couplée à l'analyse pétro-géochimique des filons correspondants.

- L'étude structurale de l'ensemble du complexe sera d'abord réalisée sur la base d'imagerie (ASTER) afin de préciser (i) la distribution spatiale des deux familles d'intrusions (acides et basiques), et (ii) la nature de leurs relations géométriques (et donc chronologiques). Les données cartographiques, complétées par des mesures structurales de terrain, permettront

aussi de quantifier les principaux paramètres géométriques des filons (longueur, épaisseur, espacement, ..).

- Le complexe filonien d'Ali Sabieh doit se situer à proximité d'une chambre magmatique en profondeur. L'étude des fabriques magnétiques, par l'Analyse de Susceptibité Magnétique (C. Aubourg), fournira des informations sur la direction et le sens d'écoulement du magma le long de chaque intrusion, ce qui permettra de préciser la position latérale ou verticale des sources magmatiques.

- La mise en place de complexes filoniens acides est généralement accompagnée d'importants processus hydrothermaux, à l'origine de cortèges minéralisés. Ces phénomènes s'expriment au niveau du compexe d'Ali Sabieh par de grandes zones d'altération, responsables pour partie de la topographie 'molle' de la région. D'un point de vue appliqué, il serait intéressant de cartographier ces zones d'altération, par divers traitements d'images satelittes, puis de dresser leur inventaire métallogénique. Cette étude devrait être entreprise dès la rentrée 2008-09 dans le cadre de la thèse de N. Moussa (UBO-IFREMER).

REFERENCES BIBLIOGRAPHIQUES

Acton, G. D., Stein, S. & Engeln, J. F. 1991. Block rotation and continental extensionin Afar: a microplate model for Afar. Tectonics 10, 501-526.

Acton, G. D., Tessema, A., Jackson, M. & Bilham, R. 2000. The tectonic and geomagnetic significance of paleomagnetic observations from volcanic rocks from central Afar, Africa. Earth. Planet. Sci. Lett.180(3-4), 225.

Al-Rousan, N. & Petrie, G. 1998. System calibration, geometric accuracy testing and validation of DEM and orthoimage data extracted from SPOT stereopairs using commercially available image processing systems. International Archives of Photogrammetry and Remote Sensing 32 (4), 8- 15.

Allègre, C. J., Treuil, M., Minster, J. F., Minster, B. & Albarède, F. 1977. Systematic use of trace element in igneous processes. Part 1: fractional crystallisation processes in volcanic suites. Contrib. Mineral. Petrol 60, 57-75.

Altherr, R., Henjes-Kunst, F., Puchelt, H. & Baumann, A. 1988. Volcanic activity in the Red Sea axial trough – evidence for a large mantle diapir? Tectonophysics 150, 121-133.

Altherr, R., Henjes-Kunst, F. & Baumann, A. 1990. Asthenosphere versus lithosphere as possible sources for basltic magma erupted during formation of the Red Sea: contraints from Sr, Pb and Nd isotopes. Earth. Planet. Sci. Lett.96, 269-286.

Angelier, J. 1975. Sur l'analyse de mesures recueillies dans des sites failles: l'utilité d'une confrontation entre les méthodes dynamiques et cinématiques. C.R.Acad. Paris, 281, 1805-1808.

Angelier, J. 1979. Determination of the mean principal stresses for a given fault population. Tectonophysics 56, 17–26.

Angelier, J. 1990. Inversion of field data in fault tectonics to obtain the regional stress-III. A new rapid direct inversion method by analytical means. Geoph. Jour. Int. 103, 363-376.

Angelier, J. 1994. Tectonic analysis of fault slip data sets. J. Geophys. Res.89, 5835-584.

Angelier, J. & Mechler, P. 1977. Sur une méthode graphique de recherche des contraintes principales également utilisable en tectonique et en sismologie: la méthode des dièdres droits. Bull. Soc. Géol. France 7, 1309-1318.

Angelier, J. & Goguel, J. 1979. Sur une méthode simple de détermination des axes principaux de contrainte pour une population de faille. C.R.A.S. 288, 307-310.

Arthaud, F. & Choukroune, P. 1976. Mise en évidence d'une phase de compression à 3,5 Ma séparant deux épisodes d'ouverture du rift océanique de Tadjoura (T.F.A.I.). C.R.A.S. 283, 13-16.

Arthaud, F., Choukroune, P. & Robineau, B. 1980a. Evolution structurale de la zone transformante d'Arta (République de Djibouti). Bull. Soc. Geol. Fr. XXII, 909-915.

Arthaud, F., Choukroune, P. & Robineau, B. 1980b. Tectonique, microtectonique et évolution structurale du golfe de Tadjoura et du Sud de la dépression Afar (Rép. de Djibouti). Bull. Soc. Geol. Fr. XXII, 901-908.

Audin, J., Vellutini, P. J., Coulon, C., Piguet, P. & Vincent, J. 1990. the 1928-1929 eruption of Kammourta volcano – evidence of tectono-magmatic activity in the Manda Inakir rift and comparison with the Asal Rift, Afar depression, Republic of Djibouti. Bull. Volc. 52, 551-561.

Audin, L. 1999. Pénétration de la dorsale d'Aden dans la dépression Afar entre 20 et 4 Ma. Unpublished Géologie et géophysique thesis, Université Paris 7 et Institut de Physique du Globe.

Audin, L., Manighetti, I., Tapponnier, P., Metivier, F., Jacques, E. & Huchon, P. 2001. Fault propagation and climatic control of sedimentation on the Ghoubbet Rift Floor: insights from the Tadjouraden cruise in the western Gulf of Aden. Geophys. J. Int. 144, 1-28.

Audin, L., Quidelleur, X., Coulie, E., Courtillot, V., Gilder, S., Manighetti, I., Gillot, P.-Y., Tapponnier, P. & Kidane, T. 2004. Paleomagnetism and K-Ar and 40Ar/39Ar ages in the Ali Sabieh area (Republic of Djiboutiand Ethiopia): constraints on the mechanism of Aden ridge propagation into southeastern Afar during the last 10 Myr. Geophys. J. Int. 158(1), 327-345.

Bai, T. & Pollard, D. D. 2000. Fracture spacing in layered rocks: a new explanation based on the stress transition. J. Struct. Geol.(22), 43-57.

Baker, J., Snee, L. & Menzies, M. 1996a. A brief Oligocene period of flood volcanism in Yemen: implications for the duration and rate of continental flood volcanism at the Afro-Arabian triple junction. Earth. Planet. Sci. Lett.138(1-4), 39.

Baker, J. A., Thirlwall, M. F. & Menzies, M. A. 1996b. Sr-Nd-Pb isotopic and trace element evidence for crustal contamination of plume-derived flood basalts: Oligocene flood volcanism in Western Yemen. Geochim. Cosmochim. Acta 60, 2559-2581.

Baker J., Chazot G., Menzies M., & Thirlwall M. 1998. Metasomatism of the shallow mantle beneath Yemen by the Afar plume-Implications for mantle plumes, flood volcanism, and intraplate volcanism. Geology 26, 5, 431-434.

Barberi, F., Borsi, S., Ferrara, G., Marinelli, G. & Varet, J. 1970. Relationships between tectonics and magmtology of the northern Afar (or Danakil depression). Sym. Roy. Soc. London, mars 1969, Phil. Trans. R. Soc. London 267, 293-311.

Barberi, F., Borsi, S., Ferrara, G., Marinelli, G., Santacroce, R., Tazieff, H. & Varet, J. 1972a. evolution of the Danakil Depression (Afar, Ethiopia) in light of the radiometric age determination. J. Géol. 80, 720-729.

Barberi, F., Tazieff, H. & Varet, J. 1972b. Volcanism of the Afar Depression: its tectonic and magmatic significance. Tectonophysics. 15, 19-29.

Barberi, F., Bonatti, E., Marinelli, G. & Varet, J. 1974. Transverse tectonics during the split of a continent: Data from the Afar rift. Tectonophysics. 23(1-2), 17.

Barberi, F., Ferrara, G., Santacroce, R. & Varet, J. 1975. Structural evolution of the Afar triple junction. In: Pilger, A., Rösler, A. (Eds.) Depression of Ethiopia. Schweizerbart, Stuttgart 1, 38-54.

Barberi, F. & Varet, J. 1977. Volcanism in Afar, small scale plate tectonics implications. Geol. Soc. Am. 88, 1251-1266.

Barrat, J. A., Jahn, B. M., Joron, J. L., Auvray, B. & Hamd, H. 1990a. Mantle heterogeneity in northeastern Africa: evidence from Nd isotopic compositions and hygromagmaphile element geochemistry of basaltic rocks from the Gulf of Tadjoura and Southern Red Sea regions. Earth. Planet. Sci. Lett. 101, 233-247.

Barrat, J. A., Jahn, B. M., Fourcade, S. & J.L., J. 1993a. Magma genesis in an ongoing rifting zone: the Tadjoura Gulf. Geochim. Cosmochim. Acta. 57, 2291-2302.

Barrat, J. A., Keller, F., Amossé, J., Taylor, R. N., Nesbitt, R. W. & Hirata, T. 1996. Determination of rare earth elements in sixteen silicate reference samples by ICP-MS after Tm addition and ion exchange separation. Geostandards Newsletter. 20, 133-139.

Barrat J.A., Fourcade S., Jahn B.M., Cheminée J.L., & Capdevila R. 1998. Isotope (Sr, Nd, Pb, O) and trace-element geochemistry of volcanics from the Erta'Ale range (Ethiopia). J. Volcanol. Geotherm. Res. 80, 85-100.

Barrat J.A., Blichert-Toft J., Gillet Ph., & Keller F. 2000. The differentiation of eucrites: the role of *in-situ* crystallization. Meteoritics Planet. Sci. 35, 1087-1100.

Barrat, J. A., Joron, J. L., Taylor, R. N., Fourcade, S., Nesbitt, R. W. & Jahn, B. M. 2003. Geochemistry of basalts from Manda Hararo, Ethiopia: LREE-depleted basalts in Central Afar. Lithos. 69, 1-13.

Barrat J.A., Jambon A., Bohn M., Blichert-Toft J., Sautter V., Göpel C., Gillet Ph., Boudouma O., & Keller F. 2003. Petrology and geochemistry of the unbrecciatted achondrite North West Africa 1240 (NWA 1240): an HED parent body impact melt. Geochim. Cosmochim. Acta. 67, 3959-3970.

Barrat J.A., Yamaguchi A., Greenwood A., Bohn M., Cotten J., Benoit M., & Franchi I.A. 2007. The Stannern trend eucrites: contamination of main group eucritic magmas by crustal partial melts. Geochim. Cosmochim. Acta. 71, 4108-4124.

Barrère, P., Boucarut, M., Clin, M., Moussie, C., Pouchan, P., Thibault, C. & Weidmann, M. 1975. Carte géologique du Territoire Français des Afars et des Issas au 1:100 000. Feuille Ali Sabieh. Bordeaux-Djibouti. Université de Bordeaux III.

Bellahsen, N., Fournier, M., d'Acremont, E., Leroy, S. & Daniel, M. 2006. Fault reactivation and rift localisation: Northeastern Gulf of Aden margin. Tectonics. 25, doi:1029/2004TC001626.

Benedicto, A., Schultz, R. A. & Solivia, R. 2003. Layer thickness and the shape of faults. Geophys. Res. Lett. 30(20), doi:10.1029/2003GL018237(2076).

Best, M. G. 2003. Igneous and metamorphic petrology. Blackwell Science, Oxford. 722p.

Betton, P. J. & Civetta, L. 1984. Strontium and neodymium isotopic evidence for the heterogeneous nature and development of the mantle beneath Afar (Ethiopia). Earth. Planet. Sci. Lett. 71, 59-70.

Beyth, M. 1991. Smooth and rough propagation of spreading Southern Red Sea - Afar depression. J. Afr. Earth. Sci. 13, 157-171.

Bizouard, H. & Richard, O. 1980. Etude de la transition dorsale océanique rift émergé: golfe de Tadjoura, Asal, Afar central. Approche pétrographique et minéralogique. Bull. Soc. Geol. Fr.VII série. 22, 935-943.

Black, R., Morton, W. & Rex, D. C. 1975. Block tilting and volcanism within the Afar in light of recent K/Ar date. In: Pilger, A., Rösler, A. (Eds.) Depression of Ethiopia. Schweizerbart, Stuttgart. 1, 296-299.

Black, R., Morton, W. & Varet, J. 1972. New data on Afar tectonics. Nature Phys. Sci. 240, 172-173.

Blichert-Toft, J. & White, W. M. 2001. Hf isotope geochemistry of the Galapagos Islands. Geochem. Geophys. Geosyst. 2, doi:10.129/2000GC000138.

Boccaletti, M., Getane, A. & Bonavia, F. 1991. Jour. of Pet. 14, 79-92.

Bohannon, R. G. 1989. Style of extensional tectonism during rifting, Red Sea and Gulf of Aden. J. Afr. Earth. Sci. 8(2-4), 589.

Bosworth, W., Philippe, H. & McClay, K. 2005. The Red Sea and Gulf of Aden Basin. J. Afr. Earth. Sci. 43, 334-378.

Bott, M. H. 1959. The mechanism of oblique slip faulting. Geol. Mag. 96, 109-117.

Boucarut, M., Chessex, R. & Clin, M. 1980. Données géochronologiques k-Ar de roches de l'Afar, partie Nord de la République de Djibouti. Schweiz. Mineral. Petrogr. Mitt. 60, 263-269.

Callot, J. P., Grigne, C., Geoffroy, L. & Brun, J. P. 2001. Development of volcanic margins: two-dimensional laboratory models. Tectonics. 20, 148-159.

Cande, S. C. & Kent, D. V. 1992. A New Geomagnetic Polarity Time Scale For The Late Cretaceous And Cenozoic. J. Geophys. Res.-Solid Earth. 97(B10), 13917-13951.

Cande, S. C. & Kent, D. V. 1995. Revised Calibration Of The Geomagnetic Polarity Timescale For The Late Cretaceous And Cenozoic. J. Geophys. Res.-Solid Earth. 100(B4), 6093-6095.

Cartwright, J. A., Trudgill, B. D. & Mansfield, C. 1995. Fault growth by segment linkage: an explanation for scatter in maximum displacement and trace length data from the Canyonlands Grabens of SE Utah. J. Struct. Geol. 17(9), 1219-1326.

Cartwright, J. A., Trudgill, B. D. & Mansfield, C. 2000. Fault growth by segment linkage: an explanation for scatter in maximum displacement And trace length data from the Canyonlands grabens of SE Utah: Reply. J. Struct. Geol. (22), 141-143.

Cassignol, C., David, B. & Gillot, P. Y. 1978. Technologie potassium-argon, C.E.N., Saclay. Rapp. CEA R-4802, pp 37.

Cassignol, C. & Gillot, P. Y. 1982. Range and effectiveness of unspiked potassium-argon dating: experimental groundwork and applications. In: G.S. Odin (Ed.), Numerical dating in stratigraphy, John Wiley & Sons, Chichester. 159-179.

Cerling, T. E. & Powers, D. W. 1977. Paleorifting between the Gregory and Ethiopian rifts. Geology. 5, 441-444.

Charbit, S., Guillou, H. & Turpin, L. 1998. Cross calibration of K-Ar standard minerals using an unspiked Ar measurement technique. Chem. Geol., 150, 147-159.

Chauvel, C. & Blichert-Toft, J. 2001. A hafnium isotope and trace element perspective on melting of the depleted mantle. Earth. Planet. Sci. Lett. 190, 137-151.

Chauvel, C., Hémond, C. 2000. Melting of a complete section of recycled oceanic crust: trace element and Pb isotopic evidence from Iceland. Geochem. Geophys. Geosyst. 1, paper, 1999GC000002.

Chazot, G. & Bertrand, H. 1993. Mantle sources and magma-continental crust interactions during early Red Sea-Gulf of Aden rifting in Southern Yemen: elemental and Sr, Nd, Pb isotope evidence. J. Geophys. Res. 98, 1819-1835.

Chen, C. Y. & Frey, F. A. 1985. Trace element and isotope geochemistry of lavas from Halaakala Volcano, East Maui: implications for the origin of Hawaiian basalts. J. Geophys. Res. 90, 8743-8768.

Chessex, R., Delaloye, M. & Fontignie, D. 1979. K-Ar datation on volcanic rocks of the Republic of Djibouti. Geodynamic evolution of the Afro-Arabian rift system. Int. Symp. Rome. 18-20 avril.

Chessex, R., Delaloye, M., Muller, J. & Weidmann, M. 1975a. Evolution of the volcanic region of Ali-Sabieh (T.F.A.I) in the light of K/Ar age determinations. In: Pilger, A., Rösler, A. (Eds.) Depression of Ethiopia. Schweizerbart, Stuttgart. 1, 220-227.

Chessex, R., Delaloye, M., Muller, J. & Weidmann, M. 1975b. K-Ar datations on volcanic rocks of the Republic of Djibouti. Geodynamic evolution of the Afro-Arabian rift system Intern. Symp, Rome. 18-20 avril.

Clayton, R. N. & Mayeda, T. K. 1963. The use of bromine pentafluoride in the extraction of oxygen from oxides and silicates for isotope analysis. Geochim. Cosmochim. Acta. 27, 43-52.

Clifton, E. A., Schlische, R. W., Withjack, M. O. & Ackermann, R. V. 2000. Influence of rift obliquity on fault-population systematics: results of experimental clay models. J. Struct. Geol. 22, 1491-1509.

Clin, M. 1991. Evolution of Eastern Afar and the Gulf of Tadjura. Tectonophysics. 198(2-4), 355.

Clin, M. & Pouchan, P. 1970. Carte géologique du territoire Français des Afars et des Issas 1/200 000. C.E.G.D.

Collet, B., Taud, H., Parrot, J. F., Bonavia, F. & Chorowicz, J. 2000. A new kinematic approach for the Danakil block using a Digital Elevation Model representation. Tectonophysics. 316(3-4), 343.

Corti, G., Bonini, M., Conticelli, S., Innocenti, F., Manetti, P. & Sokoutis, D. 2003. Analogue modelling of continental extension: a review focused on the relations between the patterns of deformation and the presence of magma. Earth. Planet. Sci. Lett. 63, 169-247.

Cotten, J., Le Dez, A., Bau, M., Caroff, M., Maury, R., Dulski, P., Fourcade, S., Bohn, M. & Brousse, R. 1995. Origin of anomalous rare-earth element and yttrium enrichments in subaerially exposed basalts: Evidence from French Polynesia. Chem. Geol. 119, 15-138.

Coulie, E., Quidelleur, X., Gillot, P. Y., Courtillot, V., Lefevre, J. C. & Chiesa, S. 2003. Comparative K-Ar and Ar/Ar dating of Ethiopian and Yemenite Oligocene volcanism: implications for timing and duration of the Ethiopian traps. Earth. Planet. Sci. Lett. 206(3-4), 477.

Courtillot, V., Galdeano, A.,& Le Mouel, J. L. 1980. Propagation of an accreting plate boundary: a discussion of new magnetic data in the Gulf of Tadjoura and Southern Afar. Earth Planet. Sci. Lett. 47, 144-160.

Courtillot, V., Achache, J., Landre, F., Bonhommet, N., Montigny, R. & Féraud, G. 1984. Episodic spreading and rift propagation: new paleomagnetic and geochronologic data from the Afar nascent passive margin. J. Geophys. Res. 89(B5), 3315-3333.

Courtillot, V., Jaupart, C., Manighetti, I., Tapponier, P. & Besse, J. 1999. On causal links betwen flood basalts and continental breakup. Earth. Planet. Sci. Lett. 166, 177-199.

Courtillot, V., Davaille, A., Besse, J., & Stock, J. 2003. Three different types of hotspots in the Earth's mantle. Earth Planet. Sci. Lett. 205, 295-308.

Cowie, P. A., John, T., R. Underhill, R., Behn, M. D., Linc, J. & Gill, C. E. 2005. Spatio-temporal evolution of strain accumulation derived from multi-scale observations of Late Jurassic rifting in the northern North Sea: A critical test of models for lithospheric extension. Earth. Planet. Sci. Lett. 234, 401-419.

Cowie, P. A. & Scholz, C. H. 1992a. Growth of faults by accumulation of seismic slip. J. Geophys. Res. 97, 11085-11096.

Cowie, P. A. & Scholz, C. H. 1992b. Physical explanation for displacement-length relationship for faults using a post-yield fracture mechanics model. J. of Struc. Geol. 14, 1133-1148.

Cox, A. & Dalrymple, G. B. 1967. Statistical analysis of geomagnetic reversal data and the precision of potassium-argon dating. J. Geophys. Res. 72, 2603-2614.

Crossley, R., Watkins, C., Raven, M., Cripps, D., Carnell, A. & Williams, D. 1992. The sedimentary evolution of the Red Sea and Gulf of Aden. J. Petrol. 15, 157-172.

Daoud, M. A., Barrat, J.-A., Maury, R. C., Taylor, R. N., Le Gall, B., Guillou, H., Cotten, J. & Rolet, J. 2008. (in prep.) Occurrence of a LREE-depleted component in the Afar plume: further evidence from Djibouti. Lithos.

Dawers, N. H., Anders, M. H. & Schloz, C. H. 1993. Fault length and displacement: scaling laws. Geology. 21, 1107-1110.

De Chabelier, J. B. & Avouac, J. P. 1994. Kinematics of the Asal rift (Djibouti) determined from the deformation of Fieale volcano. Science. 265, 1677-1681.

Defant, M. J., Maury, R. C., Ripley, E. M., Feigenson, M. D. & Jacques, D. 1991. An example of island-arc petrogenesis: geochemistry and petrology of the southern Luzon arc, Philippines. J. Petrol. 32, 455-500.

Deniel, C., Vidal, P., Coulon, C., Vellutini, P. J. & Piguet, P. 1994. Temporal evolution of mantle sources during continental rifting: the volcanism of Djibouti (Afar). J. Geophys. Res.99, 2853-2869.

Dixion, J. M. & Simpson, D. G. 1987. Centrifuge modelling of the laccolith intrusion. J. Struct. Geol. 9, 87-103.

Dixon, T. H., Ivin, E. R. & Franklin, B. J. 1989. Topographic and volcanic asymmetry around the Red Sea; constraints on rift models. Tectonics. 8, 11983-1216.

Doubre, C. 2004. Structure et mécanismes des segments de rifts volcano-tectoniques; études de rifts anciens (Ecosse et Islande) et d'un rift actif (Asal-Ghoubbet). Unpublished PhD thesis, Université du Maine.

Doubre, C., Manighetti, I., Dorbath, C., Dorbath, L., Jacques, E. & Delmond, J. C. 2007. Crustal structure and magmato-tectonic processes in an active rift (Asal-Ghoubbet, Afar, East Africa):1. Insights from a 5-month seismological experiment. J. Geoph. Res. 112, (B05405), doi:10.129/2005JB003940.

Dreyfuss, M. 1932. Etude de géologie et de géographie physique sur la côte française des Somalis. Rev. Géogr. Phys. et Géol. Fr 7, 87-88.

Drury, S. A., Kelley, S. P., Berhe, S. M., Collier, R. E. & Abraha, M. 1994. Structures related to Red Sea evolution in the northern Eritrea. Tectonics. 13, 1371-1380.

Eagles, G., Gloaguen, R. & Ebinger, C. 2002. Kinematics of the Danakil microplate. Earth. Planet. Sci. Lett. 203(2), 607-620.

Eissen, T., Juteau, J., Joron, J. L., Dupré, B., Humler, E. & Al'Mukhamedov, A. 1989. Petrology and geochemistry of basalts from Red Sea axial rif at 18° North. J. Petrol. 30, 791-839.

Etchecopar, A. 1981. An inverse problem in microtectonics for the determination of stress tensor from fault striation analysis. J. Struct. Geol. 3, 51-65.

Evans, A. L. 1988. Neogene tectonic and stratigraphic events in the Gulf of Suez rift area, Egypt. Tectonophysics. 153(1-4), 235.

Evensen, N. M., Hamilton, P. J. & O'Nions, R. K. 1978. Rare Earth abundances in chondritic meteorites. Geochim. Cosmochim. Acta. 42, 1199-1212.

Faccenna, C., Nalpas, T., Brun, J. P. & Davy, P. 1995. The influence of pre-existing thrust faults on normal fault geometry in nature and in experiments. J. Struct. Geol. 17(8), 1139-1149.

Fitton, J. G., Saunders, A. D., Noory, B. S., Hardason, B. S. & Taylor, R. N. 1997. Thermal and chemical structure of the Iceland plume. Earth. Planet. Sci. Lett. 153, 197-208.

Fitton, J. G., Saunders, A. D., Kempton, P. D. & Hardason, B. S. 2003. Does depleted mantle form an intrinsic part of the Iceland plume? Geochem. Geophys. Geosystem. 4, 2002GC000424.

Fournier, M., Gasse, F., Lépine, J.-C., Richard, O. & Ruegg, J. C. 1982. Carte géologique de la République de Djibouti à 1:100 000. Djibouti. ISERST. Ministère français de Coopération, Paris.

Francis, E. H. 1982. Magma and sediment-I. Emplacement mechanism of late Carboniferous tholeiite sills in the northern Britain. J. Geol. Soc. Lonon. 139, 1-20.

Frey, F. A., Huang, S., Blichert-Toft, J., Regelous, M. & Boyet, M. 2005. Origin of depleted components in basalt related to the Hawaiian hot spot: Evidence from isotopic and incompatible element ratios. Geochem. Geophys. Geosystem. 6, Q02L07, doi:10.129/2004GC000757.

Fuhrmann, U., Lippolt, H. & Hess, J. C. 1987. HD-B1 Biotite reference material for K-Ar chronometry. Chemical Geology. 66, 41-51.

Furman, T., Bryce, J., Rooney, T., Hana, B., Yirgu, G. & Ayalew, D. 2006. Heads and tails: 30 million years of the Afar plume. In: Yirgu, G., Ebinger, C.J., & Maguire, P.K.H. (Eds.), The Afar volcanic province within the East African Rift System. Geol. Soc. London, Sp. Pub. 259, 95-119.

Gadalia, A. 1980. Les rhyolitess du stade initial de l'ouverture d'un rift: exemple des rhyolites miocènes de l'Afar. Unpublished thesis, Universuté d'Orsay.

Galland, O. 2004. Intéractions mécanques entre la téctonique compressive et le magmatisme: expéreinces analogiques et exemple naturel. Unpublished thesis, Université de Rennes I.

Garfunkel, Z. & Beyth, M. 2006. Part 1: Plate kinematic and geodynamic framework of the Afar volcanic province. Constraints on the structural development of Afar imposed by the kinematics of the major surrounding plates. Geol. Soc. London. Spec. Pub. 259, 23-42.

Gass, J. G. 1970. Evolution of volcanism in the junction area of the Red Sea, Gulf of Aden and Ethiopian rifts. Philos. Trans. R. Soc. London 267A, 369-381.

Gasse, F. 1991. Tectonic and climatic controls on lake distribution and environments in Afar from Miocene to present, In Lacustrine Basin Exploration: Case studies and Modern Analogs, edited by B. Katz. AAPG Mem. 50, 19-41.

Gasse, F., Fournier, M. & Richard, O. 1983. Carte géologique de la République de Djibouti à 1:100 000. Djibouti. Notice explicative. ISERST, Ministère français de la Coopération, Paris.

Gasse, F., Fournier, M., Richard, O. & J.C., R. 1985. Carte géologique de la République de Djibouti à 1:100 000. Tadjoura. Notice explicative. ISERST, Ministère français de la Coopération, Paris.

Gasse, F., Varet, J., Mazet, G., Recroix, F. & Ruegg, J. C. 1986. Carte géologique de la République de Djibouti à 1:100 000. Ali Sabieh. Notice explicative. ISERST, Ministère français de la Coopération, Paris.

Gasse, F., Dagain, J., Mazet, G., Richard, O. & Fournier, M. 1987. Carte géologique de la République de Djibouti à 1:100 000. Dikhil. Notice explicative. ISERST, Ministère français de la Coopération, Paris.

Gaulier, J. M. & Huchon, P. 1991. Tectonic evolution of Afar triple junction. Bull. Soc. Geol. Fr. 162(VIII), 451-464.

Gee, M. A. M., Thirlwall, M. F., Taylor, R. N., Lowry, D. & Murton, B. J. 1998. Crustal processes: Major controls on Reykjanes Peninsula lava chemistry, SW Iceland. J. Petrol. 39, 819-839.

George, R., Rogers, N. & Kelley, S. 1998. Earliest magmatism in Ethiopia; evidence for two mantle plumes in one flood basalt province. Geology. 26(10), 923-926.

Gephart, J. W. 1990. FMSI: A fortran program for inverting fault/ slickenside and earthquake focal mechanism data to obtain the regional stress tensor. Computer and Geosciences. 16, 953-989.

Gilllespie, P. A., Walsh, J. J. & Wetterson, J. 1992. Limitation of dimension and displacement data from single fault and the consequences for data analysis and interpretation. J. Struct. Geol. 14, 1157-1172.

Gillot, P. Y. & Cornette, Y. 1986. The Cassignol technique for potassium argon dating, precision and accuracy: examples from the late Pleistocene to recent volcanics from southern Italy. Chem. Geol. 59, 205-222.

Grove, T. L. & Bryan, W. B. 1983. Fractionation of pyroxene-phyric MORB at low pressure: an experiemental stydy. Contrib. Mineral. Petrol. 84, 293-309.

Guillou, H. 2001. Contribution de la Géochronologie K-Ar à la calibration de l'échelle des temps géologiques et à la datation des variations climatiques récentes. Application à l'étude du volcanisme de point chaud, Mémoire HDR, Univerisité de Bretagne Occidentale, Brest.

Guillou, H., Singer, B. S., Laj, C., Kissel, C., Scaillet, S. & Jicha, B. R. 2004. On the age of the Laschamp geomagnetic excursion. Earth. Planet. Sci. Lett. 227(3-4), 331.

Gupta, A. & Scholz, C. 2000. Brittle strain regime transition in the Afar depression: Implications for fault growth and seafloor spreading. Geology. 1087-1090.

Gurenko, A. A. & Chaussidon, M. 1995. Enriched and depleted primitive melts included in olivine from Icelandic tholeiites: origin by continuous melting of a single mantle column. Geochim. Cosmochim. Acta. 59, 2905-2917.

Hart, S. R. 1988. Heterogeneous mantle domains: signatures, genesis and mixing chronologies. Earth. Planet. Sci. Lett. 90, 273-296.

Hart, S. R., Hauri, E. H., Oschmann, L. A. & Whitehead, J. A. 1992. Mantle plumes and entrainment: isotopic evidence. Science 256, 517-520.

Hart, W. K., Woldegabriel, G., Walter, R. C. & Mertzman, S. A. 1989. Basaltic volcanism in Ethiopia: constraints on continental rifting and mantle interactions. J. Geophys. Res. 94, 7731-7748.

Hase, K. M., Mühe, R. & Stoffers, P. 2000. Magmatism during extension of the lithosphere: geochemical constraints from lavas of the Shaban Deep, northern Red Sea. Chem. Geol. 166, 225-239.

Hegner, E. & Pallister, J. S. 1989. Pb, Sr and Nd isotopic characteristics of Tertiary Red Sea Rift volcanics from the central Sausi Arabian coastal plain. J. Geophys. Res. 94, 7749-7755.

Hémond, C., Arndt, N. T., Lichtenstein, U. & Hofmann, A. 1993. The heterogeneous Iceland plume: Nd-Sr-O isotopes and trace element constraints. J. Geophys. Res. 98, 15803-15850.

Hempton, M. R. 1987. Constraints on Arabian plate motion and extensional history of the Red Sea. Tectonics. 6, 687-705.

Hirano, A., Welch, R. & Lang, H. 2003. Mapping from ASTER stereo image data: DEM validation and accuracy assessment. ISPRS Journal of Photogrammetry & Remote Sensing. 57, 356-370.

Hoernle, K., Werner, R., Phipps-Morgan, J., Garbe-Schönberg, D., Bryce, J. & Mrazek, J. 2000. Existence of complex spatial zonation in the Galapagos plume for at least 14 m. y. Geology. 28, 435-438.

Hofmann, A. W. 1988. Chemical differentiation of the Earth: the relationship between mantle, continental crust and oceanic crust. Earth. Planet. Sci. Lett. 90, 297-314.

Hofmann, C., Courtillot, V., Feraud, G., Rochette, P., Yirgu, G., Ketefo, E. & Pik, R. 1997. Timing of the Ethiopian flood basalt event and implications for plume birth and global change. Nature. 389, 338-341.

Hofstetter, R. & Beyth, M. 2003. The Afar Depression: interpretation of the 1960-2000 earthquakes. Geophys. J. Int. 155(2), 715-732.

Huchon, P., Jestin, F., Cantagrel, J. M., Gaulier, J. M., Khirbash, S. A. & Gafaneh, A. 1991. Extensional deformations in Yemen since Oligocene and the Afar triple junction. Annales Tectonicae. 5, 141-163.

Hutchinson, R. W. & Engels, G. G. 1970. Tectonic significance of regional geology and evaporite lithofacies in northeastern Ethiopia. Bull. AAPG. 57, 741-745.

Huton, D. H. W. 1996. Syntectonic granites and the principales of effectives stress: a general solution of the space problem? In: J.L Bouchez, D.H.W & W.E. Stephens (Eds), Granite: From segregation melt to emplacement fabrics. Kluwer Adecmic Publishers, Netherland, 189-197.

Irvine, T. N. 1979. Rocks composition is determinted by crystal accumulation and sorting. In Yoder, H.S., Jr (Ed.), The evolution of the Igneous Rocks: 15th Anniv. Perspectives. Princeton University Press, Princeton, N.J., 245-306.

Irvine, T. N. & Baragar, W. R. A. 1971. A guide to the chemical classification of the common rocks. Can. Journ. Sci. 8, 523-548.

Ito, E., White, W. M. & Göpel, C. 1987. The O, Sr, Nd, and Pb isotope geochemistry of MORB. Chem. Geol. 62, 157-176.

Jackson, M. & Pollard, D. D. 1990. Flexure and faulting of sedimentary host rocks during growth of igneous domes, Henry Mountains, Utah. J. Struct. Geol. 12, 185-205.

Jestin, F. & Huchon, P. 1992. Cinématique et déformation de la jonction triple Mer Rouge-Golfe d'Aden-Rift Ethiopien depuis l'Oligocène. Bull. Soc. Geol. Fr.VIII série. 163, 125-133.

Joron, J. L., Treuil, M., Jaffrezic, H. & Villemant, B. 1980b. Etude géochimique des éléments en traces dans les séries de roches volcaniques du rift d'Asal. Identification et analyse des processus d'accrétion. Bull. Soc. Geol. Fr.VII série. 22, 851-861.

Joron, J. L., Treuil, M., Jaffrezic, H., Villemant, B. & Richard, O. 1980a. Géochimie des éléments en traces du volcanisme de l'Afar et de la mégastructure Mer Rouge-Afar-Golfe d'Aden. Implications pétrogénétiques et géodynamiques. Bull. Soc. Geol. Fr.VII série. 22, 945-957.

Kieffer, B., Arndt, N. T., Lapierre, H., Bastien, F., Bosh, D., Pecher, A., Yirgu, G., Ayalew, D., Weis, D., Jerram, D., Keller, F. & Meugniot, C. 2004. Flood and shield basalts from Ethiopia: magma from the African superswell. J. Petrol. 45, 793-834.

Kokfelt, T. F., Hoernle, K., Hauf, F., Fiebig, J., Werner, R. & Garbe-Schomberg, D. 2006. Combined trace element and Pb-Nd-Sr-O isotope evidence for recycled oceanic crust(upper and lower) in the Iceland mantle plume. J. Petrol. 47, 1705-1749.

Krantz, R. W. 1995. The transpressional strain model applied to strike-slip, oblique-convergent and oblique-divergent deformation. J. Struct. Geol. 17(8), 1125-1137.

Lahitte, P., Coulie, E., Mercier, N., Kidane, T. & Gillot, P.-Y. 2001. Chronologie K-Ar et TL du volcanisme aux extremites sud du propagateur mer Rouge en Afar depuis 300 ka. C.R.A.S- Series IIA – Earth. Planet. Sci. 332(1), 13.

Lahitte, P., Gillot, P.-Y. & Courtillot, V. 2003. Silicic central volcanoes as precursors to rift propagation: the Afar case. Earth. Planet. Sci. Lett. 207(1-4), 103.

Le Bas, M., Le Maitre, R., Streckeisen, A. & Zanettin, B. 1986. A chemical classification of volcanics rocks based on total alkalin-silica diagram. J. Petrol. 27,3, 745-750.

Le Pichon, X. & Francheteau, J. 1978. A plate-tectonic analysis of the Red Sea--Gulf of Aden Area. Tectonophysics. 46(3-4), 369.

Lépine, J. C. & J.C., Ruegg. 1976. La sismicité du T.F.A.I. Bull. Soc. Geol. Fr. XVIII, 4(XVIII). 846-851.

Lépine, J. C., J.C., Ruegg & Anis, A. M. 1980. Sismicité du rift d'Asal-Ghoubbet pendant la crise sismo-volcanique de novembre 1978. Bull. Soc. Geol. Fr.XXII. 6, 809-816.

Lépine, J. C. & Hirn, A. 1992. Seismotectonics in the republic of Djibouti, linking the Afar Depression and the Gulf of Aden. Tectonophysics. 209, 65-86.

Leroy, S. & al. 2004. From rifting to drifting in the eastern Gulf of Aden: A complete margin survey coverage of a young oceanic basin from margin to margin. Terra Nova. 16, 185-192.

Leterrier, J., Maury, R., Thonon, P., Girard, D. & Marchal, M. 1982. Clinopyroxene composition as a method of identification of magmatic affinities of paleo-volcanic series. Earth. Planet. Sci. Lett. 59, 139-154.

Lin, S. S. & Keken, P. E. 2006. Dynamics of thermochemical plumes: 2. Complexity of plume structures and its implications for mapping mantle plumes. Geochem. Geophys. Geosyst. 7, Q033003, doi:10.129/2005GC001072.

Mahood, G. A. & R.E., Drake. 1982. K-Ar dating young rhyolitic roks: A case study of the Sierra La Primavera, Jalisisco, Mexico. Geol. Soc. Am. Bull. 93, 1232-1241.

Manighetti, I. 1993. Dynamique des systèmes extensifs en Afar. Unpublished Géologie et Géophysique thesis, Université Paris 6.

Manighetti, I., P., T., Courtillot, V., Gruszow, S. & Gillot., P.-Y. 1997. Propagation of rifting along the Arabia-Somalia plate boundary: the Gulfs of Aden and Tadjoura. J. Geophys. Res. 102, 2681-2710.

Manighetti, I., Tapponier, P., Gillot, P.-Y., Jacques, E., Courtillot, V., Armijo, R., J.C., Ruegg & King, G. 1998. Propagation of rifting along the Arabia-Somalia plate boundary: into Afar. J. Geophys. Res. 103, 4947-4974.

Manighetti, I., Scholz, C. & Doubre, C. 2001. Slip accumulation and lateral propagation of active normal faults in Afar. J. Geophys. Res. 13, 667-696.

Mansfield, C. & Cartwright, J. A. 1996. High resolution fault displacement mapping from three-dimensional seismic data: Evidence for dip linkage during fault growth. J. Struct. Geol. 18, 249-263.

Marinelli, G. & Varet, J. 1973. Strcuture et évolution du Sud "Horst Danakil". C. R. Ac. Sc. Paris. 276, 1119-1122.

Marrett, R. & Allmendinger, R. W. 1992. Amount of extension on "small" faults: an example from the Viking grabben. Geology. 20, 47-50.

Marty, B., Appora, I., Barrat, J. A., Deniel, C., Vellutini, P. & Vidal, P. 1993. He, Ar, Sr, Nd, and Pb isotopes in volcanic rocks from Afar: evidence for a primitive mantle component and constraints on magmatic sources. Geochem. Journal. 27, 219-228.

Marty, B., Pik, R. & Gezahegn, Y. 1996. Helium isotopic variations in Ethiopian plume lavas: nature of magmatic sources and limit on lower mantle contribution. Earth. Planet. Sci. Lett. 144, 223-237.

McColl, R. C. 1964. Geological and structural studies on the batholithic rocks of the south California. Part 1. Structural geology of Rattlesnake mountain pluton. Bull. Geol. Soc. Am. 75, 805.

McDonald, G. A. 1968. Composition and origin of Hawaiian lavas. In: Coats R.R., Hay R.L., & Anderson C.A. (eds), Studies in volcanology: a memoir in honour of Howel Williams. Geol. Soc. Amer. Mem. 116, 477-522.

McKenzie, D. P. 1986. The geometry of propagating rifts. Earth. Planet. Sci. Lett. 77, 176-186.

McKenzie, D. P., Davies, D. & Molnar, P. 1970. Plate tectonics of the Red Sea and East Africa. Nature. 226, 243-248.

Merla G., Abbate E., Canuti P., Sagri M., & Tacconi P. 1979. Geological map of Ethiopia and Somalia and comment. Cons. Naz. Delle Ric. Ital.

Meshesha D., & Shinjo R. 2007. Crustal contamination and diversity of magma sources in the Northwestern Ethiopian volcanic province. J. Miner. Petrol. Sci. 102, 272-290.

Middlemost, E. A. K. 1989. Iron oxydation ratios, norm and the classification of volcanic rocks. Chem. Geol. 77, 19-26.

Mitchell, D. J. W., Allen, R. B., Salama, W. & Abouzakin, A. 1992. Tectonostratigraphic framework and hydrocarbon potentiel of the Red Sea. J. Pet. Geol. 15, 187-210.

Morgan, W. J. 1971. Convection plumes in the lower mantle. Nature. 230, 42-43.

Muller, J. & Boucarut, M. 1975. Evolution structurale de la région d'Arta-Ali Sabieh (T.F.A.I), Afrique orientale. Proc. Int. Symp. on the Afar region and related rift problems.

Murton, B. J., Taylor, R. N. & Thirlwal, l. M. F. 2002. Plume-ridge interaction: a geochemical perspective form the Reykjanes Ridge. J. Petrol. 43, 1987-2002.

Needham, H.D., Choukroune, P., Cheminée, J.-L., Le Pichon, X., Francheteau, J., & Tapponnier, P. 1976. The accreting plate boundary: Ardoukobâ Rift (N.E. Africa) and the oceanic Rift valley. Earth Planet. Sci. Lett. 28, 439-453.

Odin, G. S. & 35 collaborators. 1982. Interlaboratory standards for dating purposes. In: Odin G.S. (ed.), Numerical dating in stratigraphy, Wiley, Chichester, 123-149.

Paces J.B., & Bell K. 1989. Non-depleted sub-continental mantle beneath the Superior Province of the Canadian Shield: Nd-Sr isotopic and trace element evidence from Midcontinent Rift basalts. Geochim. Cosmochim. Acta. 53, 2023-2035.

Pik, R., Deniel, C., Coulon, C., Yirgu, G., Hoffmann, C. & Ayalew, D. 1998. The northwestern Ethiopian Plateau flood basalts: Classification and spatial distribution of magma types. J. Volcanol. Geoth. Res. 81, 91-111.

Pik, R., Deniel, C., Coulon, C., Yrgu, G. & Marty, B. 1999. Isotopic and trace element signatures of Ethiopian flood basalts: evidence for plume-lithosphere interactions. Geochim. Cosmochim. Acta. 63, 2263-2279.

Pitcher, W. S. 1979. The nature, ascent and emplacement of granitic magmas. J. Geol. Soc. London. 136, 627-662.

Purcell, P. G. 1975. Gravity anomalies over the Marda Fault Zone. Ethiopia. Bull. Geophys. Obs. (Ethiopia) 15, 133-140.

Ramberg, H. 1967. Gravity, deformation and the earth's crust as studied by centrifuged models. Academic Press, London, 214.

Ramberg, H. 1970. Model studies in relation to the intrusion of plutonic bodies. In: Newall, G. & Rast, N (eds). Mechanism of igneous intrusion. Spec. Iss. Geol. J(2), 261-86.

Redfield, T. F., Wheeler, W. H. & Often, M. 2003. A kinematic model for the development of the Afar Depression and its paleogeographic implications. Earth. Planet. Sci. Lett. 216(3), 383.

Richard, O. 1979. Etude de la transition dorsale océanique – rift émergé: le golfe de Tadjoura (République de Djibouti). Approche géologique, géochronologique et pétrologique. Unpublished Thèse 3ème cycle, Université de Paris XI-Orsay.

Rochette P., Tamrat E., Féraud G., Pik R., Courtillot V., Ketefo E., Coulon C., Hoffmann C., Vandamme D., & Yrgu G. 1998. Magnetostratigraphy and timing of the Oligocene Ethiopian traps. Earth Planet. Sci. Lett. 164, 497-510.

Roeser, H. A. 1975. A detailed magnetic survey of the southern Red Sea. Geol. Jb D13, 131-153.

Rogers, N. W. 2006. Basaltic magmatism and the geodynamics of the East African Rift System. In: Yirgu, G., Ebinger, C.J., & Maguire, P.K.H. (Eds.), The Afar volcanic province within the East African Rift System. Geol. Soc. London, Sp. Pub. 259, 77-93.

Roman-Berdiel, T., Gapais, D. & Brun, J. P. 1995. Analogue models of laccolith formation. J. Struct. Geol. 17, 1337-1345.

Ruegg, J. C. 1975. Structure profonde de la croûte et du manteau supérieur du Sud-Est de l'Afar d'après les données sismiques. Ann. Géophys. 31, 329-360.

Samson, S.D. & Alexander, E.C. Jr, 1987. Calibration of the intralaboratory $^{40}Ar/^{39}Ar$ dating standard MMhb-1. Chem. Geol. 6, 27-34.

Seber, D. Sandvol, E., Brindisi, C., & Barazangi, M. 2001. Crustal model for the Middle East and North Africa region: implications for the isostatic compensation mechanism. Geophys. J. Int. 147, 630-638.

Schilling, J. G. 1973. Afar mantle plume: rare earth evidence. Nature Phys. Sci .242, 2-5.

Schilling J.G., Kingsley R.H., Hanan B.B., & McCully B.L. 1992. Nd-Sr-Pb variations along the Gulf of Aden: evidence for Afar Mantle plume-continental lithosphere interaction. J. Geophys. Res. 97, 10927-10966.

Schlishe, R. W., Young, S. S., Ackermann, R. V. & Gupta, A. 1996. Geometry and scaling relations of a population of very small rift-related normal faults. Geology. 24, 683-686.

Sebai, A., Zumbo, V., Feraud, G., Bertrand, H., Hussain, A. G., Giannerini, G. & Campredon, R. 1991. 40Ar/39Ar dating of alkaline and tholeiitic magmatism of Saudi Arabia related to the early Red Sea Rifting. Earth. Planet. Sci. Lett. 104(2-4), 473.

Sichler, B. 1980. La biellette danakil: Un modèle pour l'évolution géodynamique de l'Afar. Bull. Soc. Geol. Fr.6, 925-933.

Skovgaard, A. C., Storey, M., Baker, J., Blusztajn, J. & Hart, S. R. 2001. Osmium-oxygen isotopic evidence for a recycled and strongly depleted component in the Iceland mantle plume. Earth. Planet. Sci. Lett. 194, 259-275.

Solvia, R., Schultz, R. A. & Benedicto, A. 2005. Three-dimentional displacement-length scaling and maximum dimension of normal faults in layered rocks. Geophys. Res. Lett. 32(6302), doi:10.1029/2005GL23007. J. H. 1972. Numerical Method

Spang, for Dynamic Analysis of Calcite Twin Lamellae. Geol. Soc. Am. Bull. 83, 467-472.

Sperner, B. 1993. Fault-striae analysis: a turbo pascal program package for graphical presentation and reduced stress-tensor calculation. Comp.& Geosciences. 19, 1361-1388.

Steiger, R. H. & Jäger, E. 1977a. Subcommission on geochronology: convention on the use of decay constants in geo- and cosmochronology. Earth. Planet. Sci. Lett. 36, 359-362.

Stevens, N., Garbeil, H. & Mouginis-Mark, P. J. 2004. NASA EOS Terra ASTER: Volcanic topographic mapping and capability. Remote Sensing of Environment. 90, 405-414.

Stieltjes, L. 1973. L'axe tectono-volcanique d'Asal. Unpublished thesis, Université de Paris-Sud, Orsay.

Stieltjes L., Joron J.L., Treuil M., & Varet J. 1976. Le rift d'Asal, segment de dorsale émergée: discussion pétrologique et géochimique. Bull. Soc. Géol. France. (7) 18, 851-862.

Sue, C. 2007. Extensional neotectonics around the bend of the Western/Central Alps: an overview. Int. J. Earth Sci . 96, 1101-1129.

Sue, C. & Tricart, P. 2003. Neogene to ongoing normal faulting in the inner western Alps: A major evolution of the late alpine tectonics. Tectonics. 22(5), 1050, doi: 10.1029/2002TC001426.

Sun, S. S. & McDonough, W. F. 1989. Chemical and isotopic systematics of oceanic basalts: Implications for mantle composition and processes. In: Saunders, A.D., & Norry, M.J. (Eds.), Magmatism in the ocean basins. Geol. Soc. London Sp. Pub. 42, 313-345.

Tamsett, D. & Searle, R. C. 1988. Structure and development of the midocean ridge plate boundary in the Gulf of Aden: Evidence from GLORIA side-scan sonar. J. Geophys. Res. 93, 3157-3178.

Tapponnier, P., J.C., R., Manighetti, I. & Courtillot, V. 1990. Bookshelf faulting and horizontal block rotation between overlapping rifts in southern. Geophys. Res. Letters. 17, 1-4.

Taylor, R. N., Thirlwall, M. F., Murton, B. J., Hilton, D. R. & Gee, M. A. M. 1997. Isotopic constraints on the influence of the Icelandic plume. Earth. Planet. Sci. Lett.148, 1-8.

Tazieff, H., Marinelli, G., Barberi, F. & Varet, J. 1969. Géologie de l'Afar septentrional. Bull. Volcanol. t.33, fasc. 4, 1039-1072.

Tazieff, H., Varet, J., Barberi, F. & Giglia, G. 1972. Tectinic significance of the Afar (or Danakil) depression. Nature. 235, 144-147.

Thirlwall, M., Gee, M. A., Taylor, R. N. & Murton, B. J. 2004. Mantle components in Iceland and adjacent ridges investigated using double-spike Pb isotope ratios. Geochim. Cosmochim. Acta. 68(361-386).

Treuil, M. & Varet, J. 1973. Critères pétrologiques, géochimiques et structuraux de la genèse et de la différenciation des magmas basaltiques: exemple de l'Afar. Unpublished Pétro-géochimie thesis, Université d'Orléans et Orsay.

Treuil, M. & Joron, J. L. 1975. Utilisation des éléments hygromagmatophiles pour la simplification de la modélisation quantitative des processus magmatiques. Exemples de l'Afar et de la dorsale médioatlantique. Boll. Soc. Ital. Mineral. Petrol. 31, 125-174.

Trudgill, B. D. & Cartwright, J. A. 1994. Relay ramp morphology and normal fault linkages, Canyonland National Park, Utah. Geol. Soc. Am. Bull. 106, 1143-1157.

Turner, F. J. 1953. Nature and dynamic interpretation of deformation lamellae in calcite of three marbles. Am. J. Sci. 251, 276-298.

Twiss, R. J. & Unruh, J. R. 1998. Analysis of fault slip inversion: Do they constrain stress or strain rate? J. Geophys. Res.B: Solid Earth, 103. J. Geophys. Res. 103, 12205-12222.

Ukstins, I. A., Renne, P. R., Wolfenden, E., Baker, E., Ayalew, D. & Menzies, M. A. 2002. Matching conjugate volcanic rifted margins: 40Ar/39Ar chrono-stratigraphy of pre-and syn-rift bimodal flood volcanism in Ethiopia and Yemen. Earth. Planet. Sci. Lett.198, 289-306.

Varet, J. 1975. Geological map of central and southern Afar (Ethiopia and Djibouti Republic). CNRS-CNR, Paris.

Vellutini, P. 1990. The Manda--Inakir rift, republic of Djibouti: A comparison with the Asal rift and its geodynamic interpretation. Tectonophysics. 172(1-2), 141.

Vellutini, P. J. & Piguet, P. 1995. Carte géologique de la République de Djibouti au 1:100 000: feuille de Khor Angar. In: Les formations volcaniques. Ministère Français de la Coopération et du Développement et ISERST, BRGM (1995).

Vétel, W. & Le Gall, B. 2006. Dynamics of prolonged continental extension in magmatic rifts: the Turkana Rift case study (North Kenya). In : The Afar volcanic province within the East African rift system; (eds Yirgu, G., Ebinger, C.J. & Maguire, P.K.), Geol. Soc. London. Spec. Pub. 259, 209-233.

Vidal, P., Deniel, C., Vellutini, P. J., Piguet, P., Coulon, C., Vincent, J. & Audin, J. 1991. Changes of mantle sources in the course of a rift evolution: the Afar case. Geophys. Res. Lett. 18, 1913-1916.

Volker, F., McCulloch, M. T. & Altherr, R. 1993. Submarine basalts from the Red Sea: new Pb, Sr, and Nd isotopic data. Geophys. Res. Lett. 20, 927-930. Geophys. Res. Lett. 20, 927-930.

Volker, F., Altherr, R., Jochum, K. P. & McCulloch, M. T. 1997. Quaternary volcanic activity of the southern Red Sea: new data and assessment of models on magma sources and Afar plume-lithosphere interaction. Tectonophysics. 278, 15-29.

Wallbrecher. 1986. Tektonische und gefügeanalytische Arbeitsweisen. Ferdinand Enke Verlag Stuttgart, Stuttgart.

White, R. & McKenzie, D. P. 1989. Magmatism at rift zones: the generation of volcanic continental margin and flood basalts. J. Geophys. Res. 94, 7865-7730.

White, W. M., McBirney, A. R. & Duncan, R. A. 1993. Petrology and geochemistry of the Galapagos islands: portrait of a pathological mantle plume. J. Geophys. Res. 98, 19533-19563.

Wojtal, S. F. 1994. Fault scaling laws and the temporal evolution of fault systems. J. Struct. Geol. 18, 265-280.

Wolfenden, E., Ebinger, C., Yirgu, G., Deino, A. & Ayalew, D. 2004. Evolution of the northern Main Ethiopian rift: birth of a triple junction. Earth. Planet. Sci. Lett. 224(1-2), 213.

Wolfenden, E., Ebinger, C., Yirgu, G., Renne, P. R. & Kelley, S. P. 2005. Evolution of a volcanic rifted margin: Southern Red Sea, Ethiopia. Geol. Soc. Am. Bull. v. 117; no. 7-8, 846-864.

Yamaji, A. 2000. The multiple inverse method: a new technique to separate stresses from heterogeneous fault-slip data. J. Struct. Geol. 22, 441-452.

Yamaji, A. 2003. Are the solutions of stress inversion correct? Visualization of their reliability and the separation of stresses from heterogeneous fault-slip data. J. Struct. Geol. 25, 241-252.

Yang, H.-J., Frey, F. A. & Clague, D. A. 2003. Constraints on the source components of lavas forming the Hawaiian North Arch and Honolulu volcanoes. J. Petrol. 44, 603-627.

Yoder, H. S. & Tilley, C. E. 1962. Origin of basalt magmas: an experimental study of natural and synthetic rock systems. J. Petrol. 3, 342-532.

Zak, J. & Patterson, S. R. 2006. Roof and walls of the Red Mountain Creek pluton, eastern Sierra Nevada, California (USA): implications for process zones during pluton emplacement. J. Struct. Geol. 28, 575-587.

Zindler, A., Hart, S. R., Frey, F. A. & Jakobsson, S. P. 1979. Nd and Sr isotope ratios and rare earth abundances in Reykjanes Peninsula basalts: evidence for mantle heterogeneity beneath Iceland. Earth. Planet. Sci. Lett. 45, 249-262.

Zumbo, V., Féraud, G., Vellutini, H., Piguet, P. & Vincent, J. 1995a. First 40Ar/39Ar dating on Early Pliocene to Plio-Pleistocene magmatic events of the Afar – Republic of Djibouti. J. Volc. Geoth. Res. 65, 281-295.

ANNEXES

ANNEXE A : Papier IV : Geodynamics of the Ali Sabieh antiform (Afar triple junction): new insights from paleostress analysis.

(en cours de rédaction. to *Terra Nova*)

Sue Christian[1], Mohamed A. Daoud[1,2], Bernard Le Gall[1], Joël Rolet[1].

[1] UMR 6538 Domaines océaniques, IUEM, Université de Bretagne Occidentale, place N. Copernic, 29280 Plouzané, France.

[2] IST, Centre d'Etudes et de Recherches de Djibouti, B.P. 486, Djibouti Ville, Djibouti.

Abstract

The Ali Sabieh Range is a magma-driven antiformal structure in the extensional tectonic context of the Afar triple junction. It involves Lower Miocene synrift volcanic sequences, and their Mesozoic substratum. Fault slip data analysis supplies insights about paleostress field conditions inferred to have prevailed during the growing of the Ali Sabieh antiform during Lower Miocene. Two successive tectonic events are identified as (1) a dominantly extensional setting with a least principal compressive vector oriented EW, and (2) a strike-slip regime, consistent with the extensional phase. It is therefore suggested that (i) the Ali Sabieh antiformal area might have evolved continuously from extensional to transcurrent tectonism, and/or (ii) local/regional stress permutation occurred between s1 and s2 stress axes, leading to tectonic permutation between extensional and strike-slip regimes.

Keywords: Afar Triple junction; Ali Sabieh antiform; brittle deformation; paleostress field; extension; doming.

1. Introduction.

Tectonics of triple junction zones, of either continental or oceanic type, often lead to complex strain/stress patterns, generally caused by changes in the relative trajectories of the plates involved in the system. The corresponding far stress/strain fields may also interact with more local fields of either tectonic or magmatic origin. Such a geodynamic configuration occurs in the Afar depression, Horn of Africa, where three recent rift axes converge and disrupt the eastern edge of the earlier (30 Ma-old) Afar plume-induced volcanic province.

Although its recent trap-like basaltic cover (<3 Ma-old Stratoid Basalts) displays a dominant extensional strain, structural complexities are documented in the overall Afar area. That locally expresses by reverse faulting, inferred from focal mechanism (*Hofstetter and Beyth*, 2003), and interpreted in terms of local disturbances, or variations in the fault system, in response to changes in the rift propagation directions (*Beyth*, 1991). Evidence for older compressional tectonics have also been locally reported in >3.6 Ma-old synrift volcanic series involved into the Arta transverse zone (*Arthaud et al.*, 1980). The kinematic model proposed by these authors implied stress permutation along an inferred transform fault structure. A more controversial antiform-like structure occurs in the Ali Sabieh range area (ASR), on the southeastern edge of the Afar depression (Figure 1). There, Jurassic limestones and Cretaceous sandstones outcrop in the core of a 25x25 km antiform, surrounded by Neogene volcanics (basalts and rhyolites), younging outwards of the structure. Moreover, the ASR corresponds to a structural high, with a mean altitude of 500-800m. Many interpretations have been proposed for the ASR, including extensional or compressional origins (see Chapter 3 for further details).

2. Geological context

(See Chapter 3 about the structural evolution of the Ali Sabieh range).

3. Methodology

Fault/stria analysis based on the Wallace and Bott principle (*Bott* 1959;), have long been developed and discussed (Angelier, 1975; Angelier, 1979; *Angelier and Goguel*, 1979; *Etchecopar, et al.*, 1981; *Gephart*, 1990; *Yamaji*, 2000). We refer to these publications for a complete discussion on the methods, which remains a matter of debate in terms of stress/strain (*Twiss and Unruh*, 1998; *Yamaji*, 2003).

Here, the fault-slip analysis was achieved using the TectonicsFP sofware from Sperner et al. (1993). The directions of the three principal strain/stress axes ($\sigma1 > \sigma2 > \sigma3$) were calculated using four different methods: the geometrical right dihedra solution (DD), the pressure-tension method (PBT), the numerical dynamic analysis (NDA) and the direct inversion (DI) (Table1).

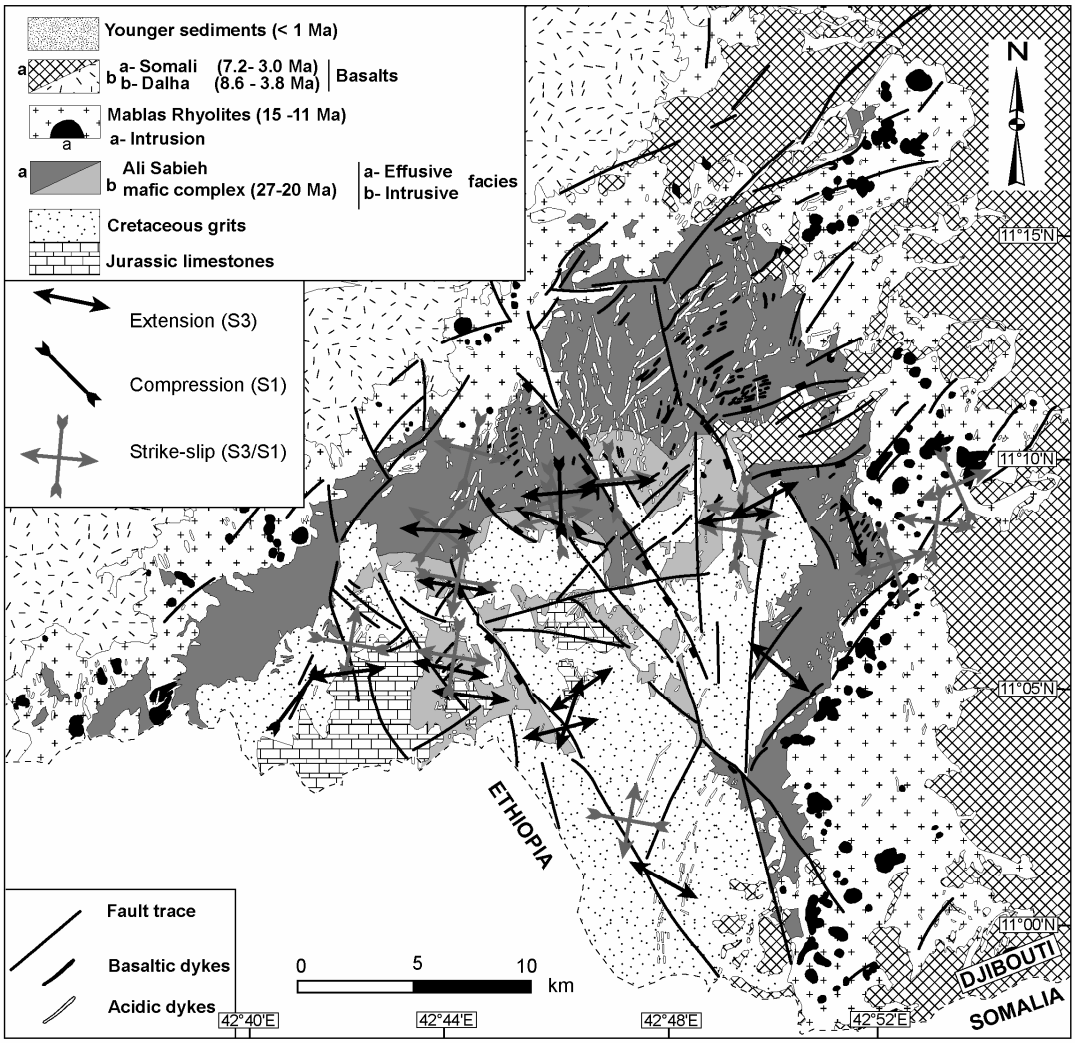

Figure 1: Paleostrain/stress maps of the ASR, calculated by Direct Inversion method (INV). Arrows show the projection on the map of the computed azimuth σ3 axis for the extensional (black) and strike-slip (grey) paleostress fields. Bars show the projection on the map of the computed azimuth σ1 axis for the reverse (black) and strike-slip (grey) paleostress fields. The shaded background represent the regional geological map, with the main faults and dyke-related lineaments.

In a first step (DD), compressive and distensive dihedra are calculated for each site, which give the possible 3D configuration of the tensor (*Angelier and Goguel*, 1979; *Angelier and Mechler*, 1977).

For the second method (PBT), the best-fit theta angle (frictional angle) for each tensor is determined. P- and T-axes are calculated stepwise for theta angles between 10 and 85 degrees, with a step of 2°. Plots obtained for P- and T- axes allow to visualize how good these axes cluster. This is quantified by the parameter R (*Wallbrecher*, 1986), which is calculated for

IDNUM	LONG - N	LAT -	TYPE	N	DD						INV							NDA							PBT					
					S1AZ	S1PL	S2AZ	S2PL	S3AZ	S3PL	S1AZ	S1PL	S2AZ	S2PL	S3AZ	S3PL	PHI	S1AZ	S1PL	S2AZ	S2PL	S3AZ	S3PL	PHI	S1AZ	S1PL	S2AZ	S2PL	S3AZ	S3PL
T01	**11°05,227**	**42°41,732**	**N**	11	126	60	330	28	235	10	199	59	349	28	86	13	0,72	125	66	323	33	228	8	0,73	130	33	334	51	234	7
T02	**11°05,041**	**42°41,590**	**R**	12	255	4	165	1	65	86	38	20	129	3	228	70	0,62	261	20	168	7	59	68	0,66	255	25	338	8	241	87
T03	**11°05,399**	**42°41,957**	**D**	15	173	2	273	81	82	9	9	1	279	51	100	39	0,04	181	1	277	81	91	9	0,5	181	2	289	83	91	8
T04_05/1	**11°08,963**	**42°46,623**	**D**	18	20	26	239	59	119	17	351	7	249	60	85	29	0,18	1	19	169	71	270	4	0,23	353	7	268	74	117	15
T04_05/2	**11°08,963**	**42°46,623**	**R**	17	112	3	227	5	163	80	5	10	273	11	135	75	0,71	340	18	248	7	137	71	0,75	322	14	227	5	137	74
T06 A	**11°09,938**	**42°47,362**	**D**	13	318	8	173	80	49	5	1	12	179	78	271	1	0,33	309	8	170	80	40	7	0,52	310	9	184	78	40	6
T06 B	**11°09,938**	**42°47,362**	**N**	8	216	86	23	4	113	1	50	63	169	14	265	23	0,91	278	74	23	4	115	16	0,36	275	75	25	6	115	18
T07	**11°05,304**	**42° 51,527**	**N**	29	225	87	47	3	317	0	306	79	55	4	146	10	0,25	291	83	48	3	139	6	0,49	284	84	47	3	138	6
T08	**11°08,040**	**42° 53,150**	**N**	16	206	74	99	5	8	15	329	73	84	7	176	15	0,19	236	82	97	6	6	6	0,44	238	81	98	8	7	5
T09	**11°07,794**	**42° 53,462**	**D**	12	359	15	217	72	92	11	353	22	201	66	87	10	0,31	5	22	199	67	97	5	0,6	6	21	203	69	97	5
T10	**11°08,056**	**42° 54,127**	**D**	20	360	8	120	75	268	13	8	16	157	72	275	9	0,57	357	10	150	79	266	5	0,61	0	8	137	72	267	8
T11	**11°09,179**	**42° 54,728**	**D**	8	146	11	343	79	236	3	103	44	295	45	199	6	0,84	166	21	12	67	260	9	0,42	164	17	11	78	254	7
T12 13 A	**11°08,550**	**42° 46,654**	**N**	11	168	84	44	3	313	5	51	68	206	20	299	9	0,35	20	87	218	3	128	1	0,54	227	87	39	10	308	0
T12_13 B	**11°08,550**	**42° 46,654**	**D**	10	205	33	30	57	297	2	175	8	68	64	269	24	0,02	178	24	359	66	268	0	0,54	176	20	20	68	264	8
T14	**11°08,173**	**42° 47,962**	**D**	16	14	8	158	80	284	6	12	53	185	37	277	4	0,88	14	28	184	62	282	4	0,33	10	9	342	87	100	1
T15	**11°08,978**	**42° 50,518**	**N**	9	33	83	192	7	283	2	39	85	160	3	251	5	0,43	305	79	207	1	117	11	0,19	292	80	56	12	148	16
T16	**11°08,567**	**42° 50,233**	**D**	8	185	16	336	72	93	8	190	1	99	49	280	41	0,07	191	10	31	80	282	3	0,42	191	5	102	78	285	9
T17	**11°08,567**	**42° 50,233**	**N**	13	171	86	336	4	66	1	116	77	359	6	268	11	0,05	197	79	336	8	67	7	0,39	188	79	333	11	65	8
T18_19/1	**11°08,160**	**42° 43,330**	**N**	17	16	78	176	11	266	4	338	69	190	18	97	10	0,52	53	69	175	12	269	17	0,51	53	72	175	10	270	20
T18_19/2	**11°08,160**	**42° 43,330**	**D**	19	327	35	166	56	62	2	8	64	166	24	260	9	0,9	57	27	177	45	308	33	0,39	55	13	166	56	285	32
T20	**11°10,110**	**42° 44,550**	**D**	20	333	2	73	79	242	11	9	38	184	52	277	3	0,81	329	10	99	75	237	11	0,55	329	8	92	82	237	8
T21_22 A	**11°07,040**	**42° 44,480**	**N**	19	243	70	34	18	127	9	156	62	22	20	285	18	0,08	191	74	27	15	296	4	0,38	185	71	27	19	297	3
T21_22 B	**11°07,040**	**42° 44,480**	**D**	10	276	1	185	64	7	26	273	2	177	9	4	21	0,57	77	4	174	62	345	28	0,67	89	3	164	82	343	20
T23	**11°05,980**	**42° 44,596**	**N**	17	237	77	345	4	76	12	322	49	204	22	99	32	0,78	146	87	348	3	258	1	0,44	127	88	349	1	259	1
T24	**11°05,980**	**42° 44,596**	**D**	10	1	16	174	74	270	2	15	11	179	78	285	3	0,26	5	18	174	72	274	3	0,51	5	17	180	73	274	2
T25	**11°05,980**	**42° 44,596**	**N**	15	89	79	186	2	277	11	249	79	19	7	110	8	0,12	69	86	188	2	278	3	0,34	65	87	185	2	276	4
T26	**11°04,447**	**42° 46,764**	**N**	13	117	62	339	22	242	17	174	55	351	35	82	2	0,19	145	66	347	22	254	8	0,51	152	61	340	32	248	6
T27	**11°02,117**	**42° 47,872**	**D**	20	129	23	286	65	36	9	97	14	323	70	190	14	0,05	109	26	276	63	17	5	0,45	106	21	278	75	19	3
T28	**11°00,747**	**42° 48,785**	**N**	10	89	82	197	3	288	7	164	55	38	22	297	26	0,86	302	82	197	2	107	7	0,49	308	83	193	8	105	8
T29	**11°04,650**	**42° 46,850**	**N**	11	73	82	322	3	231	7	263	53	115	33	15	16	0,04	247	83	126	4	35	6	0,27	261	81	130	17	36	8
T30	**11°04,930**	**42° 47,410**	**N**	22	119	85	313	5	223	1	360	83	144	5	234	4	0,15	44	87	137	0	227	3	0,4	6	84	144	11	235	7

Table 1 : *The direction of the three principal strain/stress axes ontained by using four different methods described in the text*

both P- (R(p)) and T- axes (R(t)) and gave the best theta angle for the data set. Thus, P- B- and T-axes (respectively pressure, intermediate and tension axes) are calculated with this optimum theta angle for each fault plane (*Turner*, 1953), the final axes for the data set being the barycenter of the P, B, and T distributions.

The third method (NDA) gives the strain tensors using the numerical-dynamical analysis of Spang (1972). It was calculated with a theta angle of 30°, accordingly with the Anderson's theory of fracturation (1951). The results of the NDA method are assumed to be strain parameters rather than stress parameters.

Finally, paleostress tensors have also been calculated for each site by the direct inversion method (DI) based on the minimization of a function of the differential angles between the measured and the computed striae (*Angelier*, 1990; *Angelier*, 1994).

For these two last methods, the best fitting strain/stress tensor and/or the classifications between multiple faulting events were to some degree part of an iterative sorting process in order to minimize the tolerance of angular deviation between orientations of the measured stria and the calculated one. The fluctuation factor m, representing the average of these angles, like the standard deviation sd have been calculated for each tensor for both methods. Additionally, shape ratios $\phi=[(\sigma2-\sigma3)/(\sigma1-\sigma3)]$ have also been established.

3. Analytical results

The approach above allowed us to precisely map the stress field associated to synrift brittle deformation in the study area (Figure 1), and partly allowed to further constrain the timing of the tectonic events, the volcanic rocks being dated. Paleostress fields inferred from brittle deformation display two major signals: normal and strike-slip faulting (Figure 2). The relative chronology has been determined in three polyphased sites, showing a first extensional signal, then a second strike-slip signal. We also found two marginal sites exhibiting reverse faulting, both of them being located at the periphery of the ASR (Figure 1).

In terms of stress fields, the first phase of extension corresponds to ENE-WSW to WNW-ESE oriented s3 axes (best axis at 78/01) and subvertical s1 axes (best axis at 234/87). We point out a regionally stable E-W oriented extension. The second phase is associated to E-W to ENE-WSW s3 axes (best fit at 87/11) and N-S to NNW-SSE s1 axes (best fit at 349/14). Both extensional and strike-slip fields are well constrained with 15 and 14 tensors, respectively, distributed all over the ASR, and a good internal homogeneity in terms of stress distributions.

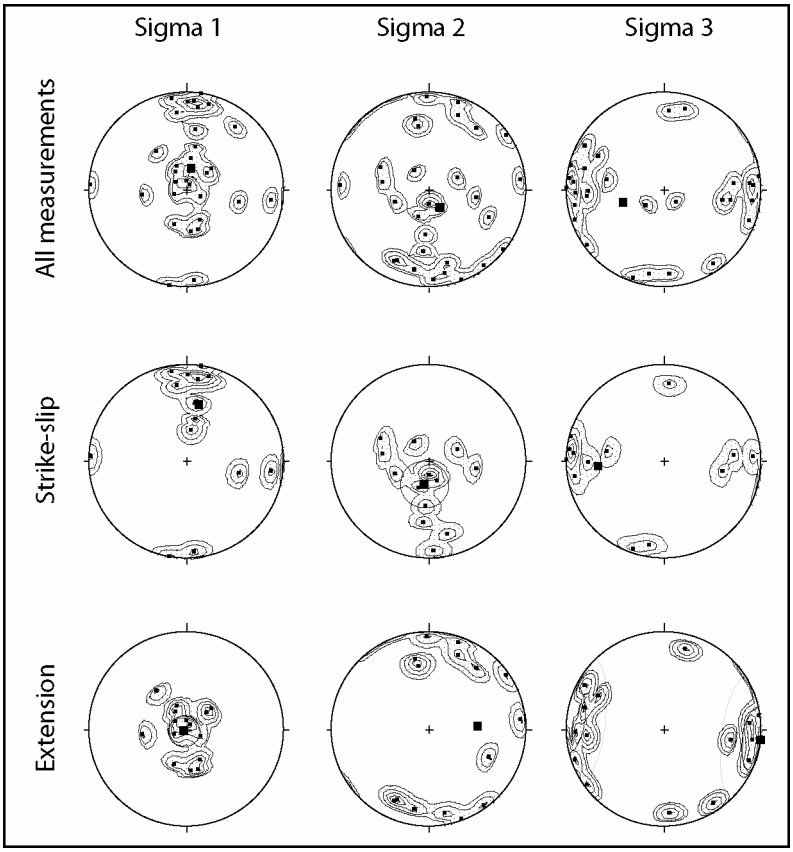

Figure 2: Statistical distribution of the strain/stress axes σ1/σ2/σ3, with the corresponding density contour diagrams, computed for the global database (top, 31 tensors), for the strike-slip phase (center, 14 tensors), and for the extensional phase (bottom, 15 tensors). Equal area projection, lower hemisphere.

Considering the regional stress data coverage, it was difficult to reach the southernmost part of the ASR.vertheless, some tensors could have been computed close to the Somalia border, along a main trail, resulting in a global paleostress transect of the ASR. The overall map (Figure 1) exhibits pretty stable regional fields both for extensional and transcurrents phases. We also obtain a good coherency in-between them, considering the s3 directions (Figure 2).

Discussion and conclusion

The stress distribution shows that these two stress fields are compatible, the s3 axes being stable (globally E-W). Thus, the ASR may have evolved continuously from extensional to transcurrent tectonism, and/or local/regional stress permutation may have occurred between s1 and s2 stress axes, leading to tectonic permutation between extension and strike-slip. Indeed, the very stable E-W direction of extension shows that the ASR's tectonics have been ruled under quite stable extensional conditions from the Neogene onwards. Such a tectonic

scenario has also been proposed in other geodynamic contexts (e.g. in the Alps, [*Sue and Tricart*, 2003; *Sue et al*., 2007]). Neither in the field nor on structural maps of the area or satellite images, large normal faults as candidate for a 30 km-wide horst could be determined. On the contrary, we observed some folds at the periphery of the ASB, which could be associated to the 2 reverse paleostress tensors we computed. In this framework, we propose that the ASR evolved as a magmatic dome rather than a horst or an anticline. The doming origin of the ASR is supported both by the internal organization of the structure, and by our detailed paleostress fields. The geodynamic context, which could have led to the ASB doming, could implies deep processes such as mantle upwelling.

ANNEXE B : Planches photos

PLANCHE n°1 : Système d'intrusion

A - Dyke basaltique subvertical au N80°E (environ 1 m de large), recoupant un empilement de laves de la Fm Goumarre, et évoluant en sill (cf. photo B) (Plaine de Djibouti, wadi Dey Dey).

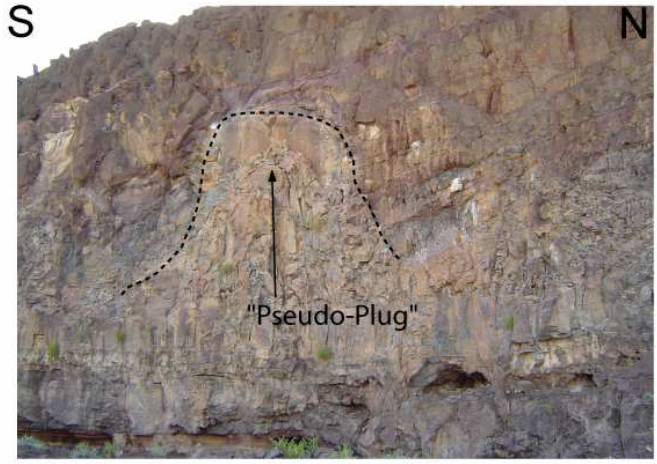

B - Sill basaltique (environ 10 m) dans les coulées supérieures de la Fm Goumarre, présentant localement des structures de type 'pseudo-plug'. (idem A).

C - Centre d'alimentation, de type plug, dans les Basaltes du Golfe, N Golfe Tadjoura.

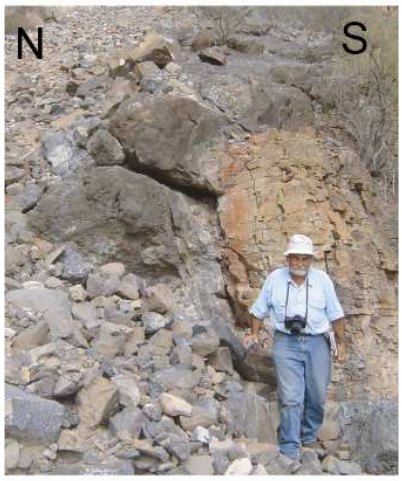

D - Dyke basaltique de la Fm 'Basaltes Somalis', en position verticale au N80°E (environ 1 m d'épaisseur), intrudant des laves de la Fm Dalha subhorizontales (Plaine de Djibouti, wadi Boulé).

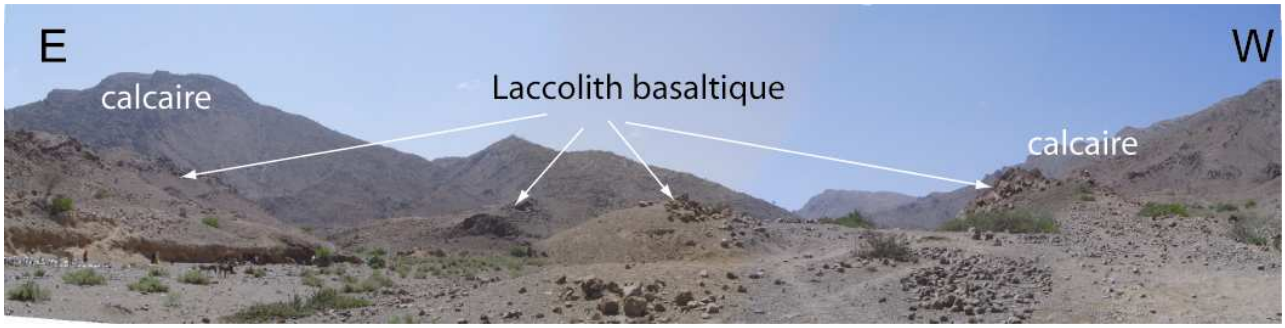

E - Partie centrale du laccolithe basaltique miocène identifié au cœur du dôme d'Ali Sabieh, sous la couverture de calcaires jurassiques.

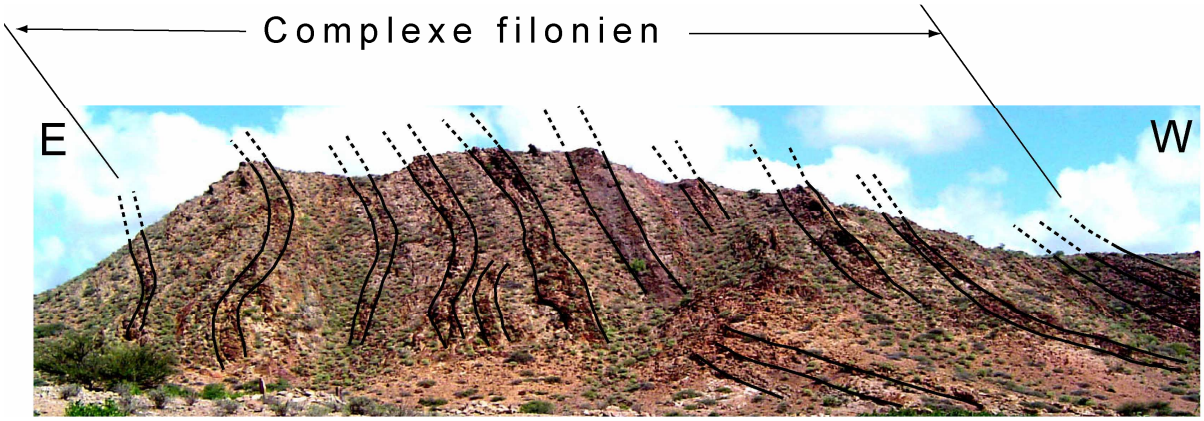

F - Réseau de dykes acides (Fm Mablas, probablement), fortement inclinés (70-80°) au S, recoupant des grès crétacés avec un faible pendage S (5-10°).

G - Intrusion basaltique de type dyke-sill recoupant les grès crétacés, déformés, à la terminaison N de l'antiforme d'Ali Sabieh.

H - Intrusion basaltique sub-horizontale (partie sommitale du laccolithe d'Ali Sabieh) recoupant les grès crétacés fortement pentés (40° au NW) (Extrémité NW de l'antiforme d'Ali Sabieh).

I - Dispositif identique sur le flanc NE de l'antiforme où les grés encaissants sont pentés à l'E.

PLANCHE n°2 : Soulèvement – Erosion– Incision – Remplissage

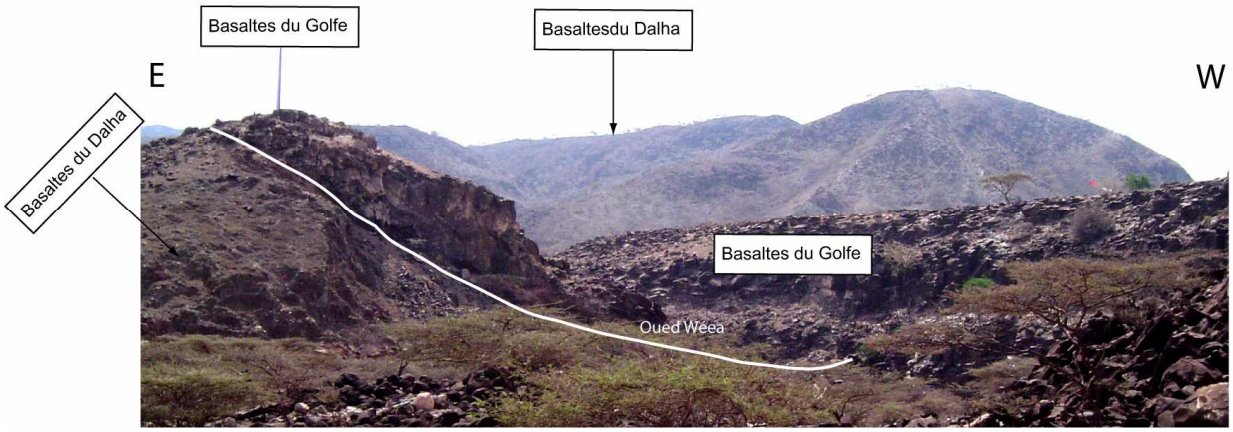

J - Basaltes du Golfe (datés à 1 Ma), en position horizontale, remplissant une paléo-vallée, actuellement perchée (300m d'altitude), creusée dans les basaltes (altérés) du Dalha.

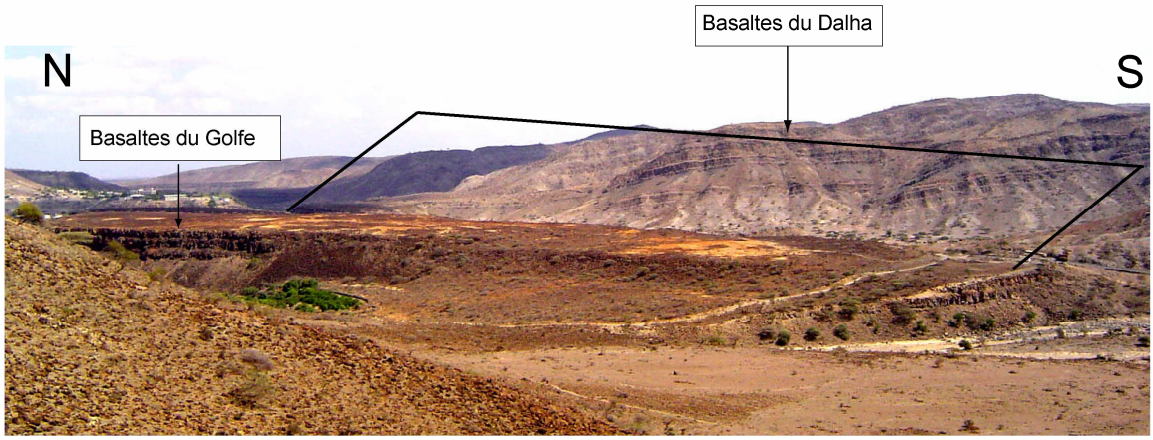

K - Partie amont du dispositif précédent avec les Basaltes du Golfe en position horizontale (premier plan) en onlap sur les Basaltes du Dalha, tiltés de 10-15° à l'E (arrière-plan).

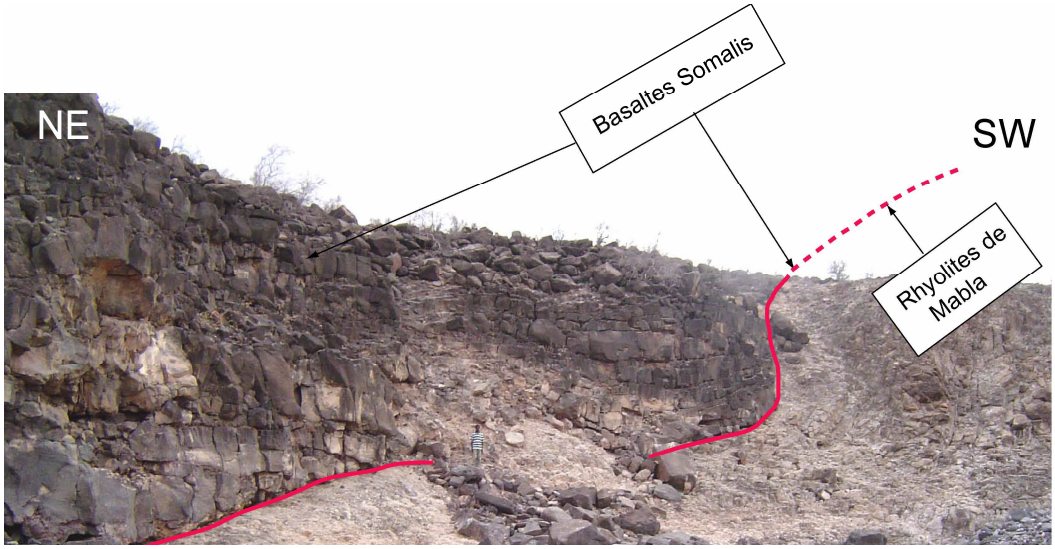

L - Basaltes Somalis, discordants sur les rhyolites (ignimbrites) de Mablas, et buttant au S le long d'un paléo-escarpement (NW Plaine de Djibouti, wadi Boulé).

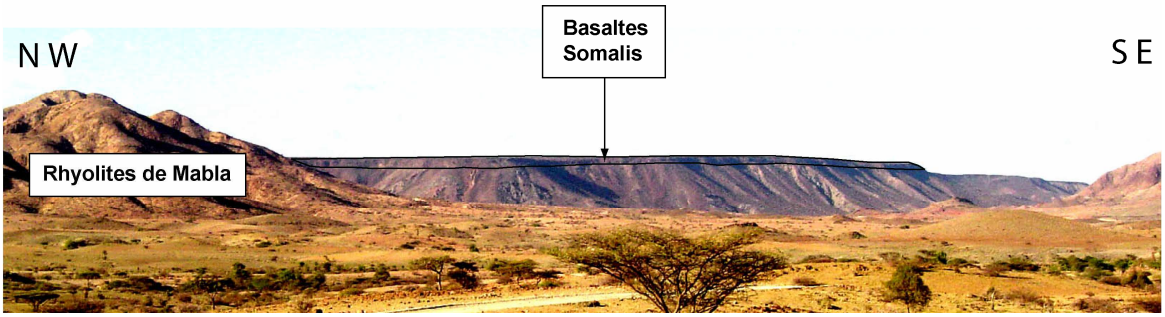

M - Basaltes Somalis en onlap sur les rhyolites de Mablas sur le flanc E de l'antiforme d'Ali Sabieh (Est Ali Addé).

N - Contact érosif entre les Basaltes du Dalha et les rhyolites de Mablas (Flanc NE de l'antiforme d'Ali Sabieh, Nord Daasbiyo).

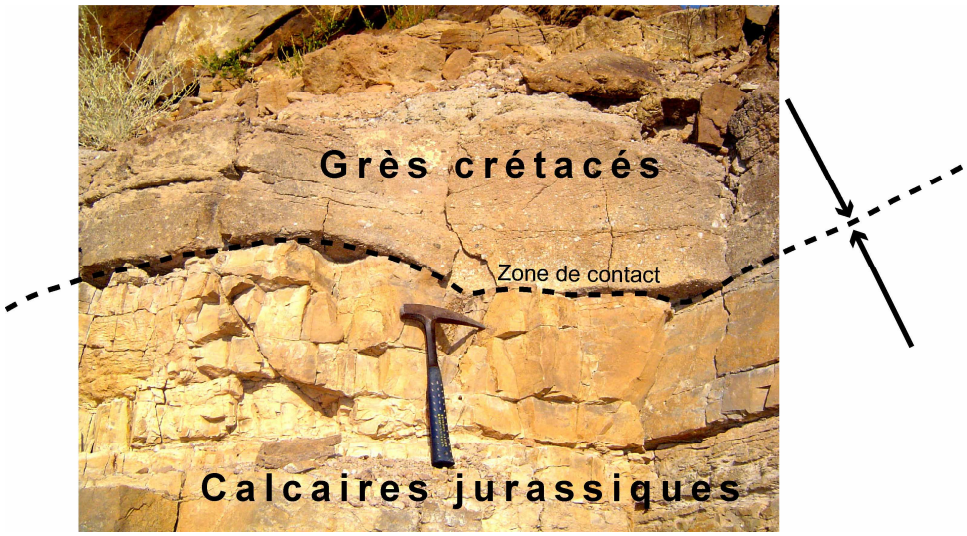

O - Contact stratigraphique concordant entre les calcaires jurassiques et les grès crétacés au cœur de l'antiforme d'Ali Sabieh.

PLANCHE n°3 : Fracturation et structures magmatiques

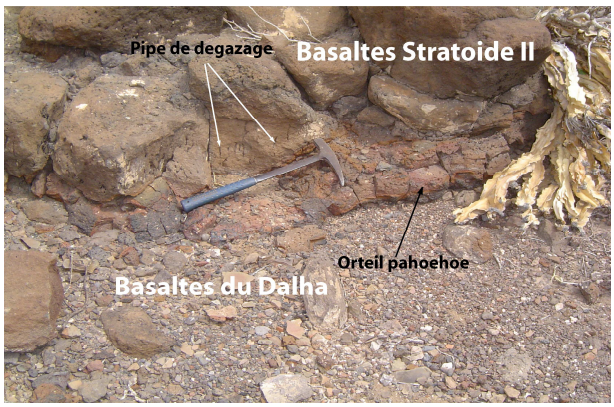

P - Protubérances bulleuses (orteils pahoehoe) indiquant le sens d'écoulement d'une coulée basale des Basaltes Stratoïdes II au-dessus de la série du Dalha (Champ de tir SW Arta).

Q - Sens d'écoulement (vers le SE)d'une coulée basaltique de la Fm basaltes Somalis déduit de structures plissées dissymétriques (Plaine de Djibouti, wadi Chabelley).

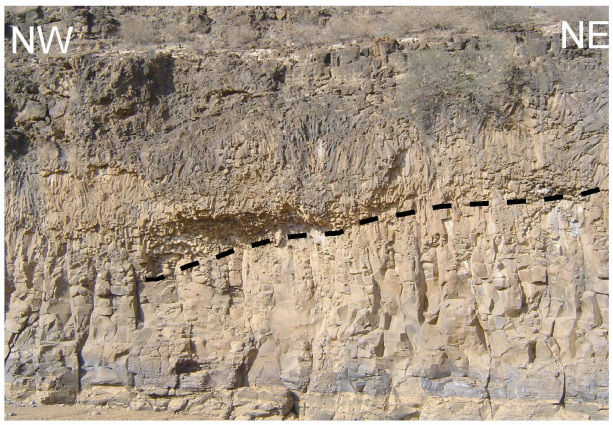

R - Prisme de refroidissement dans une coulée basaltique, d'environ 20 m d'épaisseur, de la Fm Somali. On remarque la prismation contrastée (en termes de densité/espacement) de part et d'autre d'un front de refroidissement situé vers la partie médiane de la coulée (Plaine de Djibouti, wadi Dey Dey).

S - Niveau de brèche scoriacée entre deux coulées successives des Basaltes Somalis (Plaine de Djibouti, wadi Dey Dey).

T - Faille verticale N80°E, à rejet d'environ 2 m, affectant les Basaltes Somalis (Plaine de Djibouti, wadi Dey Dey).

U - Faille verticale N120°E décalant avec un rejet apparent vertical de 2 m un sill intra-grès crétacés (SW antiforme Ali Sabieh).

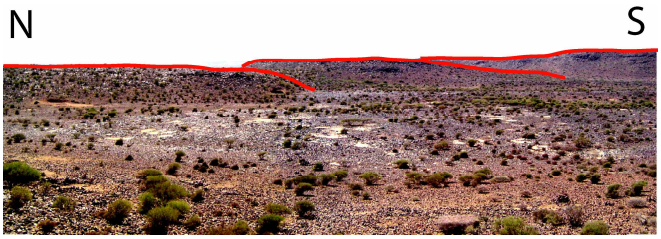

V - Réseau de failles normales en relais (NS) associées à la zone de transfert de Makarrassou (Est Lac Assal).

W - Graben assymètrique EW limité par un système de failles normales conjuguées à rejet vertical minimal de quelques dizaines de mètres (Flanc sud Golfe de Tadjoura, Ambaddo).

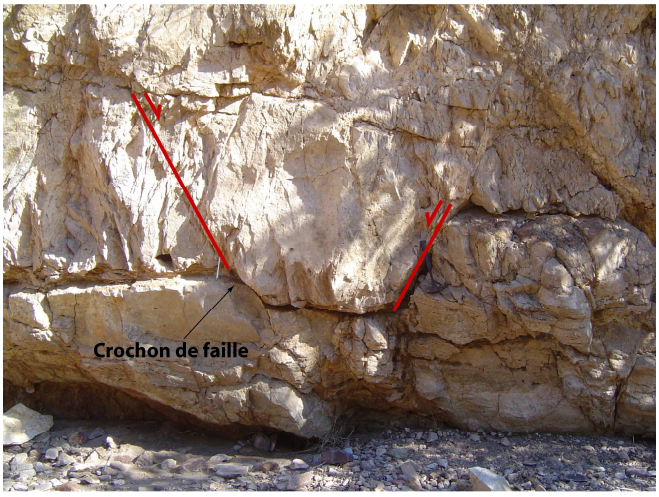

X - Mini-graben (N110°E) affectant les grès crétacés au cœur de l'antiforme d'Ali Sabieh.

Y - Dalle de calcaires jurassiques tiltés de 40° au NW et découpés par (1) un réseau de failles verticales N130°E et (2) un système de fractures conjuguées (Cœur antiforme d'Ali Sabieh).

Z - Plan de faille strié, à histoire polyphasée, recoupant les basaltes miocènes d'Ali Sabieh, et montrant des mouvements précoces de type décrochant (dextre), puis inverse (NE antiforme d'Ali Sabieh).

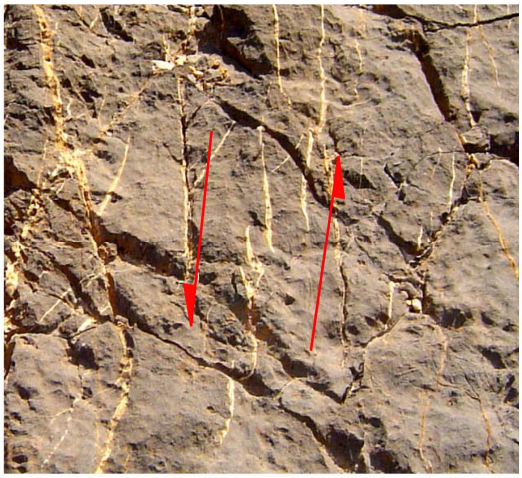

Z' – Fentes en échelon, à remplissage de calcite, associées à un décrochement sénestre dans les calcaires jurassiques (SW antiforme d'Ali Sabieh).

ANNEXE C : Composition chimique des roches

Les résultats analytiques obtenus au cours de ce travail sont réunis ici sous forme de tableaux par type de formation. Les teneurs en éléments majeurs sont données en pourcentages pondéraux, et celles des traces en ppm. Les annexes 1 à 5 concernent les données traitées et interprétées dans cette étude (x 95 échantillons). Les annexes 6 à 10 concernent des données non utilisées au cours de ce travail (x33).

Annexe 1 : Concentration en éléments majeurs (%) et en traces mesurée par ICP-AES, pour les basaltes du volcan Hayyabley (x 9 échantillons).
Annexe 2 : Concentration en éléments majeurs (%) et en traces mesurée par ICP-AES, pour les basaltes du Golfe (x 32 échantillons).
Annexe 3 : Concentration en éléments majeurs (%) et en traces mesurée par ICP-AES, pour les basaltes Goumarré (23 échatillons).
Annexe 4 : Concentration en éléments majeurs (%) et en traces mesurée par ICP-AES, pour les basaltes Somalis (x 23 échantillons).
Annexe 5 : Concentration en éléments majeurs (%) et en traces mesurée par ICP-AES, pour les basaltes d'Ali Sabieh (x 15 échantillons).
Annexe 6 : Concentration en éléments majeurs (%) et en traces mesurés par ICP-AES, pour les basaltes Stratoide I (x 6 échantillons).
Annexe 7 : Concentration en éléments majeurs (%) et en traces mesurée par ICP-AES, pour les basaltes Stratoide II (x 4 échantillons).
Annexe 8 : Concentration en éléments majeurs (%) et en traces mesurée par ICP-AES, pour des obsidiennes et une ignimbrite (x 4 échantillons).
Annexe 9 : Concentration en éléments majeurs (%) et en traces mesurée par ICP-AES, pour la série des Dalha (x 17 échantillons).
Annexe 10 : Concentration en éléments majeurs (%) et en traces mesurée par ICP-AES, pour les dyke acides d'Ali Sabieh (x 2 échantillons).

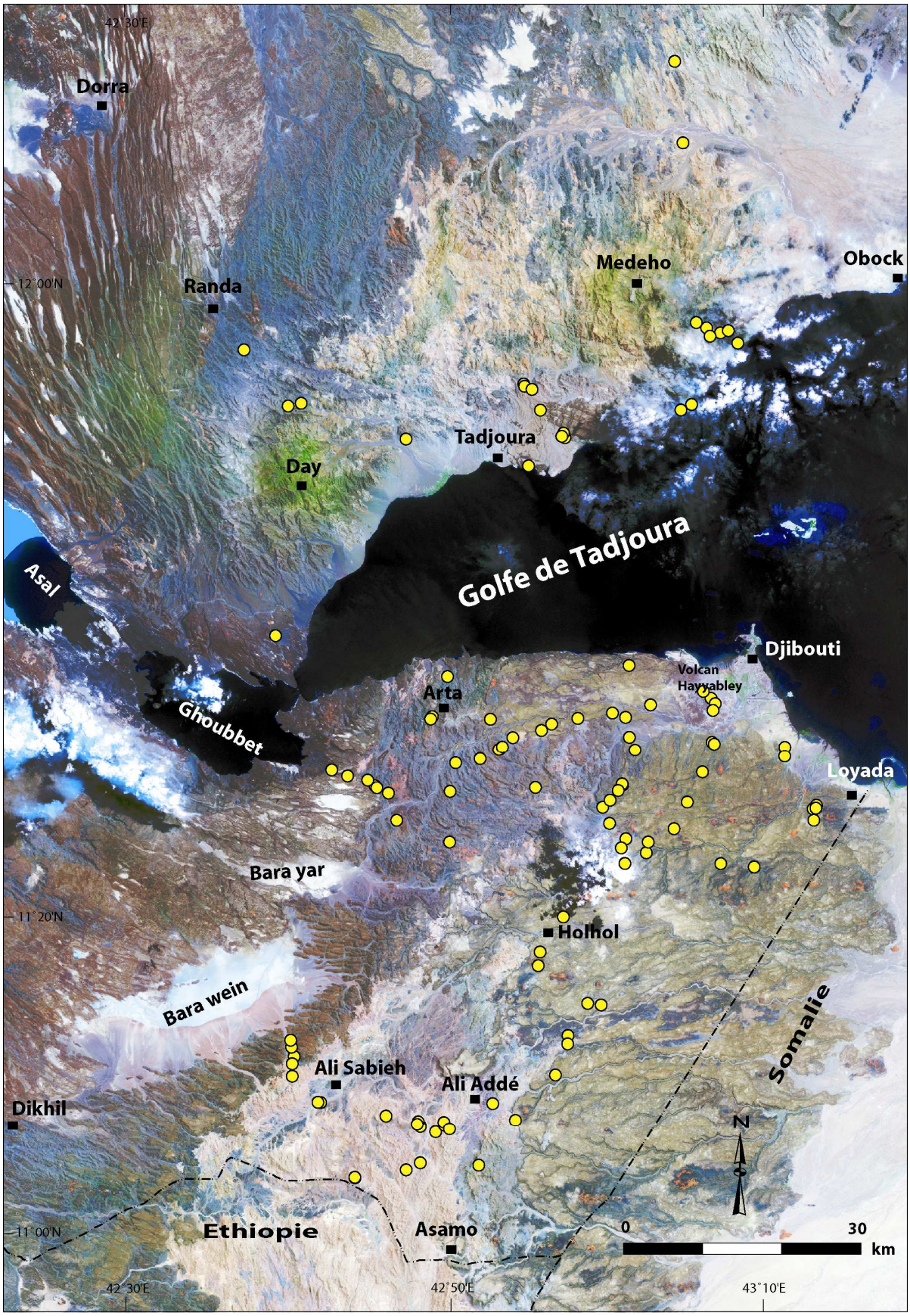

Figure 1 : Position géographique des échantillons récoltés au cours des campagnes de terrain et dont les compositions chimiques sont présentées dans les tableaux ci-dessous. (Image Aster).

Echantillon	dj54/04b	dj54/04c	dj54/04d	dj54/04g	dj54/04f	dj63/04	dj57/04	dj58/04	dj59/04
Coordonnées géographiques	11°34'07"N 43°05'04"E	11°35'07"N 43°05'04"E	11°36'07"N 43°05'04"E	11°37' 07"N 43°0 5'04"E	11°38'07"N 43°05'04"E	11°31'05"N 43°05'37"E	11°33'42"N 43°05'32"E	11°33'23"N 43°05'47" E	11 °32'59"N 43°05'39"E
SiO_2	47,15	46,5	46,8	46,8	46,6	47,2	47,2	46,6	47,6
TiO_2	0,93	0,91	0,95	0,89	0,89	0,91	0,92	0,85	0,96
Al_2O_3	16,53	16,5	16,4	16,6	17	16,7	16,52	16,6	17,05
Fe_2O_3*	10,35	10,31	10,35	10,25	10,2	10,05	10,42	9,4	10,11
MnO	0,17	0,16	0,17	0,16	0,17	0,16	0,17	0,15	0,16
MgO	9,45	9,3	8,75	9,47	9,46	9,56	9,8	9,18	9,25
CaO	12,9	13,1	13,5	12,85	12,5	13,25	12,9	13,8	12,9
Na_2O	1,99	1,92	1,9	1,98	1,98	1,99	1,96	1,96	2,08
K_2O	0,08	0,06	0,08	0,09	0,05	0,07	0,07	0,1	0,06
P_2O_5	0,07	0,07	0,07	0,07	0,07	0,08	0,07	0,07	0,07
LOI	0,46	0,92	0,72	0,49	0,63	-0,22	0,05	1,36	-0,38
Total	100,08	99,74	99,69	99,65	99,55	99,75	100,08	100,07	99,85
Rb	1,05	0,85	1	1	0,5	0,5	0,5	1,15	0,5
Sr	154	155	157	153	155	170	147	174	170
Ba	34	30	55	50	40	21	25	40	22
Sc	45	44	46	44	44	40	45	38	40
V	285	275	290	280	275	265	285	245	270
Cr	380	355	340	359	350	345	405	362	370
Co	51	52	50	52	53	54	53	48	51
Ni	198	198	175	209	208	187	210	173	175
Y	20,5	20,5	20,5	20	19,5	18,8	20	17,5	19
Zr	48	47	47	46	43	50	44	45	48
Nb	2,7	2,3	2,4	2,45	2,5	2,4	2,4	2,6	2,4
La	2,6	2,5	2,4	2,4	2,5	2,4	2,7	2,7	2,5
Ce	7,1	6,7	6,5	6,4	6,3	6	6,5	7,3	7
Nd	5,3	5,4	5,3	5,2	4,8	4,8	5,4	5,4	5,8
Sm	2	1,8	1,7	1,7	1,9	1,8	1,9	1,8	1,9
Eu	0,8	0,77	0,78	0,76	0,73	0,79	0,74	0,75	0,82
Gd	2,3	2,4	2,4	2,05	2,5	2	2,3	2,5	2,5
Dy	3,3	3,25	3,3	3,15	3,1	3,05	3,25	2,9	3,25
Er	2,1	2,15	2,1	2,1	2	1,85	2	1,8	1,9
Yb	2,18	2,15	2,2	2,1	2,08	2,07	2,1	1,75	1,9
Th	0,1	0,15	0,15	0,3	0,05	0,1	0,1	0,1	0,05

Annexe 1 : Concentration en éléments majeurs (%) et traces (ppm) des basaltes du volcan Hayyabley.

Echantillon	dj14/06	dj17/06	dj18/06bis	dj12/06	dj13/06	dj11/06	dj02/06	dj03/06	dj01/06	dj18/06	dj45/04	dj34/04
Coordonnées géographiques	11°50'55"N 43°03'36"E	11°51'12"N 43°04'14"E	11°54'54"N 43°07'00"E	11°49'10"N 42°56'35"E	11°49'26"N 42°56'30"E	11°49'12"N 42°56'30"E	11°37'14"N 42°39'10"E	11°47'29"N 42°54'23"E	11°37'14"N 42°39'10"E	11°54'54"N 43°07'00"E	11°35'38"N 43°00'34"E	11°34'54"N 42°49'35"E
SiO_2	45,8	45,7	46,3	46,6	45,75	46	46,8	46,2	46,4	45,9	46,1	46,5
TiO_2	2,11	2,86	2,92	2,57	2,93	2,72	2,61	2,71	2,61	1,98	2,46	2,71
Al_2O_3	14,6	14,76	14,35	14,3	14,97	14,18	15,33	15,35	14,85	15,35	14,55	15,4
Fe_2O_3*	14,85	15,85	15,4	15	14,75	15,9	12,87	14,5	13,03	14,2	14,62	14,42
MnO	0,21	0,22	0,22	0,22	0,21	0,23	0,19	0,21	0,19	0,21	0,21	0,2
MgO	8,15	7,54	8,2	7,2	6,4	7,46	8,48	7,65	8,8	6,75	8,5	7,4
CaO	10,1	9,9	10	9,85	11	9,95	11,2	10,45	11	11	10,45	10,2
Na_2O	2,6	2,68	2,66	2,71	2,72	2,64	2,1	2,67	2,39	2,35	2,53	2,7
K_2O	0,4	0,39	0,47	0,6	0,39	0,43	0,29	0,34	0,32	0,23	0,34	0,33
P_2O_5	0,37	0,37	0,42	0,45	0,42	0,43	0,39	0,3	0,42	0,23	0,34	0,31
LOI	0,07	-0,59	-0,83	-0,01	0,42	-0,21	0,028	-0,42	-0,18	1,54	-0,28	-0,54
Total	99,26	99,68	100,11	99,49	99,96	99,73	100,28	99,96	99,83	99,74	99,82	99,63
Rb	5,3	4,8	6,9	7,9	5,7	6,9	3	5,2	4,25	2,7	5	5,6
Sr	325	334	320	320	352	319	432	393	430	317	315	380
Ba	165	165	168	188	275	185	140	138	140	119	130	150
Sc	33	33,5	35	33	35	34	32	31,5	32	37,5	35	32
V	322	382	380	332	380	392	325	350	324	337	365	360
Cr	265	250	287	292	165	290	310	207	310	311	320	200
Co	57	57	56	52	49	57	52	53	54	57	58	56
Ni	156	140	150	130	93	139	175	135	190	153	175	145
Y	30	33	34,5	41	34,5	36,5	27	29,5	28	26,5	33	32
Zr	146	168	190	212	191	190	144	153	150	122	160	170
Nb	18	22	25	26	25	23	20,5	20,2	22	13	18	20
La	17	17,1	19,5	23	19,8	20,5	14,7	16,3	14,9	13	15,4	16,5
Ce	39	39,5	44	53	45	47,5	34,5	39	35	31	36	37,5
Nd	23,5	25	28	33	28	28	23	24,5	23,5	20	22,5	24
Sm	5,7	6	6,7	7,65	6,5	6,9	5,4	5,85	5,6	4,4	5,7	5,9
Eu	2	2,08	2,2	2,48	2,24	2,28	1,96	2,01	1,95	1,68	1,96	2,02
Gd	5,8	6,4	6,7	7,4	6,7	7	5,8	5,9	6	5	6,1	6,1
Dy	5,35	5,8	6,35	6,9	6,2	6,6	5,1	5,1	5,25	4,5	6	5,9
Er	2,8	3,2	3,3	3,8	3,2	3,4	2,6	2,7	2,6	2,5	3,1	3
Yb	2,59	3,02	3,05	3,52	3,01	3,27	2,26	2,55	2,34	2,29	2,85	2,77
Th	1,35	1,7	1,5	1,55	1,05	1,4	0,6	0,8	0,7	0,8	1,02	1,32

Annexe 2 : : **Concentration en éléments majeurs (%) et traces (ppm) des basaltes du Golfe.**

Echantillon	dj54/04a	dj64/04a	dj70/04	dj 86/05	dj 88/05	pk20-1	pk20-2	pk20-3	dj 05/05	dj04/05	dj43/04b	dj38/05
Coordonnées géographiques	11°34'07"N 43°05'04E	11°31'58"N 43°05'44"E	11°32'28"N 42°57'29"E	11°28' 09"N 42°59 '57"E	11°28'28"N 43°00'14"E	11°31'21"N 43°00'37"E	11°31'21"N 43°00'37"E	11°31'21"N 43°00'37"E	11 °30'34"N 4 2°52'48"E	11°30'33"N 42°52'44"E	11°28'26"N 42°49'51"E	11°30'34"N 42°52'56"E
SiO_2	46	46,9	45,7	45,3	45,8	46,4	46	45,6	47,7	47,1	46,5	47,4
TiO_2	2,62	2,19	2,34	2,21	2,25	2,5	2,08	2,22	3,32	2,92	2,75	2,65
Al_2O_3	14,4	15,15	15,45	15,5	15,5	14,9	15,25	14,8	12,8	13,9	14	13,87
Fe_2O_3*	14,6	14,45	13,33	13,3	13,45	14,14	12,6	13,3	16	16,7	16,55	16,1
MnO	0,21	0,21	0,19	0,19	0,2	0,2	0,17	0,18	0,24	0,24	0,24	0,23
MgO	7,6	7	6,32	6,55	6,48	7,48	7,35	6,9	5,75	6,15	6,05	6,05
CaO	10,8	11	12,74	11,55	10,9	10,95	11	10,6	10,2	10,2	10,2	10,05
Na_2O	2,54	2,62	2,62	2,67	2,7	2,42	2,33	2,39	2,59	2,7	2,69	2,71
K_2O	0,34	0,25	0,33	0,48	0,5	0,3	0,37	0,36	0,43	0,49	0,42	0,53
P_2O_5	0,38	0,25	0,31	0,27	0,28	0,36	0,28	0,29	0,48	0,39	0,35	0,38
LOI	0,37	-0,09	1,01	1,74	1,26	0,18	2,9	2,83	0,07	-0,74	-0,25	-0,5
Total	99,86	99,93	100,34	99,76	99,32	99,83	100,33	99,47	99,58	100,05	99,5	99,47
Rb	0,8	2,9	3,65	8,5	8,6	4,6	6,3	5,3	7,4	11,2	6	10,2
Sr	316	282	331	356	365	315	272	278	285	262	267	262
Ba	145	124	149	165	180	125	124	133	300	180	171	208
Sc	35	38	35	33	33	36	36,5	40	41	37	38	39
V	390	374	362	327	325	354	331	384	485	432	414	405
Cr	290	86	187	139	138	265	248	144	85	72	75	94
Co	56	53	49	53	52	51	47	47	46	58	57	56
Ni	150	94	90	103	104	135	111	81	64	79	79	79
Y	32,5	28	29	24	25	31	27,5	29,5	49	43	42	42
Zr	170	123	159	118	124	160	130	130	240	195	199	200
Nb	20	13,3	20,5	18,8	20	20,5	16,5	17,5	25	23	22	23
La	17	11,5	17,4	14,5	15,5	16,8	13,8	14	24	20,5	19,8	20
Ce	39	26	37	33	34	39	31,5	33	56	47	44,5	46
Nd	25	17	21,5	19	20	24	19,3	20	35,5	28,5	27	27,5
Sm	5,9	4,4	5,15	4,5	4,35	5,7	4,6	4,7	8,2	7	6,8	6,9
Eu	2,04	1,67	1,84	1,65	1,64	2,05	1,63	1,71	2,66	2,4	2,19	2,25
Gd	6,3	4,9	5,4	4,8	5	5,9	5	5	9,1	7,7	7,2	7,15
Dy	6,1	5,1	5,2	4,4	4,45	5,8	4,65	4,8	8,65	7,45	7,15	7,25
Er	3,2	2,8	2,7	2,3	2,35	3	2,6	2,7	4,4	4,1	3,9	4
Yb	3	2,57	2,55	2,09	2,15	2,72	2,44	2,56	4,04	3,92	3,64	3,73
Th	1,15	1,05	0,95	1,4	1,55	1,1	1,25	0,95	2,1	1,8	1,8	2,55

Annexe 2 (suite): : **Concentration en éléments majeurs (%) et traces (ppm) des basaltes du Golfe.**

Echantillon	dj44/04a	dj 60/05	dj 37/05	dj43/04b	dj44/04b	dj71/04	dj72/04	dj69/04
Coordonnées	11°11'05"N	11°32'06"N	11°32'33"N	11°28'02"N	42°11'05"N	11°33'17"N	11°31'44"N	11°32'48"N
géographiques	42°51'36"E	42°55'54"E	43°00'23"E	42°49'48"E	42°51'36"E	43°01'53"E	42°55'18"E	42°59'35"E
SiO_2	46,8	47,6	46,8	46,5	46,5	45,65	45,7	46,5
TiO_2	2,82	2,78	2,79	2,96	2,82	2,92	2,82	2,6
Al_2O_3	14,05	14,15	14,12	14,2	14	14	13,98	14,4
Fe_2O_3*	16	15,95	16,12	16,68	16,7	16,7	16,12	14,25
MnO	0,23	0,24	0,23	0,24	0,25	0,24	0,23	0,21
MgO	6,05	6,1	6,26	6,24	5,95	6,31	6,2	6,21
CaO	10,05	9,8	10	9,74	10,4	10,52	10,45	11,6
Na_2O	2,66	2,77	2,73	2,71	2,63	2,73	2,76	2,71
K_2O	0,47	0,54	0,44	0,44	0,43	0,41	0,45	0,4
P_2O_5	0,36	0,34	0,34	0,38	0,36	0,35	0,35	0,34
LOI	0,25	-0,46	-0,37	-0,73	-0,01	0,006	0,17	0,33
Total	99,74	99,81	99,46	99,36	100,03	99,89	99,23	99,55
Rb	9,9	6,8	10	8,3	8,4	5,6	6,3	7
Sr	268	264	272	266	268	277	267	321
Ba	170	158	158	155	225	296	159	174
Sc	38,5	38	38	39	39	38	37	40,5
V	405	395	393	425	422	428	416	397
Cr	90	89	90	69	76	68	66	224
Co	51	51	52	54	55	54	52	49
Ni	74	71	79	78	74	76	75	71
Y	43	42	40	42,5	43	40	39	32,5
Zr	210	204	187	195	205	187	186	175
Nb	24	25	22	22,5	22,5	22,4	22	22,5
La	22	21,5	19,5	20	20	19	18,1	19
Ce	46	49	43,5	46	45,5	42,5	41,5	42
Nd	29	29	27	28	28	27	25,8	25
Sm	7	6,8	6,7	7,1	6,8	6,45	6,1	5,75
Eu	2,26	2,22	2,13	2,3	2,26	2,2	2,1	2,02
Gd	7,6	7,6	7,3	8	7,45	7,2	6,6	5,9
Dy	7,5	7,4	7	7,4	7,3	7,15	6,9	5,75
Er	4,1	4	3,9	4,1	4,1	3,9	3,8	3,1
Yb	3,75	3,8	3,64	3,8	3,8	3,72	3,61	2,87
Th	2,1	2,55	1,8	1,85	1,75	1,7	1,65	1,4

Annexe 2 (suite): : **Concentration en éléments majeurs (%) et traces (ppm) des basaltes du Golfe.**

Echantillon	dj55/04	dj56/04a	dj56/04c	dj67/04b	dj07/04a	dj28/04	dj 78/05	dj 77/05	dj62/04c	dj60/04	dj30/04a	dj30/04c
Coordonnées géographiques	11°27'29"N 43°11'56"E	11°27'08"N 43°11'45"E	11°27'08"N 43°11'45"E	11°23'49"N 43°00'23"E	11°24'28"N 43°00'41"E	11°26'28"N 43°11'48"E	11°25'17"N 43°00'27"E	11°25'06"N 43°01'47"E	11°30'49"N 43°10'00"E	11°30'16"N 43°10'00"E	11°27'11"N 43°11'55"E	11°27'11"N 43°11'55"E
SiO_2	47,25	47	47,75	47,3	47	47,35	47,2	47,1	47,8	47,85	48	47,8
TiO_2	3,08	3,6	3,07	3,3	3,72	3,07	3,22	3,19	3,81	3,84	3,62	3,58
Al_2O_3	13,97	13,25	14	13,8	13,34	13,9	13,57	13,69	13,3	13,45	13,48	13,7
Fe_2O_3*	13,85	14,74	13,75	14,45	15	13,75	14,5	14,49	15,4	15,5	15,25	15,05
MnO	0,2	0,22	0,2	0,22	0,22	0,2	0,21	0,21	0,23	0,23	0,23	0,22
MgO	6,04	5,65	6,07	5,82	5,77	5,75	5,8	5,85	5	5	5,17	5,28
CaO	11,36	10,6	11	10,9	10,45	10,92	11,3	11	9,7	9,85	10	10,2
Na_2O	2,79	2,71	2,78	2,86	2,86	2,72	2,84	2,9	3,16	3,16	3,03	3,04
K_2O	0,59	0,75	0,66	0,6	0,71	0,68	0,61	0,63	0,82	0,79	0,81	0,74
P_2O_5	0,44	0,53	0,42	0,44	0,54	0,42	0,43	0,42	0,54	0,53	0,59	0,55
LOI	-0,07	0,31	0,18	-0,33	-0,38	0,97	0,43	-0,16	-0,41	-0,57	-0,31	-0,34
Total	99,5	99,37	99,88	99,36	99,23	99,74	100,11	99,32	99,35	99,63	99,87	99,82
Rb	9,2	13,8	14,1	9	13,8	13,6	10,5	9,3	14,7	14,8	16	12,7
Sr	385	380	366	385	378	360	390	380	380	378	378	385
Ba	240	206	174	185	210	194	218	176	243	222	223	210
Sc	37,5	37	37	37	38	37	36	37	31,5	32	33	34
V	392	450	395	424	460	420	395	380	420	430	400	425
Cr	160	126	160	62	130	158	57	74	32	30	44	50
Co	44	43	43	46	44	45	42	44	41	43	43	43
Ni	78	74	76	59	76	78	57	59	32	34	48	52
Y	36	41,5	35,5	36,5	42,5	37	36,5	36	44	44	45	43,5
Zr	230	264	222	230	275	230	219	214	296	300	280	270
Nb	33	37,5	32	33	39,5	32	32	31	42,5	44	41	39,5
La	26	30	26	27	30,5	26,5	27	26	34,5	34	34	32
Ce	59	68	58	62	68	58,5	60	56,5	76	76	76	69
Nd	34	40	34	34,5	41	34,5	35	33,5	43	43	45	42
Sm	7,7	8,65	7,6	7,6	9,1	7,8	7,6	7,4	9,2	9,5	9,7	9,05
Eu	2,5	2,81	2,45	2,55	2,87	2,52	2,46	2,46	3	3,01	3,12	2,95
Gd	7,7	8,8	7,6	7,7	8,9	7,5	7,7	7,5	9,1	8,9	10	9,4
Dy	6,9	7,8	6,8	7	8	6,95	6,65	6,6	8,2	8,2	8,5	7,9
Er	3,4	4	3,5	3,4	4	3,4	3,4	3,3	4	4	4,4	4
Yb	3,04	3,5	2,96	3,06	3,47	3,07	3	2,95	3,61	3,7	3,8	3,54
Th	2,4	2,65	2,35	2,35	3	2,07	2,55	2,5	3,05	3,1	3,4	3,1

Annexe 3 : Concentration en éléments majeurs (%) et traces (ppm) des basaltes Goumarré.

Echantillon	dj04/04as	dj81/05	dj89/05S	dj82/05
Coordonnées géographiques	11°27'30"N 43°04'09"E	11°27'09"N 42°59'02"E	11°28'33"N 43°00'11"E	11°27' 34"N 42°5 9'28"E
SiO_2	48	47,2	47,5	47,5
TiO_2	3,84	3,87	3,72	3,84
Al_2O_3	13,25	13,25	13,34	13,4
Fe_2O_3*	15,5	15,6	15,5	15,5
MnO	0,24	0,23	0,23	0,23
MgO	4,95	4,99	4,6	5,04
CaO	9,6	9,9	9,5	9,85
Na_2O	3,13	3,11	3,14	3,15
K_2O	0,75	0,78	0,83	0,76
P_2O_5	0,53	0,5	0,51	0,51
LOI	-0,48	0	0,21	-0,25
Total	99,31	99,43	99,08	99,53
Rb	14,9	11,9	15,5	12,6
Sr	810	380	375	380
Ba	305	250	225	235
Sc	32	33	32	32,5
V	465	440	420	428
Cr	28	31	31	36,5
Co	43	44	43	43,5
Ni	35	38	36,5	36,5
Y	44	42,5	44	43
Zr	293	276	275	277
Nb	45	43	41	42,5
La	33,5	32	33	32,5
Ce	74	70	72	72
Nd	44	42	43	42,5
Sm	9,5	8	9,1	9,2
Eu	3,01	2,84	2,88	2,86
Gd	9,5	9	9,3	9,25
Dy	8,3	7,85	8	7,8
Er	4,1	3,7	4,1	4
Yb	3,62	3,45	3,5	3,46
Th	3,4	3	3,15	3,1

Annexe 3 (suite) : Concentration en éléments majeurs (%) et traces (ppm) des basaltes Goumarré.

Echantillon	dj03/04	dj 73/05	dj 76/05	dj 39/05	dj75/05	dj 74/05	dj68/04	dj66/04	dj04/04e	dj32/04b	dj14/04a	dj14/04b
Coordonnées géographiques	11°29'18"N 43°05'03"E	11°11'10"N 42°56'17"E	11°15'27"N 42°58'12"E	11°15'21"N 42°59'01"E	11°13'32"N 42°57'02"E	11°13'03"N 42°57'01"E	11°24'44"N 43°00'10"E	11°25'54"N 43°03'21"E	11°27'30"N 43°04'09"E	11°23'30"N 43°08'12"E	11°18'29"N 42°55'19"E	11°18'29"N 42°55'19"E
SiO_2	49,2	48,6	48,8	48,2	47,4	49,2	50,2	49	50,3	48,8	52,25	52,4
TiO_2	3,32	3,35	2,84	3,42	3,25	3,15	3,25	3,35	3,36	3,88	3,15	3,16
Al_2O_3	13	13,2	14,22	13,36	13,45	13,3	13,1	13,22	13,2	12,9	13,25	13,3
Fe_2O_3*	15,1	15,5	14,4	16,15	15,2	15,1	14,35	15,2	14,75	15,55	14	14
MnO	0,22	0,23	0,21	0,25	0,22	0,21	0,23	0,23	0,24	0,24	0,23	0,23
MgO	4,74	4,95	4,72	4,89	5,33	5,33	4,43	4,91	4,41	4,75	4,13	4,12
CaO	9,3	9,65	9,85	9,5	10,45	9,85	9,1	9,35	8,65	9	8,04	8,03
Na_2O	2,9	2,94	3,05	3,04	2,9	2,6	3,05	2,89	3,19	2,95	3,34	3,35
K_2O	0,86	0,45	0,61	0,72	0,61	0,48	0,85	0,86	0,8	0,96	0,93	1,05
P_2O_5	0,62	0,49	0,43	0,56	0,44	0,38	0,46	0,62	0,47	0,67	0,49	0,49
LOI	0,41	0,28	0,28	-0,25	0,26	0,26	0,57	-0,19	0,07	-0,41	0,01	-0,08
Total	99,61	99,64	99,41	99,84	99,51	99,86	99,59	99,44	99,44	99,29	99,82	100,05
Rb	18	12,9	15,4	11,8	10,5	10,6	19,4	19,6	18,9	21	23,4	23,5
Sr	318	294	340	330	349	289	314	322	319	338	310	307
Ba	270	300	312	290	237	432	320	228	245	265	270	280
Sc	34	36	33	35,5	36	37,5	32,5	35	33	36	30	30,5
V	405	425	340	398	403	450	389	418	390	415	360	372
Cr	28	36	38	22	48	66	11	28	11	21	11,5	11
Co	44	43	42	43	44	46	39	42	40	42	35	36
Ni	38	39	32	24,5	39	54	24	36	25	38	23	22
Y	48,5	49	41	45	38,5	41	49,4	50	50,5	58	54	54
Zr	280	260	245	253	223	240	312	292	315	395	340	340
Nb	36,5	31	30,5	32	28	28,5	38	35,5	39	49	41	42
La	30	26,5	27	28	25	23	33,5	32	32,5	41	37	37
Ce	69	61	60	63	55	51,5	74	73	72,5	91	81	82
Nd	41,5	38,5	35,5	37,5	32,5	33	40,5	42	42	54	46,5	46,5
Sm	9,6	8,65	7,95	8,5	7,4	7,5	9	9,7	9,6	12,2	10,35	10,5
Eu	3,02	2,83	2,5	2,87	2,46	2,37	2,89	3,07	2,98	3,52	3,17	3,08
Gd	10	9,5	8,3	9,4	7,7	8	9,6	10	9,7	11,8	10,4	10,6
Dy	9	9	7,4	7,9	7	7,6	9,1	9,2	9,2	10,8	9,9	9,85
Er	4,7	4,7	3,8	4,2	3,5	3,8	4,8	4,8	4,8	5,5	5,1	5,1
Yb	4	4,15	3,4	3,9	3,19	3,38	4,45	4,2	4,32	5	4,82	4,88
Th	3	2,7	3,05	2,75	2,2	2,3	3,4	2,8	3,8	4,35	4,05	4,4

Annexe 4 : Concentration en éléments majeurs (%) et traces (ppm) des basaltes Somali.

Echantillon	dj14/04c	dj09/04a	dj09/04b	dj09/04c	Z27-1	Z27-2	Z27-3	pk20-4	dj04/04a	dj 31/05b	dj21/04
Coordonnées géographiques	11°18'29"N 42°55'19"E	11°20'37"N 42°56'42"E	11°20'37"N 42°56'42"E	11°20'37"N 42°56'42"E	11°23'51"N 43°06'12"E	11°23'51"N 43°06'12"E	11°23'51"N 43°06'12"E	11°31'21"N 43°06'37"E	11°27'30"N 43°04'09"E	11°30'35"N 43°00'57"E	11°17'40"N 42°55'12"E
SiO_2	49,86	49,45	50,1	49,8	48,4	49,15	49,6	47,65	50	48,6	49,1
TiO_2	2,88	3,02	2,88	3,07	3,34	3,33	3,17	3,24	2,82	3,14	2,85
Al_2O_3	13,85	13,42	13,5	13,5	13,4	13,35	13,25	13,75	13,3	13,54	13,65
Fe_2O_3*	14,5	14,38	14,5	14,7	15,1	14,95	14,6	14,95	14,75	15,55	15,3
MnO	0,22	0,22	0,22	0,22	0,22	0,23	0,23	0,29	0,22	0,24	0,23
MgO	4,82	4,85	4,92	5	5,45	5,01	4,62	4,35	5,1	4,98	5,35
CaO	9,24	9,45	9,15	9,4	10,1	9,55	8,88	7,78	9,8	9,7	10,1
Na_2O	3,14	3,05	3,22	3	2,85	2,94	2,81	3,3	2,7	3,05	2,7
K_2O	0,76	0,63	0,67	0,77	0,8	0,73	0,93	0,72	0,67	0,58	0,37
P_2O_5	0,41	0,44	0,4	0,45	0,49	0,48	0,49	0,51	0,39	0,38	0,36
LOI	0,05	0,32	-0,12	-0,07	0,08	0,19	1,06	2,97	-0,01	-0,11	0,3
Total	99,72	99,23	99,44	99,84	100,23	99,91	99,64	99,51	99,74	99,65	100,31
Rb	10,3	17,4	17,3	16,5	15,9	17	17,9	16,8	13,6	9,7	8,8
Sr	320	323	317	325	343	331	277	254	277	365	282
Ba	220	212	212	240	205	214	230	242	187	236	150
Sc	34,5	34	36	32,5	36	34,5	35	35	37	35	37
V	388	370	395	390	398	396	405	230	395	440	390
Cr	29	50	29	44	52	35	49	10,5	46	20	44
Co	44	43	43	42	45	43	42	34	45	45	45
Ni	42	41	41	41	61	45	42	5	42	25	41
Y	42	44	41,5	44	45	47	53,5	58	44	38,5	44,5
Zr	256	281	264	275	288	291	342	222	242	190	245
Nb	31	34	32	33,5	33,5	35,5	34	34	26	26,5	25
La	27,5	28,5	27,5	29	29,5	29,9	34	24	23,5	22,5	23
Ce	61	62,5	62	66	68,5	69	75	52	53	51,5	54,5
Nd	36	37	35,5	37,5	41	41	44	32,5	32	31,2	32
Sm	8,1	8,6	8,25	8,6	9,15	9,1	9,7	8,4	7,6	7,3	7,75
Eu	2,56	2,64	2,54	2,72	2,88	2,87	2,99	2,9	2,44	2,39	2,56
Gd	8,6	8,8	8,2	8,6	9,2	9,2	10,45	9,5	8,1	7,5	8,1
Dy	8	8,05	7,85	8,4	7,9	8	10	10,1	8	6,8	7,95
Er	4	4,2	4	4,1	4,1	4,4	5	5,8	4,1	3,6	4,1
Yb	3,68	3,78	3,66	3,82	3,81	4,01	4,65	5,42	3,76	3,21	3,85
Th	3,2	3,15	3,45	3,35	3	2,9	3,4	2,45	2,7	2,3	2,3

Annexe 4 (suite) : Concentration en éléments majeurs (%) et traces (ppm) des basaltes Somali.

Echantillon	dj 66/05	dj 70/05c	dj72/05	dj116/05	dj75/06	dj85/06	dj124/05
Coordonnées géographiques	11°04'57"N 42°44'14"E	11°08'18"N 42°49'35"E	11°08'27"N 42°53'53"E	11°05'17"N 42°47'19"E	11°05'45"N 42°51'41"E	11°09'27"N 42°52'31"E	11°05'52"N 42°48'10"E
SiO_2	48	52,1	51,9	48,4	47,8	50,4	51
TiO_2	3,63	3,32	2,61	2,67	1,62	2,62	3,44
Al_2O_3	13,2	12,35	13,3	13,75	16,32	13,9	12,5
Fe_2O_3*	14,5	13,95	12,44	13,9	12	15,3	14,15
MnO	0,22	0,21	0,21	0,24	0,16	0,2	0,19
MgO	5,23	4,66	5,05	4,1	4,02	3,15	4,63
CaO	6,4	8,65	9,5	8,65	10,2	6,7	8,8
Na_2O	3,15	2,44	2,66	2,81	2,52	2,39	2,56
K_2O	0,87	0,7	0,83	0,81	0,64	1,87	0,79
P_2O_5	0,56	0,56	0,37	0,64	0,22	0,7	0,55
LOI	3,84	0,91	1,42	3,89	4,35	1,83	0,97
Total	99,6	99,85	100,29	99,86	99,85	99,06	99,58
Rb	31	9,9	19,7	14,8	7,4	26,6	17
Sr	386	445	242	394	355	363	440
Ba	280	323	184	325	300	770	290
Sc	29	29	34	22	29	23,5	28
V	404	396	348	255	291	281	405
Cr	47	53	156	2,5	21	12	54
Co	42	42	38	37	41	37	43
Ni	30	31	79	3	55	20	31
Y	33	34	51	36,5	28,5	51,5	35
Zr	226	250	294	177	116	282	255
Nb	23	22	31	30	8	28	22
La	23	22,5	28,5	27	13,6	56	22,5
Ce	51	53,5	64,5	60	31,5	118	53
Nd	35,5	34,5	37	35	18,3	62	34
Sm	7,9	7,9	8,75	7,6	4,45	12,1	8
Eu	2,57	2,57	2,59	2,54	1,54	3,1	2,6
Gd	7,8	7,6	9,3	7,4	5,3	10,8	7,1
Dy	6,4	6,2	9,1	6,6	4,9	8,6	6,4
Er	3,1	3	4,8	3,6	2,6	4,6	3,2
Yb	2,56	2,69	4,45	3,4	2,38	3,93	2,91
Th	1,95	2,1	3,3	2,85	1,1	3,25	2,35

Annexe 5 : Concentration en éléments majeurs (%) et traces (ppm) des basaltes d'Ali Sabieh.

Echantillon	dj62/05	dj 63/05	dj68/05	dj118/05	dj93/06	dj71/05	dj84/06	dj67/05
Coordonnées géographiques	11°08'05"N 42°48'09"E	11°08'02"N 42°48'09"E	11°09'27"N 42°42'07"E	11°05' 27"N 42°4 8'19"E	11°09'27"N 42°41'57"E	11°07'54"N 42°49'54"E	11°08'20"N 42°48'01"E	11°04'59" N 42°44'13" E
SiO_2	44	44,7	42,3	44,4	43	51,5	47,1	44,8
TiO_2	2,63	3,07	3,09	2,8	2,95	3,46	1,48	0,94
Al_2O_3	9,27	13,555	11,77	10,45	11,75	12,65	14,75	23,3
Fe_2O_3*	13,52	14	14,8	14,55	14,3	14,3	10,9	6,25
MnO	0,17	0,18	0,18	0,19	0,18	0,21	0,16	0,09
MgO	12,9	8,65	9,35	13,45	10,25	4,83	7,1	3,37
CaO	13,45	10,1	15,05	11,15	14,5	9,1	11,25	12,8
Na_2O	1,01	2,02	1,68	1,89	1,61	2,67	3,17	2,96
K_2O	0,53	0,98	0,46	0,47	0,41	0,4	0,39	0,87
P_2O_5	0,21	0,35	0,27	0,25	0,23	0,6	0,2	0,19
LOI	1,86	2,31	0,69	0,48	0,61	0,26	3,46	4,38
Total	99,55	99,91	99,64	100,08	99,79	99,98	99,96	99,95
Rb	13,2	20,3	22	20,2	15,1	14,7	6,1	28
Sr	445	543	458	470	436	518	658	825
Ba	240	332	250	225	212	468	131	128
Sc	40,5	30,5	43	35	46,5	30	35	16
V	390	346	490	335	457	428	286	157
Cr	820	200	330	565	405	57	121	72
Co	78	60	70	74	61	45	43	23
Ni	270	130	138	286	132	33	61	36
Y	16	24,5	19,7	19,5	18,5	35,5	20,4	12,4
Zr	138	215	156	153	145	255	95	57
Nb	22,5	37	28,2	26	25	23	11,3	7,2
La	19,5	31	21	23	20	22,5	11,5	7
Ce	43	68	48	53	46	53,5	25,5	14,5
Nd	25	38,5	27,5	29	27,5	34,5	15	8,7
Sm	5,6	7,4	6,25	6,2	5,65	8,1	3,55	2,3
Eu	1,7	2,37	1,94	1,96	1,8	2,65	1,26	0,92
Gd	4,45	6,7	5	5,1	4,85	7,8	3,7	2,5
Dy	3,3	5	4	4,1	3,75	6,45	3,45	2,2
Er	1,4	2,1	1,7	1,8	1,7	3,1	2	1,2
Yb	1,15	1,85	1,44	1,5	1,41	2,72	1,84	1,02
Th	1,8	3,15	2,2	2,25	1,9	2,15	1,3	0,85

Annexe 5 (suite) : Concentration en éléments majeurs (%) et traces (ppm) des basaltes d'Ali Sabieh.

Echantillon	dj41/05	dj92/05	dj9305	dj 95 /05	dj94/05	dj49/05*
Coordonnées géographiques	11°31'17"N 42°53'34"N	11°29'44"N 42°50'07"N	11°32'30"N 42°48'41"N	11°32'23"N 42°52'13"N	11°32'21"N 42°48'36"N	11°50'48"N 42°55'06"E
SiO_2	47,7	46,75	47,8	47,1	47,7	52,6
TiO_2	1,9	1,97	1,71	2,08	1,75	1,82
Al_2O_3	15,1	14,86	15,1	15,1	15	15,1
Fe_2O_3*	14	13,35	13,4	13,6	13,6	12,88
MnO	0,21	0,2	0,21	0,2	0,21	0,27
MgO	6,72	7,11	7,87	7,05	7,8	2,25
CaO	11,5	12,1	11,04	11,3	11	6,1
Na_2O	2,6	2,47	2,62	2,55	2,59	4,52
K_2O	0,31	0,3	0,31	0,28	0,34	1,57
P_2O_5	0,25	0,24	0,22	0,26	0,22	0,91
LOI	-0,23	0,16	-0,27	0,09	-0,26	1,16
Total	100,06	99,51	100,01	99,61	99,95	99,18
Rb	5,5	6	6,5	6	4,6	28
Sr	234	240	282	249	220	392
Ba	130	129	333	132	127	605
Sc	40	40	37	40	38	19,5
V	378	356	348	360	350	46
Cr	74	87	235	84	232	3
Co	56	52	52	50	52	14
Ni	69	82	123	80	120	1,5
Y	28,5	27,5	28	28	29	68
Zr	102	109	94	113	93	400
Nb	15,2	14,7	14	16	14,5	58
La	11,5	11,5	10,5	13	11	51
CN	25	25,5	22	29	25	111
Nd	15,5	16	14,5	17,5	13,8	62
Sm	4,1	4,25	3,9	4,5	4,15	13,8
Nu	1,52	1,5	1,43	1,58	1,49	4,38
Gd	4,9	4,65	4,65	5,25	4,8	14
Dy	4,95	4,7	4,9	5	4,9	12,1
Nr	2,7	2,6	2,8	2,8	2,9	6,4
Yb	2,56	2,46	2,69	2,61	2,7	5,8
Th	1,05	0,9	1,15	1,1	1,15	5,15

dj49/05* : échantillon provenant d'une intrusion de la série acide de Ribta.

Annexe 6 : Concentration en éléments majeurs (%) et traces (ppm) des basaltes Stratoide I.

Echantillon	dj 44/05	dj 46/05	dj47/05	dj 52/05
Coordonnées géographiques	11°29'15"N 42°42'38"E	11°28'54"N 42°43'35"E	11°28'39"N 42°44'49"E	11°26'17"N 42°46'35"E
SiO_2	45,7	45,3	45,4	45,2
TiO_2	3,78	3,6	3,6	3,72
Al_2O_3	12,9	13,1	13,1	12,85
Fe_2O_3*	18,3	18	18,69	19,6
MnO	0,26	0,26	0,26	0,28
MgO	5,52	5,82	5,72	5,3
CaO	9,75	10,15	9,9	9,4
Na_2O	2,71	2,66	2,65	2,79
K_2O	0,56	0,57	0,53	0,42
P_2O_5	0,49	0,47	0,49	0,4
LOI	-0,63	-0,16	-0,61	-0,44
Total	99,34	99,77	99,73	99,52
Rb	13	11,2	11	7,5
Sr	255	255	256	260
Ba	200	197	290	184
Sc	42	40	39,5	44
V	440	410	475	492
Cr	58	58	67	29
Co	50	50	59	55
Ni	61	66	72	43
Y	53	52	51,5	46
Zr	264	252	245	202
Nb	31	29	29,5	23
La	25	26	24	20
Ce	57	57	54	45
Nd	36,5	36	34	30,5
Sm	8,5	8,5	8,25	7,4
Eu	2,87	2,69	2,66	2,45
Gd	9,8	9,1	8,85	8
Dy	9,1	8,8	8,85	8
Er	5,1	5,1	4,7	4,5
Yb	4,82	4,8	4,45	4,24
Th	2,35	2,35	2,45	1,55

Annexe 7 : Concentration en éléments majeurs (%) et traces (ppm) des basaltes Stratoide II.

Echantillon	dj19/06	dj10/06	dj21/06	dj23/06*
Coordonnées géographiques	11°56'07"N 43°04'29"E	11°52'02"N 42°54'34"E	11°55'19"N 43°05'20"E	11°55' 39"N 43° 6'26"E
SiO_2	69,5	77,2	71,8	73,75
TiO_2	0,32	0,1	0,32	0,35
Al_2O_3	11,25	10,95	10,03	10,15
Fe_2O_3*	3,41	2,14	4,22	4,41
MnO	0,12	0,03	0,12	0,13
MgO	0,32	0,11	0,15	0,41
CaO	1,72	0,25	0,39	0,59
Na_2O	3,98	4,1	2,11	3,34
K_2O	1,05	3,6	3,32	4,32
P_2O_5	0,03	0,03	0,02	0,01
LOI	7,68	0,69	6,96	1,78
Total	99,38	99,2	99,44	99,24
Rb	45,5	180	150	82
Sr	281	12	18	26
Ba	900	2	220	192
Sc	3,8	0,2	5	0,6
V	4	10	3	11
Cr	2	3	3	3
Co	0,6	1	0,5	0,5
Ni	1	1,5	1	1,5
Y	80,5	215	109	97,5
Zr	772	394	826	815
Nb	92	164	94	93
La	92	37,3	104	53
Ce	185	69,5	205	212
Nd	85	50,5	101	66
Sm	16,5	15	20	15
Eu	2,33	0,68	3,35	2,48
Gd	15	20,7	19	16,2
Dy	14,2	28,6	18,2	16,1
Er	7,8	19,3	10,5	9,7
Yb	7,46	18,9	10,1	9,35
Th	15	28,5	16,3	14,9

dj23/06* : échantillon d'un ignimbrite provenant de la région située au nord du Golfe de Tadjoura

Annexe 8 : Concentration en éléments majeurs (%) et traces (ppm) des obsidiennes et ignimbrite échantillonnés au nord du Golfe de Tadjoura.

Echantillon	dj 42/05	dj 53/05	dj 54/05	dj55/05	dj56/05	dj58/05	dj 59/05	dj 79/05
Coordonnées	11°27'54"N	11°26'17"N	11°12'10"N	11°11'44"N	11°10'59"N	11°12'43"N	11°13'07"N	11°26'12"N
géographiques	42°46'04"E	42°46'35"E	42°40'29"E	42°40'24"E	42°40'24"E	42°40'20"E	42°40'17"E	42°59'27"E
SiO_2	43,8	55	48,1	48,65	48,3	48,2	48,3	49,5
TiO_2	2,7	1,56	3,28	3,45	3,8	3,38	3,4	3,01
Al_2O_3	16	15,38	12,9	12,73	12,59	12,6	12,76	13,65
Fe_2O_3*	15,3	12,4	15,85	15,55	16,25	16,05	16,02	14,88
MnO	0,24	0,28	0,24	0,23	0,24	0,23	0,23	0,23
MgO	3,78	1,98	5,68	5,45	5,63	5,6	5,6	4,93
CaO	9,65	5,64	10,05	9,75	10	10,15	9,95	9,35
Na_2O	2,66	4,82	2,7	2,64	2,55	2,7	2,72	3,13
K_2O	0,48	1,75	0,59	0,76	0,78	0,64	0,64	0,62
P_2O_5	0,29	0,73	0,47	0,51	0,59	0,49	0,49	0,38
LOI	4,92	0,29	-0,42	-0,16	-0,42	-0,21	-0,53	0,1
Total	99,82	99,83	99,44	99,56	100,31	99,83	99,58	99,78
Rb	7,7	31,5	8,6	16,7	12,7	9,8	11,1	12
Sr	445	388	280	292	273	278	280	353
Ba	214	690	216	275	279	243	203	217
Sc	31	19	42	37	40	44	41	33
V	364	26	500	475	505	492	492	392
Cr	69	5,5	86	102	93	80	84	29
Co	55	11	46	45	45	46	45	42
Ni	74	1,5	64	74	67	63	62	26
Y	26	70	48	53	58	49,5	49	40
Zr	126	445	240	305	330	260	245	210
Nb	17,7	62	25	32	34	29	26	29
La	14	53	24	29,5	32,5	24,5	24	25
Ce	31	114	54	68,5	75	57	54	56
Nd	20	64	34	40,5	45	35,5	35,5	33,5
Sm	4,8	13,7	8	9,35	10,7	8,6	8	7,5
Eu	1,91	4,45	2,63	2,85	3,1	2,73	2,7	2,46
Gd	5,55	13,9	8,8	10	11,4	8,85	9,1	7,8
Dy	4,9	12,5	8,5	9,15	10,3	8,85	8,6	7,3
Er	2,45	6,7	4,5	5	5,6	4,6	4,6	3,7
Yb	2,2	6,25	4,23	4,4	5,04	4,33	4,3	6,25
Th	1,25	5,75	2,45	2,95	2,8	2,1	2,1	5,75

Annexe 9 : Concentration en éléments majeurs (%) et traces (ppm) des basaltes de la série de Dalha.

Echantillon	dj22/06	dj29/06	dj04/06	dj07/06	dj05/06	dj52/06	dj32/06	dj 83/05	dj85/05
Coordonnées géographiques	11°55'31"N 43°05'57"E	12°22'37"N 43°17'55"E	11°50'55"N 42°39'49"E	11°51' 06"N 42°4 0'36"E	11°54'17"N 42°37'07"E	11°52'13"N 42°54'07"E	11°21'37"N 43°09'32"E	11°27'35"N 42°59'28"E	11 °28'09"N 42°59'57"E
SiO_2	47,9	44,9	45,8	46,6	45,6	45,35	45,7	68,7	69,1
TiO_2	2,15	3	3,4	2,82	3,09	3,66	1,84	0,69	0,68
Al_2O_3	14,73	16,05	13,55	14,07	13,63	13,64	14,55	12,93	12,9
Fe_2O_3*	13	14,3	15,5	14,15	14,78	15,76	12,68	4,53	4,46
MnO	0,22	0,2	0,21	0,2	0,23	0,24	0,15	0,12	0,12
MgO	6,22	5,8	5,48	5,86	5,57	6,28	8,95	0,64	0,6
CaO	9,35	10,45	10,1	11,1	11,7	9,35	9,55	1,96	1,9
Na_2O	2,88	3,09	2,8	2,6	2,76	2,72	2,12	3,57	3,72
K_2O	0,58	0,62	0,59	0,51	0,55	0,58	0,34	3,74	3,22
P_2O_5	0,43	0,4	0,38	0,3	0,36	0,58	0,24	0,13	0,14
LOI	2	1,01	2,14	2,2	1,56	1,83	3,85	2,47	2,37
Total	99,46	99,82	99,95	100,41	99,83	99,99	99,97	99,48	99,21
Rb	8,6	11,9	9,5	7,7	8,7	10	6,1	103	83
Sr	296	495	367	370	388	334	304	134	128
Ba	221	298	200	190	220	278	139	665	615
Sc	30	27	39	39	365	33,5	30	7,4	7,5
V	270	345	456	400	415	356	267	13	14
Cr	68	41	75	184	110	106	315	4	4
Co	42	50	47	48	49	45	54	2,5	4
Ni	47	66	47	71	62	57	174	2	2
Y	39	31	34	26	31	43,5	22,5	89	90
Zr	242	191	190	146	162	250	115	603	610
Nb	22,5	27	28	21,5	25,5	24,5	12	86	89
La	22	21	22,4	17,2	21,5	24	11,8	81	81
Ce	49	47	49	39,5	46	54	26,5	165	167
Nd	32	30	30,5	24,5	29	36	17	78	78
Sm	7,3	6,9	7	5,45	6,8	8,4	4,35	15	15,9
Eu	2,42	2,35	2,4	1,98	2,3	3,09	1,6	2,81	2,85
Gd	7,6	6,9	7	5,6	6,45	9,2	4,5	15,2	15,1
Dy	7	5,8	6,5	5,1	6	7,8	4,15	14,4	14,7
Er	3,6	2,8	3,2	2,5	2,9	4	2,1	8,7	9
Yb	3,42	2,6	2,86	2,22	2,64	3,67	1,88	8,5	8,62
Th	1,35	2,05	1,7	1,45	1,9	1,85	1	14,8	15

Annexe 9 (suite) : Concentration en éléments majeurs (%) et traces (ppm) des basaltes de la série de Dalha.

Echantillon	dj70/05 d	dj125/05
Coordonnées géographiques	11°08'18"E 42°49'35"E	11°07'43"N 42°49'05"E
SiO_2	76,5	76
TiO_2	0,31	0,3
Al_2O_3	9	8,95
Fe_2O_3*	6,4	6,3
MnO	0,02	0,06
MgO	0,27	0,58
CaO	0,11	0,24
Na_2O	0,28	1,82
K_2O	4,46	2,55
P_2O_5	0,03	0,03
LOI	1,41	2,37
Total	98,79	99,2
Rb	113	64
Sr	11	22
Ba	270	124
Sc	0,7	0,7
V	13	26
Cr	21	4
Co	1,5	1
Ni	2,5	2
Y	56	65
Zr	455	415
Nb	148	131
La	78	96
Ce	163	184
Nd	74	81
Sm	15	15,4
Eu	2,25	2,2
Gd	12	13,2
Dy	9,9	11,2
Er	6	6,25
Yb	7,3	6,5
Th	9,2	13

Annexe 10 : Concentration en éléments majeurs (%) et traces (ppm) des dykes acides de la région d'Ali Sabieh.

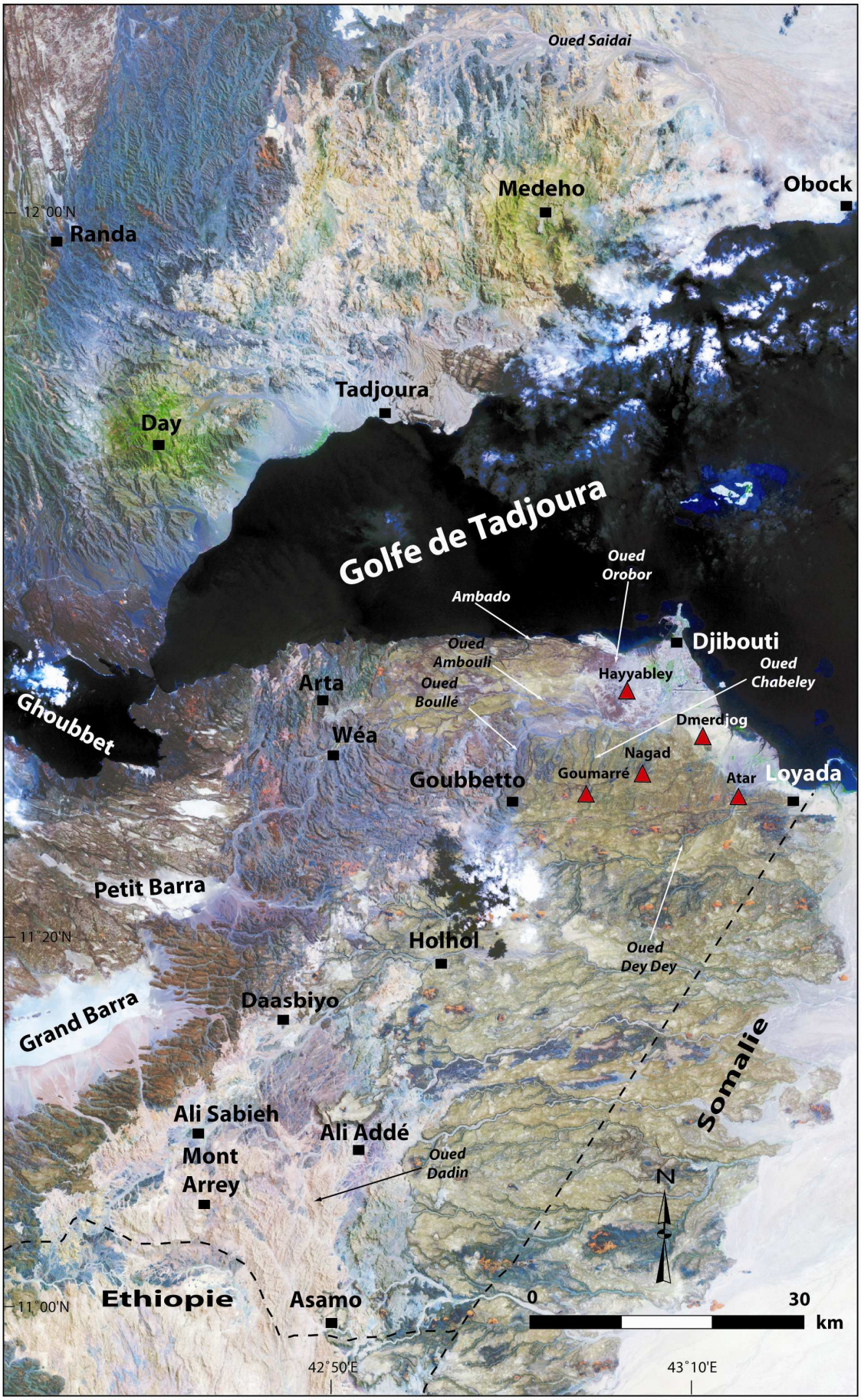
Oued Saidai
Medeho
Obock
12°00'N
Randa
Tadjoura
Day
Golfe de Tadjoura
Oued Orobor
Ambado
Djibouti
Oued Ambouli
Oued Boullé
Oued Chabeley
Hayyabley
Arta
Ghoubbet
Dmerdjog
Wéa
Nagad
Goumarré
Atar
Loyada
Goubbetto
Petit Barra
11°20'N
Holhol
Oued Dey Dey
Daasbiyo
Grand Barra
Somalie
Ali Sabieh
Ali Addé
Mont Arrey
Oued Dadin
N
Ethiopie
11°00'N
Asamo
0
30
km
42°50'E
43°10'E